New Host-Guest Materials for Light Conversion

By

Umar Sani

A thesis submitted in partial fulfilment of the requirements for the degree of

Doctor of Philosophy

School of Natural and Environmental Sciences

November 2022

Declaration

I hereby certify that this work is my own, except where otherwise acknowledged. Neither the thesis nor any of the original work comprising it has been submitted previously for a degree at this or any other University.

Dedication

This research is dedicated to my parents (Sani Adamu and Zulaihat Yunusa) and my late sister (Raliya Sani Adamu). May the Jannatul Firdaus be her final abode.

iv

Table of contents

Abstract

The studies reported in this PhD thesis describe the synthesis and optical properties of new light-harvesting materials, built using organic and organometallic chromophores as guests in a rigid host. Mesoporous silica was chosen as host because of its robustness, high chemical and thermal stability. Different dyes were successfully incorporated within specific sites of the host, that is, into micellar templates and inside the silica framework itself. To achieve such specific functionalisation, new self-assembly strategies were developed, and the obtained materials possess ordered structures and emergent optical properties.

Zinc and boron dipyrrins were inserted as guest dyes inside the micellar structures used to template the formation of the silica host (Chapters 3 and 5). The combined host-guest materials showed enhanced fluorescence efficiencies at low dye content, whereas at high concentrations in the template structure inner-filter effects are found to prevail.

Mesoporous organosilica materials (PMOs) were made for the first time using zinc quinolinolates and BOPHY dyes within the host structure (Chapters 4 and 6). The organometallic complexes undergo a significant increase in fluorescence efficiency at high concentrations in the PMO structure. Incorporation into the solid network also proved to induce charge-recombination fluorescence. The same phenomenon was observed in the BOPHY-based PMOs. Additionally, the latter materials showed fast energy migration between the single units of dye in the network. Such properties make the materials promising for application in light-harvesting and sensitisation technologies, as well as in lightings and the design of new OLEDs.

Acknowledgements

All praise and salutations are due to Allah, the lord and sustainer of the world; glory be to Him for providing me with knowledge and ability towards the successful compilation of this research.

I want to thank the best and outstanding supervisor, Dr Fabio Cucinotta, who has been committed and helpful throughout this research. He has been very kind, always ready to advise, commitments to intellectual support and guidance throughout the research; without him, this research wouldn't have been successful.

My profound and sincere gratitude goes to my parents for having the courage and wisdom to send me to school despite their meagre earnings. I wish to thank the Federal Government of Nigeria under the Petroleum Technology Development Fund Oversea Scholarship Schemes (PTDF/OSS) for giving me a rare opportunity and finding me worthy among the two hundred million people in the country to sponsor my M Sc and PhD studies in one of the world-class universities. I will forever remain indebted.

I would be ungrateful if I did not include my lovely wife (Fadila Ado Yusuf) for her excellent understanding and help throughout. The same also goes to my brothers and sisters in this acknowledgement; my eldest sister and brother (Hajiya Maryam and Barrister Hayatu) and my younger brothers and sisters (Barrister Aminu, Barrister Hamza, Abubakar, Usman, Aliyu and Amina, Aisha, Zainab and Khadija). This acknowledgement will be incomplete if I did not include my lovely children (Radeeya, Abdullahi, Abdurrahman and Khadija Umar Sani), May Allah blesses you and be your guide at all times.

I would like to thank all the members of Dr Fabio Cucinotta's group, especially Ben Jarman, Dr Marina Santana, Ruth Pollard, Abbi Mullins, and Thomas. In this piece of acknowledgement, our research collaborators are worth mentioning: The KIT group in Germany and Dr Julian Knight's group.

Life is so brief and precise; in the course of this program, I lost my grandmother (Hajiya Halima), aunt (Gwaggo Mino) and two good friends (Abdullahi Sadiq Dakin Gari and Shafiu Saidu), may their gentle souls continue to rest in peace. I have come across so many people in the course of this

Abbreviations

BODIPY: Boron Dipyrromethene

BOPHY: Bis(difluoro*bo*ron)-1,2-bis((1H-*p*yrrol-2-yl)methylene)*hy*drazine

$CDCl_3$: Deuterated Chloroform

CMQ: 5-chloromethyl-8-quinolinol

^{13}C-NMR: Carbon 13 Nuclear Magnetic Resonance

COK: Centrum voor Oppervlaktechemie & Katalyse

CT: Charge Transfer

CTAB: Cetyltrimethylammonium bromide

DCM: Dichloromethane

DDQ: 2,3-Dichloro-5,6-dicyano-1,4-benzoquinone

DSSC: Dye-Sensitised Solar Cells

FWHM: Full Width at Half-Maximum

HCl: Hydrochloric Acid

^{1}H-NMR: Proton Nuclear Magnetic Resonance

HOMO: Highest Occupied Molecular Orbitals

HR-ESI-MS: High-Resolution Electrospray Ionization Mass Spectrometry

HPLC: High Performance Liquid Chromatography

IC: Internal Conversion

ILCT: Intraligand Charge Transfer

KIT: Karlsruhe Institute of Technology

LC: Ligand Centred

LC-MS: Liquid Chromatography Mass Spectrometry

LH: Light Harvesting

LLCT: Ligand-to-ligand Charge Transfer

LUMO: Lowest Unoccupied Molecular Orbitals

MCM: Mobil Composition of Matter

MeOH: Methanol

MHz: Megahertz

MLCT: Metal-to-ligand Charge Transfer

3-MPTMS: 3-mercaptopropyl-trimethoxysilane

NIR: Near Infrared

ns: Nanosecond

OLEDs: Organic Light Emitting Diodes

PDT: Photodynamic Therapy

PMMA: Poly(methyl methacrylate)

PMO: Periodic Mesoporous Organosilica

ps: Picosecond

PV: Photovoltaic

PXRD: Powder X-ray Diffractometry

RET: Resonance Energy Transfer

SAXS: Small angle X-ray Scattering

SBCT: Symmetry-Breaking Charge-Transfer

TEM: Transmission Electron Microscope

TEOS: Tetraethyl Orthosilicate

TFA: Trifluoromethylacetic Acid

TLC: Thin-layer chromatography

THF: Tetrahydrofuran

TCSPC: Time-Correlated Single-Photon Counting

UV: Ultraviolet

Chapter 1: Introduction

1.1   Introduction

The life of humans on earth relies on energy consumption. It was reported in 2020 that 80% of this energy is directly obtained from fossil fuels.[1,2] This remains the primary source for greenhouse gases emission leading to global warming and ozone layer depletion.[3,4] Since the 1970s, there has been an increasing concern about the limited availability of fossil fuels and, concomitantly, a keen commitment in the scientific community to study the causes of climate change, particularly the anthropogenic ones: rapid population growth, industrial revolutions for more than a century.[5] Ever since the drive for moving towards a greener and more environmentally friendly energy resources has grown significantly. Several technologies have been developed through which energy can be captured, stored and converted for future usage, as the world proven reserves are at the peak of declining.[6–8] Some of these technologies are already available in the energy market, for example, wind and solar electricity. The latter is particularly attractive, considering that the energy delivered to the earth from sunlight is about 430 quintillion Joules per hour, which is more than the current global energy demand (410 quintillion Joules of energy per year)[9] and even more than that available from any other artificial or natural sources.[10] Nevertheless, renewable technologies such as solar, are still in a continuous development phase, as their performances present vast room for improvement. That is the case for photovoltaic (PV) cells, dye-sensitised solar cells (DSSCs) and photoelectrochemical cells, where progress needs to be made in regard to energy conversion efficiency, long-term stability and the costs of sourcing and processing materials.

Photoelectrochemical cells are drawing constant interest and efforts in research, especially for the prospect of fuels generation. An example of such type of device is a water-splitting cell, where sunlight is used to trigger the production of oxygen and hydrogen from water, or when coupled with a CO_2 reduction system, can be used to produce syngas or methanol. However, the conversion mechanisms responsible for producing hydrogen and methanol are quite complex, and the overall fuel production efficiency is still low. Moreover, the highest performances of such devices are generally obtained under intense illumination conditions, a situation far from the usual. Indeed, sunlight exposure varies depending on the time of the day, the season and the geographical region of the earth. In countries like the UK, for example, which sits at high latitudes and where sunlight energy is diffused rather than concentrated, capturing and storing this energy is challenging. A different situation is found at low latitudes, that is in the hot temperature regions, where

3

illumination is optimal, but solar technologies are not sufficiently developed or, in some cases, not present. The above are just some of the big challenges that the modern research in photochemistry is currently tackling.
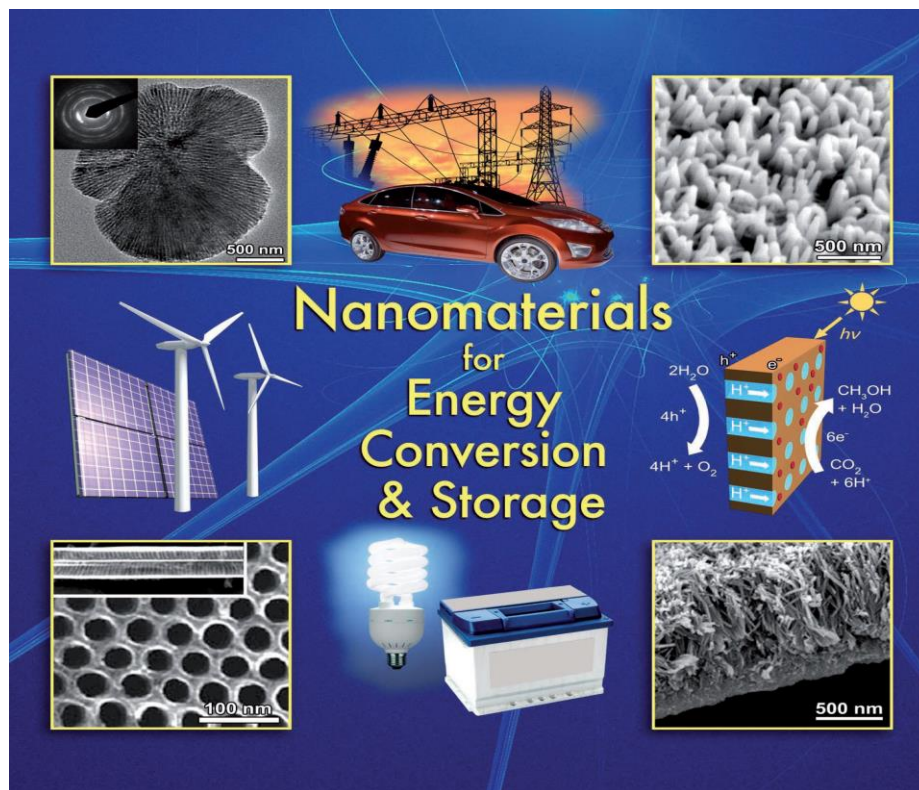
Figure 1.1: Alternative sources of energy and ways in which materials are used for energy capture and storage.[7]

1.1 General Features of Photosynthesis

In the quest for alternative and renewable energy sources and technologies by the scientific community, photocatalysis has always been looked at with interest, inspired by the use that plants make of it in the form of photosynthesis, since even before the existence of humans. The natural materials exhibited in plants and some organisms are complex and ordered structures made from simple constituents that include polymers and minerals. Nature also makes its materials so that they are highly organised, making it easy to adapt to environmental changes, repair for growth and survival. The mechanism of these relationships in the highly organised natural system is directed through energy transfers. Examples of this energy cascade in the biological system are the green

4

leaves; in these organisms, there is efficient light-harvesting and utilisation of sunlight to useful energy at maximum. These organisms are good examples of nature's design to capture, store and converts energy into a useful form.[11] A simple example could be seen in the cell membranes of *Rhodopseudomonas acidophilia*, a class of purple photosynthetic bacteria (see scheme in **Figure 1.2**).
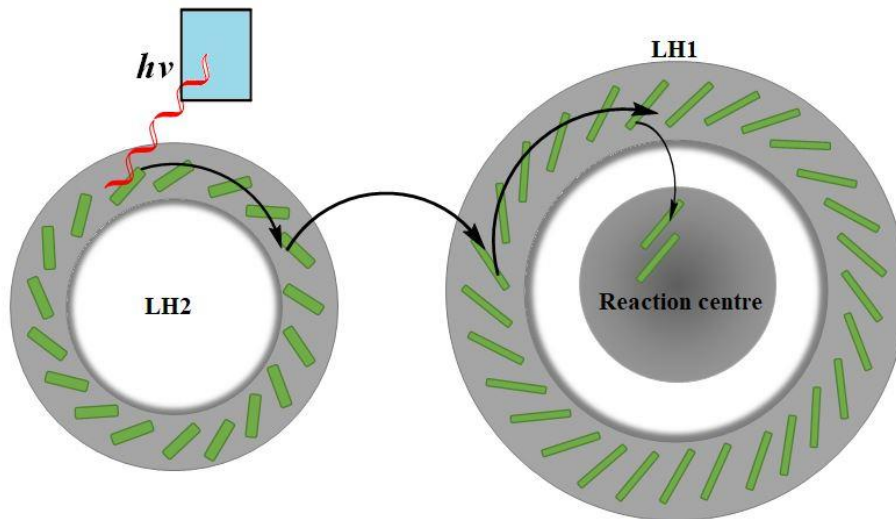
Figure 1.2: A schematic diagram of how light is harvested, arranged and transformed in chemical energy among the bacterio-chlorophyll units of Rhodopseudomonas acidophilia. High-energy photons are absorbed by a light-harvesting ring structure (LH2), transferred to a low-energy 'antenna' (LH1) and finally delivered to a reaction centre.

In higher plants, they have a more complicated system that is located in the chloroplasts, but the overall mechanism is the same.[12–14] The cells of plants and bacteria have specialised light-harvesting units through which photons are absorbed directly from the sunlight and stored in the desired locations where they can be used for chemistry. As shown in **Figure 1.2**, organised systems of chromophores absorb photons at different energies, transfer the excitation energy across the organism, and then use it to activate reaction centres this is a typical example of an antenna system. In the latter, the energy is used to catalyse the synthesis of glucose from CO_2, while oxygen is given up as a by-product. Nature has its way of simultaneously fixing carbon available in the atmosphere and forming chemical feedstocks.[15]

Within their complex light-converting architectures, molecules such as chlorophylls play a fundamental role, and they usually represent the starting point for the construction of artificial photosystems. The next section introduces the basic mechanisms of light absorption and conversion by such molecules.

1.2 Photophysical Transitions in Molecules

The physical and chemical properties of a molecule are largely determined by the electronic configuration. Therefore, knowing how electrons are distributed across chemical bonds within a molecule, the type of bonds they form and the corresponding energy states is of fundamental importance.[16,17] This allows us to understand chemical reactivity and the ability of a molecule to interact with light.

When light is irradiated on a molecule, the ground state electrons use energy from the light to undergo transitions to higher-energy orbitals. This determines a change in electronic configuration, which is then termed as an electronically excited state. Typically, the absorption of photons of appropriate energy will cause the population of excited states by promoting electrons from the highest occupied molecular orbital to the lowest unoccupied molecular orbital (HOMO → LUMO transition). In the excited state, the orientation of the spin remains the same in most cases, and a classical HOMO → LUMO transition is referred to as a spin-allowed transition.

Most ground state molecules have a closed shell structure, where the molecular orbitals contain two paired electrons and define the electronic levels. The spin multiplicity of the electronic levels can be determined by using the 2S+1 expression, where S is the sum of the total individual electronic spins. Since most ground-state electrons are paired, the value of $S = 0$; therefore, the spin multiplicity is 1, and the state is said to be a singlet. When an electronic transition such as light absorption generates an excited state, normally the excited electron maintains its original spin, and the excited state is a singlet too. In some exceptional cases, though, the electron might undergo a spin change while transitioning and, from the expression above, S will be equal to 1 and the state is said to be triplet (see **Figure 1.3**).

$\pi*$ ———	$\pi*$ $\downarrow$	$\pi*$ $\downarrow$	$\pi*$ $\uparrow$	$\pi*$ $\uparrow$
n $\uparrow\downarrow$	n $\uparrow$	n $\uparrow\downarrow$	n $\uparrow$	n $\uparrow\downarrow$
π $\uparrow\downarrow$	π $\uparrow\downarrow$	π $\uparrow$	π $\uparrow\downarrow$	π $\uparrow$

$S = 0$	$S = 0$	$S = 0$	$S = 1$	$S = 1$
$2S + 1 = 1$	$2S + 1 = 1$	$2S + 1 = 1$	$2S + 1 = 3$	$2S + 1 = 1$
Singlet	Singlet	Singlet	Triplet	Triplet
S_0	$S_1 (n \rightarrow \pi*)$	$S_2 (\pi \rightarrow \pi*)$	$T_1 (n \rightarrow \pi*)$	$T_2 (\pi \rightarrow \pi*)$
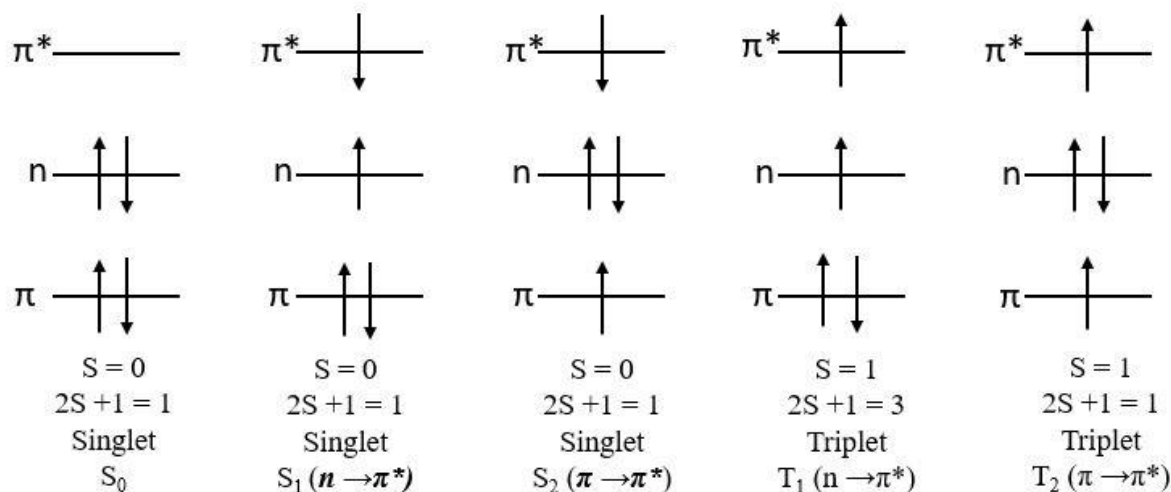
Figure 1.3: Ground and electronically excited-state configurations of small organic compounds. Readapted from reference 17.

A singlet-to-triplet transition is normally classed as a spin-forbidden transition, because of the spin conservation rule, but it may be observed with a small intensity in an absorption spectrum due to the so-called heavy-atom effect.[17]

In small organic molecules, the lowest singlet state S_1 and triplet state T_1 are generated by the promotion of electrons from the n molecular orbital to the $\pi*$ molecular orbital, while the S_2 and T_2 excited states are the results of electron promotion from a π molecular orbital to the $\pi*$ molecular orbital. However, the situation depicted in **Figure 1.3** is only applicable to organic molecules with low electron density. Larger molecules such as metal complexes with high electron density have molecular orbitals that are densely populated and hybridised or mixed across different atoms, making it very difficult to draw a clear-cut distinction between metal-centred and ligand-centred orbitals.[17,18]

Once electronically excited, all molecules reside for a very short time span in the excited state before dissipating their excess energy and returning to the ground state configuration. The release of the absorbed energy by the excited-state molecules can take different forms: it can be partly or entirely in the form of heat, through intramolecular vibrations or collisions with other molecules (e.g. solvent), and this is known as non-radiative decay; or it can take the form of photon emission, which is a radiative transition. The latter is normally a fast spin-allowed transition ($S_1 \rightarrow S_0$) and

it is known as fluorescence, which has a lifetime in the ps-ns range. In the presence of heavy atoms within the molecular structure (e.g. in transition metal complexes), though, the spin-orbit coupling can induce a spin transition on the excited electron, turning the single state S_1 into a triplet state T_1. The excited triplet can then decay to the ground singlet state by light emission in the form of phosphorescence, which, being a spin-forbidden process, takes longer than fluorescence to occur (up to milliseconds or even seconds).

The processes of excitation, fluorescence and phosphorescence in both organic and inorganic molecules are summarised using a Jablonski diagram in **Figure 1.4**.
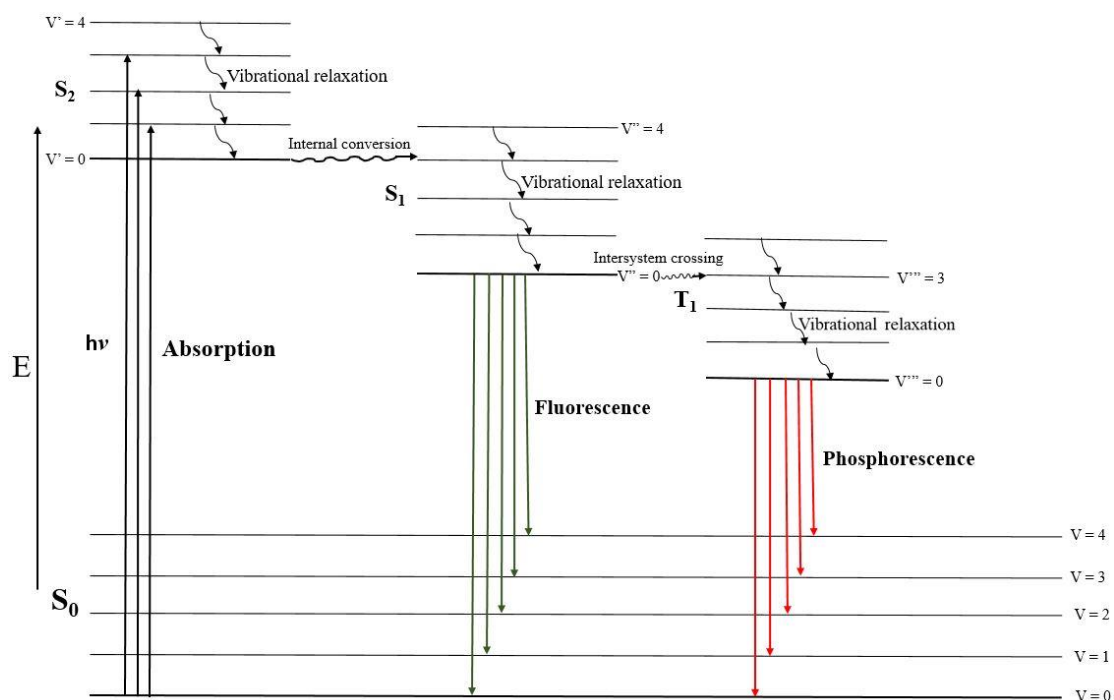
Figure1.4: Jablonski diagram showing the photophysical processes occurring in molecules; readapted from reference 17.

As shown in **Figure 1.4**, higher-lying excited states such as S_2 undergo rapid internal conversion to populate the lowest-lying S_1 state. This is a non-radiative transition and it typically occurs from the lowest vibrational sub-level of the S_2 state to the iso-energetic vibrational sub-level of the S_1 state. From the latter, fast vibrational relaxation brings the molecule down to the lowest vibrational sub-level, a process often termed as state equilibration, where the molecular geometry slightly

rearranges to find its minimum energy configuration. The same kind of process might occur concomitantly with a spin transition, and this takes the name of intersystem crossing.

The natural dye molecules or pigments present in photosynthetic organisms perform the processes described above of light absorption and energy conversion between electronic states with minimal non-radiative or thermal losses. Specific energy-harvesting units act as energy donors towards other units and eventually reaction centres, and the overall efficiency of the conversion process is guaranteed by the high organisation of pigments and enzymes within scaffold structures.

1.3 Host Structures in Light-harvesting Systems

Natural photosynthesis utilises protein membranes as scaffolds where molecules like chlorophylls absorb and channel the excitation energy to suitable reaction sites, in a process that dampens thermal losses and provides long-term stability.[19]

Many artificial light-harvesting systems mimic the energy transfer cascades exhibited in nature by using nanostructured materials; these are often assembled via non-covalent interactions as in the chlorophyll-protein complexes present in green plants. Non-covalent chemistry has been used to build supramolecular photosystems such as dendrimers, multi-porphyrin arrays, organo-gels, polymers, etc., whereby chromophores can perform directional energy transfer.[20]

However, these examples usually operate in a solution phase or at liquid interfaces, which imply high reorganisation energies and ultimately cause low conversion yields. Also, such systems tend to photo-degrade over time upon exposure to light, and the lack of self-repairing mechanisms makes them inadequate for industrial-scale applications. A strategy to circumvent this limitation consists in using host materials such as nano-containers to form photosystems where molecular dyes are highly organised in the available space.[21] Host-guest chemistry offers a promising way to achieve this, with many examples of light-harvesting systems reported in the literature, making use of porous hosts such as zeolites, metal-organic frameworks and layered clays with pore sizes from less than 2 nm up to half a micron.[21–23]

1.3.1 **Mesoporous Silicates**

An appealing class of scaffold-like materials that can be considered for light-harvesting applications is mesoporous silica. The development of porous silicates was aimed at tackling the disadvantages and size limits of zeolites, which can not accommodate guest molecules larger than 4-7 Å.[24]

Research on porous silicates began in 1992 when Kresge's group at the Mobil Oil Company developed the first periodic mesoporous silica known today as the M41S phase.[25] The synthesis was based on a sol-gel synthetic route that uses a pre-assembled template to generate the porous structure.[25] The process is schematised in **Figure 1.5**. An amphiphilic surfactant is added in water past its critical micellar concentration. It then self-assembles into spherical micelles, with the hydrophilic and hydrophobic ends of the linear structure pointing, respectively, outwards to the water interface and inwards to the centre of the micelles. The spherical micelles may merge into rod-like structures under certain reaction conditions, such as a high concentration of surfactant or the addition of ionic species that favour electrostatic binding. One of such species is often the silica precursor itself, that is tetraethyl orthosilicate (TEOS) or sodium silicate; when this hydrolyses, it starts polymerising around the micelles, keeping them arranged into a hexagonal columnar array.
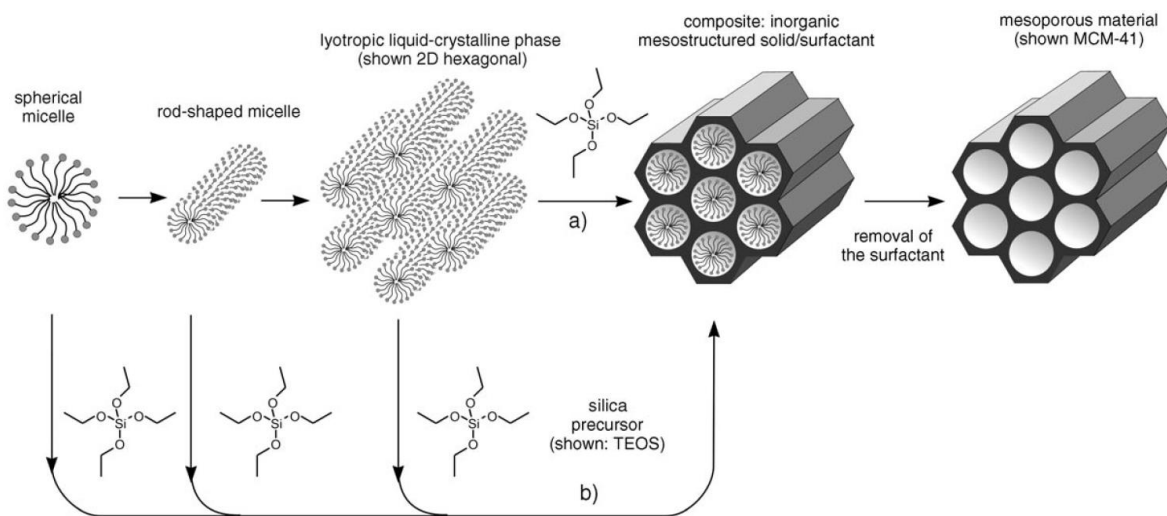
Figure 1.5: Formation of mesoporous materials by structure-directing agents: a) true liquid-crystal template mechanism, b) cooperative liquid-crystal template mechanism.[25]

This is defined as a cooperative liquid-crystal templated mechanism. The silica growth is a multi-step process triggered by the following reactions:

$$(RO)_3\text{-Si-OR} + H_2O \leftrightarrows (RO)_3\text{-Si-OH} + ROH \qquad (1.0)$$

$$(RO)_3\text{-Si-OH} + HO\text{-Si-}(OR)_3 \leftrightarrows (RO)_3\text{-Si-O-Si-}(OR)_3 + H_2O \qquad (1.1)$$

$$(RO)_3\text{-Si-OR} + HO\text{-Si-}(OR)_3 \leftrightarrows (RO)_3\text{-Si-O-Si-}(OR)_3 + ROH \qquad (1.2)$$
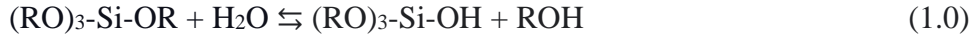
The -OR groups are turned into -OH group by hydrolysis; this step is achieved at a non-neutral pH, in either acidic or basic conditions. The condensation reaction then proceeds by the formation of an oxo-bridge between two silicon atoms, as in steps 1.1 and 1.2. The process continues as polymerisation of successive orthosilicate unites until full consumption of the precursor and formation of an extensive network of SiO_2.[26] As the final step, the micellar template is removed after the silica synthesis, by either Soxhlet extraction or calcination. This will allow guest molecules to be inserted into the pore spaces by diffusion or by covalent attachment using the reactivity of the surface silanol groups.[27]

Kresge and co-workers developed different varieties of mesoporous silica, the very first one being the hexagonal Mobil Composition of Matter (MCM). The surfactant used for MCM-41, the most common silica material, is hexadecyltrimethylammonium bromide (CTAB), and the synthesis is carried out at temperatures between 50° and 80° C, and a pH of 12. Silica materials of MCM type have typical pore diameters between 30 and 40 Å.[28] The main advantage of the synthesis process is that the pore sizes can be fine-tuned depending on the length of the surfactant used for the template. Small pores can easily be produced by using tetradecyltrimethylammonium bromide (TTAB), whereas large pores up to nearly 100 Å can be obtained using surfactants like CTAB or longer jointly with swelling agents such as 1,3,5-trimethyl benzene (TMB).[29]

Another class of porous silicates was synthesised by Zhao and co-workers in 1998, and it is called Santa Barbara Amorphous (SBA). The most common type, SBA-15, is made using gemini Pluronic surfactants, which are triblock copolymers with polyethylene and polypropylene glycol units. This type of silica is known to have larger pore diameters than the classical MCM-41, up to 90-95 Å.[30,31] A silica type with a similar pore size to SBA but different and, to some extent, more convenient synthetic process is COK. Made using the same Pluronic-based templates, it uses sodium silicate

as precursor rather than TEOS. Sodium silicate is commonly available as a water solution, containing 10% sodium hydroxide and 27% SiO_2 in water, and it is also called water glass. Silica formation using such precursor is rapid and occurs at very mild conditions such as room temperature and pH around 6.5-6.8.[32,33]

COK and MCM silica types are those explored in this thesis, which also presents new strategies to modify or hybridise the structure of the materials via the incorporation of light-active molecules. The advantage of the above two silica types is indeed the relative ease of modification and functionalisation in comparison with other silicates. The most important modification routes are described in the next section and have opened up the possibility of incorporating chromophores within the silica scaffold itself, making it an optically active host. The resulting materials, the so-called PMO (periodic mesoporous organosilica), are attracting increasing attention as potential photocatalytic systems for water splitting and CO_2 reduction.[34,35]

1.3.2 Strategies for Silica Modification

The advantage of silica modification through the formation of hybrid organic/inorganic materials is the possibility to obtain new materials with emergent properties, which can be different from those of the individual organic and inorganic components.[25]

Mesoporous silicates can be chemically modified through various means, including post-synthetic or in-situ strategies, which use precursors containing silane-reactive functional groups.[25] There are three main different pathways to silica modification: 1) post-synthetic functionalisation, through the attachment of organic groups, which is also called "surface grafting" (**Figure 1.6**); 2) co-condensation, where the usual silica precursor (TEOS or sodium silicate) is co-polymerised with an organic molecule bearing one alkoxysilane group (**Figure 1.7**), and 3) PMO formation, which uses bis-silylated organic/metalorganic molecules, to incorporate them as bridging units within the siloxane network (**Figure 1.8**).[29]

Surface grafting is carried out by reacting organosilanes $((R'O)_3SiR)$, chlorosilanes $(ClSiR_3)$ or silazanes $(HN(SiR_3)_3)$ with the terminal silanol groups present on the outer and inner (pores) silica surface. A wide variety of organic molecules can be introduced by this method, by varying the organic residue R. The main advantage of post-synthetic modification is that the regular

mesoporous structure of the silica material is maintained. On the other hand, as the amount of organic groups introduced increases, the lining of the inner surface makes the width of the pores gradually shrink, especially if bulky R groups are used. Another, probably more severe disadvantage of the grafting method is that it may cause the organosilanes to react rapidly as they diffuse through the pore openings. This often results in a non-homogeneous distribution of molecules, which would primarily be found near the pores aperture and could even block or hinder the diffusion of guests further into the material. Where R groups are dye molecules, such an effect can be responsible for intermolecular quenching of luminescence.[25]
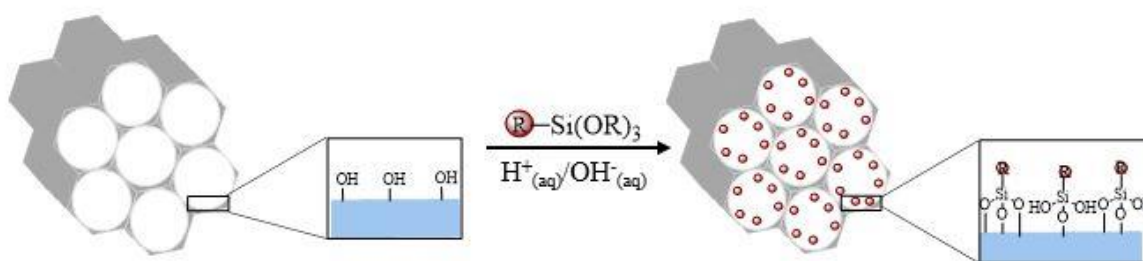
Figure 1.6: Post-synthetic functionalisation of mesoporous silica by surface grafting, where an organic molecule (R) bearing an alkoxysilane group (Si(OR)$_3$) is covalently attached on the silica surface.

The second and the third modification methods are both one-pot strategies and see the organosilanes react simultaneously with TEOS or sodium silicate to form the solid network around the micellar template. However, the two methods differ in regards to their final outcomes. The co-condensation with a mono-silylated R group yields a material with the organic residues attached covalently to the pore surface (see **Figure 1.7**); the majority of them protrude from the inner surface, as the internal surface of the pores is larger than the outer surface of a silica particle. The key advantage of such a co-condensation method over the surface grafting is that the organic groups are generally more homogeneously distributed over the entire material, which reduces luminescence quenching between neighbouring dyes, and there are no such drawbacks as pore blockage. On the other hand, though, the concentration of the organic groups added in the hybrid material should not exceed a molar ratio of 40% in respect to TEOS or sodium silicate; beyond such value, an ordered and non-amorphous silica material would hardly form. Another

disadvantage of this method is that the organic functionality might be chemically damaged or even cleaved in the process of template removal after synthesis. It is then always suitable to use only extraction methods such as Soxhlet with non-aggressive solvents at mild pH and to avoid calcination.[25]
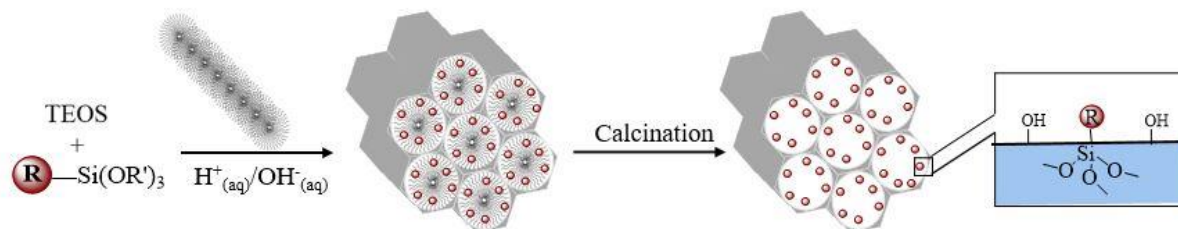
Figure 1.7: Co-condensation of TEOS with a mono-silylated organic molecule R to make a surface-modified mesoporous silica material.

Where co-condensation is carried out with a bis-silylated R molecule, this becomes an integral part of the silica network during the growth process around the template. The resulting material would no longer be regarded as classic mesoporous silica and take the form of a hybrid framework, which is commonly referred to as PMO (see **Figure 1.8**). The synthesis of PMO materials expands the range of functionalities that host scaffolds have and, where R is a light-active unit, it renders the host no longer inert. The PMO method also provides a homogeneous distribution of dye molecules within the solid structure, which is usually maintained regular and ordered over long scales, as long as R groups are relatively small and reactive during the synthetic process.
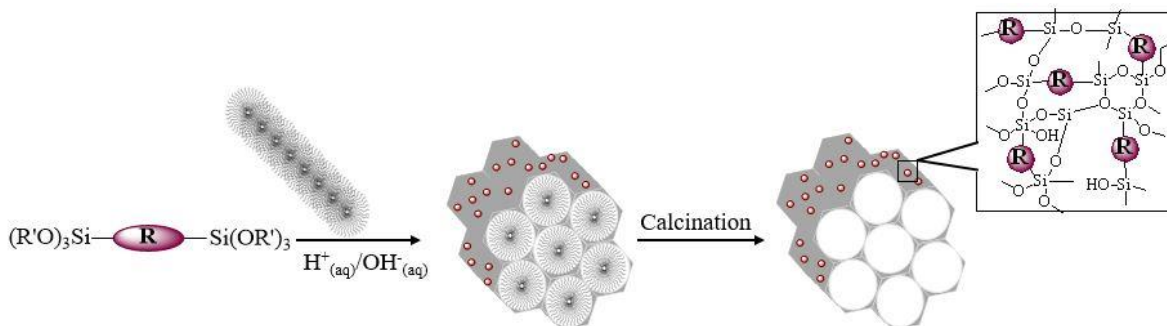
Figure 1.8: Synthesis of Periodic Mesoporous Organosilica (PMO) by direct co-condensation with a bis-silylated organic bridge R.

Removal of templates by calcination is the best common method of removing templates under air at 550ºC. This method has its drawbacks ranging from the shrinkage of the framework, and distortion of the ordered porosity, to the generation of a large amount of CO2, etc. Due to the above limitations that the calcination method portrays, new technologies are being studied to achieve detemplating without pore shrinkage and destruction of the templates, which includes chemical methods (ionic liquid, solvent extraction, and chemical oxidation) and physical methods (microwave-assisted treatment, supercritical CO_2, ozone treatment, plasma technology, etc.).[36]

The microwave-assisted treatment can be used to remove templates from MCM-41 and SBA-15. It can be carried out by mixing samples with HNO_3 and H_2O_2 at $200^0\,C$ and a pressure of 1.3MPQ, which can be created by microwave radiation. The templates can be removed within2-3munites in both samples, and complete removal can be confirmed by Fourier transform infrared spectroscopy.[36]

Ozone treatment can be carried out using low-pressure mercury lamps to generate ozone. The lamp will emit ultraviolet light and show two peaks in the UV-light range (254nm and 185nm). The energy values generated are usually higher than bonding energies in organic compounds. The inorganic bond in the template is being broken down by the U-light and aids the removal of a template.

Ionic liquid treatment is aimed at increasing access of enzymes to cellulose and, at the same time, improving the hydrolysis process.[37] The removal of templates from P-123 can best be achieved by this method at $120^0\,C$ for 12 hours. It has advantages over calcination by causing less shrinkage of the pores, and the regular arrays are maintained.[36]

Solvent extraction is common method of template removal by using different solvents such as water, dichloromethane, acetonitrile, ethanol, methanol, acetone etc. Using water to remove templates appears to be less effective, and methanol has the highest impact. The extraction time with this method is usually 6 hours with methanol and 48 hours with water.[36]

Since their early development, small organic functionalities such as ethylene and phenylene spacers have been gradually replaced by more complex units (e.g. metal complexes).[38–41] Inagaki's group is among the first reporting the synthesis of PMOs and their use as solid-state sensitisers and lighting materials.[42,43]

The major disadvantage in the chemistry of PMOs is that the organic or organometallic silylated precursors are not commercially available, and they must be synthesised, often in-situ, using air-sensitive conditions.

Some of the dyes used in the research work presented in this thesis have been modified with alkoxysilane groups or surfactant chains and they are introduced in the next part.

1.4 Light-active Molecules

1.4.1 Dipyrromethenes and their Complexes

Half of the work described in this thesis is centred on dipyrromethenes, also called dipyrrins (see **Figure 1.9**), and their organic and inorganic complexes. Their relative ease of synthesis and modification, together with their excellent optical properties, have generated vast interest in the scientific community since their discovery.[44] The synthetic strategy includes an acid-catalysed reaction that involves condensation between an aldehyde and a pyrrole to form a saturated dipyrromethane. This is usually unstable, even at low temperatures, and can form porphyrin if excess pyrrole is not used. The dipyrromethane is then oxidised quickly after formation to give the unsaturated dipyrromethene by using either 2,3-dichloro-5,6-dicyanoquinone (DDQ) or p-chloranil. For this research, p-chloranil was always preferred, as it gives dipyrromethenes higher yields than DDQ. The dipyrromethene is then deprotonated to form an anionic bidentate ligand that can be used to coordinate a large variety of elements, such as B, Zn, Al and several transition metals.[45]
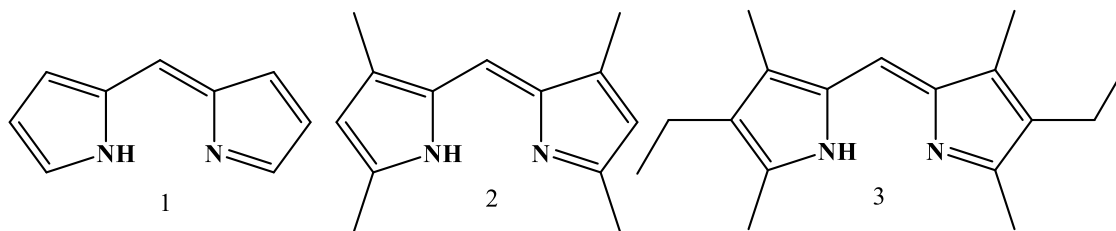
Figure 1.9: Structure of three common dipyrromethenes.

BODIPY dyes

16

The most commonly studied among the dipyrromethene complexes are the *bo*ron *dipy*rromethenes (BODIPYs). The central core is formed by a 4,4-difluoro-4-bora-3a,4a-diaza-s-indacene structure, where the dipyrrin coordinates a boron difluoride group (see **Figure 1.10**).[46] They have numerous applications, ranging from optics to biology, and their use is still growing. The first studies started back in 1968 by Treibs and Kreuzer,[12,44] but their applications as laser dyes and biological probes began in the 1990s.
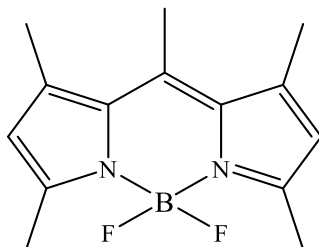
Figure 1.10: Typical structure of a BODIPY dye.

BODIPYs have ideal photophysical characteristics that includes well-defined absorption and emission bands, high molar extinction coefficients (between 50,000 and 100,000 M^{-1} cm^{-1}), small Stokes shifts, high fluorescence quantum yields (in some cases, approaching unity), and good thermal and photochemical stability.[47]

The ability to introduce different substituents in its core structure can result in variations of spectral properties and improvement of the luminescence efficiency and photostability.[48–50] BODIPYs made with both substituted and unsubstituted pyrrole rings usually display high fluorescence yields in most solvents, whereas BODIPYs with substituents only at the meso-position are known to have low quantum yields.[51] Often aryl substituents are attached to that position, which can induce free rotation around the bond and provide an efficient thermal pathway of excited-state deactivation. Generally, though, all BODIPYs have optical properties that can be fine-tuned across the entire visible spectrum, down to the near-infrared region (NIR). For example, when alkyl or other electron-donating substituents are attached to the pyrrole positions, significant bathochromic shifts can be obtained, although this would decrease the luminescence quantum yields.[46,47]

It is also possible to substitute the fluorides on the boron centre with carbon or oxygen. This can be done using substituents such as methyl and methoxy, or even bulkier groups like aryl and polyethylene glycol chains, to mention a few.[52]

17

Metal dipyrromethenes

Dipyrromethene ligands are not only limited to complexation with boron; they can also coordinate a variety of metal ions, although only very few are highly luminescent.[53,54] The most common examples of stable compounds are with first-row transition metal ions (e.g. Fe, Cu, Ni and Zn). Their optical properties resemble those of boron dipyrrins, with intense absorption bands in the blue-green region ($\varepsilon \approx 10^5$ M^{-1} cm^{-1}) and mirror-image emissions with small Stokes shifts.[55] Coordination to the metal ions, though, introduces vibrational deactivation channels to the excited states, and light emission usually takes place with low quantum yields unless some structural rigidity is enforced. **Figure 1.11** shows a typical example of a weakly emissive metal complex in the form of a zinc(II) bis-dipyrromethene. The complex has a fluorescence quantum yield of 0.16 in toluene and it is the subject of the investigation presented in Chapter 3.
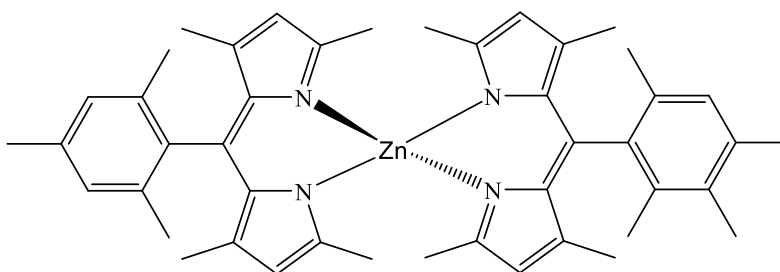
Figure 1.11: Structure of a bis-dipyrromethene complex with zinc(II) as the central metal ion.

Since zinc(II) possesses a full d-shell, it is optically inert and does not alter the absorption and emission energy of the ligands significantly. In some cases, especially with heteroleptic complexes, new types of optical transitions can be introduced, such as ligand-to-ligand charge transfer (LL'CT), where an electron is formally transferred from one ligand to another.

Metal ions with unfilled d-shells would potentially enable the occurrence of metal-to-ligand charge transfer (MLCT) transitions, but these are not commonly observed.[55] An interesting effect is the activation of the triplet states of dipyrromethenes by means of the strong spin-orbit coupling induced by coordination with heavy metal ions, such as iridium(III). This has led to the detection of room temperature phosphorescence, which is also red-shifted towards the NIR in comparison with the usual green-yellow fluorescence.[56]

BOPHY dyes

This is a new family of chromophores derived from dipyrromethene-based structures. They show some similarities with the BODIPY dyes described earlier in this chapter. The basic BOPHY structure consists of two BF_2 groups coordinated by a hydrazine Schiff base linked to two pyrrole rings; the full name is (bis(difluoro*bo*ron)-1,2-bis((1H-*p*yrrol-2-yl)methylene)*hy*drazine), and the structure is shown in **Figure 1.12**, next to a BODIPY for comparison. BOPHY dyes are rigidly planar with an inversion centre (C_{2h} symmetry); as in BODIPYs, the α, β and meso-positions can be easily functionalised with a wide range of substituents in order to fine-tune the optical properties.[57]
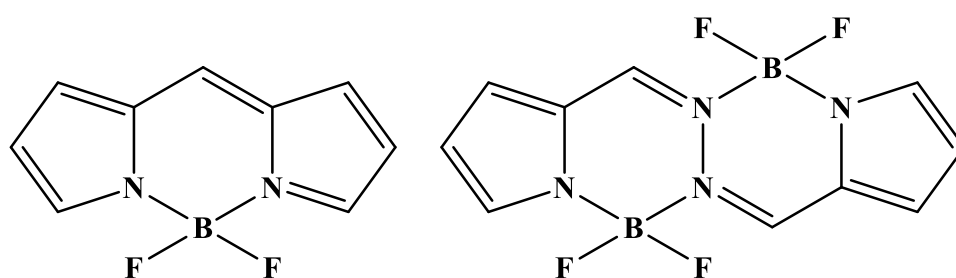
Figure 1.12: Structure of BODIPY (left) and BOPHY (right).

The first synthesised BOPHY chromophore was reported by two groups in 2014.[58,59] They were able to confirm the structure by X-ray crystallography, which also showed the formation of intramolecular C-H⋯F hydrogen bonds between the fluorine atoms and the hydrogens at the *α*- and *meso*-positions.[60] The unfunctionalised BOPHY shown above possesses the typical optical properties of organic fluorophores, that is, intense and structured absorption and emission bands, high emission quantum yield (0.95) and a short excited-state lifetime (2 ns).[53,58] The absorption falls in the blue region of the visible spectrum, with two distinct vibronic peaks at 424 and 442 nm, whereas the emission peaks at 465 and 518 nm, with a moderate Stokes shift from the lowest-energy absorption peak.

Generally, BOPHY dyes have absorption and emission at higher energies (more blue-shifted) than BODIPYs.[58,60–62] They also tend to be more stable to light exposure and air for some days, contrary to BODIPYs.[53] Moreover, most BOPHYs exhibit good fluorescence properties in the solid-state as well as in solution, whereas that is not the case for BODIPYs, which undergo fluorescence quenching in the same state.[63]

1.4.2 **Quinolinolates and their Complexes**

Another class of conjugated ligands with appealing optical properties is that of quinolines. Hydroxyquinolines, in particular, have been widely studied because of their ability to coordinate various light metal ions such as aluminium(III) and first-row transition metal ions like zinc(II). The first studies on metal quinolinolates were carried out with tris-chelated aluminium complexes, often abbreviated as Alq_3. They quickly showed great potential for use in OLEDs due to their electroluminescence, good electron transport properties and the ability to form stable thin films for use in devices.[64,65] Alq_3 and analogous compounds such as Znq_2 display a green-yellow light emission, originating from excited states localised on the ligand. This is typical of metal ions that are optically inert or unable to induce the formation of luminescent excited states with at least partial metal localisation, such as MLCT states. Instead, the metal ions play a structural role only, holding multiple ligands to increase the light-absorption and conversion ability. Where metal quinolinolates possess rigid structures, the vibrational deactivation pathways can be reduced, leading to more efficient luminescence. The latter, as anticipated earlier, usually takes the form of ligand-centred fluorescence with some charge-transfer character under ambient conditions, while phosphorescence rarely appears.[66–68]

Vogler's group has extensively studied metal quinolinolates, also called metal oxinates, since the late 1990s. They prepared the first zinc(II) complexes and found that the central metal ion prefers distorted tetrahedral coordination.[66] Znq_2 shows strong absorption bands in the UV region, around 260-270 nm (e = 39,000 M^{-1} cm^{-1}), due to $\pi \rightarrow \pi^*$ intraligand transitions, and weak bands at 350-410 nm (e = 4,500 M^{-1} cm^{-1}), due to mixed $\pi/n \rightarrow \pi^*$ transitions.[35,67,69]

Despite their attractiveness for opto-electronic applications, metal oxinates have limited quantum yields, between 0.12 for Alq_3 and 0.26 for Znq_2.[68,69] They are still subject of ongoing investigations, with the aim to develop new synthetic strategies for more efficient light-emitting complexes.[64,65,70,71] Zinc(II) quinolinolates were used for the studies presented in Chapter 4 of this thesis (see also **Figure 1.13**), where the target is to design new solid-state materials with enhanced fluorescence properties.
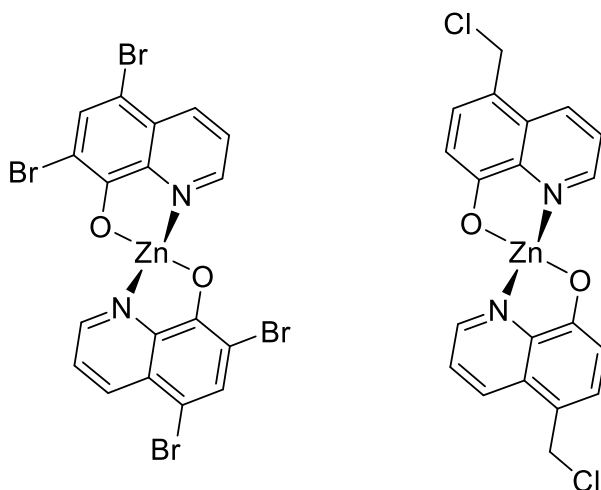
Figure 1.13: Structures of the homoleptic bis-quinolinolate zinc(II) complexes that are subject of the studies presented in this thesis.

It will be expected that by attaching or incorporating each type of dye will bring about a different photophysical characteristics. Some of the dyes will be added in the micellar template, added as core-surfactants and or as bridging units in the mesoporous wall. The direction and orientation of each molecule will determine the possibilities of energy transfer and enhanced luminescence characteristics.

1.5 Aims of the Thesis

The overall target of the research work discussed in this thesis is to design new photo-active materials using the host-guest chemistry of mesoporous silica and organosilica. A variety of organic dyes and metal complexes is showcased in the following chapters, and their optical properties will be compared with those of the solid-state materials prepared by using them as building blocks. All such molecules are chromophores absorbing and emitting in the UV-visible region of the spectrum, and for most of them the first objective is the successful synthesis, purification and incorporation into porous materials.

Chapter 3 and 4 present zinc(II) bis-dipyrromethenes and bis-quinolinolates, respectively, whereas Chapter 5 and 6 cover the use of organic BODIPY and BOPHY dyes. All solid-state materials will be built using micellar templates consisting of CTAB and Pluronic surfactants, to generate mesoporous MCM-41 and COK-12 silica, respectively. The zinc(II) dipyrrins and the BODIPYs are incorporated into the micellar templates at different concentrations to study the effect this has on the luminescence efficiency and photostability. The zinc(II) oxinates and the BOPHYs, instead, are co-condensed with the silica precursors in order to make them an integral part of the materials themselves. All new organic/inorganic hybrids are fully characterised structurally and optically, with a special emphasis on the solid-state analysis. This included time-resolved luminescence spectroscopy to elucidate the excited-state dynamics and determine the time scales of light-induced phenomena such as energy migration within the materials.

The final aim of these studies is to identify the most convenient synthetic routes to prepare the best performing antenna materials, with high luminescence quantum yields and the ability to act as sensitisers. Such two characteristics are of key importance for the development of new materials for OLEDs and photovoltaic devices.

References

(1) Fossil Fuels | Topics | EESI. https://www.eesi.org/topics/fossil-fuels (accessed 2021-12-20).

(2) Report: Global fossil fuel use not yet in decline, despite renewable energy pledges. edie.net. https://www.edie.net/news/10/Report--Global-fossil-fuel-use-not-yet-in-decline--despite-renewable-energy-pledges/ (accessed 2021-12-20).

(3) Reza Mirnezami, S.; Polytechnique Montreal, C.P. 6079, City-Center Branch, Montreal (QC) Canada H3C 3A7. Do Oil-Producing Countries Have Normal Oil Overconsumption? An Investigation of Economic Growth and Energy Subsidies. AIMS Energy **2015**, 3 (3), 267–283.

(4) Zhuang, B.; Liu, Q.; Wang, T.; Yin, C.; Li, S.; Xie, M.; Jiang, F.; Mao, H. Investigation on Semi-Direct and Indirect Climate Effects of Fossil Fuel Black Carbon Aerosol over China. Theor Appl Climatol **2013**, 114 (3–4), 651–672.

(5) SVS, N. SVS: Global Temperature Anomalies from 1880 to 2018. https://svs.gsfc.nasa.gov/cgi-bin/details.cgi?aid=4626 (accessed 2021-09-29).

(6) Connolly, J. Photochemical Conversion and Storage of Solar Energy; Elsevier, 2012.

(7) Liu, J.; Cao, G.; Yang, Z.; Wang, D.; Dubois, D.; Zhou, X.; Graff, G. L.; Pederson, L. R.; Zhang, J.-G. Oriented Nanostructures for Energy Conversion and Storage. ChemSusChem **2008**, 1 (8–9), 676–697.

(8) Cristescu, C.; Dumitrescu, C.; Drumea, P.; Dulgheru, V.; Kedzia, K. Technologies of Capture and Storage of Energy from Renewable Sources. **2016**.

(9) Harrington, R. This incredible fact should get you psyched about solar power. Business Insider. https://www.businessinsider.com/this-is-the-potential-of-solar-power-2015-9 (accessed 2021-12-10).

(10) Crystalline Silicon Solar Cells - [PDF Document]. documents.pub. https://documents.pub/document/crystalline-silicon-solar-cells.html (accessed 2021-09-29).

(11) Multifunctional surface structures of plants: An inspiration for biomimetics | Elsevier Enhanced Reader. https://reader.elsevier.com/reader/sd/pii/S0079642508000704?token=DE48AEC656B34E78AB C963D7A7EC8BADA764C125DA9857BF3C5E2E976C21129EB9C738724C2E49222CADC5 9AB8A7D2A6&originRegion=eu-west-1&originCreation=20210929142810 (accessed 2021-09-29).

(12) Deisenhofer, J.; Epp, O.; Miki, K.; Huber, R.; Michel, H. Structure of the Protein Subunits in the Photosynthetic Reaction Centre of Rhodopseudomonas Viridis at 3Å Resolution. Nature **1985**, 318 (6047), 618–624.

(13) Kühlbrandt, W.; Wang, D. N.; Fujiyoshi, Y. Atomic Model of Plant Light-Harvesting Complex by Electron Crystallography. Nature **1994**, 367 (6464), 614–621.

(14) Functional Architecture of the Major Light-harvesting Complex from Higher Plants | Elsevier Enhanced Reader. https://reader.elsevier.com/reader/sd/pii/S0022283600951799?token=3A3803EB6AFE3DCC73 AC6472813290996997031F74983B8C064330C1F4D8E57445428CDDF77E2B897F3F061F8E A921B2&originRegion=eu-west-1&originCreation=20210929140811 (accessed 2021-09-29).

(15) Balzani, V.; Credi, A.; Venturi, M. Photochemical Conversion of Solar Energy. ChemSusChem **2008**, 1 (1–2), 26–58.

(16) Jacobson, M. Z.; Delucchi, M. A.; Bauer, Z. A. F.; Goodman, S. C.; Chapman, W. E.; Cameron, M. A.; Bozonnat, C.; Chobadi, L.; Clonts, H. A.; Enevoldsen, P.; Erwin, J. R.; Fobi, S. N.; Goldstrom, O. K.; Hennessy, E. M.; Liu, J.; Lo, J.; Meyer, C. B.; Morris, S. B.; Moy, K. R.; O'Neill, P. L.; Petkov, I.; Redfern, S.; Schucker, R.; Sontag, M. A.; Wang, J.; Weiner, E.; Yachanin, A. S. 100% Clean and Renewable Wind, Water, and Sunlight All-Sector Energy Roadmaps for 139 Countries of the World. Joule **2017**, 1 (1), 108–121.

(17) Wayne, R. P. Principles and Applications of Photochemistry; Oxford University Press: Oxford [England] ; New York, 1988.

(18) Molecular Fluorescence Spectroscopy. http://www.pci.tu-bs.de/aggericke/PC4/Kap_I/mol-fluo.htm (accessed 2021-11-02).

(19) Hu, X.; Damjanovic, A.; Ritz, T.; Schulten, K. Architecture and Mechanism of the Light-Harvesting Apparatus of Purple Bacteria. Proceedings of the National Academy of Sciences **1998**, 95 (11), 5935–5941.

(20) Aratani, N.; Kim, D.; Osuka, A. Discrete Cyclic Porphyrin Arrays as Artificial Light-Harvesting Antenna. 13.

(21) Calzaferri, G.; Lutkouskaya, K. Mimicking the Antenna System of Green Plants. Photochem. Photobiol. Sci. **2008**, 7 (8), 879–910. https://doi.org/10.1039/B804682B.

(22) O'Keeffe, M.; Peskov, M. A.; Ramsden, S. J.; Yaghi, O. M. The Reticular Chemistry Structure Resource (RCSR) Database of, and Symbols for, Crystal Nets. Acc. Chem. Res. **2008**, 41 (12), 1782–1789.

(23) Ishida, Y.; Shimada, T.; Takagi, S. Artificial Light-Harvesting Model in a Self-Assembly Composed of Cationic Dyes and Inorganic Nanosheet. J. Phys. Chem. C **2013**, 117 (18), 9154–9163.

(24) Hoffmann, F.; Cornelius, M.; Morell, J.; Fröba, M. Silica-Based Mesoporous Organic–Inorganic Hybrid Materials. Angewandte Chemie International Edition **2006**, 45 (20), 3216–3251.

(25) Hoffmann, F.; Cornelius, M.; Morell, J.; Fröba, M. Silica-Based Mesoporous Organic–Inorganic Hybrid Materials. Angewandte Chemie International Edition **2006**, 45 (20), 3216–3251.

(26) Brinker, C. J.; Scherer, G. W. Sol-Gel Science: The Physics and Chemistry of Sol-Gel Processing; Academic Press, 2013.

(27) Hoffmann, F.; Fröba, M. Vitalising Porous Inorganic Silica Networks with Organic Functions—PMOs and Related Hybrid Materials. Chem. Soc. Rev. **2011**, 40 (2), 608–620.

(28) Kresge, C. T.; Leonowicz, M. E.; Roth, W. J.; Vartuli, J. C.; Beck, J. S. Ordered Mesoporous Molecular Sieves Synthesized by a Liquid-Crystal Template Mechanism. Nature **1992**, 359 (6397), 710–712.

(29) Beck, J. S.; Vartuli, J. C.; Roth, W. J.; Leonowicz, M. E.; Kresge, C. T.; Schmitt, K. D.; Chu, C. T. W.; Olson, D. H.; Sheppard, E. W.; McCullen, S. B.; Higgins, J. B.; Schlenker, J. L. A New Family of Mesoporous Molecular Sieves Prepared with Liquid Crystal Templates. J. Am. Chem. Soc. **1992**, 114 (27), 10834–10843.

(30) Zhao, D.; Feng, J.; Huo, Q.; Melosh, N.; Fredrickson, G. H.; Chmelka, B. F.; Stucky, G. D. Triblock Copolymer Syntheses of Mesoporous Silica with Periodic 50 to 300 Angstrom Pores. Science **1998**, 279 (5350), 548–552.

(31) Zhao, D.; Huo, Q.; Feng, J.; Chmelka, B. F.; Stucky, G. D. Nonionic Triblock and Star Diblock Copolymer and Oligomeric Surfactant Syntheses of Highly Ordered, Hydrothermally Stable, Mesoporous Silica Structures. J. Am. Chem. Soc. **1998**, 120 (24), 6024–6036.

(32) Jammaer, J.; Aerts, A.; D'Haen, J.; Seo, J. W.; Martens, J. A. Convenient Synthesis of Ordered Mesoporous Silica at Room Temperature and Quasi-Neutral PH. J. Mater. Chem. **2009**, 19 (44), 8290.

(33) Jammaer, J.; van Erp, T. S.; Aerts, A.; Kirschhock, C. E. A.; Martens, J. A. Continuous Synthesis Process of Hexagonal Nanoplates of P6m Ordered Mesoporous Silica. Journal of the American Chemical Society **2011**, 9.

(34) Inagaki, S.; Guan, S.; Fukushima, Y.; Ohsuna, T.; Terasaki, O. Novel Mesoporous Materials with a Uniform Distribution of Organic Groups and Inorganic Oxide in Their Frameworks. J. Am. Chem. Soc. **1999**, 121 (41), 9611–9614.

(35) Waki, M.; Mizoshita, N.; Maegawa, Y.; Hasegawa, T.; Tani, T.; Shimada, T.; Inagaki, S. Enhanced Fluorescence Detection of Metal Ions Using Light-Harvesting Mesoporous Organosilica. Chemistry – A European Journal **2012**, 18 (7), 1992–1998.

(36) Ghaedi, H.; Zhao, M. Review on Template Removal Techniques for Synthesis of Mesoporous Silica Materials. Energy Fuels **2022**, 36 (5), 2424–2446.

(37) Wang, Y.; Yang, R. T. Template Removal from SBA-15 by Ionic Liquid for Amine Grafting: Applications to CO_2 Capture and Natural Gas Desulfurization. ACS Sustainable Chem. Eng. **2020**, 8 (22), 8295–8304.

(38) Asefa, T.; MacLachlan, M. J.; Coombs, N.; Ozin, G. A. Periodic Mesoporous Organosilicas with Organic Groups inside the Channel Walls. Nature **1999**, 402 (6764), 867–871.

(39) Melde, B. J.; Holland, B. T.; Blanford, C. F.; Stein, A. Mesoporous Sieves with Unified Hybrid Inorganic/Organic Frameworks. Chem. Mater. **1999**, 11 (11), 3302–3308.

(40) Nicole, L.; Boissière, C.; Grosso, D.; Hesemann, P.; Moreau, J.; Sanchez, C. Advanced Selective Optical Sensors Based on Periodically Organized Mesoporous Hybrid Silica Thin Films. Chem. Commun. **2004**, No. 20, 2312–2313.

(41) Cornelius, M.; Hoffmann, F.; Fröba, M. Periodic Mesoporous Organosilicas with a Bifunctional Conjugated Organic Unit and Crystal-like Pore Walls. Chem. Mater. **2005**, 17 (26), 6674–6678.

(42) Mizoshita, N.; Goto, Y.; Maegawa, Y.; Tani, T.; Inagaki, S. Tetraphenylpyrene-Bridged Periodic Mesostructured Organosilica Films with Efficient Visible-Light Emission. Chem. Mater. **2010**, 22 (8), 2548–2554. https://doi.org/10.1021/cm9034787.

(43) Van Der Voort, P.; Esquivel, D.; De Canck, E.; Goethals, F.; Van Driessche, I.; Romero-Salguero, F. J. Periodic Mesoporous Organosilicas: From Simple to Complex Bridges; a Comprehensive Overview of Functions, Morphologies and Applications. Chem. Soc. Rev. **2013**, 42 (9), 3913–3955.

(44) Treibs, A.; Kreuzer, F.-H. Difluorboryl-Komplexe von Di- und Tripyrrylmethenen. Justus Liebigs Annalen der Chemie **1968**, 718 (1), 208–223.

(45) Yu, L.; Muthukumaran, K.; Sazanovich, I. V.; Kirmaier, C.; Hindin, E.; Diers, J. R.; Boyle, P. D.; Bocian, D. F.; Holten, D.; Lindsey, J. S. Excited-State Energy-Transfer Dynamics in Self-Assembled Triads Composed of Two Porphyrins and an Intervening Bis(Dipyrrinato)Metal Complex. Inorg. Chem. **2003**, 42 (21), 6629–6647.

(46) Uppal, T. Synthesis and Characterization of Red and Near-Infrared BODIPY-Based Fluorophores for Various Biological Applications. LSU Doctoral Dissertations **2012**.

(47) Boens, N.; Leen, V.; Dehaen, W. Fluorescent Indicators Based on BODIPY. Chem. Soc. Rev. **2012**, 41 (3), 1130–1172.

(48) Monsma Jr., F. J.; Barton, A. C.; Chol Kang, H.; Brassard, D. L.; Haugland, R. P.; Sibley, D. R. Characterization of Novel Fluorescent Ligands with High Affinity for D1 and D2 Dopaminergic Receptors. Journal of Neurochemistry **1989**, 52 (5), 1641–1644.

(49) Saki, N.; Dinc, T.; Akkaya, E. U. Excimer emission and energy transfer in cofacial boradiazaindacene (BODIPY) dimers built on a xanthene scaffold. **2006**.

(50) Wan, C.-W.; Burghart, A.; Chen, J.; Bergström, F.; Johansson, L.; Wolford, M.; Kim, T.; Topp, M.; Hochstrasser, R.; Burgess, K. Anthracene-BODIPY Cassettes: Syntheses and Energy Transfer. Chemistry (Weinheim an der Bergstrasse, Germany) **2003**, 9, 4430–4441.

(51) Trofimov, B. A. Preparation of Pyrroles from Ketoximes and Acetylenes. In Advances in Heterocyclic Chemistry; Katritzky, A. R., Ed.; Academic Press, 1990; Vol. 51, pp 177–301.

(52) Loudet, A.; Burgess, K. BODIPY Dyes and Their Derivatives: Syntheses and Spectroscopic Properties. Chem. Rev. **2007**, 107 (11), 4891–4932.

(53) Bismillah, A. N.; Aprahamian, I. Fundamental Studies to Emerging Applications of Pyrrole-BF $_2$ (BOPHY) Fluorophores. Chem. Soc. Rev. **2021**, 50 (9), 5631–5649.

(54) Wood, T. E.; Thompson, A. Advances in the Chemistry of Dipyrrins and Their Complexes. Chem. Rev. **2007**, 107 (5), 1831–1861. https://doi.org/10.1021/cr050052c.

(55) Baudron, S. A. Luminescent Dipyrrin Based Metal Complexes. Dalton Trans. **2013**, 42 (21), 7498.

(56) Hanson, K.; Tamayo, A.; Diev, V. V.; Whited, M. T.; Djurovich, P. I.; Thompson, M. E. Efficient Dipyrrin-Centered Phosphorescence at Room Temperature from Bis-Cyclometalated Iridium(III) Dipyrrinato Complexes. Inorg. Chem. **2010**, 49 (13), 6077–6084.

(57) Li, X.; Ji, G.; Son, Y.-A. Tunable Emission of Hydrazine-Containing Bipyrrole Fluorine–Boron Complexes by Linear Extension. Dyes and Pigments **2016**, 124, 232–240.

(58) Tamgho, I.-S.; Hasheminasab, A.; Engle, J. T.; Nemykin, V. N.; Ziegler, C. J. A New Highly Fluorescent and Symmetric Pyrrole–BF $_2$ Chromophore: BOPHY. J. Am. Chem. Soc. **2014**, 136 (15), 5623–5626.

(59) Yu, C.; Jiao, L.; Zhang, P.; Feng, Z.; Cheng, C.; Wei, Y.; Mu, X.; Hao, E. Highly Fluorescent BF $_2$ Complexes of Hydrazine–Schiff Base Linked Bispyrrole. Org. Lett. **2014**, 16 (11), 3048–3051.

(60) Kasha, M. Characterization of Electronic Transitions in Complex Molecules. Discuss. Faraday Soc. **1950**, 9, 14.

(61) Yu, C.; Jiao, L.; Zhang, P.; Feng, Z.; Cheng, C.; Wei, Y.; Mu, X.; Hao, E. Highly Fluorescent BF $_2$ Complexes of Hydrazine–Schiff Base Linked Bispyrrole. Org. Lett. **2014**, 16 (11), 3048–3051.

(62) Boodts, S.; Fron, E.; Hofkens, J.; Dehaen, W. The BOPHY Fluorophore with Double Boron Chelation: Synthesis and Spectroscopy. Coordination Chemistry Reviews **2018**, 371, 1–10.

(63) Rurack, K.; Kollmannsberger, M.; Daub, J. Molecular Switching in the Near Infrared (NIR) with a Functionalized Boron–Dipyrromethene Dye. Angewandte Chemie International Edition **2001**, 40 (2), 385–387.

(64) Matsumura, M.; Akai, T. Organic Electroluminescent Devices Having Derivatives of Aluminum-Hydroxyquinoline Complex as Light Emitting Materials. Jpn. J. Appl. Phys. **1996**, 35 (Part 1, No. 10), 5357–5360.

(65) Hopkins, T. A.; Meerholz, K.; Shaheen, S.; Anderson, M. L.; Schmidt, A.; Kippelen, B.; Padias, A. B.; Hall, H. K.; Peyghambarian, N.; Armstrong, N. R. Substituted Aluminum and Zinc Quinolates with Blue-Shifted Absorbance/Luminescence Bands: Synthesis and Spectroscopic, Photoluminescence, and Electroluminescence Characterization. Chem. Mater. **1996**, 8 (2), 344–351.

(66) Kunkely, H.; Vogler, A. Optical Properties of Zinc(II) 5,7-Diiodo-8-Quinolinolate in Solution. Phosphorescence under Ambient Conditions. Chemical Physics Letters **2003**, 376 (1), 226–229.

(67) Kunkely, H.; Vogler, A. Photoluminescence of 8-Quinolinato(Tetracarbonyl)Rhenium(I). Inorganic Chemistry Communications **1998**, 1 (10), 398–401.

(68) Montalti, M.; Credi, A.; Prodi, L.; Gandolfi, M. T. Handbook of Photochemistry, 3rd ed.; CRC Press: Boca Raton, 2006.

(69) Ballardini, R.; Varani, G.; Indelli, M. T.; Scandola, F. Phosphorescent 8-Quinolinol Metal Chelates. Excited-State Properties and Redox Behavior. Inorg. Chem. **1986**, 25 (22), 3858–3865.

(70) Kai, Y.; Morita, M.; Yasuoka, N.; Kasai, N. The Crystal and Molecular Structure of Anhydrous Zinc 8-Quinolinolate Complex, [Zn(C9H6NO)2]4. BCSJ **1985**, 58 (6), 1631–1635.

(71) Cucinotta, F.; Jarman, B. P.; Caplan, C.; Cooper, S. J.; Riggs, H. J.; Martinelli, J.; Djanashvili, K.; La Mazza, E.; Puntoriero, F. Light-Harvesting Antennae Using the Host-Guest Chemistry of Mesoporous Organosilica. ChemPhotoChem **2018**, 2 (3), 196–206.

Chapter 2: Instrumentation and Principles of Operation

2.1   Introduction

This chapter will aim to describe various techniques used in the research work presented in this thesis. The methods include structural analysis of molecules (NMR) and materials (XRD and TEM), and photophysical characterisation of both, using UV-visible steady-state and time-resolved spectroscopy.

2.2   Structural Characterisation

2.2.1   Nuclear Magnetic Resonance (NMR)

This is a simple technique used in analytical chemistry research and functions to determine a compound's molecular structure. After successful synthesis of an organic molecule, the structural elucidation of the synthesised compound can be elucidated using a variety of techniques, and the first among is the NMR. The principle involves measuring the interaction between nuclei and radio-frequency energy in a sample to generate a spectrum. Different sets of spectra can be measured, and the most common is 1D. The 2D spectra consist of proton NMR or denoted as ^{1}H, carbon (^{13}C), and also fluorine (^{19}F), silicon (^{29}Si) and phosphorus (^{31}P) are regarded as 2D NMR spectra.[1]

Because of the nuclear spin that atomic nuclei possess, they can behave like bar magnets. Nuclear magnets can arrange themselves in $2\,l + 1$ ways when exposed to a magnetic field, where l is the nuclei spin quantum number.[2] When the mass number of nuclei is odd, their spin state becomes 1/2, 3/2, 5/2, and so on. Suppose the spin of a nuclei is 1/2. In that case, they can only take up to two orientations: a high energy orientation, which is opposed to the applied magnetic field, and a low energy orientation, which is aligned with the magnetic field. The following equation calculates the difference in energy.

$$\Delta E = \frac{h\gamma B_O}{2\pi} \qquad\qquad (2.1)$$

In the above equation, γ and B_0 are the magnetogyric ratios and the strength of the applied magnetic field, respectively.

To determine the difference in the number of nuclei having low (N_β) and high (N_α) energy, we used the Boltzmann distribution equation:

$$\frac{N_\beta}{N_\alpha} = \exp(\frac{-\Delta E}{kT}) \qquad\qquad (2.2)$$

The distribution changes if the radio-frequency equals that of the natural precession of the nuclear magnets in the magnetic field, in which case N_β will increase due to the promotion of the nuclei from the α state to the β state.[2] The frequency of the magnet depends on the nature of the nucleus and the applied field strength. The higher the field strength, the more significant the difference would be between N_β and N_α. For such reason, high-field instruments with 200-750 MHz are widely used, as they are found to be more sensitive.
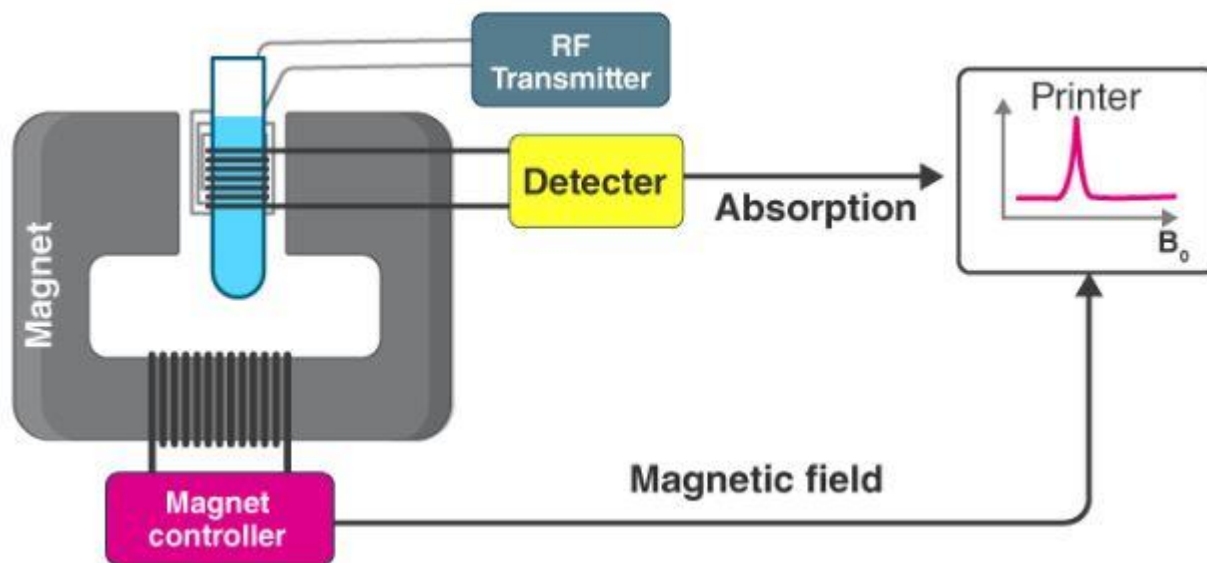
Figure 2.1: Schematic diagram of the Nuclear Magnetic Resonance instrumentation adapted from Byjus.com.[3]

The above **Figure 2.1** shows a schematic representation of the NMR instrument.[3] In a typical measurement, few milligrams of samples are dissolved in a deuterated solvent and transferred into an NMR tube. The tubes are placed into a probe or sample holder that aids in positioning the sample into a strong magnetic field, e.g. 300, 400, 500 or 700 MHz. The magnetic moment within the nucleus then aligns with the static magnetic field from the instrument's magnet.[4] The probe coils generate the secondary moment that causes the nuclear magnetisation to rotate, eventually inducing

the nuclei to be excited. At the end of the process, a resonance signal is generated by the net magnetisation precession around the static magnetic field; such signal is then recorded as a function of time.

2.2.2 Transmission Electron Microscopy (TEM)

TEM is a well-known technique for the morphological characterisation of silica materials.[5]
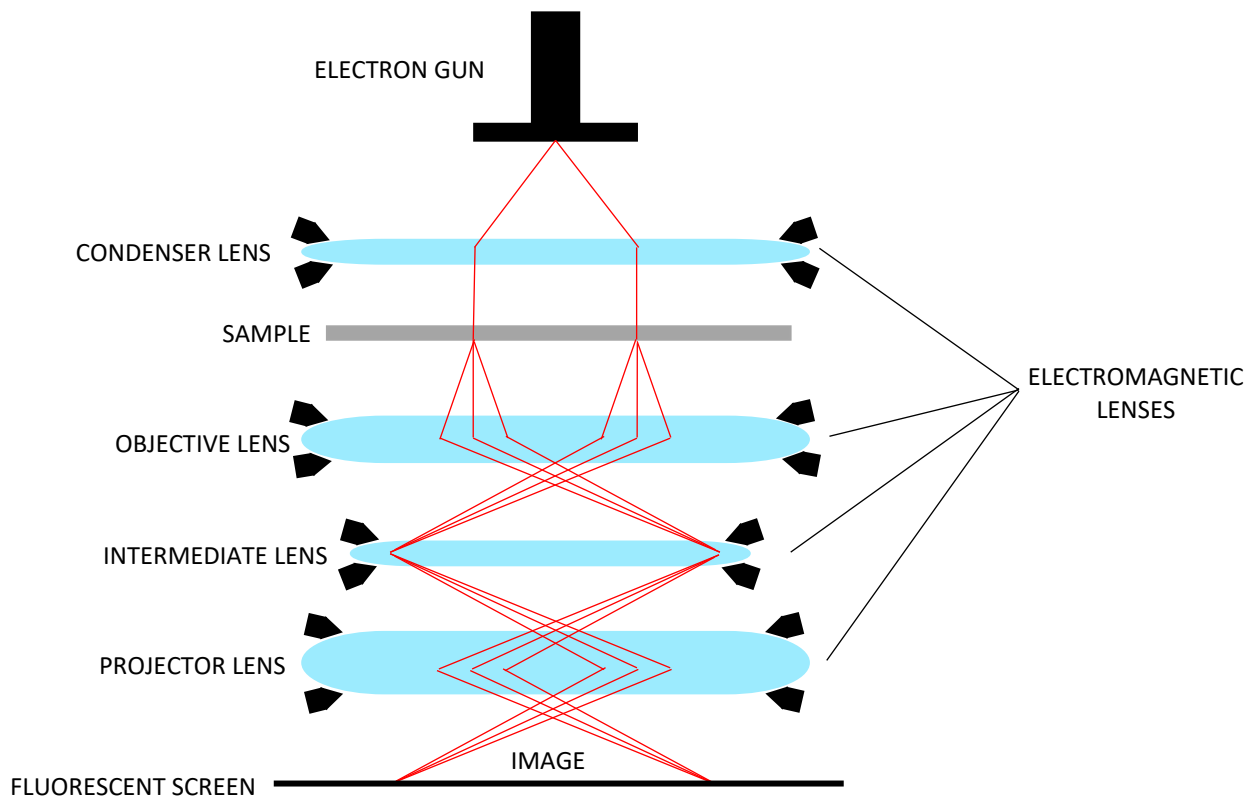
Figure 2.2: Schematic diagram of a Transmission Electron Microscope.[6]

Figure 2.2 is a schematic representation of a conventional Transmission Electron Microscope (TEM). The operation principle is by irradiating a thin specimen with an electron beam containing the same current density. The electron energy ranges between 60-150 KeV. The electron gun emits electrons in the form of a uniform beam; this passes through the sample and generates an image. A condenser lens, made of iron, cobalt or nickel-cobalt alloys, is responsible for collimating the beam onto the sample plane: the process uses the electromagnetic field generated by a current that

33

is passed to the lens via a wire coil and the field is then used to deflect the electrons direct them onto the sample in question.[7] Then, a certain number of electrons passes through the sample, each at different angles in respect to the original incident angle, and are collected by the objective, intermediate and projective lens, to be finally directed to a screen, where an image of the sample is displayed. The number of electrons that pass through the sample depends on the density of the material under investigation.[8] For the acquisition to be as accurate as possible, the measurement is best carried out under vacuum, since collisions with particles present in air may affect the direction of the electrons.

All TEM images presented in this thesis were obtained from a JEOL JEM 1400 microscope, using an acceleration voltage of 120 kV), a JEOL JEM 2100 (acceleration voltage 200 kV) and a Hitachi HT7800 (acceleration voltage 120 kV).

The diameter of pore spaces in all the silica samples were measured using the same equation below:

$$\frac{Length\ of\ a\ measured\ pore\ (cm)\ x\ length\ of\ a\ pore\ from\ the\ instrument\ (nm)}{length\ of\ a\ scale\ bar\ on\ the\ TEM\ image} \quad (2.3)$$

The diameter of a pore can be obtained by picking at random any pore from the image and using any scale bar to measure, and the length of a measured pore and scale bar can be obtained by using a ruler (cm) to measure their lengths respectively. Example: for a silica sample with 200 nm from the machine, a measured pore length of 0.05 cm and the length of a scale bar is 1.9 cm. The actual pore diameter will be:

$$\frac{0.05\ cm\ x\ 200\ nm}{1.9\ cm}$$

5.26 nm

2.2.3 X-ray Diffractometry (XRD)

X-ray diffraction (XRD) is a characterisation technique which can help determine a molecules structure. Upon elastic scattering of a plane wave of X-rays (all photons are travelling parallel to one another), spherical waves move outwards from the sample. These waves interfere constructively and destructively giving high intensities of X-rays seen in specific directions or

more commonly known as reflections. Through computer software, it is possible to examine the reflections to determine the positions of atoms. However, this analysis can only be performed if the sample being used is a perfect single crystal. Bragg reflection planes are formed from the translational symmetry in the arrangement of the atoms of a single crystal. The space between these planes, d, can be determined using the equation below:

$$n\lambda = 2d \cdot sin\theta \qquad (2.4)$$

Where n is the number of Bragg planes passed through before reflection takes place, λ is the wavelength of the X-rays and θ is the angle of scattering from the Bragg plane.

For solid-state samples that are larger in scale than molecules, such as bulk materials (e.g., metal oxides, silica), another technique must be used. Powder X-ray diffractometry (PXRD) is the technique of choice and it was used to characterise all mesoporous silica and organo-silica materials in this thesis. PXRD samples consist of ordered materials with a periodic arrangement over specific dimensions in space. An example is given by mesoporous silicates and aluminosilicates, where ordered one-dimensional pores run through the entire material and are spaced at regular intervals. When subjected to X-ray analysis, they give rise to a diffraction pattern, seen as peaks at specific scattering angles. In a typical experiment, X-rays are generated and sent towards the surface of a flattened sample at a variable angle with 2θ values. The scattered X-rays are then collected by a detector which is again at a variable angle, with the resultant X-ray intensity being plotted against 2θ. Powder X-ray diffractograms in this thesis were obtained with an ARL XTRA48 diffractometer using Cu Kα radiation ($\lambda = 1.54062$ Å).
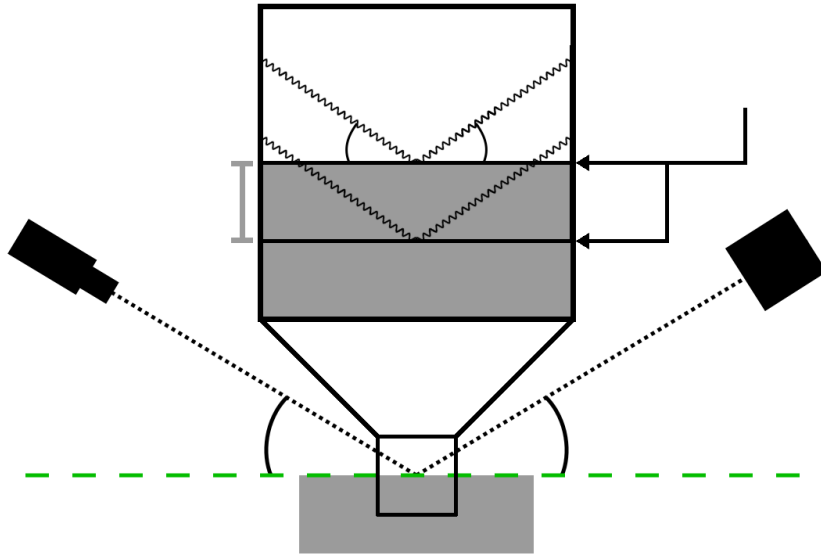
Figure 2.3: Schematic diagram of an X-ray diffractometry tube.[9]

2.3 Optical Characterisation

2.3.1 UV-visible Absorption Spectroscopy

The principles of photochemistry involve the study of chemical and physical behaviours that a molecule undergoes that result from the interactions with visible light.[10] When matter interacts with UV-visible light, the valence electrons are promoted from the ground to the excited state. This is also referred to as an electronic transition from the highest occupied molecular orbital (HOMO) to the lowest unoccupied molecular orbital (LUMO).

From the quantum theory, we know that light is quantised. Absorption and emission of light by matter involve the transfer of energy in the form of photons. These photons are known to have wave-like and particle-like properties, and each has specific energy, given by Planck's law that explains the direct relationship between frequency and energy as follows:

$$E = h\nu \qquad (2.5)$$

Where E is the specific energy of the photon measured in Joules (J), h is Planck's constant (6.63×10^{-34} J/s), and ν stands for the frequency of oscillation of the electromagnetic field carried by the photon, measured in Hertz (Hz) or s^{-1}. It is scientifically more conventional to use the speed of light in relation to the path length of the photons, as expressed in the equation below:

$$E = \frac{hc}{\lambda} \qquad (2.6)$$

Where λ is the wavelength measured in meters and c is the speed of light (3×10^8 m/s).

When a molecule is exposed to light, a fraction of it will be absorbed, causing electronic transitions in the molecule, whereas the remaining part will be transmitted. A typical UV-visible absorption spectrometer detects the fraction of transmitted light intensity (I) in respect to the incident light intensity (I_0), as expressed by equation 2.6:

$$T = \frac{I}{I_O} \qquad\qquad (2.7)$$

Where T is defined as transmittance. The most commonly used property is absorbance (A), which is connected with transmittance and is expressed by the Beer-Lambert's law

$$A = \log(\frac{I_O}{I}) = \varepsilon c l \qquad\qquad (2.8)$$

Where c (in units of molarity) is the concentration of the molecule in the sample, l is the path length that light traverses (in cm) and ε is the molar extinction coefficient (in M^{-1} cm^{-1}), which is an expression of the absorption probability for a molecule at a specific wavelength.[11]
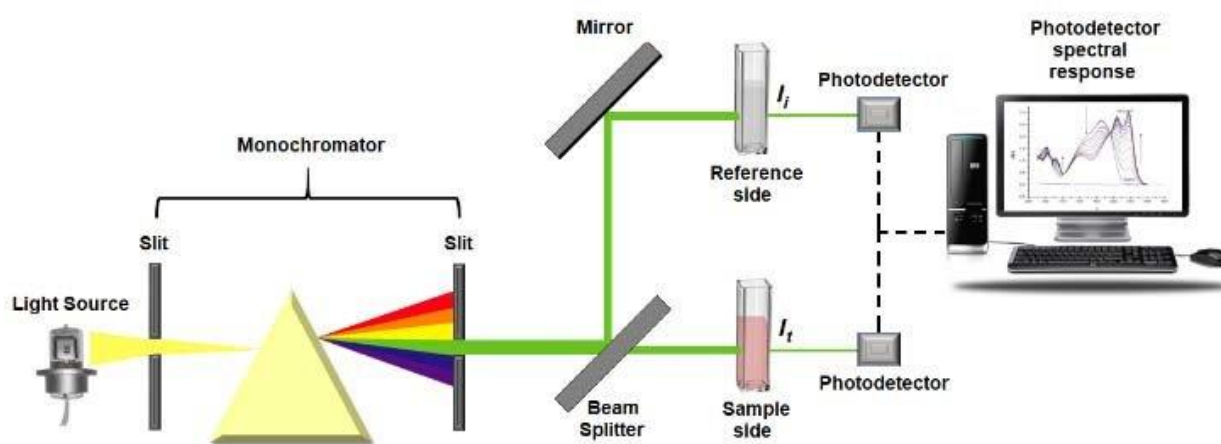
Figure 2.4: The Schematic diagram of a double beam UV-vis spectrometer.[12]

The principle of operation of UV-visible spectrometers depends on the type of instrumental setup (single- or double-beamed). For the single-beamed, two measurements are carried out, the first one being the reference (typically the sole solvent) and the second being the sample. The above schematic diagram 2.4 is for the double beam UV-visible spectrometer. It consists of three main components: light source, monochromator and detector.[12] A Xenon arc lamp is largely employed as the main light source and covers the range of 200 – 700 nm; another common light source is a tungsten-halogen lamp that covers the range of 200 – 1000 nm. The monochromator is the second component and is made up of three parts: an entrance slit, a dispersion device and an exit slit. The dispersion device functions to produce an angular light dispersion, typically through a prism, which yields the desired range of wavelengths, with the exit slit that allows them to pass through the

sample. The excitation light is then passed down to two paths via a beam splitter: one path leads to the reference and the other to the sample. The detector records the intensity of the transmitted light over the wavelength range, by transforming the light intensity signal into an electrical signal.

2.3.2 Steady-state Photoluminescence Spectroscopy

Upon light absorption, several processes take place immediately, including the reverse quantum transition from the excited state back to the ground state. Such process, where energy is released in the form of photons, is generally termed photoluminescence and it occurs either in the form of fluorescence or phosphorescence (see **Chapter 1**, section **1.3**).

A fluorimeter, or photoluminescence spectrometer, is used to detect and study light emission, and the working scheme of such instrument is shown in **Figure 2.5**.
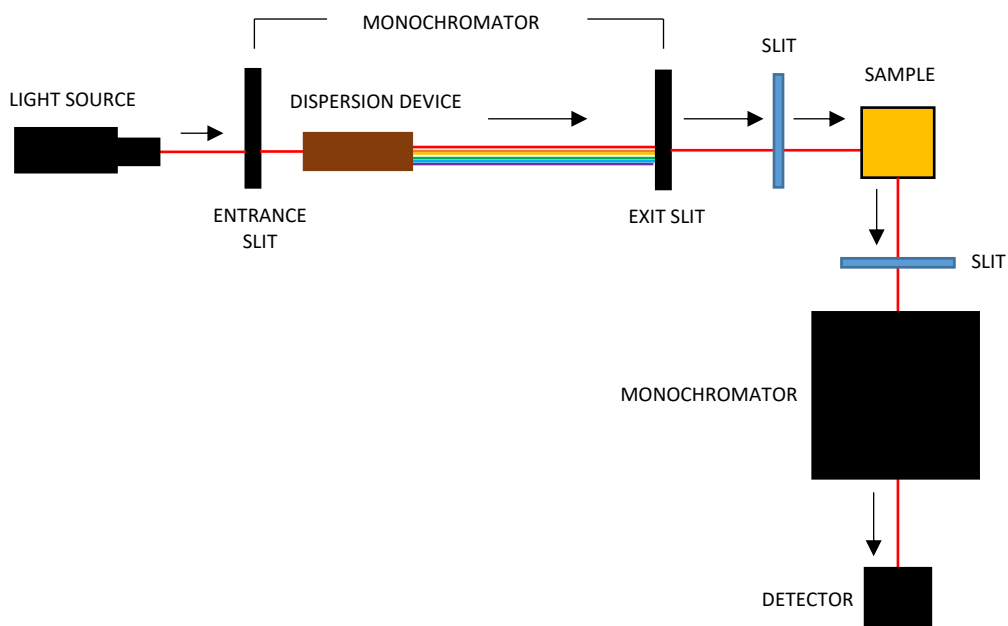
Figure 2.5: Schematic diagram of a fluorimeter.[13]

As in UV-visible absorption spectrometry, a Xenon arc lamp is used as the light source. A beam of light from the lamp is sent to the monochromator that selects or differentiates the exact wavelength at which the molecule of study absorbs. There are also entrance and exit slits whose

width can be varied and adjusted to obtain an optimum signal. This, in turn, affects the intensity of luminescence recorded by the detector as well as the spectral resolution. The lamp and the detector are angled at 90 degrees to each other, to avoid that the excitation beam reaches the detector and to reduce scattering effects caused by the sample and the sample cell (usually a quartz cuvette) upon excitation.[14]

Before measuring the emission spectra, an excitation wavelength is defined where the molecule absorbs. By measuring emission spectra, it is possible to determine the emission efficiency, which is quantified with the photoluminescence quantum yield (Φ_{PL}). The definition of absolute Φ_{PL} is given as the ratio between the number of photons emitted and the number of photons absorbed.[14]

$$\Phi_{PL} = \frac{photons\ emitted}{photons\ absorbed} \qquad (2.9)$$

Direct measurements of both photon numbers may be performed by using an integrating sphere device, where the intensity of the emitted light is recorded at all directions from the sample. The most common measurement of Φ_{PL}, which is also more accurate for solution samples, is by the relative method. A standard or reference sample, with a known Φ_{PL}, is chosen and compared with the sample under study. The standard is expected to emit over the same wavelength range as the unknown sample and both should have the same absorbance (typically 0.1 or below) at the same excitation wavelength. The following formula is then used to obtain the quantum yield of the unknown sample (Φ_S) in the comparison with that of the reference (Φ_R):[15]

$$\frac{\Phi_S}{\Phi_R} = \frac{I_S}{I_R} \ x \ \frac{(1-10^{-A_R})}{(1-10^{-A_S})} \ x \ \frac{n_R^2}{n_S^2} \qquad (2.10)$$

where I_R and I_S are the emission intensities of the reference and the sample, respectively, A_R and A_S are the absorbance of the reference and the sample, respectively, and n_R and n_S are the refractive indexes of reference's solvent and sample's solvent, respectively. To determine the quantum yield of the sample with high precision and accuracy, the emission spectra of both the reference and the sample are measured at the same excitation wavelength, and all other parameters are kept equal, such as the width of the excitation and emission slits, and the use of filters).

The above formula has been used to calculate all the quantum yields reported in the following chapters of this thesis. For all dye-doped silica materials described here, the free dyes in solution were used as the respective references and the measurements of the materials were carried out from diluted suspensions of 50 nm sized nanoparticles. Such fine suspensions were made iso-absorptive with the relative standards, by working in equimolar conditions and has a known quantum yield for our samples, where the dyes are attached to the silica or within the micelles. The quantum yield of the free dye in the solution is used as the standard and compared with that of the hybrid.

All the steady-state measurements presented in this thesis were performed using an Edinburgh FLS980 photoluminescence spectrometer. The instrument is equipped with a 450 Watt Xenon arc lamp, Czerny Turner monochromators (1.8 nm/mm^{-1} dispersion; 1800 grooves/mm^{-1}) and a Hamamatsu photomultiplier tube (in fan associated TE cooling housing, at a -20^0 C operating temperature).

2.3.3 Time-resolved Photoluminescence spectroscopy

The steady-state spectroscopy only gives information on a molecule's photoluminescence properties, which can be considered fundamental. However, it does not provide details on the kinetics of deactivation of the excited state. Time-resolved measurements are then required, in that they enable detection of the excited state lifetime and help determining whether the emission mechanism is by fluorescence or phosphorescence. The most common technique used for measuring the excited state decay of a molecule is called time-correlated single-photon counting (TCSPC).
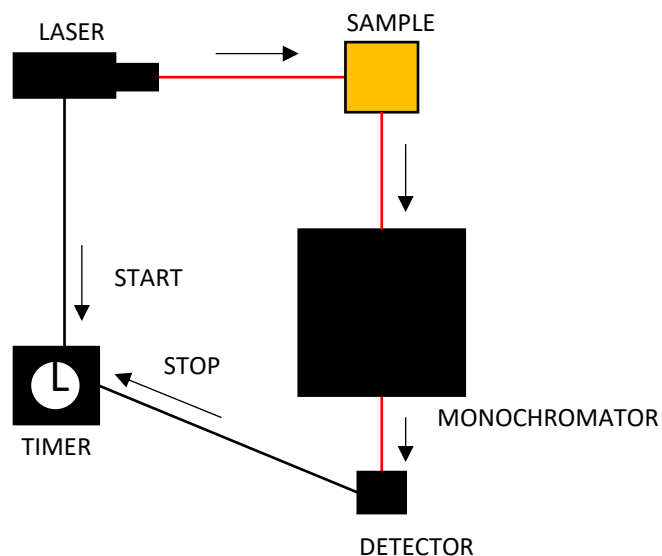
Figure 2.6: Schematic diagram of a TCSPC spectrometer adapted from Prashant Kamat Laboratory.[16]

Figure 2.6 shows a working scheme of a typical TCSPC spectrometer. In our instrument, we have two different sets of lasers, 372 nm and 475 nm. The pulse from the laser is used to irradiate the sample at a specific emission wavelength, and this will send a signal to start a timer. At 90^0 to the monochromator, the sample will emit through the filter and then the emission light intensity is recorded by the detector. The timer will automatically stop immediately after the emitted photons reach the detector. To determine a molecule's decay profile, the time difference between sample excitation and photon emission is recorded by the detector. Rather than time directly, the instrument measures an electrical property that depends on it. In the process, an electrical pulse accompanying laser excitation is directed to the timer, setting the start input of a time-to-amplitude (TAC) converter. An electrical response relative to the sample luminescence is used as the stop. The function of the start and the stop pulses is to initiate and stop the charging of a capacitor, respectively. The time between the two pulses is directly proportional to the final voltage and can then be determined. A different number of photons will be emitted at different time delays after excitation and the overall trend is typically a gradual decrease in photons per time from the excitation time until the end of the decay process. Several repetitions of start-stop measurements

42

are then carried out at different time delays upon excitation, resulting in the generation of a histogram of emission intensities per time, which gives a decay curve. Statistically, each emitted photon will take a different time to reach the detector. That is equivalent to say that there will be a different number of molecules in the excited state at different time delays after excitation. We can define n(t) the number of excited molecules at a time t and n_0 the initial population of molecules in the excited state. Being luminescence a first-order process, the decay function of n(t) is given by:

$$n(t) = n_0 \, e^{-\frac{t}{\tau}} \qquad (2.11)$$

Where τ is the lifetime of the excited state. This indicates that the probability of the excited state decay decreases exponentially with time and a typical determination of an accurate lifetime value consists in running several thousands of measurement cycles over a wide time scale, followed by an exponential fitting of the decay curve. In some samples, the decay profile may give a multi-exponential trend, indicating two or more decay processes occurring in the sample.[17]

To ensure acquisition of an accurate decay profile, the emission rate from the sample must be kept low compared to the excitation rate (typically, up to 4% of the laser rate), as this enables the detector to differentiate between the emission and the excitation signals.[18] For all measurements reported in this thesis, the fitting analysis was performed on the fluorimeter software F980, with numerical data reconvolution based on Marquardt-Levenberg algorithm.

The Edinburgh FLS980 spectrometer was used for all the time-resolved measurements reported in this thesis. The instrument has a built-in time-correlated single photon counting (TCSPC) module and two sets of lasers: an EPL_375 (exciting at 370.8 nm) and an EPL_475 (471.8 nm), both featuring a 61.1 ps pulse width.

The actual measured lifetime can be determined by multiplying each lifetime with its relative percentage and sum it all, which is then divided by the total sum of relative percentage obtained from the fittings. If we use figure x as an example, the average lifetime will be:

Fix	Value / ns	Std. Dev / ns	Fix	Value	Std. Dev	Rel %
τ_1 ☐	0.7674	0.00254	B_1 ☐	752060.875	1614.0457	36.72
τ_2 ☐	2.5797	0.00765	B_2 ☐	327262.969	1674.5775	53.71
τ_3 ☐	10.2635	0.04927	B_3 ☐	14667.857	173.6645	9.58
τ_4 ☐			B_4 ☐			
			A ☐	359.940		

$$\chi^2 : 3.320$$

Figure 2.7: Example of a measured lifetime from TCSPC instrument showing the lifetimes and relative percentages after fittings.

If we select two lifetimes with high relative percentages, it will be:

$$T_F = \frac{(0.77 \; x \; 0.37) + (2.58 \; x \; 0.54)}{(0.37 + 0.54)}$$

$$T_F = 5.08 \; ns$$

K_R this can be determined using equation x:

$$K_R = \frac{\Phi_F}{T_F \; x10^{-9}} \qquad (2.12)$$

While KNR can be calculated using equation x as follows:

$$K_{NR} = \frac{1 - \Phi_F}{T_F \; x10^{-9}} \qquad (2.13)$$

2.3.4 **Luminescence Anisotropy**

The origin of anisotropy in fluorescence spectroscopy is found in the existence of transition moments for absorption and emission that lie along specific directions within the structure of a fluorophore. When fluorophores are excited with polarised light, only those having their absorption transition moments oriented along the electric field vector of the incident light are preferentially excited and would subsequently emit light. In homogeneous solutions with low viscosity, fluorophores are randomly oriented at all directions and the rate of rotational diffusion is typically faster than the rate of emission. Under these conditions, the final emission is depolarized and the

anisotropy of the solution close to zero.[12] On the contrary, high-viscosity solutions and solid-state samples may have non-zero anisotropy and show polarised emission. In cases where rotational diffusion is hindered or even suppressed, the only way emission can become depolarized is by resonance energy transfer (RET) of energy among fluorophores. Such type of RET between chemically identical molecules is termed homotransfer and typically occurs for fluorophores which display small Stokes shifts. In fact, homotransfer among fluorescent molecules was one of the earliest observations in fluorescence and it was detected by a decrease in the anisotropy of fluorophores at higher concentrations.[14]

Typical fluorescence anisotropy measurements begin with steady-state emission and excitation spectra. Linearly polarised light beams of vertical (V = 0°) and horizontal (H = 90°) orientation are used to excite the sample and detect the sample emission, as shown in **Figure 2.7**.
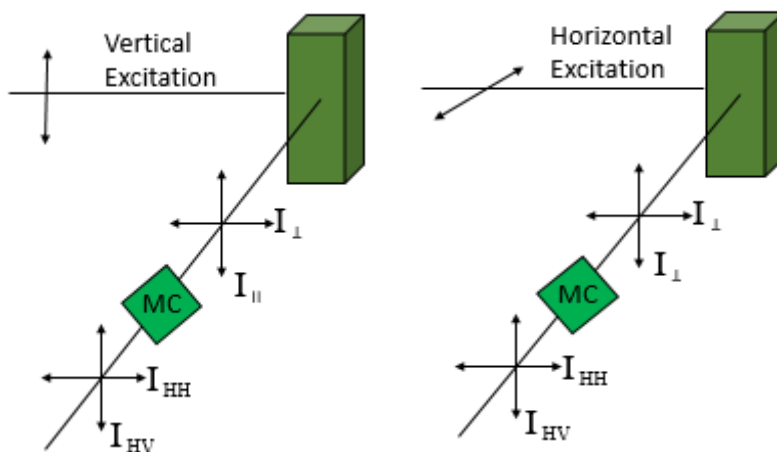
Figure 2.7: Scheme showing the measurement of fluorescence anisotropy for vertical and horizontal orientations; MC indicates a monochromator.[14]

Normally, four emission anisotropy spectra are recorded (I_{VV}, I_{VH}, I_{HV} and I_{HH}), after which an emission wavelength is selected, where the intensity difference is the largest. Two anisotropy excitation scans are then taken and a correction factor, called G-factor, is obtained at the selected emission wavelength:

$$G = \frac{I_{HH}(\lambda_{em})}{I_{HV}(\lambda_{em})} \qquad (2.14)$$

The G-factor is an experimental correction for the polarization bias of the detection system rather than a factor related to the physical properties of the sample. For example, G = 2 means that the detection system detects horizontally polarised light "twice as good" as vertically polarised light. The difference between the two steady-state measurements is in term of G-factor correction: in the excitation anisotropy, only one G-factor is needed as the emission wavelength is fixed, whereas in emission the whole curve of the G-factor is necessary and each emission wavelength has a specific G-factor value.[12]

The G-factor is then used to carry out time-resolved anisotropy measurements. The sample is excited using vertically polarized light pulses while the intensity decay of the sample is measured through a polarizer oriented vertically, VV, and horizontally, VH, to the sample. The anisotropy decay, r(t), is then calculated as:

$$r(t) = \frac{I_{polarised}(t)}{I_{total}(t)} = \frac{G \cdot I_{VV}(t) - I_{VH}(t)}{G \cdot I_{VV}(t) + 2I_{VH}(t)} \qquad (2.15)$$

The acquisition process is in TCSPC mode and it yields two curves of polarised time-resolved intensity decay. At the end of the measurement, the anisotropy function, also termed anisotropy profile, is calculated from the two anisotropy decay curves and displayed separately, to then be numerically analysed using an exponential tail fit.[14] The latter gives a value that can be interpreted as the fluorescence depolarisation time, or polarisation transfer time.

References

(1)   Hydrogen   (Proton,   Deuterium   and   Tritium)   NMR. http://chem.ch.huji.ac.il/nmr/techniques/1d/row1/h.html (accessed 2022-06-25).

(2) Rodger, C. A. Spectroscopic Methods in Organic Chemistry, Fifth Edition. Concepts in Magnetic Resonance **1997**, 9 (5), 355–356.

(3) NMR Spectroscopy (Nuclear Magnetic Resonance) - Principle, Working, Chemical Shift, Instrumentation & Applications of NMR Spectroscopy https://byjus.com/chemistry/nmr-spectroscopy/ (accessed 2021 -11 -02).

(4) Ernst, R. R.; Bodenhausen, G.; Wokaun, A. Principles of Nuclear Magnetic Resonance in One and Two Dimensions. 9.

(5) Reimer, L. *Transmission Electron Microscopy: Physics of Image Formation and Microanalysis*; Springer, 2013.

(6) Marturi, N. Vision and Visual Servoing for Nanomanipulation and Nanocharacterization in Scanning Electron Microscope. **2013**.

(7) Introduction   to   Electron   Microscopy   -   2nd   Edition https://www.elsevier.com/books/introduction-to-electron-microscopy/wischnitzer/978-0-08-009670-4 (accessed 2021 -10 -22).

(8) Zuo, J. M.; Spence, J. C. H. Introduction and Historical Background. In *Advanced Transmission Electron Microscopy: Imaging and Diffraction in Nanoscience*; Zuo, J. M., Spence, J. C. H., Eds.; Springer: New York, NY, 2017; pp 1–18.

(9) Characterization of Solids. In *Tutorial Chemistry Texts*; Abel, E. W., Ed.; Royal Society of Chemistry: Cambridge, 2007; pp 48–80.

(10)   Wayne, R. P. *Principles and Applications of Photochemistry*; Oxford University Press: Oxford [England] ; New York, 1988.

(11) Introduction. In *Spectrochemical Analysis by Atomic Absorption and Emission*; Royal Society of Chemistry: Cambridge, 2007; pp 1–15.

(12) Owens, T. *Fundamentals of modern UV-visible spectroscopy: a primer.*; Hewlett Packard, 1996; pp 1- 68.

(13) Molecular Fluorescence Spectroscopy http://www.pci.tu-bs.de/aggericke/PC4/Kap_I/mol-fluo.htm (accessed 2021 -11 -02).

(14) Lakowicz, J. R. *Principles of Fluorescence Spectroscopy*; Springer Science & Business Media, 2013.

(15) *Standardization and Quality Assurance in Fluorescence Measurements I: Techniques*; Resch-Genger, U., Ed.; Springer Series on Fluorescence; Springer Berlin Heidelberg: Berlin, Heidelberg, 2008; Vol. 5.

(16) Spectroscopy Facilities || The Prashant Kamat lab at the University of Notre Dame https://www3.nd.edu/~kamatlab/facilities_spectroscopy.html (accessed 2021 -11 -02).

(17) Fast fluorescence lifetime imaging techniques: A review on challenge and development https://www.worldscientific.com/doi/epdf/10.1142/S1793545819300039 (accessed 2021 -10 -28).

(18) Roy, K.; Kayal, S.; Ravi Kumar, V.; Beeby, A.; Ariese, F.; Umapathy, S. Understanding Ultrafast Dynamics of Conformation Specific Photo-Excitation: A Femtosecond Transient Absorption and Ultrafast Raman Loss Study. *J. Phys. Chem. A* **2017**, *121* (35), 6538–6546.

Chapter 3: Turning weak emitters into outstanding luminescent materials using rigid host media

3.1 Introduction

The search for ever more efficient and sustainable energy solutions requires the development of new materials that are capable of high conversion rates with the least possible energy losses. Such target is desirable and currently tackled for different types of conversion processes, e.g. light-to-electricity and electricity-to-light, and the primary step typically undertaken is the design of molecular dyes with controlled light absorption and emission bandwidths alongside high transition efficiencies.[1]

3.1.1 Dipyrromethenes (dipyrrins)
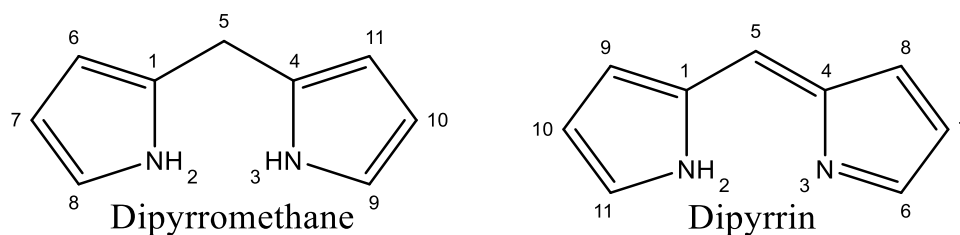
Figure 3.1: Left; structure of a typical dipyrromethane from unsubstituted pyrrole and Right; the structure of dipyrrin/dipyrromethene after oxidation with p-chloranil or DDQ.

Dipyrrins belong to the class of π-conjugated molecules having one or two degrees of unsaturation with intense absorption in the visible region.[2,3] The structure of these compounds consists of two pyrrole rings bridged by an sp^2 carbon (see **Figure 3.1**) and resembles half of a porphyrin ring. The most common dipyrrins have substituents at the α-, β- and *meso*-position (5-position), with the latter, considered as the point of introduction of important substituents in the synthetic routes.[2,3] The nitrogen atoms in the structure provides the coordinating ability, and therefore they are termed ligands. Among the various classes of ligands studied so far, dipyrrins present attractive advantages over others, such as simple, high-yielding and cheap synthetic routes, wide coordinative versatility towards semi-metals like boron and several metal ions, and finely tuneable optical activity through structural modification on the pyrrole rings by the introduction of specific substituents.[2,4,5] Alongside boron dipyrrins (known as BODIPY), the most extensively studied dipyrrin-based dyes so far, metal dipyrrins have recently gained attention. They have been the subject of a growing number of studies on the application of their optical properties for energy conversion.[6–9] Examples

51

of metals used for complexation with dipyrrins include copper, nickel, cobalt and iridium. After successful complexation with any of the metals mentioned above, the resulting complexes can be used as luminescent dyes.[1,2,5]

3.1.2 Zinc dipyrrin complexes
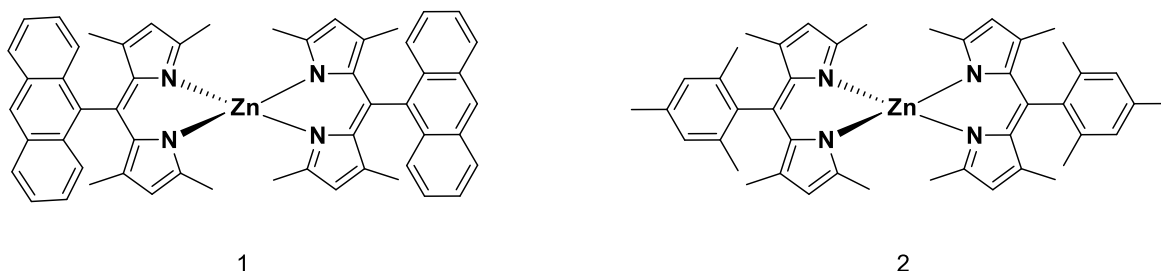
Figure 3.2: The complexes (1 and 2) used in this chapter were obtained from our research collaborators at KIT.

The search for luminescence properties in new metal dipyrrins has recently intensified in the field of photochemistry, as such complexes find use as probes to sense metal ions in living systems and as light-absorbing and light-emitting dyes in optoelectronic devices.[10,11] Generally, metal dipyrrins are emissive, with few exceptions that show low quantum yields.[2,5,12] Within this class of compounds, zinc(II) dipyrrins are particularly attractive because of the presence of an earth-abundant central ion and the ability to form supramolecular structures and coordination polymers,[13–16] commonly exhibiting a linear geometry, due to the easy functionalisation on the meso- position of the dipyrrin. Despite their strong absorption in the blue-green region, though, with molar extinction coefficients above 300,000 M^{-1} cm^{-1}, they are typically weak emitters because of the strongly competitive non-radiative deactivation pathways introduced by the distorted tetrahedral coordination and a certain structural flexibility.[6] Two examples are represented by the zinc(II) dipyrrins that were investigated for this study: they are homoleptic complexes and possess anthracene and mesitylene groups as substituents on the meso-position of the dipyrrin core (see **Figure 3.2**). As will be discussed in the next section, they have intense absorption in the visible region, although fluorescence is barely observable.[17]

One of the possible solutions that have been recently adopted to improve the emission quantum yields of such zinc complexes is the use of bulky coordinating ligands that are able to impose a high structural rigidity to the whole complexes. This strategy involves the design of suitable multi-step synthetic routes, with the aim of expanding the dipyrrin core from the α- or the β-positions, so as to introduce sterically hindering groups.[8,18] An alternative solution, which we used in this chapter, for increasing the luminescence efficiency without having to introduce lengthy synthetic modifications is to impart the desired rigidity by encapsulation of the complexes into a spatially constraining host structure. This may, in principle, also help circumvent another strict limitation to fluorescence efficiencies that homoleptic bis(dipyrrinato) zinc complexes suffer from the presence of symmetry-breaking charge-transfer excited states, which become the lowest-lying states in polar solvents and, being prone to non-radiative decay, lead to fluorescence quenching.[7]

3.1.3 Aims of this Chapter

The aim of the research studies presented in this chapter is to demonstrate how the photoluminescence properties of the two weakly emissive zinc(II) dipyrrins mentioned above can be improved by encapsulation into a rigid host material. For this purpose, we adapted a synthetic methodology that is used to prepare a mesoporous silica material named COK-12. The use of ordered mesoporous silica as a rigid host for dye molecules has been attracting great interest in the field of photochemistry in recent years,[19,20] due to a series of multiple advantages. These include: design of bifunctional host-guest materials, enhanced chemical stability and protection to the guest molecule, homogeneous dispersion of guest dyes, rigid pore spaces that can be tailored to adapt towards different sizes of guests.[19,21,22]

The next section will show that the luminescence properties of the target dyes can effectively be manipulated and improved, owing to the spatial and environmental constraints imposed by the insertion into mesoporous silica.

3.2 Results and Discussion

3.2.1 Absorbance spectra

Complexes 1 and 2 were first synthesised and reported, respectively, by Nishihara's and Thompson's groups.[7,8] Figure 3 shows the steady-state absorbance spectra of the two free dyes from dichloromethane solutions at 4×10^{-6} M concentration.
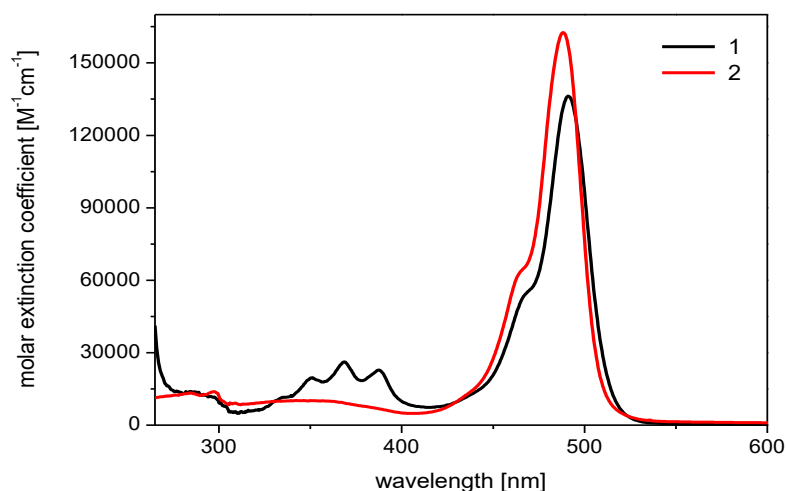
Figure 3.3: Absorption spectra of 1 and 2 recorded from 10^{-6} M dichloromethane solutions.

Both complexes show similar absorbance bands, which are typical of BODIPY chromophores. The maximum absorbance for 1 and 2 was observed at 488 nm, and it corresponds to the lowest-energy $\pi \rightarrow \pi^*$ singlet transition, as illustrated in the Jablonski diagram in **Figure 3.4**. The complexes exhibit a high degree of light absorption, as can be noticed from the large molar extinction coefficients, above 100,000 M^{-1} cm^{-1}, which is the typical range for dipyrrins. Complex 1 shows an additional absorption band around 350 – 390 nm due to the $\pi \rightarrow \pi^*$ transition within the anthracene moiety. A Jablonski diagram summarising all-optical transitions in 1 is shown in **Figure 3.4.** Both complexes show fluorescence quantum yields below 1% in mildly polar solvents, such as chloroform and dichloromethane, whereas the values are 2% (complex 1)[18] and 16% (complex 2) in cyclohexane, the least polar solvents used by the above groups (see also Table 3.1).
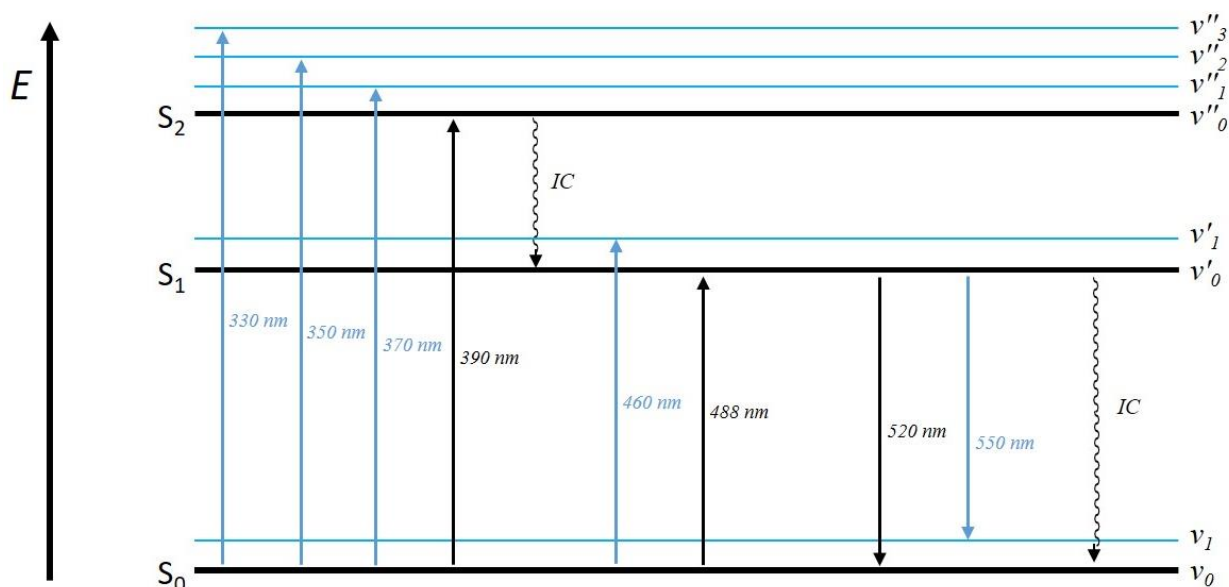
Figure 3.4: Jablonski diagram showing the optical transitions of excitation and emission for complexes 1 and 2 at their respective wavelengths. E = Energy, S = singlet state, v = vibrational levels and IC = internal conversion.

3.2.2 Synthetic strategy used for the host-guest materials

The experimental approach we used for improving the fluorescence yields of the complexes further above the values obtained in the solution takes advantage of the well-established soft-template route used for all types of mesoporous silica materials. A micellar template is made by using amphiphilic surfactants able to self-assemble in water and form rod-like micelles; after this first step, a suitable silica precursor is added, which hydrolyses and polymerise around the template, forming the final silica network.[23] Due to the insolubility of the zinc dipyrrins in water, their addition during the self-assembly process leads to their spontaneous diffusion and encapsulation into the solvent-free, rigidified, hydrophobic core of the micelles. In order to prepare the mesoporous silica used in this study, COK-12, the micelles are built using the Gemini surfactant Pluronic-P123. To enable a homogeneous dispersion of the dyes, minimise intermolecular aggregation, quenching effects and prevent structural disruption of the micelles and, consequently, of the silica particles, we applied a recent strategy established in our group,[24] using a low loading

of complexes, at a 99:1 molar ratio of Pluronic-P123:complex for each of the host-guest systems, hereafter named 1S and 2S.
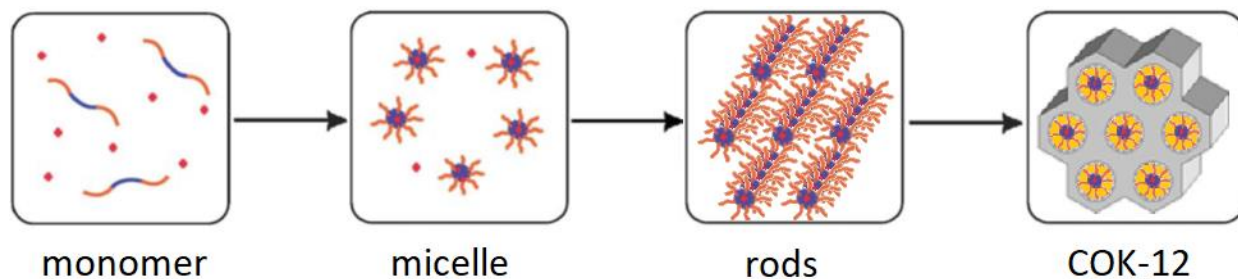
Figure 3.5: The synthetic route for the preparation of the two host-guest silica materials 1S and 2S.
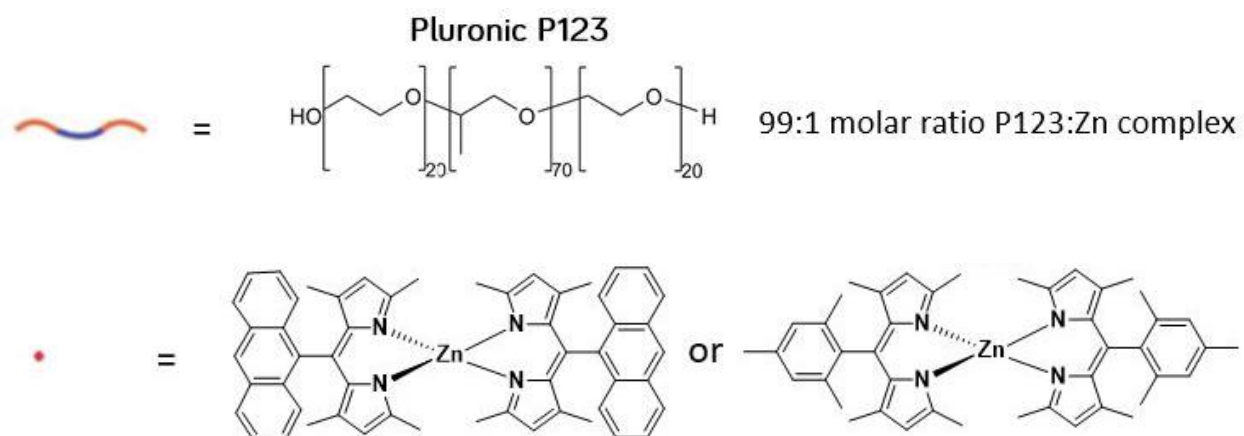
3.2.3 **Structural analysis**
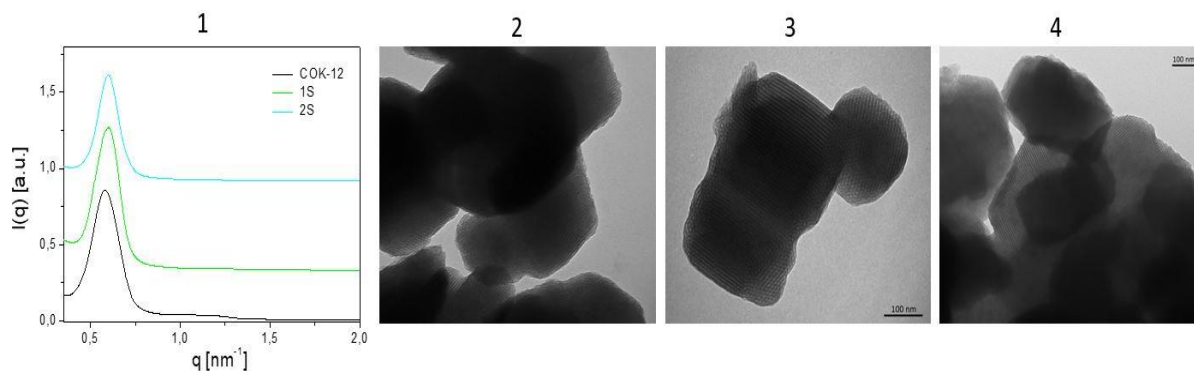
Figure 3.6: 1: SAXS profiles of the dye-loaded silica materials, as compared with standard COK-12 silica. 2, 3 and 4: TEM micrographs of the standard COK-12, 1S and 2S, respectively.

The final samples were characterised by small-angle X-ray scattering (SAXS, Fig. 3.6(1)) and transmition electron microscopy (TEM, Fig. 3.6(3) and 3.6(4)), which confirm that the structural order and the morphology of the COK-12 silica particles are essentially preserved after dye-loading. The SAXS data are reported in **figure 3.6(1)** show that the most intense peaks for the silica materials occur at q values of 0.64- 0.66 degrees, and the q ratios of the main peak to the much weaker additional peaks at higher q values conform, within experimental error, to the theoretical q ratios of 1:√3:2:√7 that correspond to the 2D hexagonal reflections of (10), (11), (20) and (21), respectively. The structures are, thus, consistent with literature values for COK-12 silica[25] and prove that the dye-doped P-123 micelles maintain the same structural order of plain silica, that is, the hexagonal columnar order. This can be indeed visualised from the TEM micrographs in **figure 3.6(2)**, where the silica particles show a highly ordered morphology with well visible parallel channels. Therefore, as the pore channels do not undergo a detectable distortion (*i.e.* expansion), following encapsulation of the complexes, we can infer that the latter must experience considerably strong spatial constraints once entrapped into the hydrophobic core of the cylindrical micelles. UV-visible spectroscopy studies were then carried out on the samples to evaluate the effects that such a structural rigidity exerts on the optical properties of the complexes. The pore diameter was calculated using equation 2.3 (chapter 2, page 34).

3.2.4 **Photophysical Analysis**
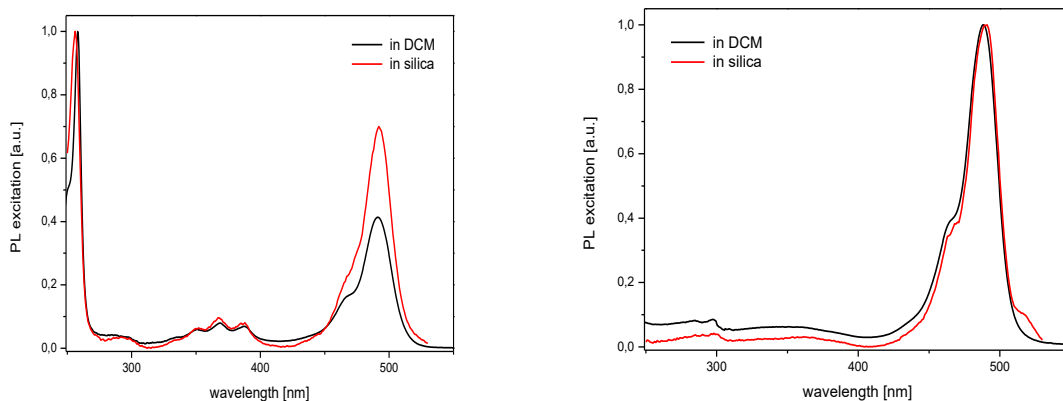
Figure 3.7: Excitation spectra of the complexes 1 (left) and 2 (right) from 4 x 10^{-6} M dichloromethane solutions (black lines), compared with equimolar suspensions of the host-guest silica samples in water (red lines). All spectra were recorded at λ_{em} = 550 nm, with both excitation and emission slits at 5 nm.

The excitation spectra of the dyes within the silica materials are shown in **Figure 3.7**, in comparison with the spectra recorded from the free dyes in dichloromethane solutions. Both samples show nearly identical excitation profiles, indicating that the optical properties of the dyes are preserved upon encapsulation in the silica. An interesting difference can be observed in the case of complex 1, whose excitation peak at 488 nm is more intense in silica than in solution. This could be a first indication from the spectroscopy analysis that the complex experiences a high structural rigidity within the silica/micellar matrix and that such rigidity reflects into a larger spatial overlap between the ground and the excited state.
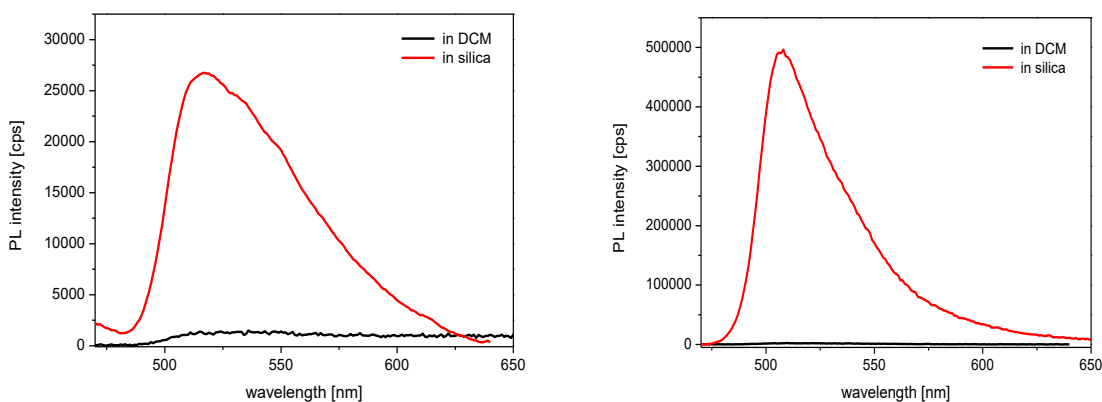
Figure 3.8: Emission spectra of the complexes 1 (left) and 2 (right) from 4 x 10^{-6} M dichloromethane solutions (black lines), compared with equimolar suspensions of the host-guest silica systems in water (red lines). All spectra were recorded at $\lambda_{exc} = 450$ nm, with both excitation and emission slits at 5 nm.

The photoluminescence spectra of the samples 1S and 2S are reported in **Figure 3.8** and show enormous differences in comparison with the spectra from the free dyes in solution. First, the fluorescence intensities at 510-520 nm are impressively enhanced in silica. Second, the emission bandwidth becomes much narrower in silica than in solution for both complexes, with the full width at half-maxima (FWHM) reducing from values that exceed 4300 cm^{-1}, which are hardly measurable with absolute precision in solution due to the extremely weak and broad emission, to values in silica of ~2300 cm^{-1} for 1 and ~1200 cm^{-1} for 2. Such an effect is indicative of restricted vibrational freedom of the complexes within the constrained micellar environment; moreover, considering that the FWHM in the emission band of 2 becomes close to the value in excitation, ~1100 cm^{-1}, it suggests that the structural rigidification forces the geometries of the ground and the excited state to be more similar to one another. The fluorescence quantum yields of all samples were recorded, and all data, including excited-state lifetimes and rate constants, are displayed in Table 3.1.

Table 3.1. Photophysical properties of the zinc complexes.

Sample	Φ_F	$\tau_F^{[c]}$ / ns	k_R / s^{-1}	k_{NR} / s^{-1}
1[a]	0.003 0.02[d]	1.75	$1.71 \cdot 10^6$	$5.70 \cdot 10^8$
1S[b]	0.035	0.43	$8.14 \cdot 10^7$	$2.24 \cdot 10^9$
2[a]	0.005 0.16[d]	1.40 2.4[d]	$3.57 \cdot 10^6$ $7.5 \cdot 10^{7[d]}$	$7.11 \cdot 10^8$ $3.41 \cdot 10^{8[d]}$
2S[b]	0.550	1.34	$4.10 \cdot 10^8$	$3.36 \cdot 10^8$

From the table: a = free complex in10^{-6} M dichloromethane solutions; b = from equimolar water suspensions and confirmed by solid-state measurements using an integrated sphere; c = laser excitation at 475 nm, pulse width 62 ps, recorded at 530 nm; d = in cyclohexane.[18]

A comparative analysis of the quantum yields allows us to make some important observations: a 10-fold increase in the emission of 1 occurs upon incorporation, and the enhancement is even 100-fold in the case of 2 (see Table 3.1, comparing with the values in dichloromethane solution). The high sensitivity of luminescence quantum yields and lifetimes on solvent polarity deserves further clarification here in light of previous research. As it was demonstrated by Nishihara and Thompson,[7,8] homoleptic zinc bis-dipyrrins undergo photoinduced charge transfer from one ligand to the second one, which breaks the symmetry of the excited state. The latter is indeed defined as a symmetry-breaking charge-transfer (SBCT) state and becomes the lowest state even in mildly polar solvents such as dichloromethane. Since SBCT states are typically non-emissive in nature, this leads to a total emission quenching in dichloromethane, with fluorescence yields of 0.3% and 0.5% for 1 and 2, respectively, whereas in relatively apolar solvents such as cyclohexane, the above values increase up to 2% and 16%.[18] Such trend reaches its extreme in the solvent-free and apolar environment of the micellar structures within the silica channels: therein, the absence of solvent

stabilisation and the rigid environment further reduce the non-radiative deactivation pathways and lead to emission quantum yields of 3.5% and 55%, respectively, for 1 and 2. The excited-state lifetimes were also measured and showed relatively milder effects from solution to solid state: a reduction by a factor of four for 1, whereas no significant change for 2. All the different values of T_F, K_R and K_{NR} were obtained through using different equations in chapter (see page 34 and 44).
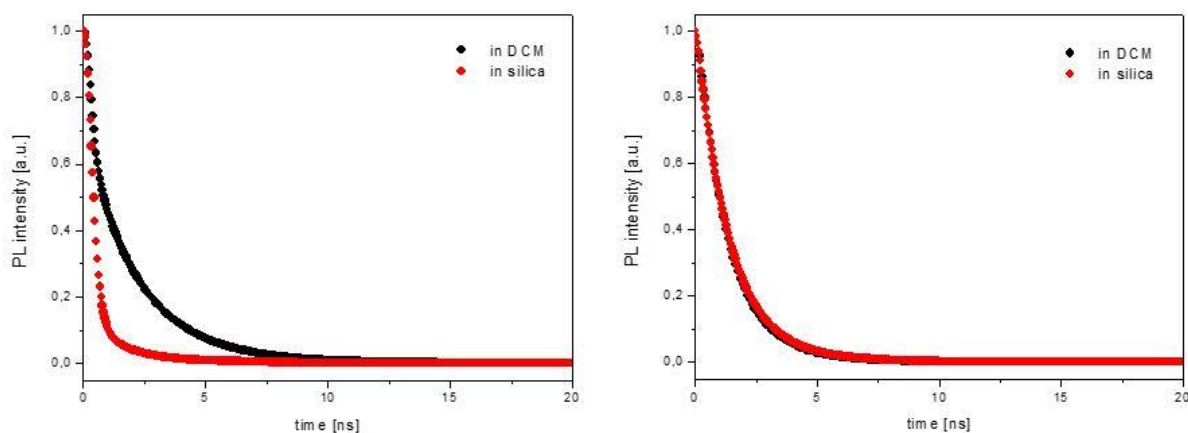
Figure 3.9: Excited-state decay profiles of the complexes 1 (left) and 2 (right) from 4 x 10^{-6} M dichloromethane solutions (black lines), compared to the profiles recorded from equimolar water suspensions of 1S and 2S (red lines), all measured at 530 nm under laser excitation at 472 nm.

Figure 3.9 shows the comparison between the excited decay profiles of the two free dyes in solutions and when encapsulated in silica, which is summarised in Table 1. For both complexes, the radiative rates increase dramatically, nearly 50-fold for 1 and over 100-fold for 2, and we consider this a further effect of the encapsulation of the complexes. Considering the restricted vibrational and rotational degrees of freedom within the silica host, significant geometrical distortions in the complexes from the ground to the excited state are energetically unfavoured; this may translate in an increased probability of radiative deactivation taking place from an excited state conformation near the initial Franck-Condon form. Such a situation has also been demonstrated in previous examples of dipyrromethene complexes, where rigidification of the organic backbones with sterically hindered groups proved to increase the radiative rate.[18,26]

On the other hand, the non-radiative rate almost quadruples for 1, whereas it halves for 2, showing that 1 is more affected by non-radiative quenching than 2, once it is encapsulated inside the silica

template. We ascribe this behaviour to the effect that a partial intermolecular aggregation may have on 1, resulting from the tendency of the anthracene moieties to undergo π-stacking in a more constrained environment than in fluid solution. Such an effect could not be observed for 2, where the sterically hindered mesityl group prevents aggregation. Indeed, the reduced vibrational deactivation pathways in 2 contribute to a much larger increase in emission quantum yield than for 1, as discussed earlier.
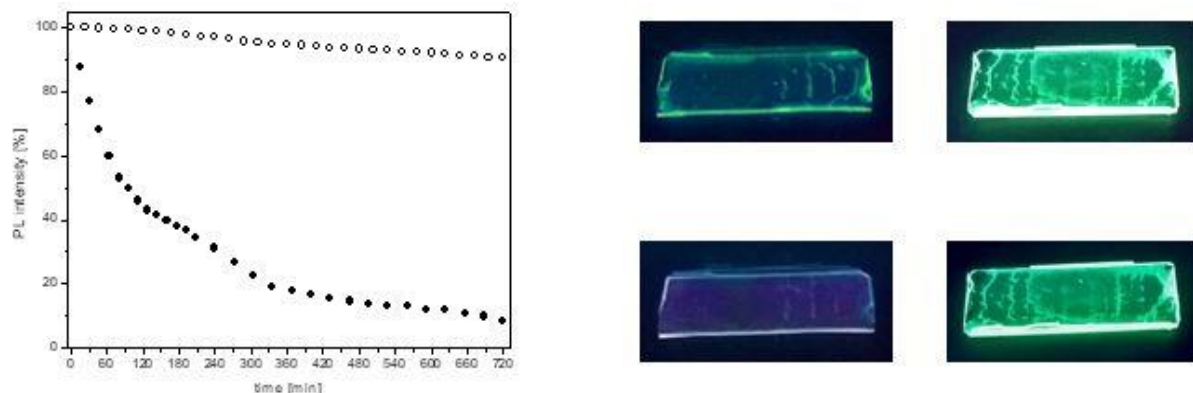
Figure 3.10: Left: Photoluminescence stability tests performed on thin polymer films doped with the free complex 2 (black circles) and with silica particles embedding the complex (white circles); irradiation wavelength = 450 nm; detection wavelength = 520 nm. Right: Photographs of the 2-doped (middle) and the 2S doped PMMA films (further right), under UV light (365 nm), before (top pictures) and after (bottom pictures) the irradiation tests.

Since the 2S sample shows a promising photoluminescence efficiency, we tried to further exploit its properties for the design of new luminescent solar concentrators.[27,28] For this purpose, thin films were prepared by dispersion of the luminescent silica particles in a transparent polymer, polymethyl methacrylate (PMMA), and the photostability of such films was tested against steady UV light irradiation over the course of twelve hours. For comparison, the tests were carried out also on polymeric films doped with the free complexes, using the same concentration of complexes present in the films containing the silica particles. The results are shown in **figure 3.10**, which reports the observed trend in photoluminescence intensity, together with photographs of the polymeric films exposed to UV light before and after the stability tests. It is evident that complex 2, once incorporated into the silica, retains its luminescence intensity throughout the test, whereas

the emission from the free complex dispersed in PMMA halves its intensity in less than two hours of irradiation and photo-bleaches almost completely after twelve hours.

3.3 Conclusion

This chapter presented the results of the strategy employed to successfully improve the poor luminescence properties of two bis-dipyrrinato zinc(II) complexes through incorporation into mesoporous silica. The two dyes (1 and 2) were embedded by self-assembly within the micelles formed by the Pluronic-P123 surfactant in water. Such dye-doped micelles were subsequently used as a template for the growth of a silica network, enabling the formation of robust solid-state light-active materials. The TEM and SAXS analysis presented here confirms the retention of the pore spaces even after the insertion processes. The UV-visible spectroscopy analysis, carried out using both steady-state and time-resolved techniques, shows that both complexes become intensely luminescent once trapped into the silica/micellar matrix. This is attributed to the effects of the high structural rigidity on the radiative rates and results into a 10-fold increase in fluorescence quantum yield for complex 1 and a 100-fold increase for complex 2. The latter also showed an enhanced photostability when inserted into silica, as confirmed from the irradiation tests from thin transparent films.

It can then be concluded that the assembly strategy used in this study proved effective, and it also serves as a means to suppress photoinduced degradation of the complexes. This may anticipate the potential use of these systems for applications in sensitisation (e.g. solar concentrators) and light-emission technologies.

3.4 Experimental Section

3.4.1 Materials and Methods

All air- and water-sensitive experiments were performed under a nitrogen atmosphere by using standard vacuum-line techniques. All chemicals were obtained commercially (Sigma Aldrich, Acros organics and Honeywell) and used without further purification. "H_2O" refers to high purity water with a conductivity of 0.04 μS cm^{-1}, obtained from a Milli-Q purification system. Thin-layer chromatography (TLC) was carried out on silica plates (silica gel 60 F254, Merck 5554) and visualised by a UV lamp (254 nm). Preparative column chromatography was carried out using

silica gel (Merck Silica Gel 60, 230:400 mesh) pre-soaked in the starting eluent. ^{1}H and ^{13}C NMR spectra were recorded with either Bruker Ascend 300 or Bruker 500 Ascend spectrometers operating at 25 °C. CDCl$_3$ was used as internal standard for both ^{1}HNMR (δH = 7.26 ppm) and ^{13}C NMR (δC = 77.16 ppm) spectra. Fluorescence spectra and lifetimes were measured using an Edinburgh FLS980 photoluminescence spectrometer, equipped with a 450 W Xenon arc lamp, Czerny Turner excitation and emission monochromators (1.8 nmmm@1 dispersion; 1800 groovesmm@1), time-correlated single photon counting (TCSPC) module and a Hamamatsu R928P photomultiplier tube (in fan assisted TE cooled housing, operating temperature -20 °C). For lifetime measurements, samples were excited with an EPL-475 (471.8 nm; 62.6 ps pulse width) picosecond pulsed diode laser, and data analysis was performed on the F980 software with numerical data reconvolution based on the Marquardt-Levenberg algorithm. Luminescence quantum yields were measured using as reference a basic ethanol solution of fluorescein. Transmission electron microscopy images were taken on a 100 kV CM100 TEM (FEI).

3.4.2 Synthesis of dipyrromethene ligand (1a)
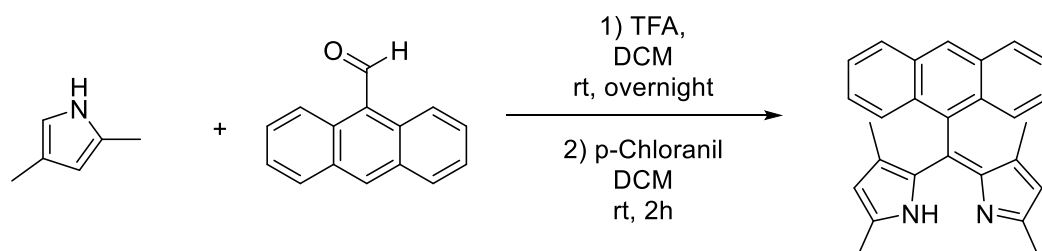
Figure 3.11: Synthetic route of dipyrromethene ligand from anthracene-9-cabaldehyde as starting materials.

To 20 mL of dry DCM, 2,4-dimethylpyrrole (1 mL, 9.71 mmol, 2,3 equiv.) was added, followed by the addition of the 9-anthracenecarboxaldehyde (866 mg, 4.20 mmol, 1 equiv.). 2 drops of trifluoromethylacetic acid (TFA) were added, and the reaction mixture was stirred at room temperature and in the dark. The reaction was monitored by thin-layer-chromatography (TLC). After the indicated time, p-Chloranil (1032 mg, 4.20 mmol, 1 equiv.) was added for oxidation at the meso position. The reaction mixture was stirred at room temperature for 2 more hours. Distilled water (20 mL) was added, and the mixture was extracted with DCM 3 times (10 mL). The organic phases were dried over anhydrous Na$_2$SO$_4$ and purified through alumina gel

(Cyclohexane/Ethylacetate 95:5). A large orange fraction was collected, concentrated and recrystallised from DCM/MeOH. A brownish crystalline solid was obtained as the product (632 mg; 40% yield). ^{1}H NMR (CDCl$_3$, 300 MHz) δ 8.52 (s, 1H), 8.02-7.98 (m, 4H), 7.49-7.34 (m, 4H), 5.77 (s, 2H), 2.41 (s, 6H), 0.51 (s, 2H).

3.4.3 Synthesis of dipyrromethene ligand (2a)
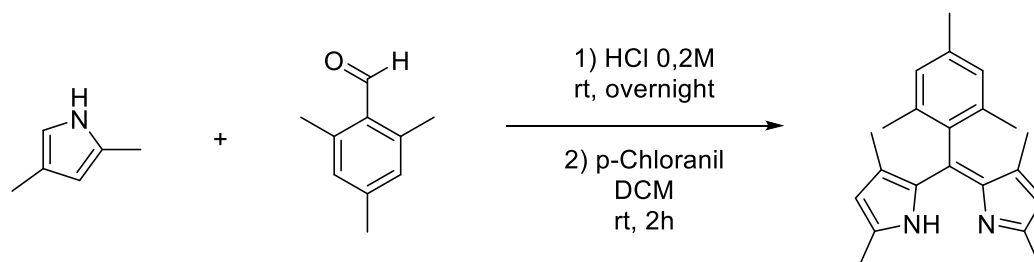
Figure 3.12: Synthetic route of dipyrromethene ligand from 2,4-dimethyl-1*H*-pyrrole and 2,4,6-trimethylbenzaldehyde as starting materials.

To 25 mL of 0.2 M aqueous HCl, 2,4-dimethylpyrrole (1 mL, 9.71 mmol, 2.1 equivalence) was added, followed by the 2,4,6-trimethylbenzaldehyde (0.67 mL, 4.56 mmol, 1 equiv.). The reaction mixture was stirred at room temperature in the dark. After 12 hours, a sticky solid was formed. 10 mL of dichloromethane (DCM) was added. The organic phase was separated, and the water phase was extracted 3 times (10 mL) with DCM. The organic layers were combined, dried over anhydrous Na$_2$SO$_4$ and filtered. The amount of solvent was reduced to 20 mL, and p-Chloranil (1121 mg, 4.56 mmol, 1 equivalence) was added. The reaction mixture was stirred at room temperature for 2 more hours. 20 mL of water were added, and the mixture was extracted with DCM 3 times (10 mL), dried over anhydrous Na$_2$SO$_4$ and processed through alumina gel (Cyclohexane/Ethylacetate 95:5). A large orange fraction was collected, concentrated and recrystallised from DCM/CH$_3$OH, obtaining an orange crystalline solid (525 mg; 36% yield). ^{1}H NMR (CDCl$_3$, 300 MHz) δ 6.90 (s, 2H), 5.85 (S, 2H), 2.34 (s, 12H), 2.32 (s, 3H), 2.09 (s, 6H), 1.29 (s, 6H).

3.4.4 Complexation reaction of 1a with zinc.
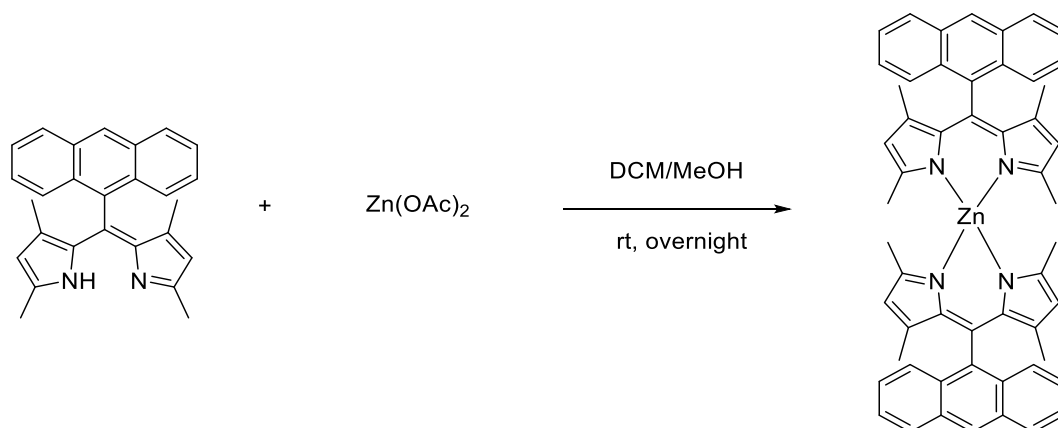
Figure 3.13: Complexation reaction using dipyrromethene ligand (1a) and zinc acetate dihydrate as starting materials to obtain complex 1.

Following the general procedure, the reaction of 1a (150 mg, 0.40 mmol, 2 equiv.) with zinc acetate (36 mg, 0.20 mmol, 1 equiv.) in a 2:1 mixture of DCM and Methanol gave 1 as an orange powder (146 mg; yield 89%). ^{1}H NMR (CDCl$_3$, 300 MHz) δ 8.57 (s, 2H), 8.02 (t, J = 7.4 Hz, 8H), 7.43 (dt, J = 26.0, 6.8 Hz, 8H), 5.89 (s, 4H), 2.34 (s, 12H), 0.48 (s, 12H). ^{13}C NMR (CDCl$_3$, 75 MHz) δ 156.79, 143.88, 140.78, 136.50, 131.60, 130.87, 126.32, 125.39, 120.35, 120.27, 16.55, 14.95. HR-ESI-MS: calcd for C$_{54}$H$_{46}$N$_4$Zn (M$^+$): 814.301, found: 814.299.
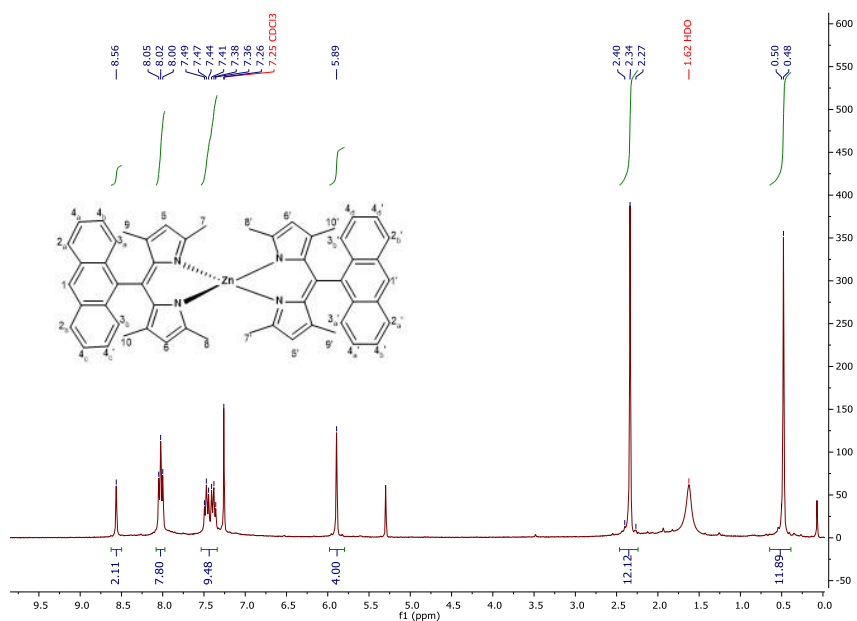
Figure 3.14: ^{1}H NMR Spectrum of **1** in CDCl3.
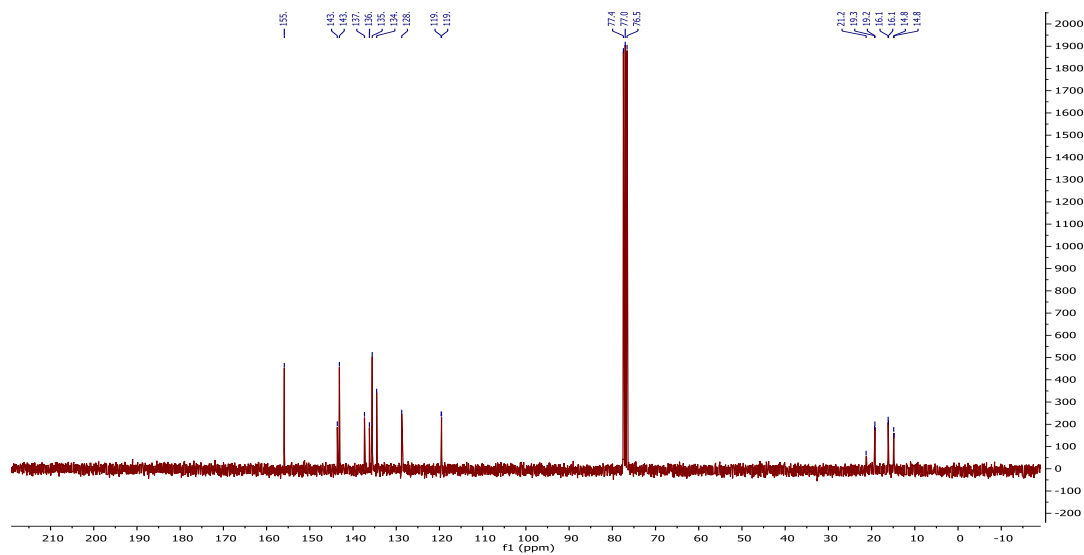
Figure 3.15: [1]C NMR Spectrum of **1** in CDCl3.
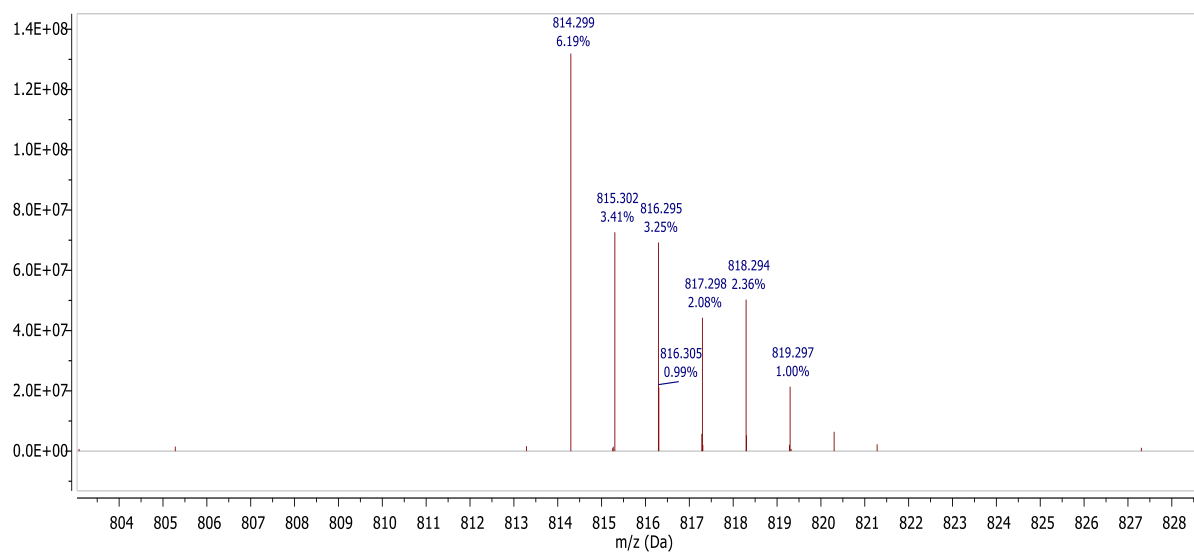
Figure 3.16: Mass spectra of **1** calculated for $C_{54}H_{46}N_4Zn$ (M[+]): 814.301, found: 814.299.

3.4.5 Complexation reaction of 2a with zinc.
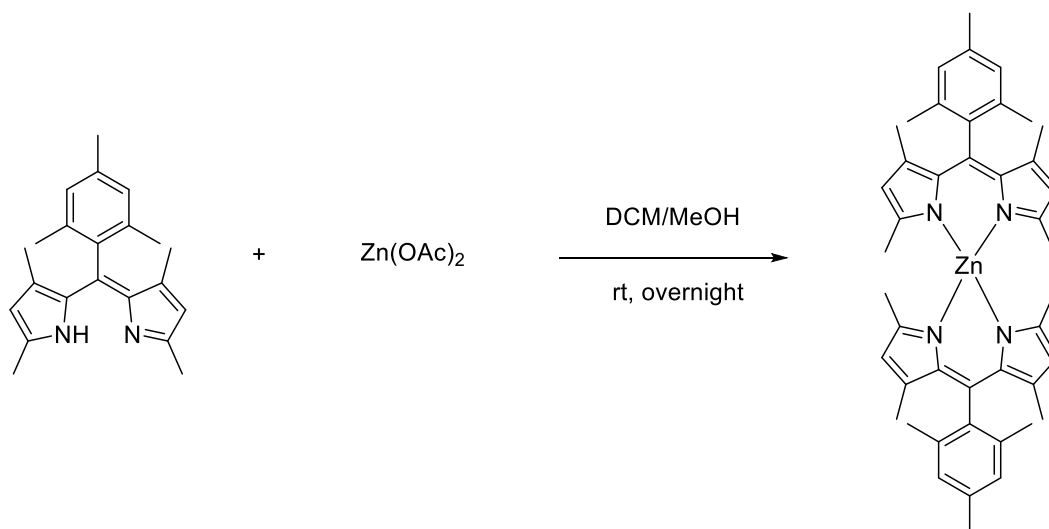
Figure 3.17: Complexation reaction using dipyrromethene ligand (2a) and zinc acetate dihydrate as starting materials to obtain complex **2**.

To a DCM solution (10 mL) of 2a (105 mg, 0.32 mmol, 2 equiv.), was added a methanol (5 mL) solution of zinc acetate (30 mg, 0.16 mmol, 1 equiv.). After stirring overnight the solvent was reduced by a rotary evaporator. The orange precipitate was filtered and rinsed with cold methanol (105 mg; 91% yield). ^{1}H NMR (CDCl$_3$, 300 MHz) δ 6.93 (s, 4H), 5.91 (s, 4H), 2.34 (s, 6H), 2.11 (s, 12H), 2.03 (s, 12H), 1.30 (s, 12H). ^{13}C NMR (CDCl$_3$, 75 MHz) δ 155.90, 143.64, 143.16, 137.35, 136.22, 135.56, 134.54, 128.73, 119.59, 119.52, 21.28, 19.31, 19.24, 16.16, 16.11, 14.88, 14.81.
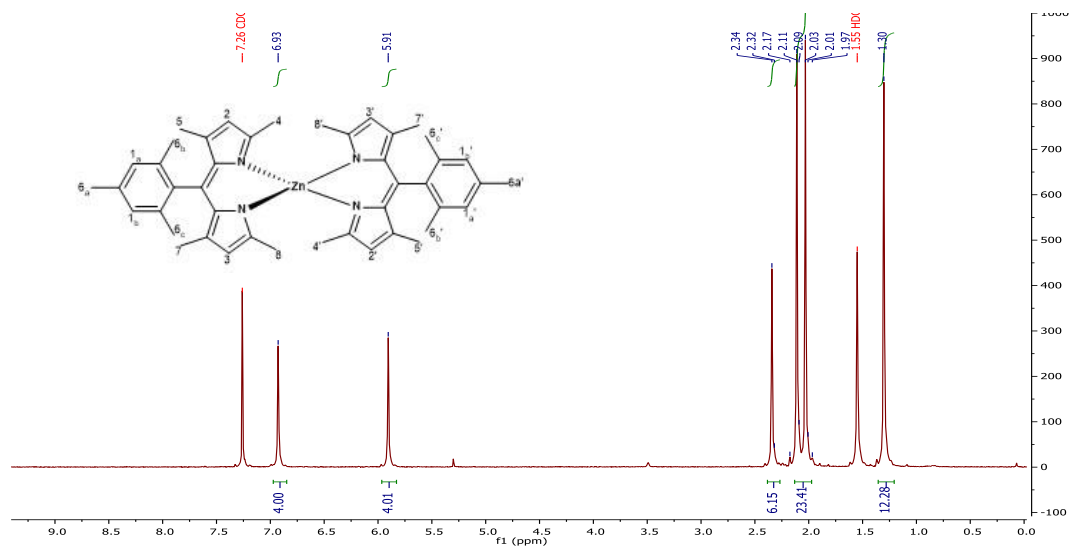
Figure 3.18: ^{1}H NMR Spectrum of **2** in CDCl$_3$.
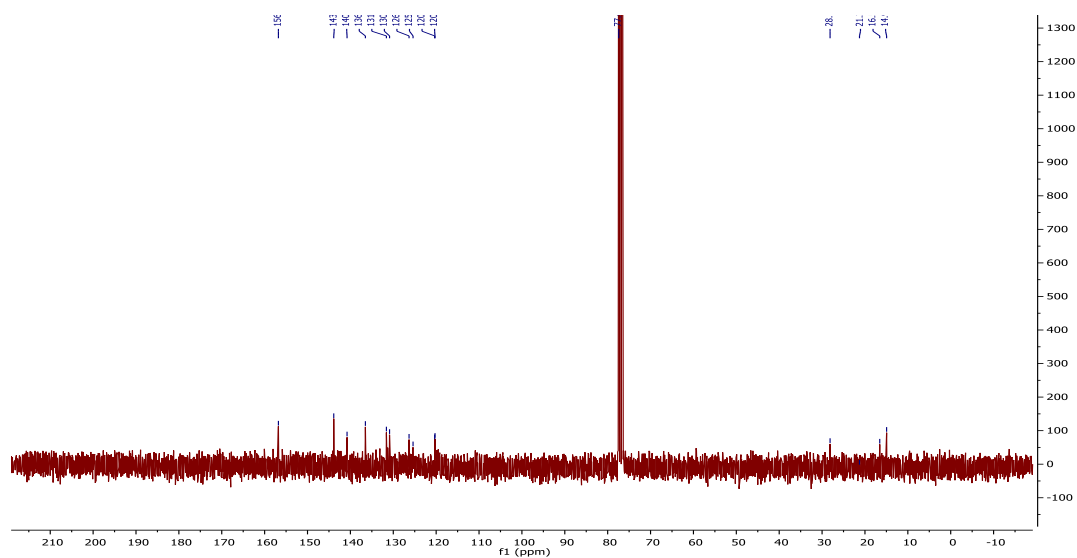
Figure 3.19: ^{1}C NMR Spectrum of **2** in CDCl$_3$.
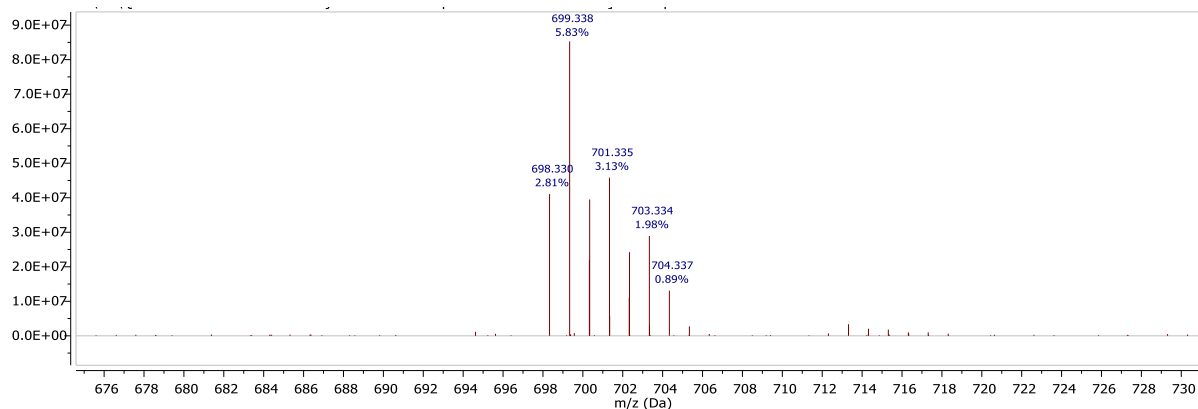
Figure 3.20: HR-ESI mass of **2** calculated for $C_{44}H_{51}N_4Zn$ (MH$^+$): 699.340, found: 699.338.

3.4.6 Synthesis of dye-doped COK-12 silica samples 1S and 2S.

Citric acid monohydrate (954 mg, 4.97 mmol) and trisodium citrate dihydrate (793.5 mg, 3.07 mmol) were dissolved in 27 ml of H_2O. To this solution, Pluronic-P123 and the dye **1** or **2** were added in a 99:1 ratio (0.169 mmol P123, 1.71 mmol **1** or **2**), and the resulting suspension was left stirring at room temperature overnight, during which time it turned into a clear solution with a slight orange tint. A sodium silicate water solution (1.8 mL, 21.97 mmol) was diluted with H_2O (7.5 mL) and added dropwise to the reaction mixture. The mixture was then stirred for 10 min, turning cloudy, and left undisturbed for 24 h, during which a white precipitate formed. Finally, the mixture was filtered under vacuum, the solid residue washed with H_2O repeatedly, until the foaming from the physisorbed surfactant ceased, and then dried in a vacuum desiccator overnight, leading to a light pink powdery solid, which photoluminescenced bright green under UV-visible light.
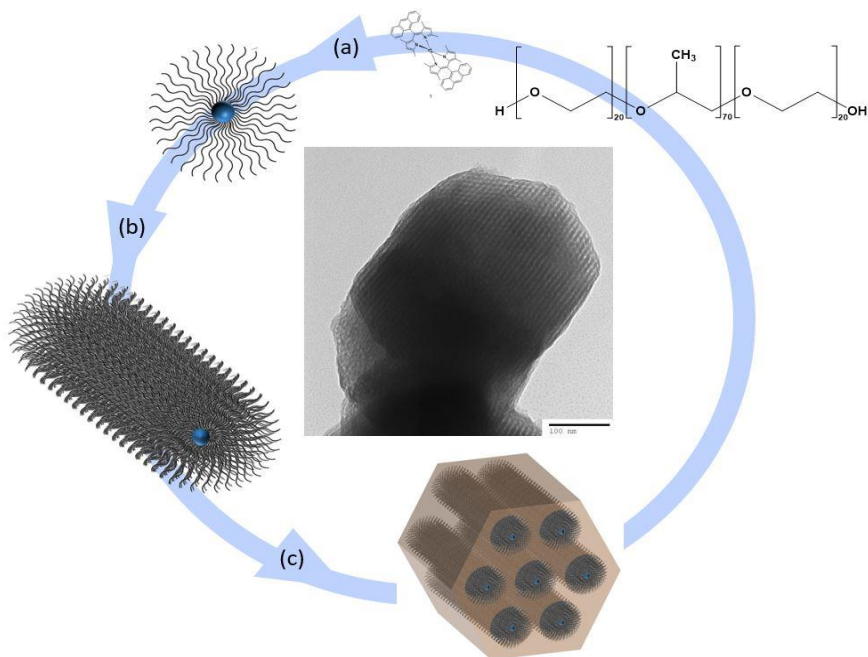
Figure 3.21: The scheme used in the preparation route for the silica hybrids: Pluronic-P123 and dye 1 (a) formation of micelles (b) micellar transition from sphere-to-rod (c) silica polycondensation and (d) TEM image showing the pore spaces.

3.4.7   UV-Visible spectroscopy

10 mg each of 1 and 2 were dissolved in 10 mL DCM (spectroscopic grade) as stock solutions, and two each portion; four different concentrations of 10^{-6} M (2, 4, 6 and 8) were prepared from the stock and measured the absorbance for each. The relative absorbance were used to determine the molar extinction coefficients.

3.4.8   Fluorescence spectroscopy

2.4 mg each of 1S and 2S were dissolved in 8 mL cyclohexane (spectroscopic grade), and fluorescein was used as a reference for both complexes. The samples' excitation, emission, lifetime and anisotropic measurements were recorded using the same conditions each with the reference sample. The data from the emission spectra was used to find the quantum yields.

3.4.9 **Film preparation**

Polymethyl methacrylate (PMMA) films with an average thickness of 3 mm were prepared according to the following procedures:

1. A control film containing the polymer only was made by dissolving 45 mg of PMMA in 5 ml of HPLC grade toluene, followed by slow solvent evaporation until the solution was reduced to 2 ml; the solution was then drop casted onto a microscopy glass slide (1 x 4 cm^2) inserted into a Teflon support of matching size and left to dry at room temperature.

2. The polymer film containing the free complex **2** was made by dissolving 45 mg of PMMA in 5 ml of HPLC grade toluene, to which were added 10 µl of a dichloromethane solution of **2** (1 mg / 10 ml); the solution was left stirring and allowed to reduce to 2 ml, and the following steps were carried out as above. The polymer film containing the **2S** particles was made by dissolving 45 mg of PMMA in 5 ml of HPLC grade toluene, to which were added 0.9 mg of **2S**, corresponding to an equimolar amount of **2** in respect to the film containing the free complex; the subsequent steps followed the same route as above.

References

(1)   Bessette, A.; S. Hanan, G. Design, Synthesis and Photophysical Studies of Dipyrromethene-Based Materials: Insights into Their Applications in Organic Photovoltaic Devices. *Chemical Society Reviews* **2014**, *43* (10), 3342–3405.

(2)   Wood, T. E.; Thompson, A. Advances in the Chemistry of Dipyrrins and Their Complexes. *Chem. Rev.* **2007**, *107* (5), 1831–1861.

(3)   Laha, J. K.; Dhanalekshmi, S.; Taniguchi, M.; Ambroise, A.; Lindsey, J. S. A Scalable Synthesis of Meso-Substituted Dipyrromethanes. *Org. Process Res. Dev.* **2003**, *7* (6), 799–812.

(4)   Loudet, A.; Burgess, K. BODIPY Dyes and Their Derivatives: Syntheses and Spectroscopic Properties. *Chem. Rev.* **2007**, *107* (11), 4891–4932.

(5)   Baudron, S. A. Luminescent Dipyrrin Based Metal Complexes. *Dalton Trans.* **2013**, *42* (21), 7498.

(6)   Sazanovich, I. V.; Kirmaier, C.; Hindin, E.; Yu, L.; Bocian, D. F.; Lindsey, J. S.; Holten, D. Structural Control of the Excited-State Dynamics of Bis(Dipyrrinato)Zinc Complexes: Self-Assembling Chromophores for Light-Harvesting Architectures. *J. Am. Chem. Soc.* **2004**, *126* (9), 2664–2665.

(7)   Trinh, C.; Kirlikovali, K.; Das, S.; Ener, M. E.; Gray, H. B.; Djurovich, P.; Bradforth, S. E.; Thompson, M. E. Symmetry-Breaking Charge Transfer of Visible Light Absorbing Systems: Zinc Dipyrrins. *J. Phys. Chem. C* **2014**, *118* (38), 21834–21845.

(8)   Sakamoto, R.; Iwashima, T.; Kögel, J. F.; Kusaka, S.; Tsuchiya, M.; Kitagawa, Y.; Nishihara, H. Dissymmetric Bis(Dipyrrinato)Zinc(II) Complexes: Rich Variety and Bright Red to Near-Infrared Luminescence with a Large Pseudo-Stokes Shift. *J. Am. Chem. Soc.* **2016**, *138* (17), 5666–5677.

(9)   Sakamoto, R.; Iwashima, T.; Tsuchiya, M.; Toyoda, R.; Matsuoka, R.; Kögel, J. F.; Kusaka, S.; Hoshiko, K.; Yagi, T.; Nagayama, T.; Nishihara, H. New Aspects in Bis and

Tris(Dipyrrinato)Metal Complexes: Bright Luminescence, Self-Assembled Nanoarchitectures, and Materials Applications. *J. Mater. Chem. A* **2015**, *3* (30), 15357–15371.

(10)   Mbatia, H. W.; Burdette, S. C. Photochemical Tools for Studying Metal Ion Signaling and Homeostasis. *Biochemistry* **2012**, *51* (37), 7212–7224.

(11)   Nolan, E. M.; Lippard, S. J. Small-Molecule Fluorescent Sensors for Investigating Zinc Metalloneurochemistry. *Acc. Chem. Res.* **2009**, *42* (1), 193–203.

(12)   Antina, E. V.; Kuznetsova, R. T.; Antina, L. A.; Guseva, G. B.; Dudina, N. A.; V'yugin, A. I.; Solomonov, A. V. New Luminophors Based on the Binuclear Helicates of D-METALS with BIS(DIPYRRIN)S. *Dyes and Pigments* **2015**, *113*, 664–674.

(13)   Sakamoto, R.; Hoshiko, K.; Liu, Q.; Yagi, T.; Nagayama, T.; Kusaka, S.; Tsuchiya, M.; Kitagawa, Y.; Wong, W.-Y.; Nishihara, H. A Photofunctional Bottom-up Bis(Dipyrrinato)Zinc(II) Complex Nanosheet. *Nat Commun* **2015**, *6* (1), 6713.

(14)   Matsuoka, R.; Toyoda, R.; Sakamoto, R.; Tsuchiya, M.; Hoshiko, K.; Nagayama, T.; Nonoguchi, Y.; Sugimoto, K.; Nishibori, E.; Kawai, T.; Nishihara, H. Bis(Dipyrrinato)Metal(II) Coordination Polymers: Crystallisation, Exfoliation into Single Wires, and Electric Conversion Ability. *Chem. Sci.* **2015**, *6* (5), 2853–2858.

(15)   Sakamoto, R.; Yagi, T.; Hoshiko, K.; Kusaka, S.; Matsuoka, R.; Maeda, H.; Liu, Z.; Liu, Q.; Wong, W.-Y.; Nishihara, H. Photofunctionality in Porphyrin-Hybridized Bis(Dipyrrinato)Zinc(II) Complex Micro- and Nanosheets. *Angewandte Chemie* **2017**, *129* (13), 3580–3584.

(16)   Matsuoka, R.; Nabeshima, T. Functional Supramolecular Architectures of Dipyrrin Complexes. *Front. Chem.* **2018**, *6*.

(17)   Tsuchiya, M.; Sakamoto, R.; Shimada, M.; Yamanoi, Y.; Hattori, Y.; Sugimoto, K.; Nishibori, E.; Nishihara, H. Bis(Dipyrrinato)Zinc(II) Complexes: Emission in the Solid State. *Inorg. Chem.* **2016**, *55* (12), 5732–5734.

(18)   Tungulin, D.; Leier, J.; Carter, A. B.; Powell, A. K.; Albuquerque, R. Q.; Unterreiner, A. N.; Bizzarri, C. Chasing BODIPY: Enhancement of Luminescence in Homoleptic Bis(Dipyrrinato) Zn [II] Complexes Utilising Symmetric and Unsymmetrical Dipyrrins. *Chem. Eur. J.* **2019**, *25* (15), 3816–3827.

(19)   Beck, J. S.; Vartuli, J. C.; Roth, W. J.; Leonowicz, M. E.; Kresge, C. T.; Schmitt, K. D.; Chu, C. T. W.; Olson, D. H.; Sheppard, E. W.; McCullen, S. B.; Higgins, J. B.; Schlenker, J. L. A New Family of Mesoporous Molecular Sieves Prepared with Liquid Crystal Templates. *J. Am. Chem. Soc.* **1992**, *114* (27), 10834–10843.

(20)   Jammaer, J.; Aerts, A.; D'Haen, J.; Seo, J. W.; Martens, J. A. Synthesis and Characterization of Cok-12 Ordered Mesoporous Silica at Room Temperature under Buffered Quasi Neutral PH. In *Studies in Surface Science and Catalysis*; Gaigneaux, E. M., Devillers, M., Hermans, S., Jacobs, P. A., Martens, J. A., Ruiz, P., Eds.; Scientific Bases for the Preparation of Heterogeneous Catalysts; Elsevier, 2010; Vol. 175, pp 681–684.

(21)   Katiyar, A.; Yadav, S.; Smirniotis, P. G.; Pinto, N. G. Synthesis of Ordered Large Pore SBA-15 Spherical Particles for Adsorption of Biomolecules. *Journal of Chromatography A* **2006**, *1122* (1), 13–20.

(22)   Lofgreen, J. E.; Ozin, G. A. Controlling Morphology and Porosity to Improve Performance of Molecularly Imprinted Sol–Gel Silica. *Chem. Soc. Rev.* **2014**, *43* (3), 911–933.

(23)   Fabbiani, M.; Confalonieri, G.; Morandi, S.; Arletti, R.; Quartieri, S.; Santoro, M.; Di Renzo, F.; Haines, J.; Fantini, R.; Tabacchi, G. Steering Polymer Growth by Molding Nanochannels: 1, 5-Hexadiene Polymerization in High Silica Mordenite. **2020**.

(24)   Mesoscopic FRET Antenna Materials by Self-Assembling Iridium(III) Complexes and BODIPY Dyes - Bagnall - 2018 - Chemistry – A European Journal - Wiley Online Library

(25)   Jammaer, J.; Aerts, A.; D'Haen, J.; Seo, J. W.; Martens, J. A. Convenient Synthesis of Ordered Mesoporous Silica at Room Temperature and Quasi-Neutral PH. *J. Mater. Chem.* **2009**, *19* (44), 8290.

(26)   Kee, H. L.; Kirmaier, C.; Yu, L.; Thamyongkit, P.; Youngblood, W. J.; Calder, M. E.; Ramos, L.; Noll, B. C.; Bocian, D. F.; Scheidt, W. R.; Birge, R. R.; Lindsey, J. S.; Holten, D. Structural Control of the Photodynamics of Boron−Dipyrrin Complexes. *J. Phys. Chem. B* **2005**, *109* (43), 20433–20443.

(27)   Debije, M. G.; Verbunt, P. P. C. Thirty Years of Luminescent Solar Concentrator Research: Solar Energy for the Built Environment. *Advanced Energy Materials* **2012**, *2* (1), 12–35.

(28)   Meinardi, F.; Bruni, F.; Brovelli, S. Luminescent Solar Concentrators for Building-Integrated Photovoltaics. *Nature Reviews Materials* **2017**, *2* (12), 1–9.

Chapter 4: A Comparative Study of Two Weakly Luminescent Zinc Quinolinolates via Incorporation into PMOs: Routes to Improved Emission Efficiency and Charge-Recombination in the Solid State.

4.1 Introduction

As reported in the previous chapter, most zinc(II) based dyes show weak fluorescent properties, especially in solution. Such limitation was successfully overcome in zinc(II) dipyrrins by rigidifying the environment around the dyes through encapsulation into a host-guest silica structure. The present chapter discusses a similar approach but makes use of an alternative encapsulation strategy and a different class of dye molecules. Still based on zinc(II) as the central metal ion, the complexes are built using quinolinolates as bidentate ligands.

Zinc(II) quinolinolates have been used as both light-emitters and charge-transport materials in recent years, and several studies focused on the effects of the substituents on their emissive properties.[11–13] For example, research on the electroluminescence properties of complexes where the quinolinolate ligand bears halogens (Cl, I or Br) at either 5 or 5,7 positions showed a red-shifted emission (563 nm) as opposed to that of the unsubstituted complex (464 nm).[14,15]

For the purpose of the studies presented in this chapter, though, the electronic effects arising from the substituents on the ligands are of minor importance. That is because the main focus is the incorporation of the complexes into a mesoporous silica structure by co-condensation with a silicate reagent. The process is shown schematically in **Figure 4.1,** and the detailed description of the condensation strategy and mechanism can be found in **Chapter 1**.
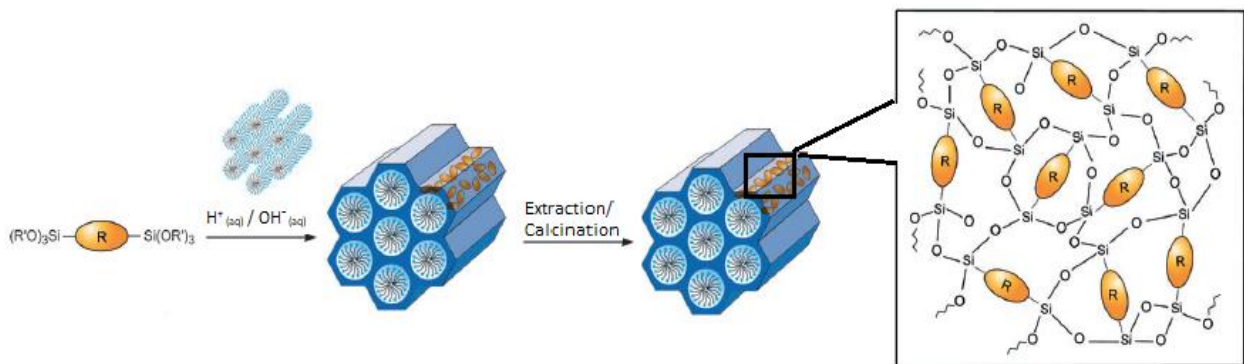
Figure 4.1: General synthetic route of Periodic Mesoporous Organosilica (PMOs) using bis-silylated dyes. R = Organic/organometallic dye.[4,5]

The choice of the substituents on the complex is then solely dictated by the need for converting them into trialkoxysilane groups, indicated as –Si(OR')$_3$ in **Figure 4.1**. Thus, the focus was placed

on two zinc(II) quinolinolate structures, which are shown in **Figure 4.2**: **A**, a complex with dibrominated ligands, and **B**, one with chloromethylated ligands.
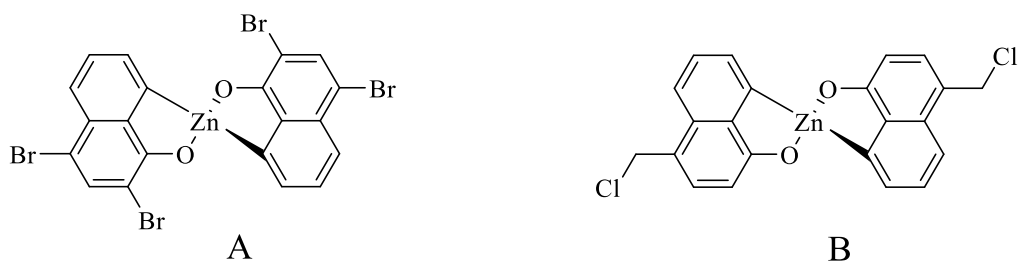
Figure 4.2: Structures of the two homoleptic zinc(II) bis-quinolinolates.

4.1.1 Aims of this Chapter

The primary targets are to assess the impact of rigidification on the optical properties of the dye and to explore the effects of different dye loadings. It is hypothesised that an increase in the amount of dye that the silica framework is doped with will reduce the intermolecular distances, such that luminescence quenching may occur at a certain critical concentration. On the other hand, since zinc(II) quinolinolates show luminescence with a strong charge-transfer (CT) character, it is also reasonable to expect that the close proximity of dye units within the PMO network would enhance such character and may promote charge-recombination phenomena.

The following section describes the synthesis route for both complexes, the incorporation into silica and the analysis of the final materials. The ultimate target is to establish an efficient method to optimise the fluorescence yields and to explore the luminescence mechanism of the dyes in the PMO materials.

4.2 Results and Discussion

A common synthetic strategy was pursued in order to obtain antenna materials containing the zinc(II) quinolinates as building blocks, which consisted of three main steps: synthesis of the complexes, silylation and co-polymerisation into silica hybrids, or simply PMOs. In all cases, the starting point was to use a zinc(II) salt and an 8-hydroxyquinoline as precursors.

4.2.1 Complex A: Synthesis and Characterisation

The dibrominated 8-hydroxyquinoline needed to make complex **A** is commercially available and used in a 2:1 ratio with zinc(II) acetate dehydrate. The complexation reaction (see **Figure 4.3**) is relatively straightforward, owing to the following advantages: (i) it does not require dry conditions, (ii) it is carried out in ethanol below its boiling point, (iii) it reaches completion within 4.5 hours and (iv) it leads to the formation of a yellow precipitate that needs no column purification (see ^{1}H NMR spectrum in **Figure 4.17**).
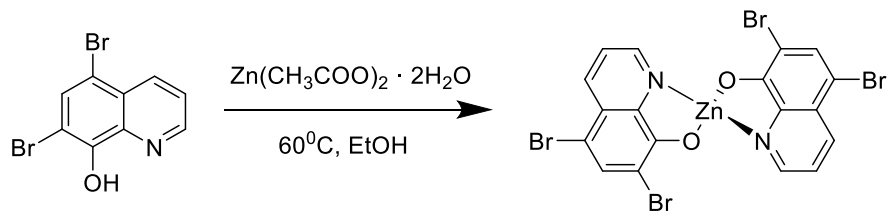
Figure 4.3: Synthesis of complex **A**.

The optical properties of this complex were then studied by means of steady-state and time-resolved UV-visible spectroscopy and used as a reference to make a comparison with the final PMO hybrids. This is because of the instability of the silylated derivative of **A**, which is the actual precursor used for the synthesis of silica materials. Indeed, previous studies have shown that the alkoxysilanes may easily hydrolyse and polycondense over short times upon exposure to air moisture. On the other hand, the effects of the bromide and alkoxysilane substituents on the photophysical properties are minimal, which makes complex **A** a valid reference.[16]

The UV-visible absorption and emission spectra are shown in **Figure 4.4** and exhibit profiles that are very similar to those reported for the unsubstituted zinc(II) bis-quinolinolate, ZnQ_2.[12] A strong absorption peak is observed at 265 nm with a molar extinction coefficient of 141,361 M^{-1} cm^{-1}, followed by two less intense and broader peaks at 345 nm and 405 nm ($\varepsilon \sim 30,000$ M^{-1} cm^{-1}).
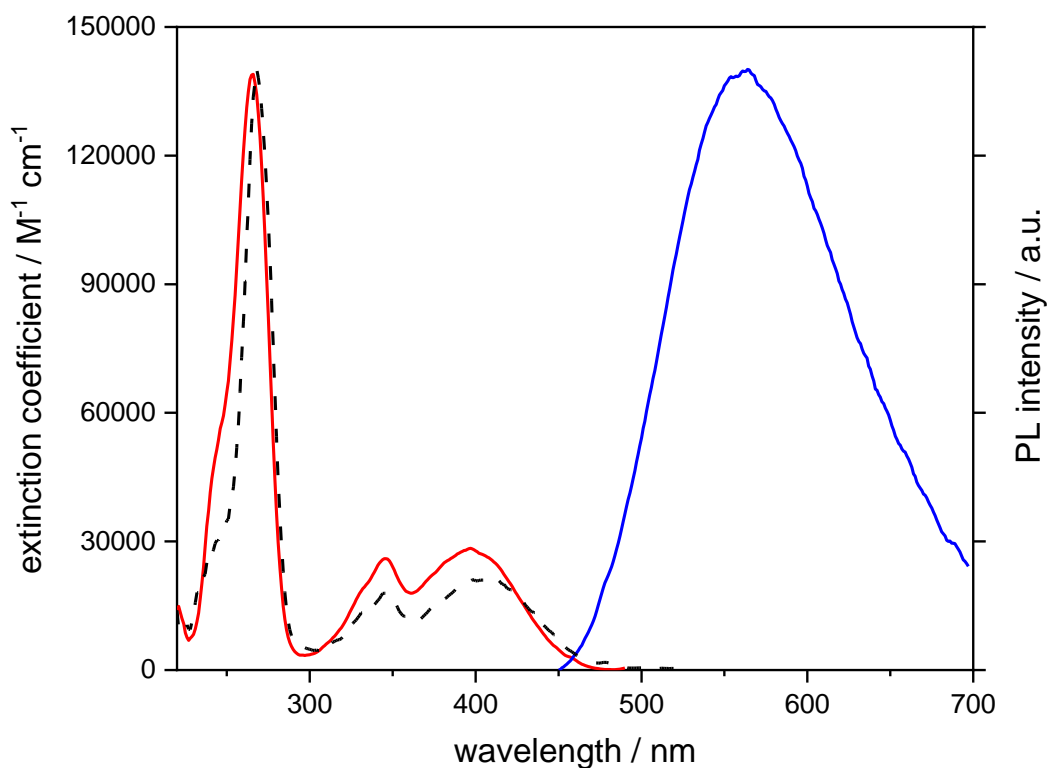
Figure 4.4: Absorption (red), emission (blue) and excitation (dashed black) spectra of complex **A**, recorded from a 10^{-6} M ethanol solution; emission was measured at $\lambda_{exc} = 265$ nm, whereas excitation was measured at $\lambda_{em} = 550$ nm.

The first peak is assigned to an LC $\pi \rightarrow \pi^*$ transition, as it is also seen in the spectrum of the free ligand (see **Appendix 3**),[14] whereas the longer wavelength peaks are attributed to spin-allowed transitions of mixed $\pi\pi^*/n\pi^*$, or intraligand charge transfer (ILCT) character. The lowest-energy band, in particular, is structureless and known to be metal-dependent, and it is typically considered a CT band originating from a shift of electron density from the lone pairs of the phenolic oxygen to the nitrogen atom of the quinoline system.[1,2] The broad emission band at 563 nm is due to a fluorescence transition originating from the above mentioned CT singlet state, and a confirmation of such an assignment is found from the very small overlap between absorption and emission.[1,2,17] This is typical of charge-transfer excited states, which undergo large geometrical changes before the light is emitted and give rise to large Stokes shifts.[3]

The luminescence quantum yield of **A** is 26% in ethanol, and the time-resolved measurements further confirmed the fluorescence, as the excited-state lifetime is 4.4 ns. Using these data, the rate constants for radiative and non-radiative decay are calculated as, respectively, 5.9×10^7 s^{-1} and 1.7 $\times 10^8$ s^{-1} (see also **Table 4.1**).

4.2.2 Complex A: Silylation and PMO Formation

Following the synthesis of **A**, the next step is an alkoxysilylation reaction to convert the four bromide groups into trialkoxysilane groups. The procedure reported by DeShong's group was employed,[19] which uses n-butyllithium (n-BuLi) to produce an aryllithium intermediate and, in the following step, tetraethyl orthosilicate (TEOS) to obtain the final product (see **Figure 4.5**).
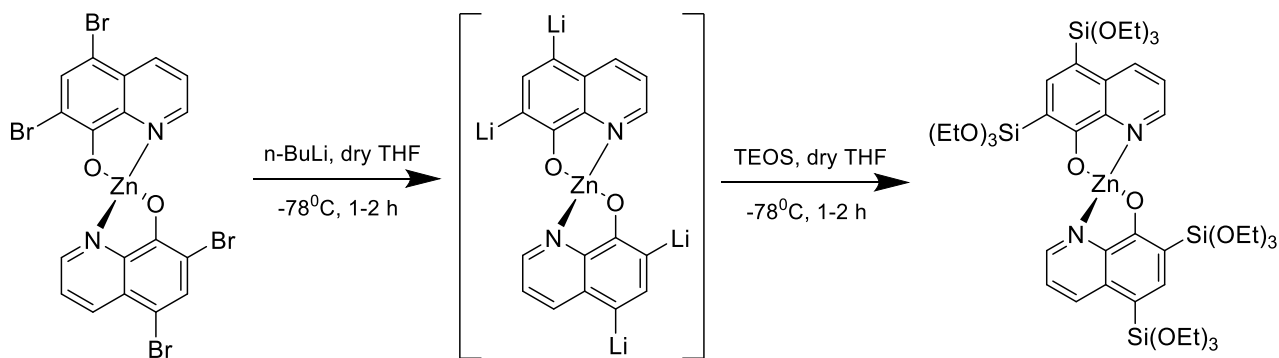
Figure 4.5: Scheme of the attempted alkoxysilylation of complex **A**.

Both steps were initially carried out in a dry ice bath due to the usually high reactivity of butyllithium and the intermediates involved in its reactions. However, reaction temperatures and times had to be varied in order to obtain a product and were finally adjusted to 78°C and two hours for both steps. Only partial silylation was achieved, though.

From the NMR spectrum of the crude (see Experimental section, **Figure 4.18**), there is no conclusive evidence that one product only was obtained. Deducing from the proton count of the aromatic and the ethyl groups, it is possible that the crude contains a mixture of mono- and bis-silylated products, at the 5 and 5' positions of the ligands, with the disubstituted one being predominant. Purification was not pursued, though, because typically, it is a very challenging

process for alkoxysilanes due to their high affinity for the silica used in column chromatography. It was then decided to carry on with the silica formation by using the crude product, considering that any partially silylated derivatives would react during the co-condensation and so will effectively become part of the final PMO.

The co-condensation method used for the formation of the silica hybrids was based on the synthesis of COK-12,[20] which is presented in Chapter 1 and is also employed in the studies discussed in Chapter 3. The first step of such synthesis, involving the preparation of a micellar template, was maintained unaltered, whereas the second step was modified: to sodium silicate, the typical precursor of the polymerisation, the crude obtained from the alkoxysilylation reaction was added as a co-reactant. The relative amount of complex in respect to sodium silicate was estimated, for simplicity, assuming that the product was pure bis-silylated. Six different materials were then prepared, where the molar ratio of the zinc complex vs sodium silicate was varied between 1%, 2%, 5%, 10%, 20% and 100% (see Experimental sections **4.4.4** and **4.4.5** for the detailed procedure). The dye was pre-dissolved in the required volume of water, added into the reaction mixture together with the sodium silicate solution and stirred for additional ten minutes. Previous work in the group involved pre-dissolving dyes in minimum amounts of dimethyl sulphoxide where solubility in water was an issue, but the relatively high quantity of zinc complex employed here would have required such large amounts of co-solvent that it could disrupt the micellar templates and yield amorphous silica. For this reason, only water was used, and the dissolution of the complex was facilitated with the aid of an ultrasonic bath. The final work-up, through washing, of the solid obtained after the co-condensation was also used to remove any unreacted precursor **A** or other non-silylated intermediates that were carried over from the previous reaction.

4.2.3 PMO Materials with Complex A: Structural and Optical Study

The synthesised hybrid materials were analysed by TEM and powder XRD in order to verify whether the porous arrangement of the silica was maintained. The TEM images reported in **Figure 4.6** show that, at different loadings of the silylated complex, a mesoporous material was obtained, with ordered uniform pore sizes (ranging between 5.2 to 7.9 nm). It is also possible to notice that the parallel porous structure was preserved, except for the sample with 100% loading, in which it is very difficult to identify the pores.
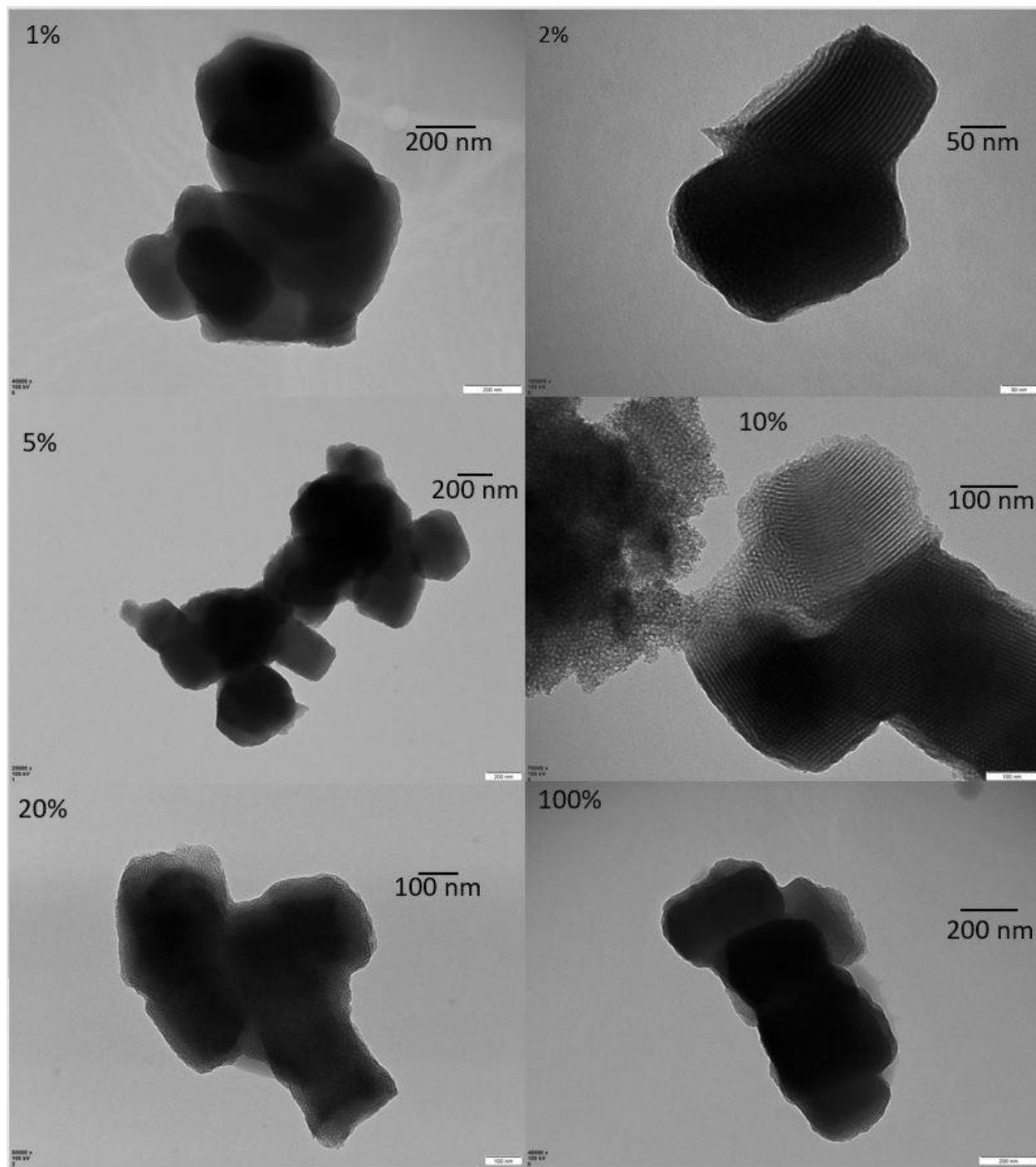
Figure 4.6: TEM images of the PMO materials with six different loadings of complex **A**, between 1 and 100%.

Confirmation of the structural order, at least in the samples up to 20% loading, was sought through powder XRD analysis. However, this proved inconclusive, as the main features expected for

mesoporous silica of COK-12 type could not be captured in the 2θ regions of access, which is from 1° on (see **Figure 4.7**). The pore diameter was calculated using equation 2.3 (chapter 2, page 34). The pore diameters calculated does not fall within the typical range of a COK-12 silica.
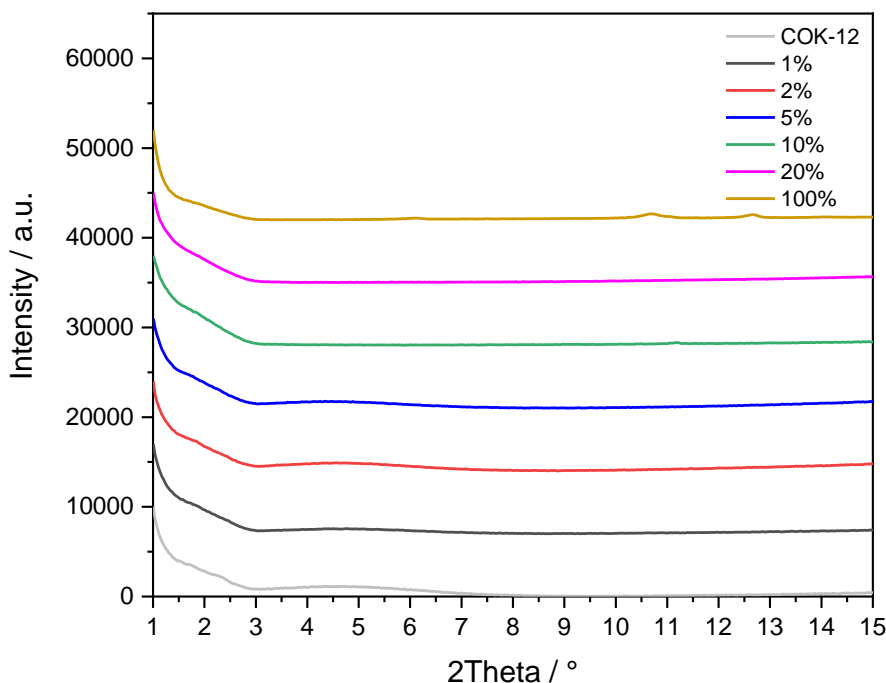
Figure 4.7: Powder XRD profiles of the PMO materials made using complex **A** at different loadings, compared with plain COK-12 silica.

The powder X-ray diffractograms only show the decreasing part of the main signal typically recorded for COK-12, which falls at 0.9° and corresponds to the (100) crystallographic plane.[20] The secondary low-intensity peaks, usually found at 1.7° (110) and 2.3° (210), are not clearly distinguishable within the broad signal between 1.5° and 3°, except for the plain silica sample, where the 210 reflection emerges as a shoulder peak. This indicates that the PMO hybrids have a low degree of order on the long-range scale.

The photoluminescence studies were carried out from 0.3 mg/ml suspensions of the materials in cyclohexane, as this was found to be the optimal trade-off between signal intensity and light scattering induced by the particles.[18]
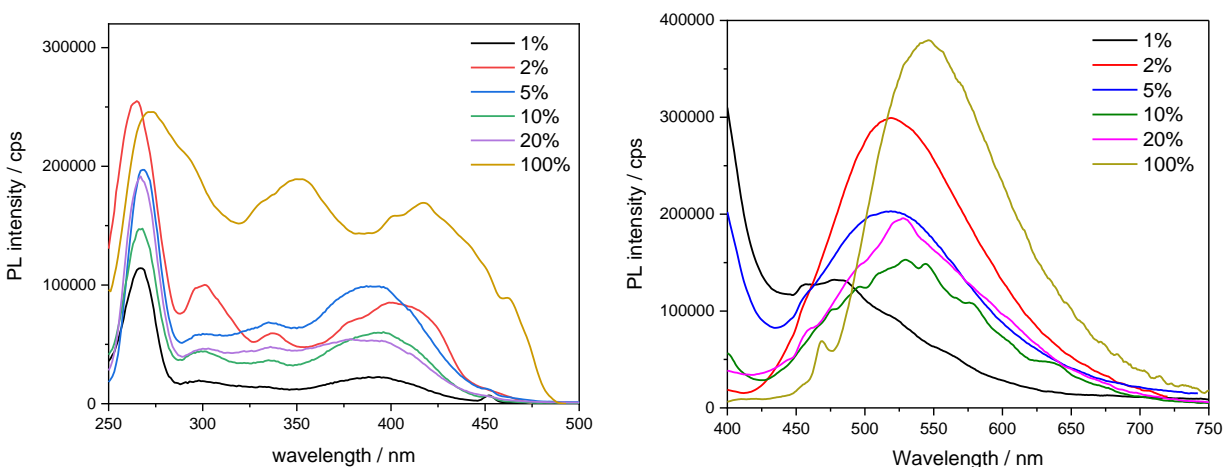
Figure 4.8: Excitation spectra (left) and emission spectra (right) of the hybrid PMO-A materials, recorded from 0.3 mg/mL cyclohexane suspensions; excitation spectra were measured at $\lambda_{em} = 520$ nm and emission spectra were measured $\lambda_{exc} = 265$ nm.

The emission spectra (**Figure 4.8**, right) were measured at the same excitation wavelength of 265 nm and show some differences in the photophysical properties as the dye loading increases. In terms of emission intensity, there seems to be no linear correlation with the dye loading, which can be interpreted by considering that the effects of intermolecular aggregation and light scattering are random throughout the series. The PMO-A with 1% dye loading shows the lowest emission intensity among all samples, and this can well be a result of the lowest concentration of the dye within the silica. As the loading progressively increases, the emission intensity oscillates above the value of the 1% sample until it reaches the highest value at 100% dye loading. On the other hand, by comparing the emission energies, it is possible to notice a more coherent trend. Indeed, the emission maximum gradually red-shifts with increasing loading, from 480 nm at 1% to 553 nm at 100%.

Such trends are also reflected in the photoluminescence excitation spectra (**Figure 4.8**, left). They were all recorded at an emission wavelength of 520 nm and confirmed that the signal intensity does not increase proportionally with the dye loading. For all samples but 100%, maxima in

intensity are observed at 267 nm and, more weakly, at 300 nm, 335 nm and 400 nm. This is in good agreement with the absorption spectrum of the free complex **A** (see **Figure 4.4**), confirming that the complex maintains its structural integrity and the typical LC and CT transitions once part of the silica framework. Interestingly, the peaks mentioned above broaden and red-shift in the 100% sample. Such an effect can be attributed to the intermolecular interactions that arise between the complexes at the maximum loading; the latter may even induce the formation of ground state dimers within the solid-state structure. Such species typically show a larger delocalisation of the excitation energy over the π-orbitals than in monomers, which ultimately leads to a progressive reduction of the HOMO-LUMO gap.[19–21]
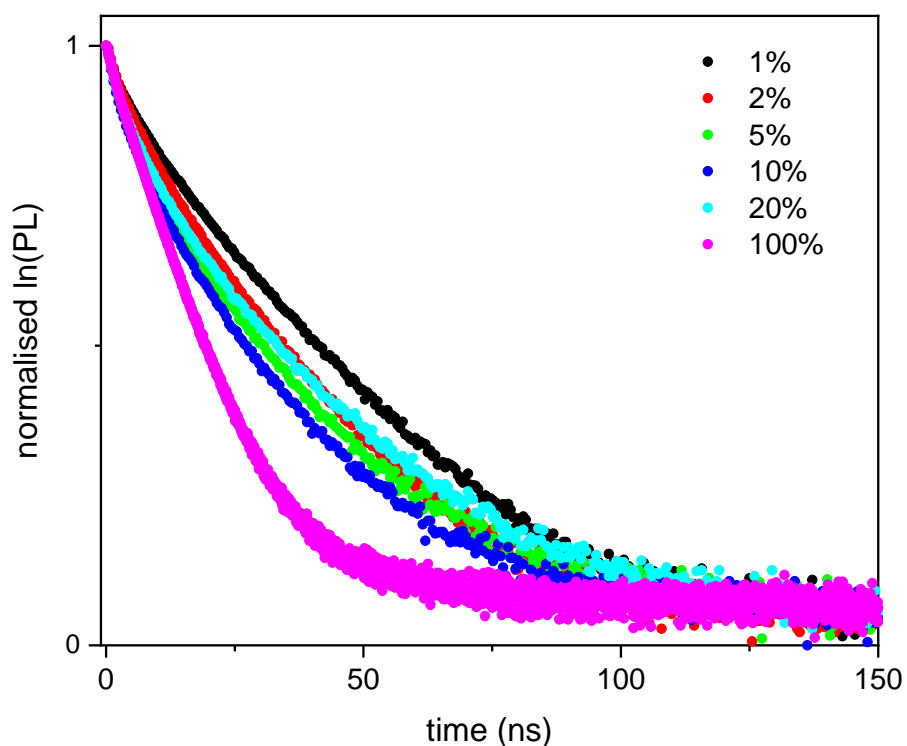
Figure 4.9: Excited-state decays of the PMO-A hybrids recorded at λ_{em} = 520 nm.

The excited-state lifetimes are shown in **Figure 4.9** and have a common characteristic: they are bi-exponential decays. The single decay traces are reported in **Table 4.1**, together with the weighted averages, and the data seem to indicate a certain trend within the sample series: the short decay

component in each sample resembles the free dye's lifetime; also, all values show an overall reduction as the dye-loading increases, with the average lifetimes ranging from 11.7 ns (1% PMO) to 5.3 ns (100% PMO). Such a decrease might be attributed to the fact that, at high concentrations, self-quenching between neighbouring **A** units becomes more likely to occur. This is in accordance with a previous study by Vu and co-workers, who investigated aggregation processes occurring among fluorescent dyes embedded in polymeric matrices.[22] It was found that, at increasing concentrations, additional pathways of excited-state deactivation arise, including fluorescence quenching by aggregated species, such as ground state dimers, excimers and so-called statistical pairs of dyes,[23,24] which act as non-fluorescent traps of the excitation energy. In our case, the formation of dimers and excimers agrees with the steady-state results since a progressive red-shift of the emission maximum is observed with increasing dye loading. Within this picture, the lack of complete consistency in the 2-20% range may reflect the inability of the single **A** units to disperse within the solid matrix in a perfectly homogeneous manner.

Sample	Decay Traces (Relative Weight)* [ns]	Average τ_{PL} [ns]	Φ_{PL}	k_r [s^{-1}]	k_{nr} [s^{-1}]
A	4.4	-	0.26	5.9×10^7	1.7×10^8
1%	5.9 (36%) – 14.9 (64%)	11.7	0.04	3.4×10^6	8.2×10^7
2%	5.4 (48%) – 13.4 (52%)	9.6	0.05	5.2×10^6	9.9×10^7
5%	4.7 (57%) – 13.2 (43%)	8.4	0.17	2.0×10^7	9.9×10^7
10%	4.5 (56%) – 12.7 (44%)	8.1	0.12	1.5×10^7	1.1×10^8
20%	5.2 (57%) – 15.9 (43%)	9.7	0.14	1.4×10^7	8.9×10^7
100%	4.2 (76%) – 8.6 (24%)	5.3	0.56	1.1×10^8	8.3×10^7

Table 4.1: Excited-state lifetimes, fluorescence quantum yields, radiative rate constants (k_r) and non-radiative rate constants (k_{nr}) of the PMO-A materials, in comparison with complex A (shown in grey).

*Recorded at 520 nm from 0.3 mg/ml cyclohexane suspensions, using a 375 nm laser excitation. All the different values of T_F, K_R and K_{NR} were obtained through using different equations in chapter (see page 34 and 44).

On the other hand, while the short decay (4-6 ns) can be associated with the lifetime of single **A** units within the materials, the presence of an unusually long decay trace (~ 9-16 ns) with a significant relative weight must have a different origin. This may well be a case of charge-recombination fluorescence, which is more commonly shown in the solid-state than in dilute solutions. Charge-transfer excited states are particularly prone to show such type of delayed fluorescence; indeed, the phenomenon has been previously observed in crystalline solids of CT dyes.[25] It must also be considered that the electroluminescent properties ZnQ_2 is known for arising from the occurrence of recombination emission in highly aggregated states. The construction of a solid network where ZnQ_2-like units are brought in close proximity would favour the phenomenon.

Such behaviour is further investigated in the following section, which describes an analogous complex and a synthetic route that allows more reliable silylation and control over the concentration of complex into the PMO materials.

4.2.4 **Complex B: Synthesis and Characterisation**

The chloromethylated 8-hydroxyquinoline required to make complex **B** is not commercially available and was synthesised in house. The procedure is based on Blanc chloromethylation[41,42] and is shown in **Figure 4.10**. The original conditions, which require bubbling HCl gas through the reaction solution, were changed in favour of a safer procedure that uses a Lewis acid catalyst in aqueous concentrated HCl. The first attempts used the original room temperature conditions, at which the 8-hydroxyquinoline starting material was reacted with formaldehyde and zinc chloride in 12 M HCl for 12 hours. However, it was found that such conditions were not sufficiently effective to produce the desired product in appreciable yields, as demonstrated by NMR and LC-MS (see **Figure 4.19** and **Appendix 2**). The latter showed the presence of the starting material as a major product and, after a repeat at 30 °C yielded the same result, and it was decided to push the temperature further in order to overcome the activation barrier for the chloromethylation. Indeed, it was finally found that increasing the temperature up to 55 °C grants the final product with a 95% yield and no need for column chromatography (see Experimental section **4.4.5** and **Figure 4.20**).
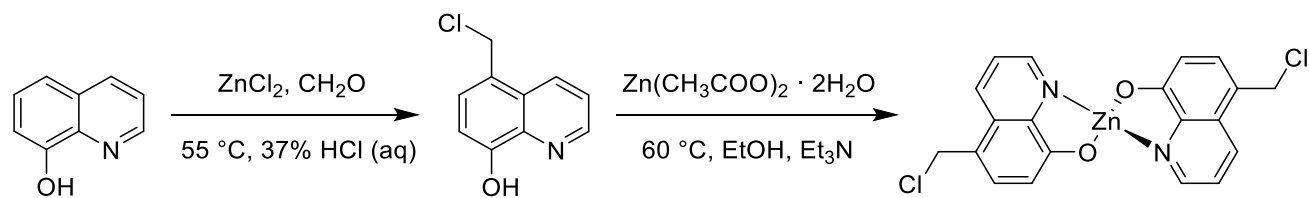
Figure 4.10: Synthesis of complex **B**.

Once the synthesis of the ligand was optimised, complexation with zinc(II) acetate was carried out in analogous conditions as for complex **A**. To improve the product yield, the reaction was repeated with the addition of a mild base to ensure deprotonation of the hydroxyl group on the chloromethylated ligand. Triethylamine was found to be the best choice, as other bases like sodium hydroxide tend to deprotonate at a very fast rate and on multiple sites, causing the formation of unwanted by-products such as 5-hydroxymethyl-8-hydroxyquinoline.[26] Complex **B** was finally obtained with 84% yield, in the form of yellow fibrous crystalline strands that would dissolve readily in D_2O, where NMR analysis was conducted (see **Figure 4.21**).

The UV-visible spectroscopy analysis was then carried out and showed that complex **B** possesses similar optical properties to complex **A**. The data shown in **Figure 4.11** are obtained from dimethylformamide solutions, because the complex, contrary to **A**, is not fully soluble in ethanol. Incomplete solubility would undermine the full reliability of the data, particularly the molar extinction coefficient, the luminescence quantum yield and the excited-state lifetimes. From a qualitative viewpoint, though, absorption and emission bands are not expected to be dramatically affected by solubility issues and are shown in the Appendix for the sake of comparison, also in respect to the free ligand (see **Appendix 3**). The absorption spectrum in dimethylformamide shows the same three transitions observed from complex **A**: the intense $\pi \rightarrow \pi^*$ LC transition at 270 nm (55,134 $M^{-1} cm^{-1}$) and the two weak ILCT bands ($\varepsilon \sim 4,700$ $M^{-1} cm^{-1}$) at 344 nm and 410 nm. The free chloromethylated hydroxyquinoline, on the other hand, only shows the two high-energy bands, the LC at 244 nm and the ILCT at 320 nm, blue-shifted as compared with the complex, while the third band is absent since it arises as a consequence of coordination with the metal ion. This further confirms the successful complex formation.
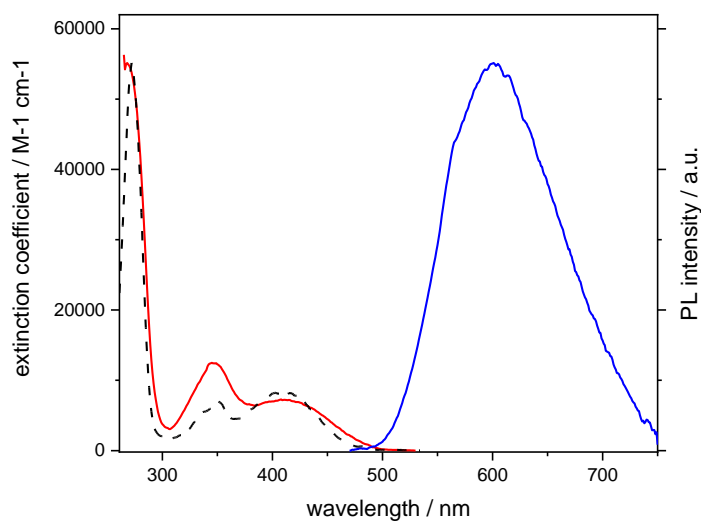
Figure 4.11: Absorption (red), emission (blue) and excitation (dashed black) spectra of complex **B**, recorded from a 10^{-6} M dimethylformamide solution; emission was measured at $\lambda_{exc} = 265$ nm, whereas excitation at $\lambda_{em} = 560$ nm.

The emission spectrum shows the broad CT band centred at 600 nm, red-shifted compared to the emission in ethanol (587 nm) and the emission of complex **A** in ethanol (563 nm). It can be deduced that the excited state of complex **B** has a more pronounced charge-transfer character than **A**, which makes it more sensitive to solvent polarity. Should this be the case, the enhanced sensitivity to the medium might be the reason behind the fast excited-state deactivation in dimethylformamide, as the fluorescence lifetime is 2.2 ns (see **Table 4.2**), half of that recorded for **A**. Also, the very low fluorescence quantum yield of 0.3% would indicate that the deactivation of the excited state is predominantly non-radiative.
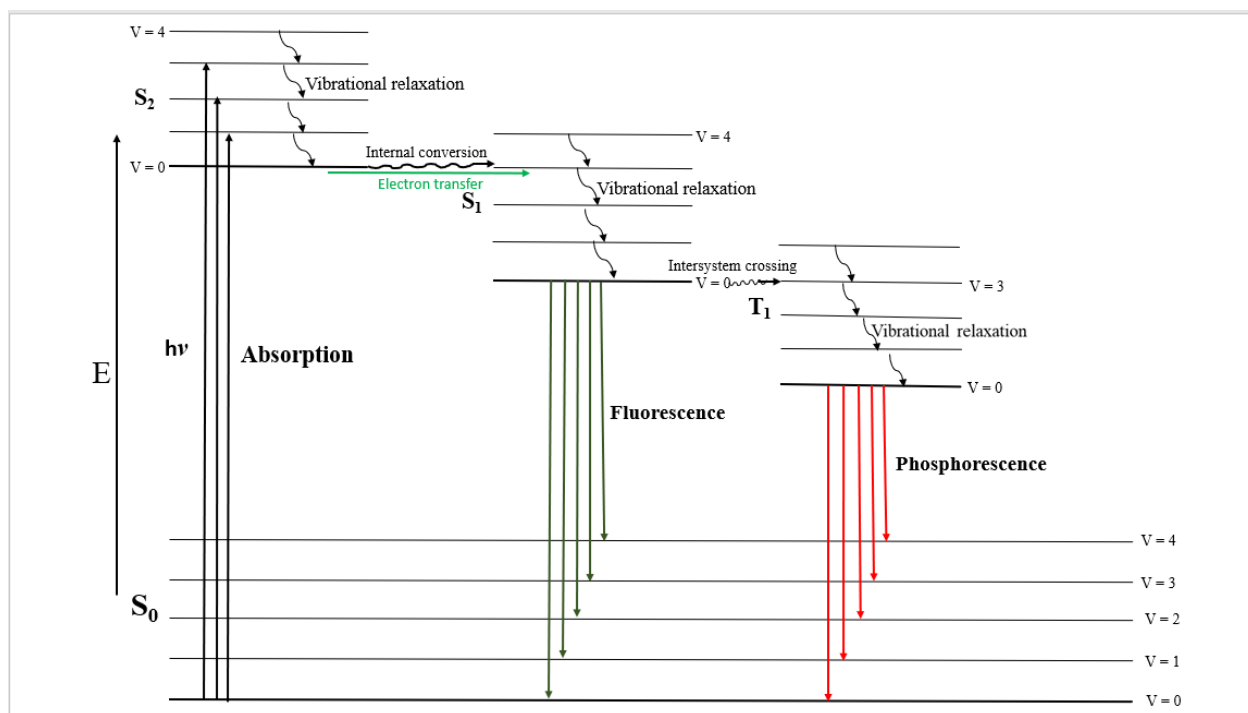
Figure 4.12: Jablonski diagram showing the photophysical processes and electron transfer occurring in molecules.

4.2.5 Complex B: Silylation and PMO Formation

Silylation of complex **B** (see **Figure 4.12**) was achieved via a substitution reaction with 3-mercaptopropyl-trimethoxysilane (3-MPTMS). Using two equivalents of it, the two chloride groups on the ligands are subjected to a nucleophilic attack by the terminal thiols of 3-MPTMS and become leaving groups.
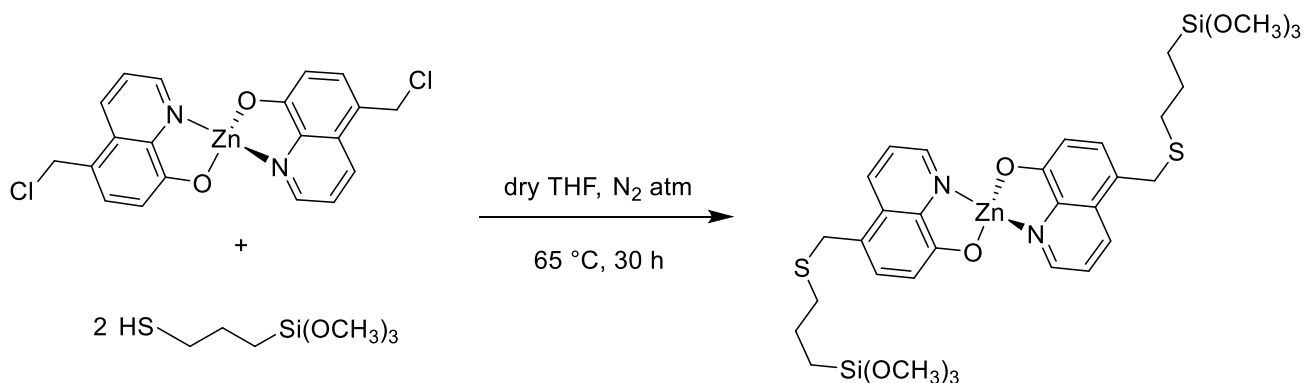
Figure 4.12: Silylation reaction on complex **B**.

The same procedure reported in reference 27 was used, where dry conditions are employed, and the final product is stored in a dried and sealed vial, and used within 12 hours from the synthesis, owing to the strong tendency of alkoxysilanes to hydrolyse. As for complex **A** and its silylated derivative, it can be assumed that the optical properties of **B** remain mostly unaltered upon silylation; therefore, the precursor complex **B** is used as a reference in the spectroscopy analysis of the PMO-B materials.

The latter were synthesised through the same co-condensation route used for complex **A**, but with tetraethoxy-orthosilicate (TEOS) instead of sodium silicate and using CTAB micelles as a template rather than Pluronic P-123 (see Experimental section **4.4.8**). The procedure resembles the synthesis of mesoporous silica of MCM-41 type, and it was applied here to provide a comparison with the COK-12 route described previously. It was also planned to test whether the MCM-41 route could lead to more ordered materials than the COK-12 ones and in a shorter time, as reported by Inagaki's group in their works on PMOs built with organic bridges.[28–30] Although the original target was to prepare and analyse six materials with the same molar ratios used for complex **A**, and it was only possible to synthesise up to four hybrids (1%, 2%, 5% and 10%), due to time constraints dictated by the health emergency.

4.2.6 PMO Materials with Complex B: Structural and Optical Study
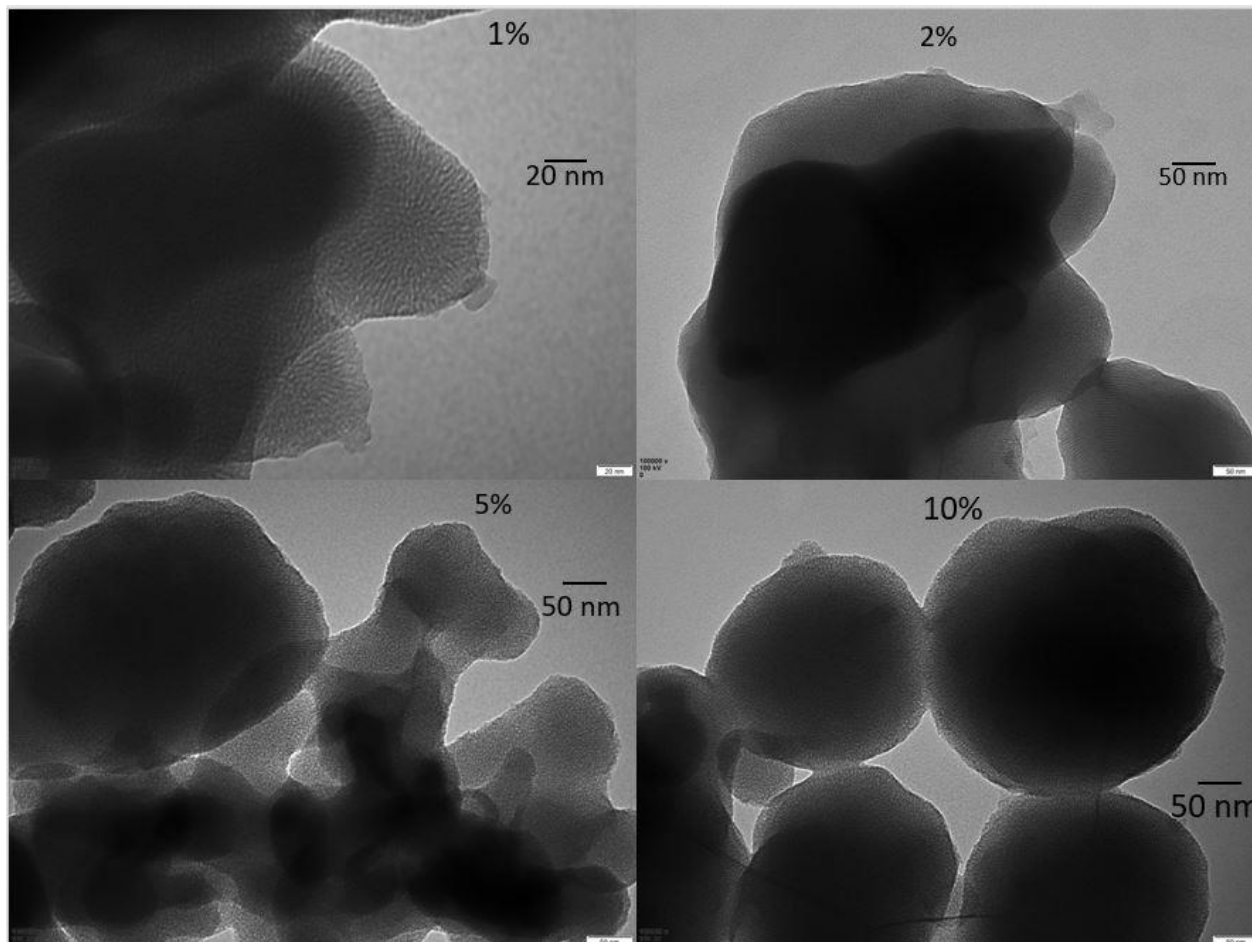
Figure 4.13: TEM images of PMO materials with four different loadings of complex **B**, between 1 and 10%.

The structure and the morphology of the hybrid materials synthesised at different loadings were analysed using TEM and powder XRD. The TEM images obtained (see **Figure 4.13**) show that the porosity and the uniform hexagonal structure of the material is maintained even at the highest loading (10%). All samples possess well-defined pore spaces (with an average size of 4.6 nm), which suggests that the framework of the hybrid material is more resilient to the higher loadings of complex **B**. The pore diameter was calculated using equation 2.3 (chapter 2, page 34).
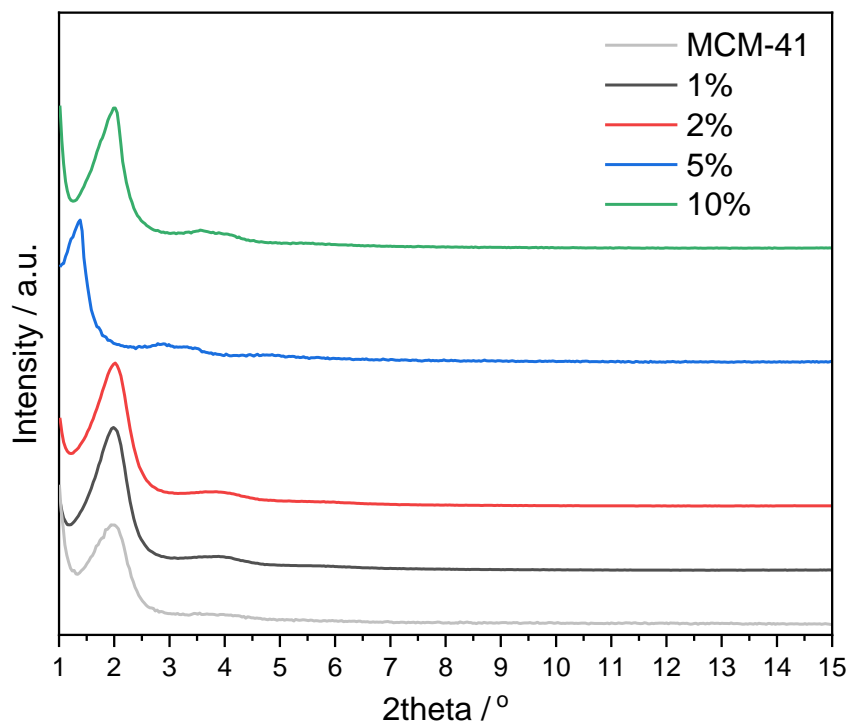
Figure 4.14: Powder XRD profiles of the PMO materials made using complex **B** at different loadings, compared with plain MCM-41 silica.

This is confirmed by the XRD profiles, shown in **Figure 4.14**. The typical pattern from the hexagonal arrangement of pores shown by the sample of plain MCM-41 silica is seen with little variation in the 1%, 2% and 10% samples. The main reflection from the (100) plane dominates at 1.97 – 2.02°, which gives a d-spacing of 4.3 – 4.4 nm.[31–33] It is also possible to observe the higher-order secondary peak at 3.6 – 3.7° (110) and even the (200) reflection at 4.1° in the 10% sample. The 5% material represents the exception in this sample series and we ascribed that to be due to experimental error in the synthesis. The hexagonal pattern is maintained, but all reflections are shifted to lower 2θ values: 1.38° (100), 2.89° (110) and 3.32° (200). The d-spacing obtained from the main reflection is 6.4 nm, which indicates an increased pore spacing compared to the other samples. While such an effect could be rationalised as a consequence of the increased dye content within the silica framework in respect to the 1% and 2% materials, it seems counter-intuitive that the 10% should not follow the same trend and give an even larger d-spacing. It could be

hypothesised that units of complex start packing more tightly beyond 5% loadings, but this would need further investigation.
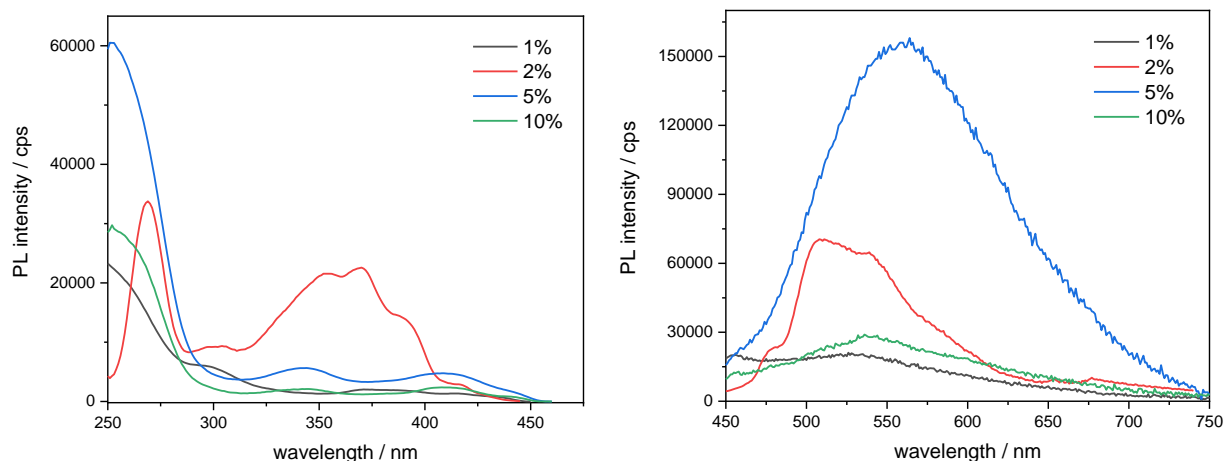
Figure 4.15: Excitation (left) and emission spectra (right) of the hybrid PMO-B materials, recorded from 0.3 mg/mL cyclohexane suspensions; excitation spectra were measured at $\lambda_{em} = 540$ nm and emission spectra were measured $\lambda_{exc} = 265$ nm.

The steady-state photoluminescence spectra of the samples at different loadings of complex **B** are shown in **Figure 4.15** and share some similarities with the **PMO-A** materials. The emission intensity increases with the dye loading up to 5%, to then drop at 10%, possibly as a result of intermolecular quenching at such high concentrations of dye within the network. Interestingly, all samples give higher emission yields than the free complex **B** in solution, with the highest enhancement factor of 16 seen in the 5% sample; this is accompanied by lower non-radiative rates and slightly larger radiative ones, except for the 10% material (see **Table 4.2**). This is interpreted by considering the enhanced rigidity that units of complex experience inside the solid framework. Most vibrational and rotational degrees of freedom are reduced to a great extent, at least up to 5% loading. Beyond that, it is possible that the closer proximity between neighbouring chromophores opens up new pathways for energy dissipation by aggregation and π-stacking, thus reducing the efficiency of fluorescence. As stated earlier, in the analysis of the steady-state data, such a possibility should be verified in future studies.

Table 4.2. Excited-state lifetimes, fluorescence quantum yields, radiative rate constants (k_r) and non-radiative rate constants (k_{nr}) of the hybrid PMO-B materials, in comparison with complex B (shown in grey).

Sample	Decay Traces (Relative Weight)* [ns]	Average τ_{PL} [ns]	Φ_{PL}	k_r [s^{-1}]	k_{nr} [s^{-1}]
B	2.2	-	0.003	1.4×10^6	4.5×10^8
1%	1.1 (14%) – 5.3 (49%) – 19.9 (37%)	10.1	0.015	1.5×10^6	9.7×10^7
2%	0.8 (31%) – 3.6 (45%) – 17.5 (23%)	5.9	0.033	5.6×10^6	1.6×10^8
5%	1.1 (11%) – 5.5 (48%) – 18.1 (41%)	10.2	0.048	4.7×10^6	9.3×10^7
10%	1.3 (14%) – 4.8 (55%) – 20.4 (31%)	9.2	0.008	8.7×10^5	1.1×10^8

*Recorded at 540 nm from 0.3 mg/ml cyclohexane suspensions, using a 375 nm laser excitation.

In terms of emission energy, all samples display a blue shift compared to the free complex, as observed in the PMO-A materials, with fluorescence maxima between 530 and 560 nm. This may well be another consequence of the incorporation into the hybrid silica framework and the nearly total absence of solvent interaction. This reduces the stabilisation of the excited CT state, which emits at shorter wavelengths. The same effect might also explain the apparent hypsochromic shift of the excitation peaks, particularly the highest-energy transition in the 1%, 5% and 10% samples, and the CT broadband at 370 nm in the 2% sample. This was not seen in the PMO-A hybrids and could be taken as a confirmation of the enhanced rigidity effect imposed by a solid structure. However, the strong scattering caused by the PMO particles in the suspension at short wavelengths must also be taken into account, as it would alter the excitation profiles and the relative maxima.

To gain more insights on the deactivation dynamics of the excited-states in the materials, a time-resolved analysis was performed. The emission decay profiles (**Figure 4.16**) show that all four samples have a relatively long fluorescence lifetime and a multiple-exponential trend, compared to complex **B** in solution (2.2 ns, see also **Table 4.2**). As observed for the PMO-A hybrids, the

main decay component resembles the lifetime of the free complex and is generally longer (3.6 – 5.5 ns).
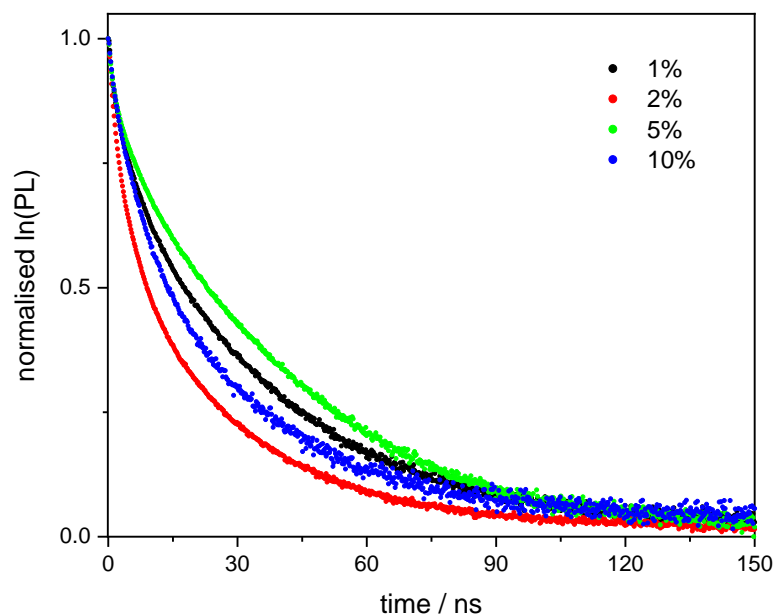
Figure 4.16: Excited-state decays of the PMO-B hybrids recorded at λ_{em} = 540 nm.

In addition to this, a shorter decay trace is found (0.8 – 1.1 ns) and attributed to a small fraction of dye units that are partially quenched by neighbouring units or the solid matrix. A long decay trace (17.5 – 20.4 ns) is also recorded, as in the PMO-A hybrids and would confirm the occurrence of charge-recombination in the materials. To test the hypothesis further, UV-vis spectroscopy was run on a thin solid-state film of complex **B,** and the decay profile indeed shows a much longer lifetime than in solution (see **Appendix 4** and **5**). Data analysis showed a multi-exponential decay as well, with an average excited state decay time of 1.92 μs.

4.3 Conclusions

Two zinc(II) bis-quinolinolate complexes have been synthesised and characterised spectroscopically. They show light emission in the green region of the visible spectrum from a charge-transfer excited state localised over the organic ligands. Their fluorescence quantum yields are rather low in solution (0.26 for complex A and 0.003 for complex B) and, as an attempt to

improve them, incorporation into a rigid host was pursued. The complexes were functionalised with alkoxysilane groups on both ligands and co-polymerised with a silicate source to make new PMO materials. Although alkoxysilylation proved to be difficult in terms of granting a pure final product, the PMO synthesis was successful and mesoporous material with ordered structures were obtained, as confirmed by powder XRD and TEM. The materials also revealed some interesting optical properties. The PMOs built from complex A show an increase in quantum yields with the concentration of complex, reaching a value of 0.56 at 100% dye-loading. On the other hand, the PMOs built using complex B have the highest quantum yield, 0.05, at 5% loading, beyond which the value drops. This could be due to the presence of the longer alkyl side groups in B as opposed to A, which could provide vibrational deactivation routes from the excited state and make the non-radiative decay rates relatively higher in comparison with the PMO-A series. Both types of materials, though, have an emerging property in common: the presence of a long-lived fluorescence decay component, up to 20 ns. This could be evidence of charge-recombination luminescence and would fit well with the electroluminescence properties that the zinc(II) quinolinolates are known for. Further research on the new PMO materials is headed towards tests in light-emitting devices.

4.4 Experimental Section

4.4.1 Synthesis of complex A

Zinc acetate dihydrate (281 mg, 1.5 mmol) and 5,7-dibromo-8-hydroxyquinoline (909 mg, 3 mmol) were dissolved in 100 mL ethanol and stirred under reflux (78^0C) for 4.5 hours a bright yellow precipitate formed. The residue was cooled to room temperature, filtered and washed with ethanol. Yield = 908 mg (91%). ^{1}H NMR δ_H (300 MHz, d6-DMSO): 8.48 (d, 2H), 8.43 (d, 2H), 7.94 (s, 2H), 7.77 (dd, 2H).
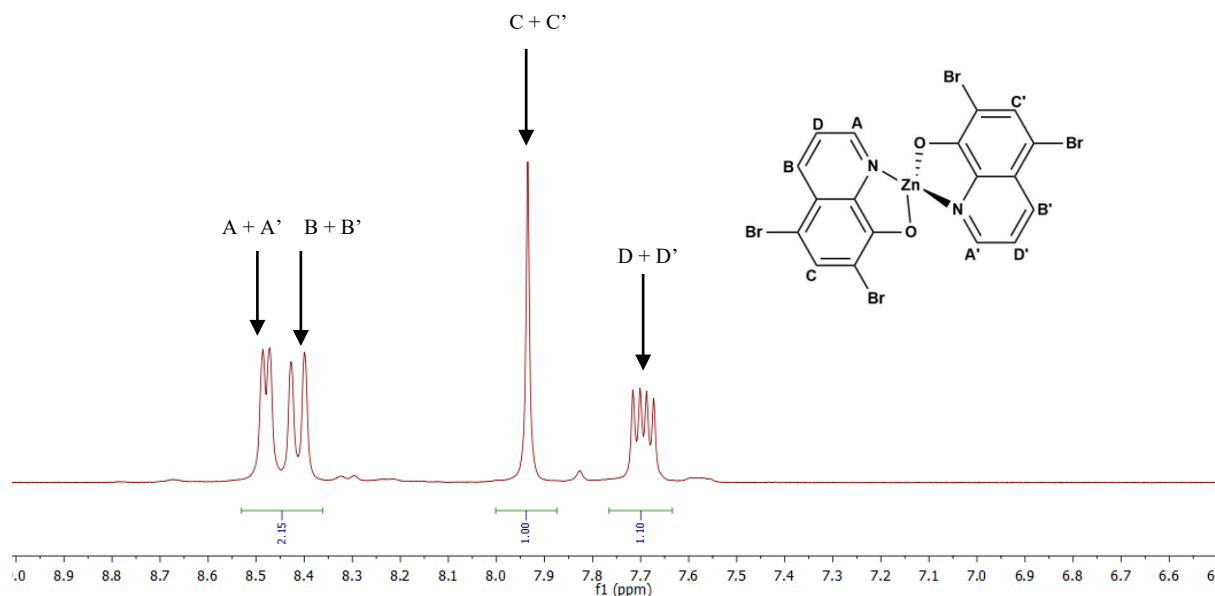
Figure 4.17: ^{1}H NMR spectrum of complex A in DMSO.

4.4.2 Silylation of complex A

Complex A (100 mg, 0.15 mmol) was dissolved under a nitrogen atmosphere in anhydrous THF (20 mL) at -78^0 C. ^{n}BuLi (2.5 in hexane, 270 µL, 0.0042 mmol) was added dropwise in excess to the solution. The solution turned dark orange and stirred for 2 hours at the same temperature. To another flask containing TEOS (450 µL, 2.02 mmol) and 20 mL anhydrous THF, the solution of flask one was added dropwise and stirred at -78^0 C for 2 hours. The mixture was quenched with 2 mL water and allowed to cool up to room temperature. The solvent (THF) was removed under

reduced pressure, and an orange-yellow solid was obtained. Yield = 1278.5 mg (85%). ^{1}H NMR δ_H (400MHz, d6-DMSO): 8.60 (2H, d), 8.27 (2H, d), 7.63 (2H, d), 7.45 (2H, d), 6.65 (2H, d), 3.75 (12H, s), 1.25 (14H, s).
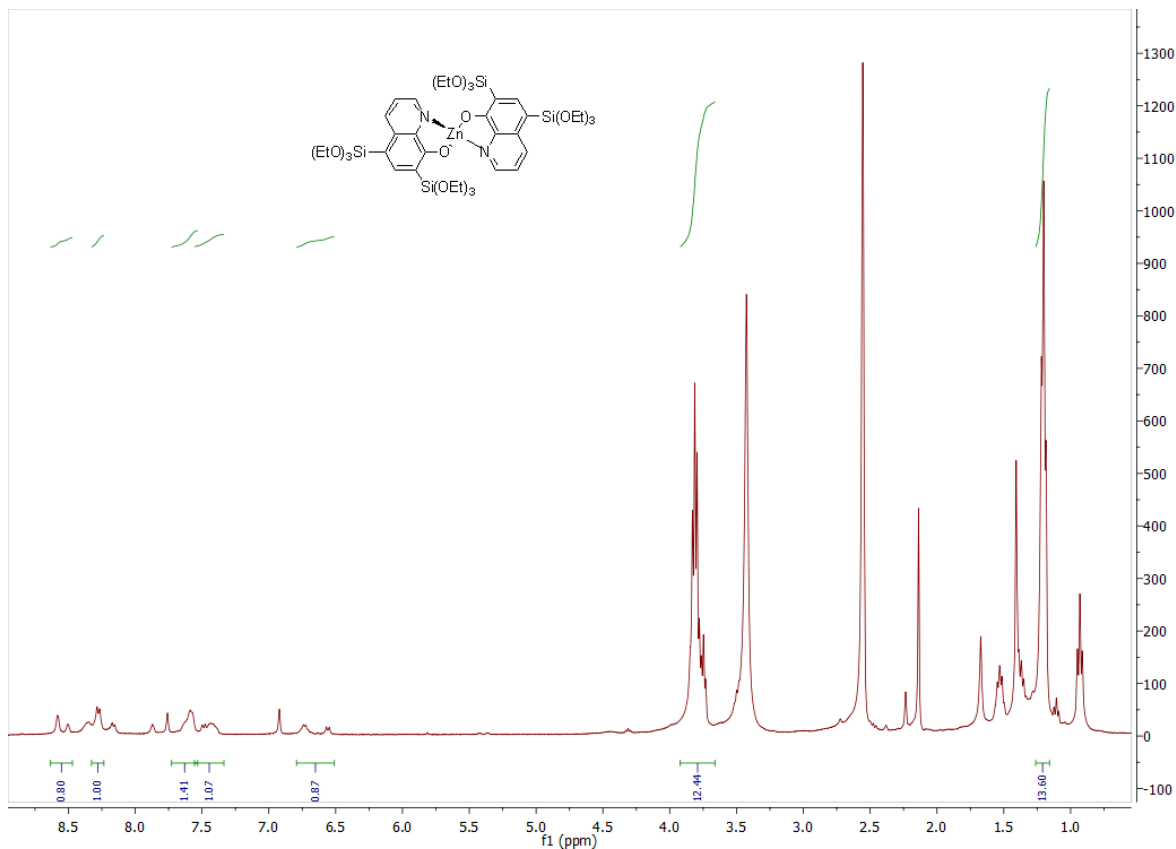
Figure 4.18: ^{1}H NMR spectrum of complex A after silylation, recorded in DMSO.

4.4.3 Synthesis of the PMO-A hybrids with 1%, 2%, 5%, 10% and 20% dye loading

Citric acid monohydrate (91 mg, 0.472 mmol), trisodium citrate dihydrate (86 mg, 0.293 mmol) and Pluronic-P123 (95 mg, 0.0163 mmol) were dissolved in water (2.5 mL). The mixture was stirred for 1 hour at room temperature. The silylated complex Zn(Si(OEt$_3$)$_2$q)$_2$ was dissolved in water (1.1 mL) and added dropwise in the solution, which turned pale yellow. After 30 minutes, sodium silicate/H$_2$O solution was added dropwise, and a cloudy grey mixture formed. The stirring bar was removed after 30 minutes, and a stopper was used to cover the flask. The mixture was left resting at room temperature for 24 hours. It was then filtered and washed with water and left to dry for two days. The solution was stirred for 10 minutes. The addition of Zn(Si(OEt$_3$)$_2$q)$_2$ and sodium

silicate/H_2O solution was performed in the following ratios: 99:1 (0.0206 mmol, 2.02 mmol), 98:2 (0.0412 mmol, 2.02 mmol), 95:5 (0.103 mmol, 1.96 mmol), 90:10 (0.206 mmol, 1.86 mmol) and 80:20 (0.412 mmol, 1.66 mmol).

4.4.4   Synthesis of the PMO-A hybrids with 100% dye loading

Citric acid monohydrate (91 mg, 0.472 mmol), trisodium citrate dihydrate (86 mg, 0.293 mmol) and Pluronic-123 (95 mg, 0.0163 mmol) were dissolved in water (2.5 mL). The mixture was stirred for 1 hour at room temperature. $Zn(Si(OEt_3)_2q)_2$ (207 mg, 2.06 mmol) was dissolved in water (1.1 mL) and added dropwise, which turned pale yellow. The solution was stirred for 17 days, the formation of silica started after two weeks and was completed on the 17th day. The completion of the synthesis was confirmed by washing the filtrate with ethanol and the washing was clear and does not fluoresce under UV-lamp. To confirm this further, we measured the absorbance of the washing and it appeared like a blank measurement.

Synthesis of 5-chloromethyl-8-quinolinol (CMQ)

8-quinolinol (5.76 g, 40 mmol) and 37% formaldehyde (6.4 mL) were dissolved in concentrated HCl (50.00 mL) with ultrasound bath and stirred for 5 minutes each, and the mixture turned transparent brown solution. Zinc chloride (0.6 g, 6.50 mmol) was then added. The solution was stirred at 55^0 C for 12 hours and turned cloudy yellow. The solution was filtered and washed with excess acetone (150 mL) and air-dried in the fume hood. ^{1}H NMR (400 MHz, Deuterium Oxide) δ 9.09 (dd, J = 8.6, 1.3 Hz, 1H), 8.87 (dd, J = 5.4, 1.3 Hz, 1H), 7.97 (dd, J = 8.7, 5.4 Hz, 1H), 7.54 (d, J = 8.0 Hz, 1H), 7.17 (d, J = 8.0 Hz, 1H), 4.91 (s, 2H).
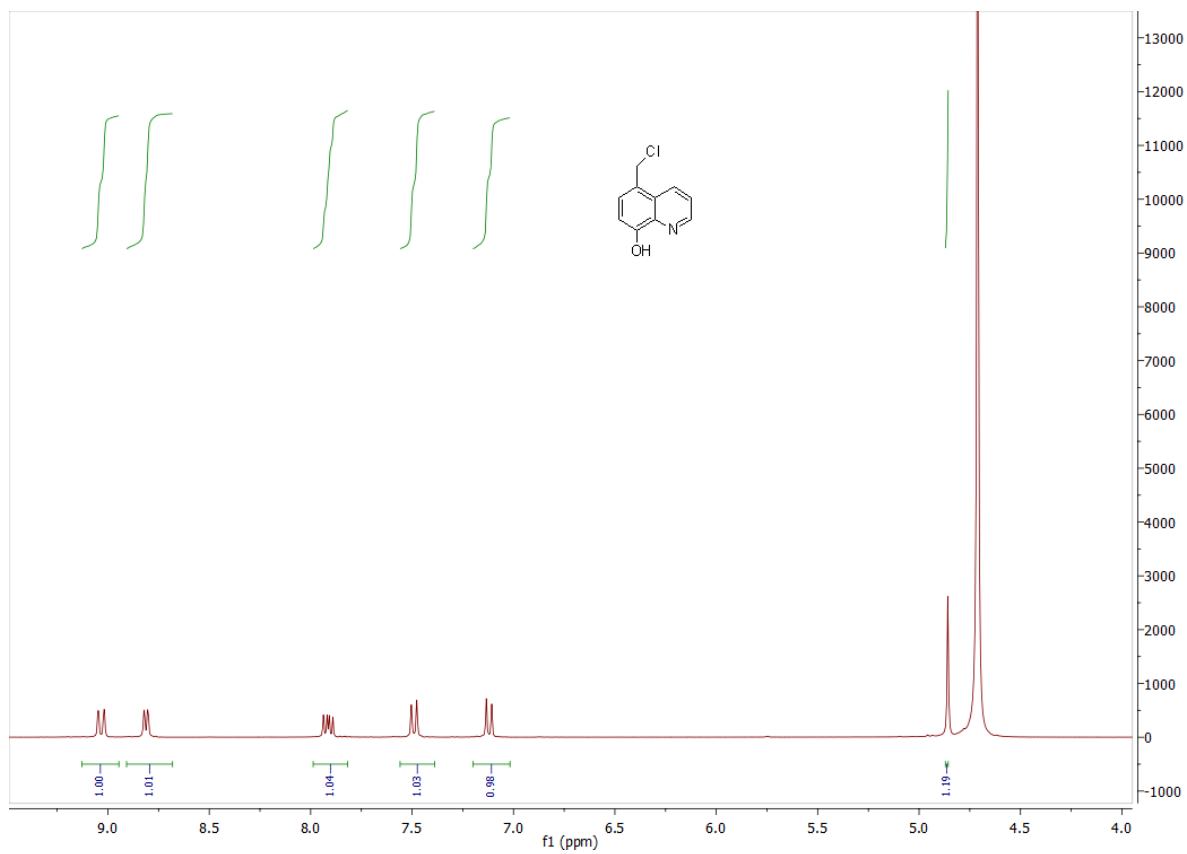
Figure 4.19: ^{1}H NMR spectrum, recorded in D$_2$O, of the product from the first attempt to synthesise the ligand CMQ at room temperature.
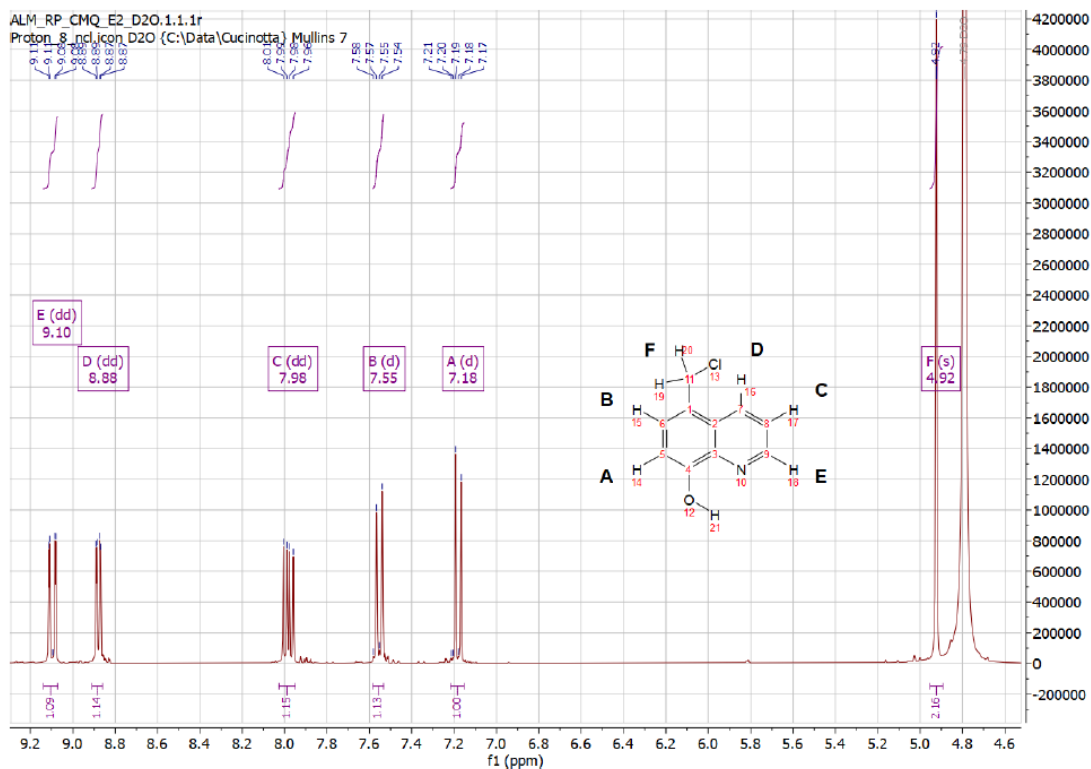
Figure 4.20: ^{1}H NMR spectrum of the ligand CMQ, recorded in D$_2$O.

4.4.5 Synthesis of Zn(II) bis(5-chloromethyl-8-quinolinolate), complex B

CMQ (0.842 g, 4.35 mmol) and zinc acetate (0.477 g, 2.175 mmol) were dissolved in ethanol (40 mL). Triethylamine was added (100 μl), and the solution was refluxed to 78^0 C for 3 hours, after which the solution turned transparent yellow. It was then rotary evaporated and gave a thick orange-brown oil, and was further dried under nitrogen to give fibrous yellow crystalline strands. Yield = 0.8257 g (84.27%) ^{1}H NMR (700 MHz, Deuterium Oxide) δ 9.30 (d, J = 8.5 Hz, 1H), 9.12 (dd, J = 5.4, 1H), 8.20 (dd, J = 8.6, 5.3 Hz, 1H), 7.80 (d, J = 7.9 Hz, 1H), 3.60 (s, 2H).
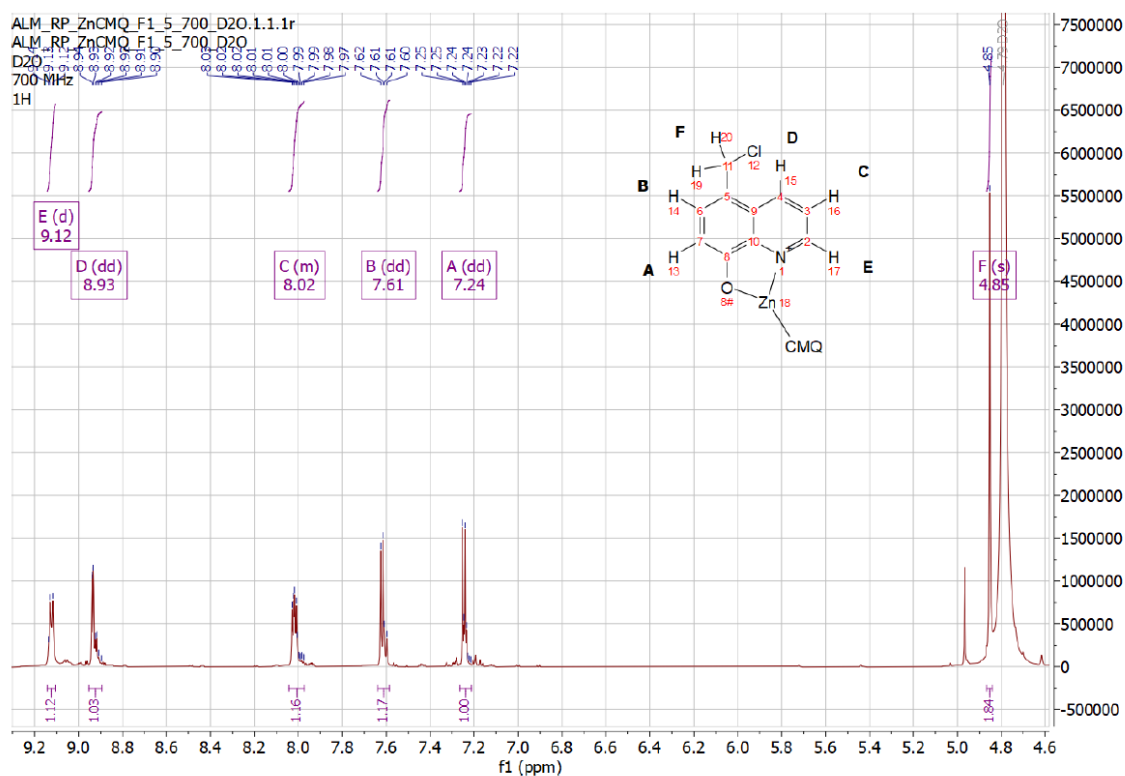
Figure 4.21: ^{1}H NMR spectrum of complex B in D$_2$O.

4.4.6 Silylation of complex B

Complex B (1.00 g, 2.22 mmol) was dissolved in THF (20 mL) under a nitrogen atmosphere. The sample was stirred and heated to 65^0 C. 3-mercaptopropyltrimethoxysilane 93-MPTMS) (0.80 mL, 4.44 mmol) was added and refluxed for 30 hours under nitrogen. The solution was filtered under vacuum, washed with excess THF (40 mL) and dried overnight in the air. A dark orange solid was obtained. Yield = 0.7546 g (44.02%).
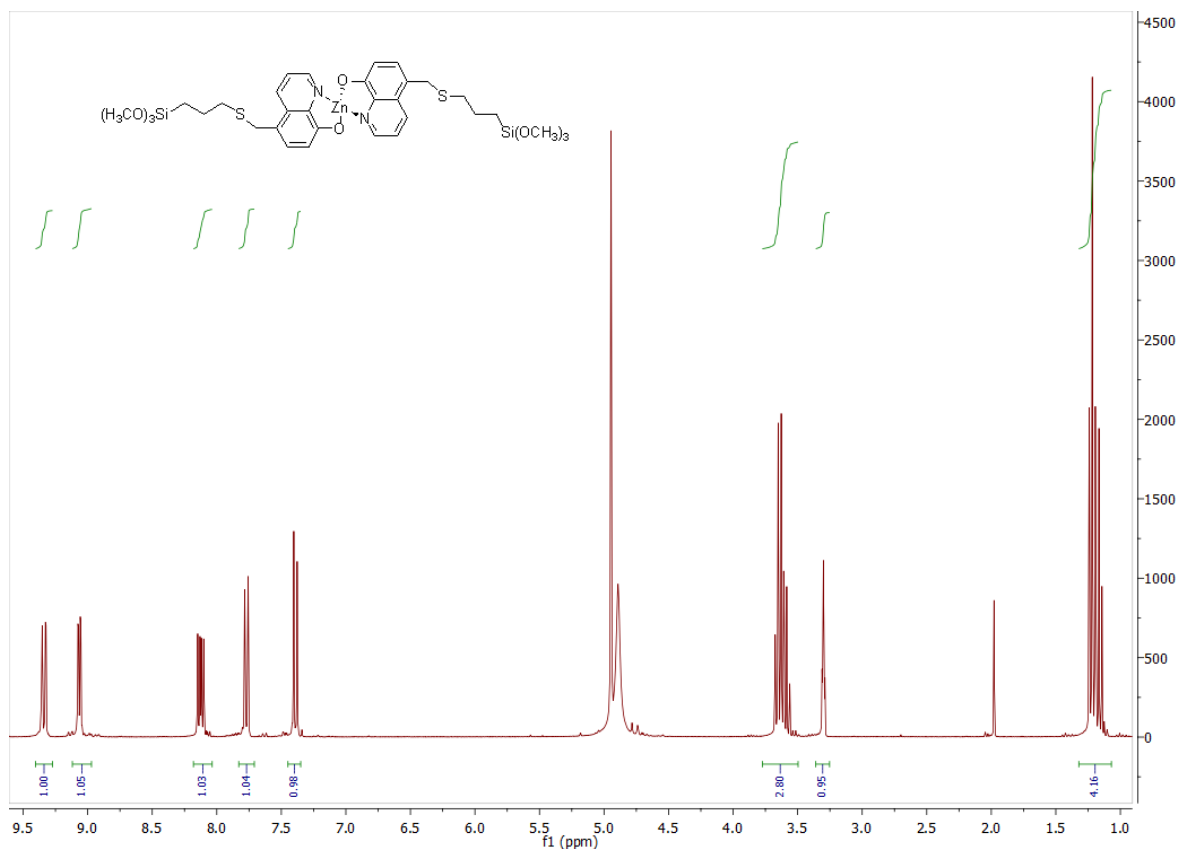
Figure 4.22: ^{1}H NMR spectrum, recorded in D$_2$O, of complex B after silylation.

4.4.7 Synthesis of the PMO-B hybrids with 1%, 2%, 5% and 10% dye loading

Cetyltrimethylammonium bromide was dissolved in 30 mL of water using an ultrasound bath. This is then followed by the addition of 2 molar NaOH (0.13 mL, 0.26 mmol). The solution was heated to 80^0 C. Complex 2 was dissolved in a minimal amount of water (6 mL) and added dropwise concurrently with TEOS (360 μL), forming a homogeneous turbid orange mixture. The mixture was refluxed for 2 hours, stopped and allowed to cool down to room temperature. The mixture was filtered under the vacuum and washed with water. The filtrate was dried in the desiccator, and a pink solid product was obtained that fluoresced lightly under a UV lamp. The CTAB and BOPHY 2 were added for each reaction in the following ratios; 99:1 (69.3 mg, 0.198 mmol and 1.54 mg, 2.00 μmol), 98:2 (68.6 mg, 0.196 mmol and 3.08 mg, 4.00 μmol) 95:5 (66.5 mg, 0.190 mmol and 5.14 mg, 10.00 μmol) and 90:10 (63.00 mg, 0.18 mmol and 10.28 mg, 20.00 μmol).

References

(1) Kunkely, H.; Vogler, A. Optical Properties of Zinc(II) 5,7-Diiodo-8-Quinolinolate in solution. Phosphorescence under Ambient Conditions. *Chemical Physics Letters* **2003**, *376* (1), 226–229.

(2) Kunkely, H.; Vogler, A. Photoluminescence of 8-Quinolinato(Tetracarbonyl)Rhenium(I). *Inorganic Chemistry Communications* **1998**, *1* (10), 398–401.

(3) Montalti, M.; Credi, A.; Prodi, L.; Gandolfi, M. T. *Handbook of Photochemistry*, 3rd ed.; CRC Press: Boca Raton, 2006.

(4) Hoffmann, F.; Cornelius, M.; Morell, J.; Fröba, M. Silica-Based Mesoporous Organic–Inorganic Hybrid Materials. *Angewandte Chemie International Edition* **2006**, *45* (20), 3216–3251.

(5) Hoffmann, F.; Fro, M. Vitalising Porous Inorganic Silica Networks with Organic Functions—PMOs and Related Hybrid Materialsw. **2011**, 14.

(6) Kimyonok, A.; Wang, X.; Weck, M. Electroluminescent Poly(Quinoline)s and Metalloquinolates. *Journal of Macromolecular Science, Part C: Polymer Reviews* **2006**, *46* (1), 47–77.

(7) Thejo Kalyani, N.; Dhoble, S. J. Novel Materials for Fabrication and Encapsulation of OLEDs. *Renewable and Sustainable Energy Reviews* **2015**, *44*, 319–347.

(8) Tang, C. W.; VanSlyke, S. A. Organic Electroluminescent Diodes. 4.

(9) Chen, C. H.; Shi, J. Metal Chelates as Emitting Materials for Organic Electroluminescence. *Coordination Chemistry Reviews* **1998**, *171*, 161–174.

(10) Wang, S. Luminescence and Electroluminescence of Al(III), B(III), Be(II) and Zn(II) Complexes with Nitrogen Donors. *Coordination Chemistry Reviews* **2001**, *215* (1), 79–98.

(11) Du, N.; Mei, Q.; Lu, M. Quinolinate Aluminum and Zinc Complexes with Multi-Methyl Methacrylate End Groups: Synthesis, Photoluminescence, and Electroluminescence Characterization. *Synthetic Metals* **2005**, *149* (2), 193–197.

(12)   Nishal, V.; Kumar, A.; Kadyan, P. S.; Singh, D.; Srivastava, R.; Singh, I.; Kamalasanan, M. N. Synthesis, Characterization, and Electroluminescent Characteristics of Mixed-Ligand Zinc(II) Complexes. *Journal of Elec Materi* **2013**, *42* (6), 973–978.

(13)   Rai, V. K.; Srivastava, R.; Chauhan, G.; Saxena, K.; Bhardwaj, R. K.; Chand, S.; Kamalasanan, M. N. Synthesis and Electroluminescence Properties of Zinc(2,2′ Bipyridine)8-Hydroxyquinoline. *Materials Letters* **2008**, *62* (17), 2561–2563.

(14)   Kido, J.; Ohtaki, C.; Hongawa, K.; Okuyama, K.; Nagai, K. 1,2,4-Triazole Derivative as an Electron Transport Layer in Organic Electroluminescent Devices. *Jpn. J. Appl. Phys.* **1993**, *32* (Part 2, No. 7A), L917–L920.

(15)   Terenzi, A.; Lauria, A.; Almerico, A. M.; Barone, G. Zinc Complexes as Fluorescent Chemosensors for Nucleic Acids: New Perspectives for a "Boring" Element. *Dalton Trans.* **2015**, *44* (8), 3527–3535.

 (16)   Corma, A.; Díaz, U.; Ferrer, B.; Fornés, V.; Galletero, M. S.; García, H. Controlling the Emission of Blue-Emitting Complexes by Encapsulation within Zeolite Cavities. *Chem. Mater.* **2004**, *16* (7), 1170–1176.

(17)   Ballardini, R.; Varani, G.; Indelli, M. T.; Scandola, F. Phosphorescent 8-Quinolinol Metal Chelates. Excited-State Properties and Redox Behavior. *Inorg. Chem.* **1986**, *25* (22), 3858–3865.

(18)   Cucinotta, F.; Jarman, B. P.; Caplan, C.; Cooper, S. J.; Riggs, H. J.; Martinelli, J.; Djanashvili, K.; La Mazza, E.; Puntoriero, F. Light-Harvesting Antennae Using the Host-Guest Chemistry of Mesoporous Organosilica. *ChemPhotoChem* **2018**, *2* (3), 196–206.

(19)   Chambers, R. W.; Kajiwara, T.; Kearns, D. R. Effect of Dimer Formation on the Electronic Absorption and Emission Spectra of Ionic Dyes. Rhodamines and Other Common Dyes. *J. Phys. Chem.* **1974**, *78* (4), 380–387.

(20)   Etherington, M. K.; Kukhta, N. A.; Higginbotham, H. F.; Danos, A.; Bismillah, A. N.; Graves, D. R.; McGonigal, P. R.; Haase, N.; Morherr, A.; Batsanov, A. S.; Pflumm, C.; Bhalla, V.; Bryce, M. R.; Monkman, A. P. Persistent Dimer Emission in Thermally Activated Delayed Fluorescence Materials. *J. Phys. Chem. C* **2019**, *123* (17), 11109–11117.

(21)   Imbrasas, P.; Lygaitis, R.; Kleine, P.; Scholz, R.; Hänisch, C.; Buchholtz, S.; Ortstein, K.; Talnack, F.; Mannsfeld, S. C. B.; Lenk, S.; Reineke, S. Dimers or Solid-State Solvation? Intermolecular Effects of Multiple Donor–Acceptor Thermally Activated Delayed Fluorescence Emitter Determining Organic Light-Emitting Diode Performance. *Advanced Optical Materials n/a* (n/a), 2002153.

(22)   Vu, T. T.; Dvorko, M.; Schmidt, E. Y.; Audibert, J.-F.; Retailleau, P.; Trofimov, B. A.; Pansu, R. B.; Clavier, G.; Méallet-Renault, R. Understanding the Spectroscopic Properties and Aggregation Process of a New Emitting Boron Dipyrromethene (BODIPY). *J. Phys. Chem. C* **2013**, *117* (10), 5373–5385.

(23)   Boulu, L. G. Theoretical Investigation of Fluorescence Concentration Quenching in Two-Dimensional Disordered Systems. Application to Chlorophyll a in Monolayers of Dioleylphosphatldylchollne. **1987**, *86*, 5.

(24)   Santos, M. B. On the Distribution of the Nearest Neighbor. *American Journal of Physics* **1986**, *54* (12), 1139–1141.

(25)   Al-Aqar, R.; Atahan, A.; Benniston, A. C.; Perks, T.; Waddell, P. G.; Harriman, A. Exciton Migration and Surface Trapping for a Photonic Crystal Displaying Charge-Recombination Fluorescence. *Chem. Eur. J.* **2016**, *22* (43), 15420–15429.

(26)   Burckhalter, J. H. Amino- and Chloromethylation of 8-Quinolinol. Mechanism of Preponderant Ortho Substitution in Phenols under Mannich Condi Tionsla,b. **1961**, 6.

(27)   Yang, Y.; Zhang, Y.; Hao, S.; Kan, Q. Periodic Mesoporous Organosilicas with Bis(8-Quinolinolato) Dioxomolybdenum(VI) inside the Channel Walls. *Journal of Colloid and Interface Science* **2011**, *362* (1), 157–163.

(28)   Inagaki, S.; Guan, S.; Fukushima, Y.; Ohsuna, T.; Terasaki, O. Novel Mesoporous Materials with a Uniform Distribution of Organic Groups and Inorganic Oxide in Their Frameworks. *J. Am. Chem. Soc.* **1999**, *121* (41), 9611–9614.

(29)   Asefa, T.; MacLachlan, M. J.; Grondey, H.; Coombs, N.; Ozin, G. A. Metamorphic Channels in Periodic Mesoporous Methylenesilica. *Angewandte Chemie International Edition* **2000**, *39* (10), 1808–1811.

(30)   Inagaki, S.; Guan, S.; Ohsuna, T.; Terasaki, O. An Ordered Mesoporous Organosilica Hybrid Material with a Crystal-like Wall Structure. *Nature* **2002**, *416* (6878), 304–307.

(31)   Marler, B.; Oberhagemann, U.; Vortmann, S.; Gies, H. Influence of the Sorbate Type on the XRD Peak Intensities of Loaded MCM-41. *Microporous Materials* **1996**, *6* (5), 375–383.

(32)   Kruk, M.; Jaroniec, M.; Kim, J. M.; Ryoo, R. Characterization of Highly Ordered MCM-41 Silicas Using X-Ray Diffraction and Nitrogen Adsorption. *Langmuir* **1999**, *15* (16), 5279–5284..

(33)   Kruk, M.; Jaroniec, M.; Sakamoto, Y.; Terasaki, O.; Ryoo, R.; Ko, C. H. Determination of Pore Size and Pore Wall Structure of MCM-41 by Using Nitrogen Adsorption, Transmission Electron Microscopy, and X-Ray Diffraction. *J. Phys. Chem. B* **2000**, *104* (2), 292–301.

Appendix

181130_U+FA_pos
30-Nov-2018
2
181130_U+FA_pos 40 (0.665) Cm (5:58)

TOF MS ES+
4.26e5

Exact Mass: 1000.30
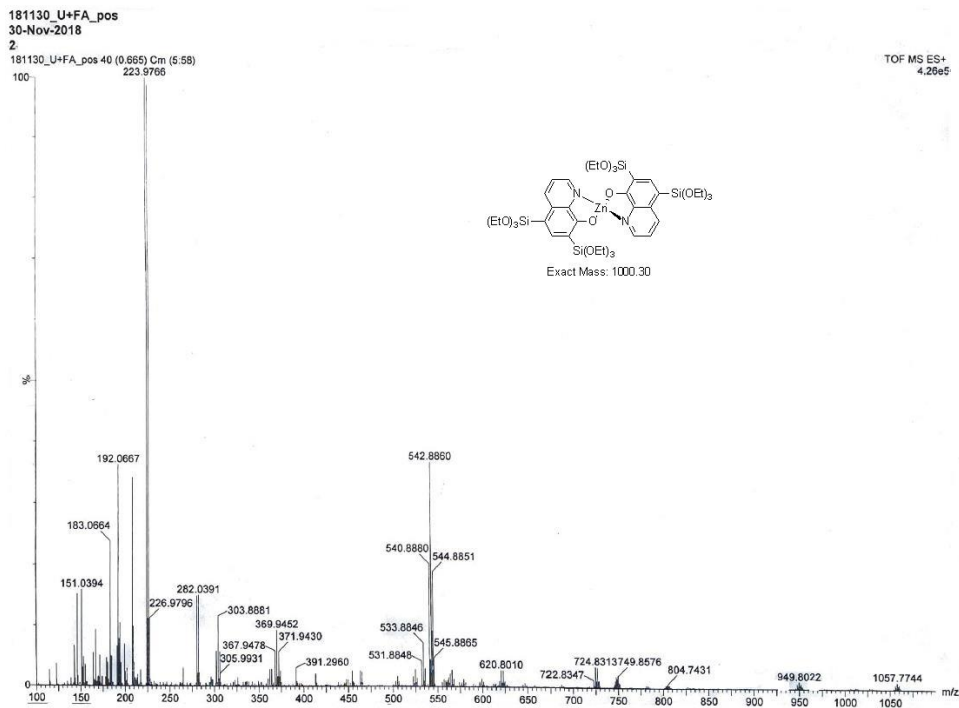
Appendix 1: Mass spectrum of the silylated complex A.

CMQ_1, Atmospheric Solids Analysis Probe (ASAP), RT 0.9229 mins, Scan# 33, NL 1.644E6, 2/18/2020 3:16 PM, mz [57.00-563.60]
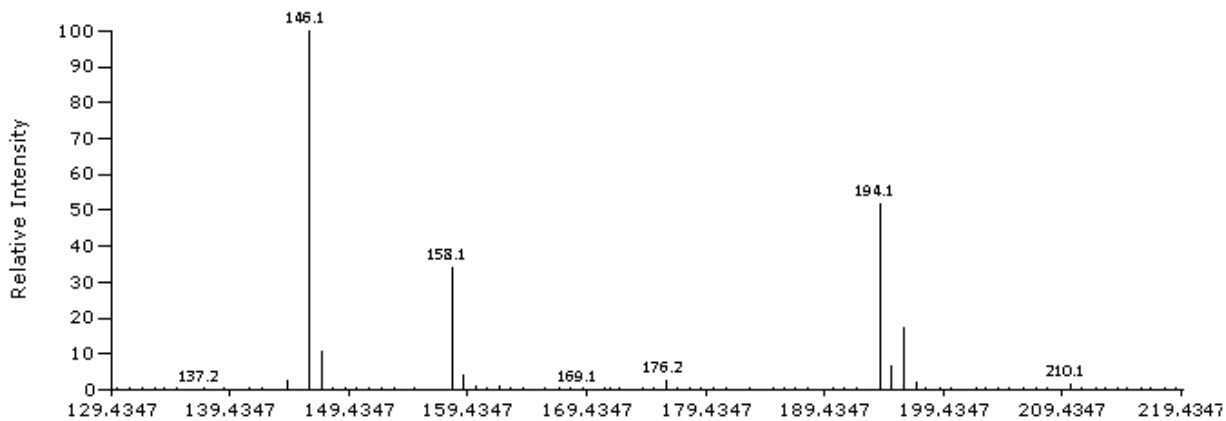
Appendix 2: LC-MS results for the identification of a sample of Batch C (5-chloromethyl 8-quinolinol), showing its two highest intensity peaks as the starting material (Mr = 146.1 gmol^{-1}) and the desired product (194.1 gmol^{-1}).

113
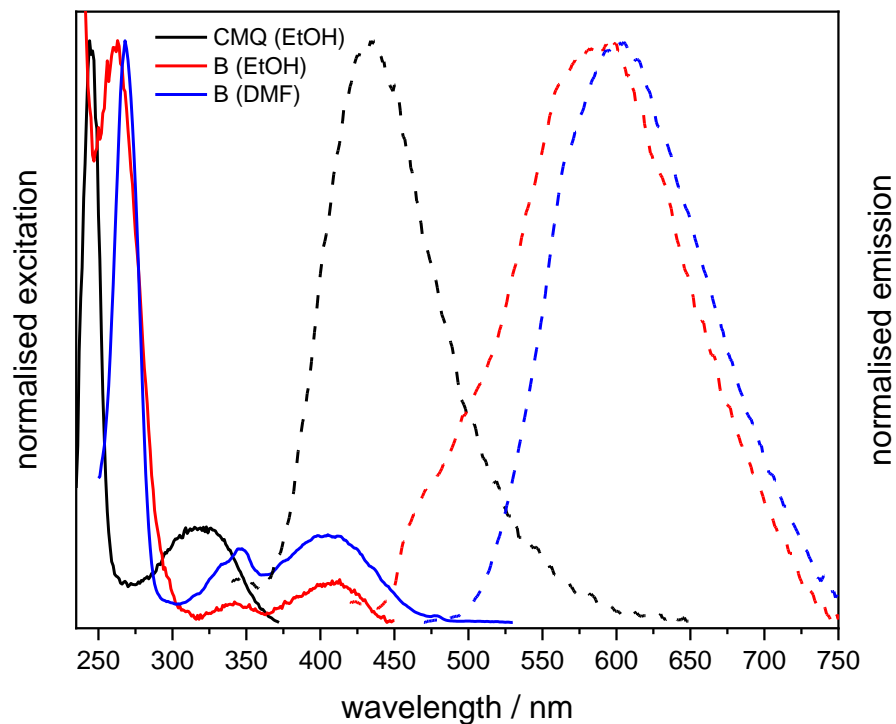
Appendix 3: Normalised excitation (solid lines) and emission spectra (dashed lines) of the free ligand 5-chloromethyl-8hydroxyquinoline in ethanol (CMQ, black), complex **B** in ethanol (red) and complex **B** in dimethylformamide (blue), all recorded from micromolar solutions; emission was measured at λ_{exc} = 265 nm, whereas excitation at λ_{em} = 460 nm for CMQ and 560 nm for **B**.
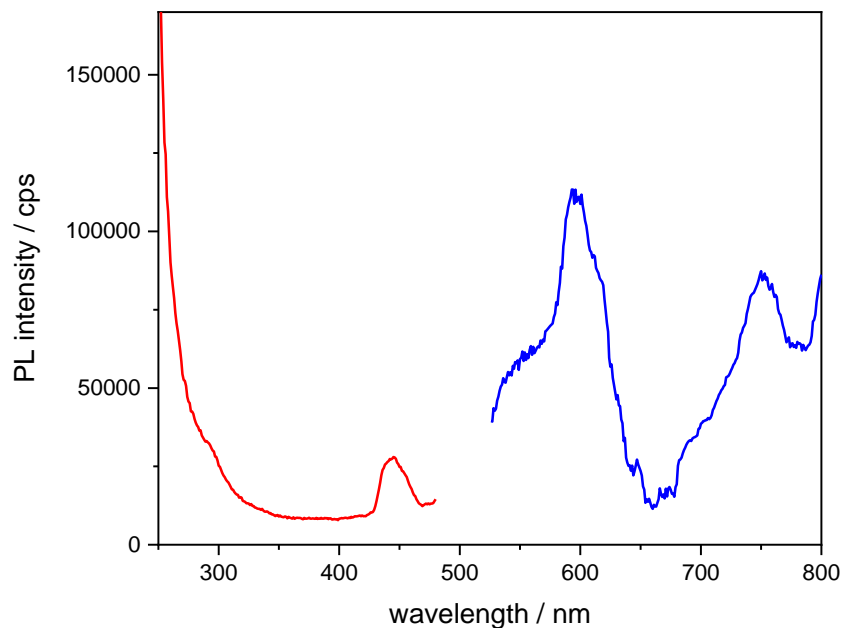
Appendix 4: Excitation (red) and emission spectra (blue) of complex **B**, recorded from a solid thin film; emission was measured at λ_{exc} = 265 nm, whereas excitation at λ_{em} = 600 nm.
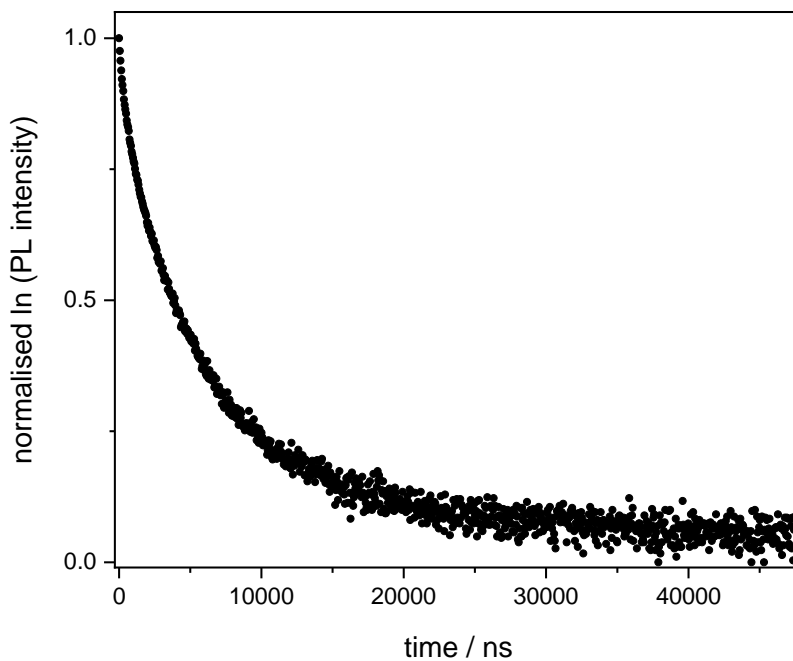
Appendix 5: Excited-state decay of complex **B** in the solid-state, recorded at λ_{em} = 600 nm.

Chapter 5: Monochromatic Light-Harvesting Antennae using BODIPY-doped MCM41 silica

5.1   Introduction

This chapter presents a new series of optical materials built using the host-guest chemistry of mesoporous silica, whereby the guests are dye molecules with structural similarities with those presented in Chapter 3. Therein, zinc bis-dipyrromethenes were encapsulated into the micellar template of COK-12 silica. In the present chapter, the guest dyes are boron dipyrromethenes (BODIPY), and they are used to build the template itself when making the silica materials. The dye used in this study termed BPJ2 (see **Figure 5.1**), is a BODIPY dye that has been previously synthesised in the group. BODIPY dyes and many of their derivatives display attractive optical properties, such as high molar absorption coefficients and high fluorescence quantum yields; they are also relatively easy to synthesise, and it is possible to tune their spectroscopic properties across the whole UV/visible/NIR region via chemical functionalisation.[1–3] Such properties have granted them a wide variety of applications as laser dyes, fluorescent biosensors and light-harvesting arrays for use in solar energy collection devices.[4–6]
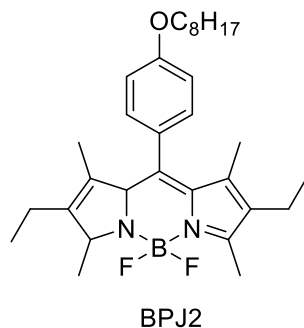
BPJ2

Figure 5.1: Structure of the BODIPY dye BPJ2.

Previous work in the group utilised the BODIPY dye BPJ2 as an additive to the micellar template employed for the synthesis of MCM-41 silica.[7] The procedure that was followed to prepare the dye-doped materials included a final drying step in an oven set at 80 °C, and such thermal treatment was found to be responsible for the formation of a new chemical species, tracked by optical spectroscopy and showing blue-shifted absorption and emission bands compared with BPJ2. This caused the formation of a donor-acceptor pair within the silica template, which engaged in energy transfer over a time range between 20 and 80 ps. Also, preliminary experiments on a different synthetic route using a room temperature drying step indicated that no new species were formed

and that only the BPJ2 dye was present in the final materials. It was then decided to carry out further investigations into such single-dye doped materials by exploiting the room temperature synthesis.

5.1.1 Aim of this chapter

This chapter shows the synthesis and the optical properties of a new series of monochromatic antenna materials. These are prepared by constructing a micellar template for mesoporous silica with a green-yellow emitting BODIPY dye as a co-surfactant. Moreover, the content of the dye in the template was varied in order to explore the effects of the different concentrations on the structural and optical properties of the materials. The overall purpose is to obtain light-harvesting silica particles and investigate whether energy migration between dye molecules can be observed and luminescence yields could be maximised. Proving that would enable further exploitation of the materials as solid-state sensitisers to use in solar energy conversion devices.

To make sure that only one chromophore is responsible for light absorption and emission within the silica particles, these were dried at room temperature using a vacuum desiccator instead of a high-temperature oven typically used after silica synthesis. The photophysical properties of the silica materials were then studied in different environments, i.e. as a suspension and in the solid-state; the latter is important as it enables the detection of anisotropic luminescence and polarisation transfer which can be taken as a measure of the energy migration rate in the materials. This kind of analysis was performed for the first time in the group on the materials presented in this chapter.

5.2 Results and Discussion

5.2.1 Synthesis and characterisation of MCM-41 doped with BPJ2

Normally, BODIPY dyes are chemically stable at ambient temperature. However, looking at how BPJ2 will be incorporated into MCM-41 at high temperature (80 °C) and high pH (~12),[8] we would expect structural degradation of the complex. Not only the structure of the complex could be affected during the synthesis of silica, also the close-packing of the dyes can alter the design of the micelles and the photoluminescence properties of the final materials.[12-14] Previous reports have shown that self-assembly of BODIPY dyes induces the formation of H- or J-aggregates, the latter being the most common and showing red-shifted fluorescence.[9–11]

Despite the relatively harsh temperature and pH used in the silica synthesis, the BPJ2 dye studied in the group has shown some excellent chemical stability.[7] The synthetic route for the preparation of dye-doped silica is schematised in **Figure 5.2**, which shows that the dye is added to the cetyltrimethylammonium bromide (CTAB) surfactant to form a micellar template with the hexagonal arrangement in water. This first step is followed by the base-catalysed hydrolysis and poly-condensation of tetraethyl orthosilicate (TEOS), which forms a silica network around the template.
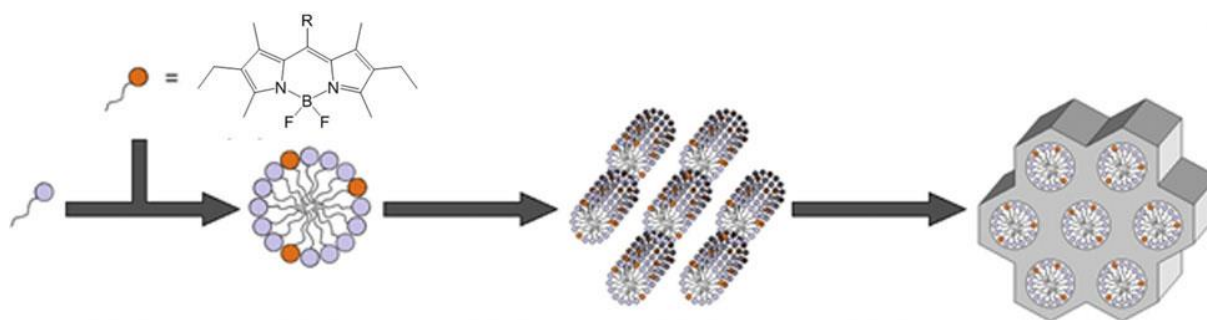
Figure 5.2: The synthetic routes of the dye-doped MCM-41 built from a mixture of surfactant (CTAB, light violet) and co-surfactant (BPJ2, orange) at different loadings; the R group at the meso position of the BODIPY is a phenyl ring bearing a $-OC_8H_{17}$ chain. From a previous paper in the group.[7]

The addition of the dye was done at different BPJ2:CTAB molar ratios, namely 1:99, 10:90, 20:80, 30:70 and 50:50. The silica samples obtained from such additions are labelled after the dye content, e.g. 1%, 10% etc. As mentioned earlier, the synthesis conditions did not affect the stability of the dye during the two hours of the reaction. Also, it was found that the use of increasing amounts of BPJ2 in the micellar template did not cause major deviations from the classical silica structure and morphology, as it will be explained in the next section.

5.2.2 Structural Analysis

Structure and morphology of the materials were analysed using powder XRD and TEM. The diffractograms shown in **Figure 5.3** are compared against that obtained for standard MCM-41, synthesised using plain CTAB micelles.
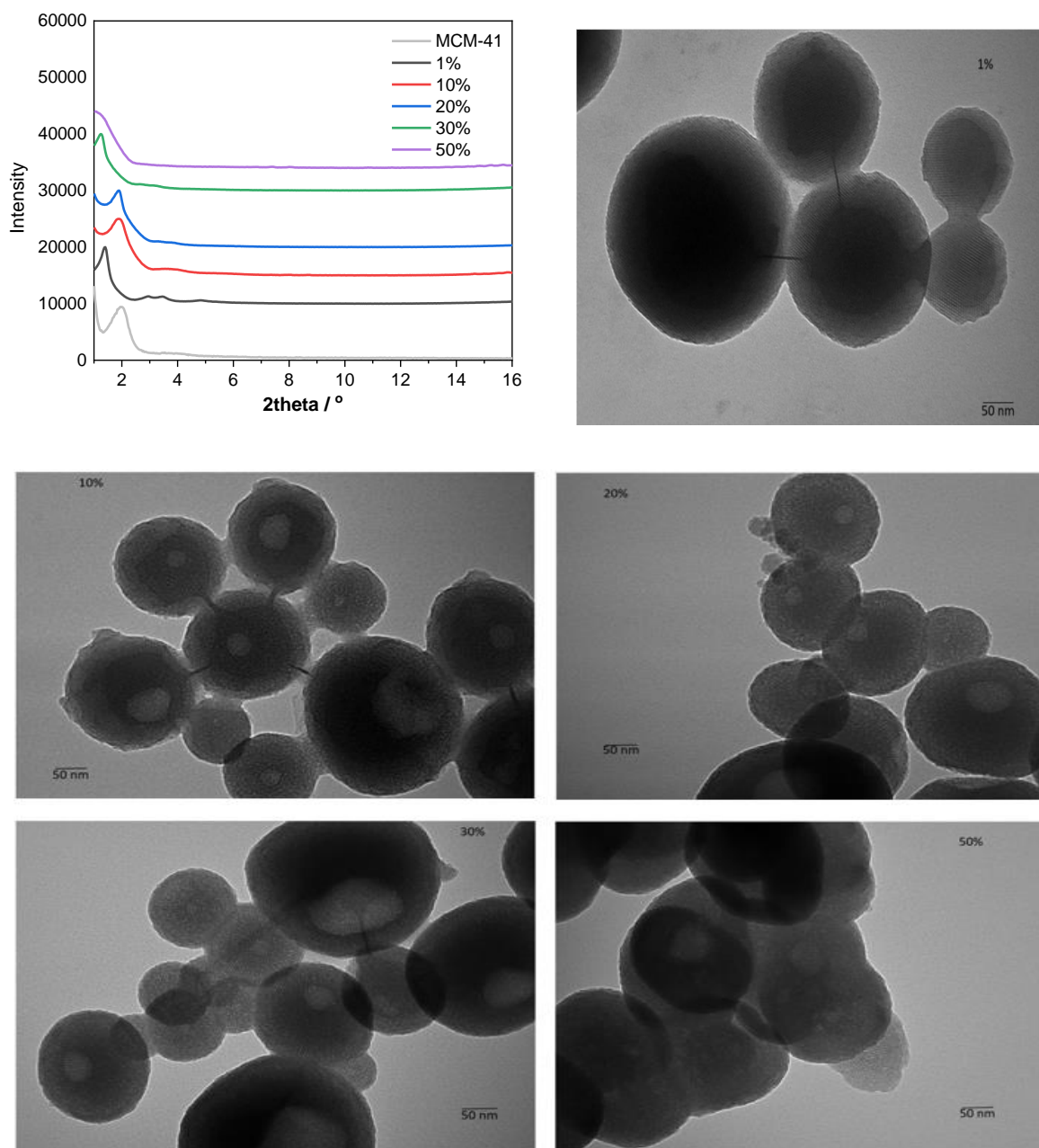
Figure 5.3: X-ray diffractograms (top left) and TEM images of the hybrid silica samples at different loadings (1-50%).

The samples with 10% and 20% of dye loading show a similar profile to that of classical MCM-41, with the main reflection from the (100) plane visible at 2θ values of 1.91° and 1.87°, respectively. Such values give a d-spacing of 4.6 – 4.7 nm, which is only slightly larger than the 4.5 nm obtained from plain silica. This can be taken as an indication that replacing CTAB molecules with BPJ2 does not alter the shape of the cylindrical micelles and their mutual arrangement, which generates the typical hexagonal pattern in silica.[15] It is also possible to observe the higher-order secondary peak (110) at 3.3 – 3.5° in the two samples.

On the other hand, the pore spacing is found to increase up to 6.2 nm, 7.1 nm and 8 nm at 1%, 30% and 50% dye loading, respectively, as indicated by the downshift of the 2θ values. This is also accompanied by a signal broadening, particularly evident in the 50% sample, which may well reflect a loss of regularity in the hexagonal arrangement. Previous studies in our group indicated that such an effect may be expected at high loadings, where the large dye content could cause an expansion of the template and, in turn, the whole structure.[7,16] It is rather surprising, though, that such an expansion would occur at 1% loading. A tentative explanation is that the dispersion of the dye molecules within the template is not homogenous; it could also be possible that the relatively few dye molecules in the 1% sample cluster up at the hydrophobic core of the micelles, causing the overall structure to swell, but further investigation is needed to verify such hypothesis.

The TEM images indicate that the inner structure of the silica is maintained across all samples, so as the overall near-spherical morphology of the MCM-41 particles. The parallel arrangement of the template is only visible from the 1% sample, though, and the particle size appears to increase at the highest loading of 50%.

5.2.3 Photophysical Analysis

UV-visible luminescence studies were carried out on the five silica materials using the same conditions described in the previous chapters for similar samples; that is, by preparing 0.3 mg/ml suspensions in cyclohexane, which is found to limit the intense scattering normally observed from silica particles.[15,19]

Excitation and emission spectra are reported in **Figure 5.4** and show a trend that is consistent with the presence of only one chromophore, the BPJ2 dye, whose light-absorbing and emitting properties are preserved once incorporated in the micelle/silica systems (see also **Appendix 5.1**). Looking at the 1% sample, it is possible to note the typical optical profile of the dye, with the excitation maximum at 526 nm and the emission at 536 nm, corresponding to the $S_0 \rightarrow S_1$ and the $S_1 \rightarrow S_0$ transitions, respectively. This is quite different in comparison with the BPJ2-silica materials previously studied in the group, which were dried in an oven at 80 °C and showed the appearance of additional excitation and emission peaks, blue-shifted in respect to the BPJ2 bands.[16]
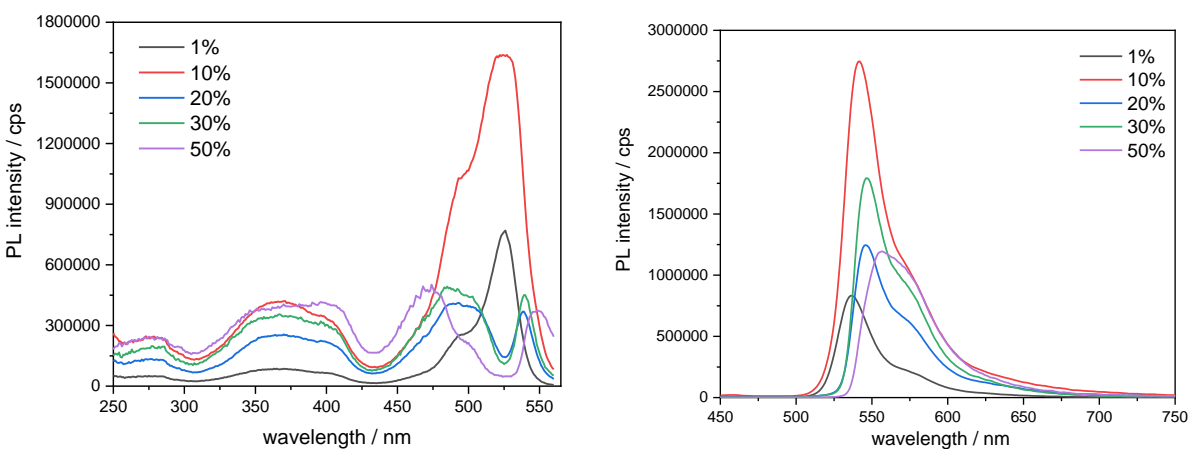
Figure 5.4: Excitation (left) and emission spectra (right) of the hybrid silica materials, recorded from 0.3 mg/mL cyclohexane suspensions; excitation spectra are measured at λ_{em} = 580 nm and emission spectra at λ_{exc} = 350 nm.

With excitation and emission slits being equal across all samples, the 10% dye-loaded silica shows the highest photoluminescence intensity in the series. Above such loading, an interesting effect can be noted in the samples: the emission bands appear as though they were red-shifted, and the

excitation shows a depletion region in the 500-540 nm range. This can be explained as an inner-filter effect caused by the high concentration of dye in the micelles. Beyond 10% loading, light emitted by the dye in the region of overlap with the absorption spectrum (see **Appendix 5.1**) is re-absorbed by neighbouring molecules before it can exit the cuvette to be detected. Such an effect can be appreciated more evidently in **Figure 5.5**, where the excitation and the emission spectra of the 30% sample are shown normalised, and the net cut-off in both profiles is clearly visible.[18–20] As a result, the emission intensity is depleted at low wavelengths, rather than actual red-shifted; for a red-shift to take place, the second vibronic transition, traceable around 575 nm, would have to fall at longer wavelengths as well as the first, but this is not the case here.
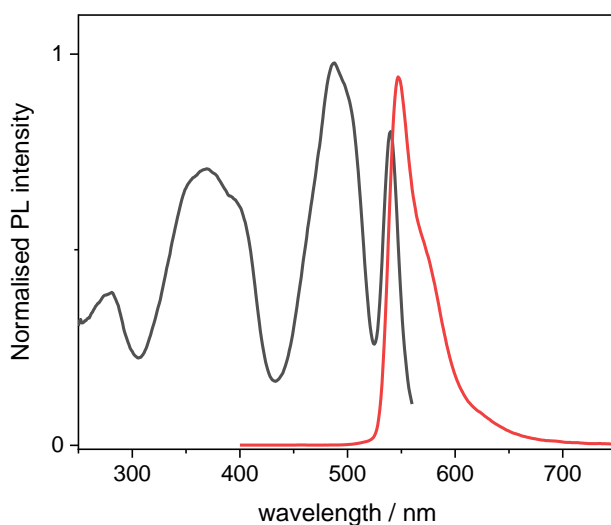
Figure 5.5: Normalized excitation (black) and emission (red) spectra of the 30% dye-loaded silica, recorded at λ_{em} = 580 nm and λ_{exc} = 350 nm, respectively.

Because of such an effect, the quantum yields of all samples are underestimated, especially at 20%, 30% and 50% dye-loading (**Table 5.1**). The most emissive sample appears to be the 10%, with a fluorescence yield of 62%, which is higher than that of the free BPJ2 dye in solution (48%).[7]

Table 5.1: Excited-state lifetimes (τ), fluorescence quantum yields (Φ), radiative rate constants (k_r) and non-radiative rate constants (k_{nr}) of the silica samples.

sample	τ / ns	Φ	k_r / s^{-1}	k_{nr} / s^{-1}
1%	4.71	0.16	3.40 x 10^6	2.09 x 10^8
10%	4.65	0.62	1.33 x 10^7	2.02 x 10^8
20%	5.27	0.28	5.31 x 10^6	1.84 x 10^8
30%	5.50	0.38	6.91 x 10^6	1.75 x 10^8
50%	6.29	0.33	5.25 x 10^6	1.54 x 10^8

The table also reports the results of the fitting of the excited-state decay curves, which are shown in **Figure 5.6**. The decays are mono-exponential, and all but the 50% sample show values in good accordance with those recorded from the free dye and the dye-loaded silica in the previous study, being all in the 4.7 – 5.5 ns range. The sample with the highest concentration of BPJ2 has an excited-state lifetime of about 6.3 ns, which is not unusual for a BODIPY dye[1,21,22] and might reflect the fact that the dye molecules are exposed to a particularly rigid local environment within the micelles, which lowers the k_{nr}.
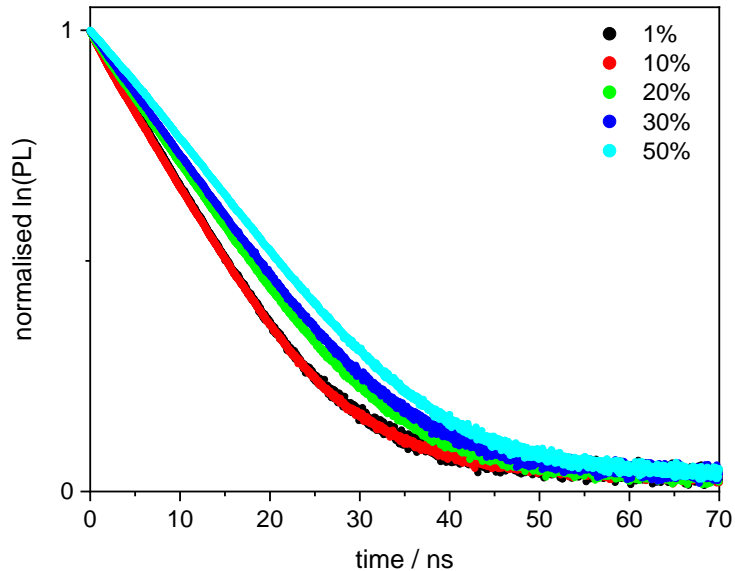
Figure 5.6: Excited-state decay profiles of the silica hybrids, recorded from 0.3 mg/ml cyclohexane suspensions at λ_{em} = 540 nm, using a 371.8 nm laser excitation.

Another interesting feature is observed at high loadings, above 20%, from the excitation spectra. If the emission wavelength is set at 720 nm, which is in the descending part of the fluorescence curve, it is possible to scan a wide area of excitation and notice an additional band around 625 nm (see **Figure 5.7** and also **Appendix 5.2**). The band reaches the highest intensity at 50% loading and slightly red-shifts to 634 nm.
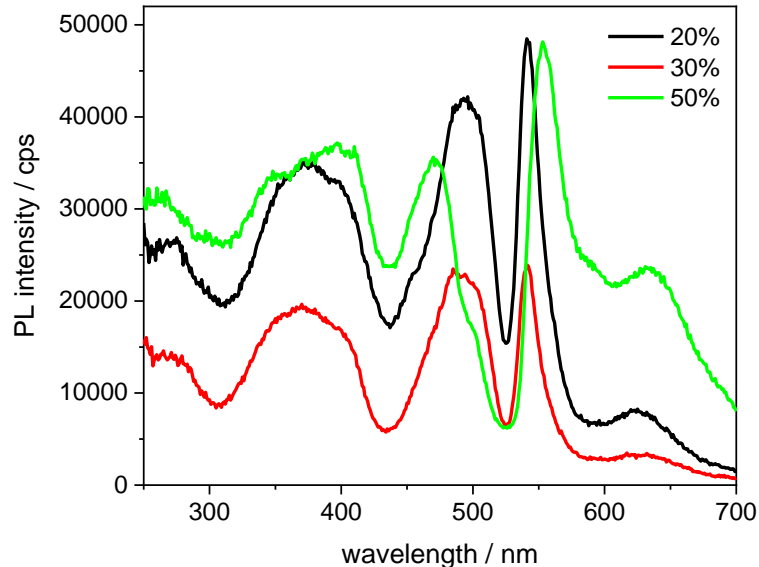
Figure 5.7: Excitation spectra of the 20%, 30% and 50% samples, recorded from 0.3 mg/mL cyclohexane suspensions at λ_{em} = 720 nm; excitation and emission slits = 5 nm.

This behaviour is attributed to the formation of ground-state dimers and J-aggregates within the micelles where the BPJ2 dye is dispersed; such species typically absorb and emit light at longer wavelengths than the respective monomers, and previous studies on BODIPY dyes have shown that their formation is a common occurrence at high concentrations.[9,21,23]

Further time-resolved analysis was carried out in light of the above findings. An excited-state lifetime was recorded for the 50% dye-doped silica, and the decay profile is shown in **Figure 5.8**. A bi-exponential fitting of the decay curve yielded two-time traces: 6.40 ns, with a relative weight of 77%, and 0.78 ns, with a 13% weight. The first trace matches with that obtained at 540 nm and can be confirmed as the decay of single units of BPJ2 within the template; the second and short trace, instead, can be attributed to dimeric/aggregated species, whose emission cannot be isolated because of the overlap with the monomer emission band.
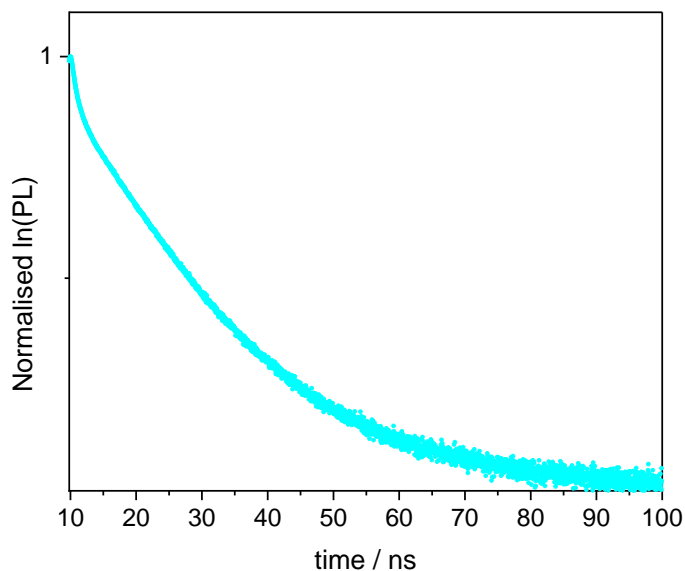
Figure 5.8: The time-resolved analysis of the luminescence at long wavelengths of 50% silica hybrids, recorded from 0.3 mg/ml cyclohexane suspensions at $\lambda_{em} = 750$ nm, using 371.8 nm laser excitation.

5.2.4 Fluorescence Anisotropy Studies

The BODIPY-doped silica samples were analysed in the solid-state, from thin powder films and by using excitation and emission polarisers during steady-state and time-resolved measurements. The use of polariser filters, as explained in Chapter 2, allows analysis of the sample response to vertically and horizontally polarised light. The materials that showed a significant response and measurable kinetic traces were the 1% and the 10% dye-doped samples. Excitation and emission spectra from the two materials (see **Appendix 5.3** and **5.4**) indicate that there is a preferred orientation of dye molecules within the template, as the detected fluorescence intensity is the highest when the emission polariser is set to the horizontal orientation. The G-factor, which measures the extent of anisotropy and is obtained from the excitation spectra, is 1.69 at 580 nm for the 1% sample and 4.12 at 730 nm for the 10% sample. Excited-state anisotropy decays were then measured by recording the fluorescence lifetimes of the samples at the above emission wavelengths and at both vertical and horizontal polarisations (see **Figure 5.9**).
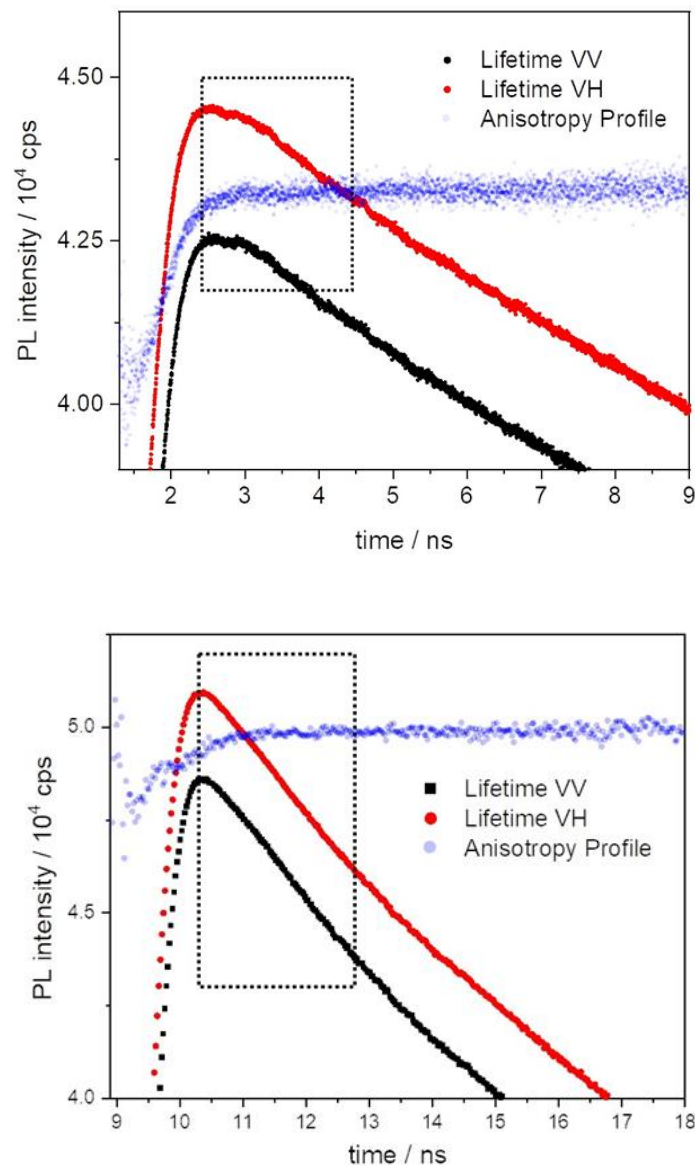
Figure 5.9: Fluorescence anisotropy decay profiles (black and red) of the 1% (top) and 10% (bottom) samples, recorded at 580 nm and 730 nm, respectively. The blue profile is the anisotropy curve generated from the two decays.

The decay profiles indicate a difference in intensity at the two polarisations of emitted light and the anisotropy curve, which is generated from a combination of the decays, shows a slight difference between the decay times. From the point of maximum intensity, which corresponds to the moment the laser pulse goes off, there is a small mismatch in the decay trend at the two different orientations. The anisotropy profile measured such mismatch and generated a differential kinetic

trace; this was then fitted in the region indicated with the dotted squares, and the values obtained were 404 ps for the 1% and 705 ps for the 10% sample. Such time traces are indicative of the polarisation transfer times, which is the time that it takes for the emission light to change its orientation from V to H. In our case, this can be interpreted as the transfer time or energy migration time, assuming that the transfer of excitation energy between neighbouring dye molecules with slightly different orientations is the phenomenon responsible for the changes in the direction of the emitted light. The shorter transfer time at 1% loading appears to confirm the hypothesis made from the XRD analysis that, at such low loading, the dye molecules are not evenly dispersed and might cluster up within small domains of the template. Further analysis would be required, though, for example, to test whether a templated synthesis at different experimental conditions yielded the same result.

It was generally noted that the measurements required several repeats and long acquisition times in order to yield reproducible and significant kinetic traces. Also, all such traces were found to drop rapidly at greater dye concentrations than 10%. This was expected because of the increasingly small distances between dye units within the template, which would make the transfer faster and fall below the time detection limit of the instrument (~70 ps). The same trend was observed in the previous work of the group, where energy transfer times between a donor and an acceptor species dropped below 100 ps as the dye loading increased and could only be measured by femtosecond transient absorption spectroscopy.[7]

5.3   Conclusions

The studies presented in this chapter show that it is possible to design light-harvesting materials using BODIPY dyes assembled within host-guest silica materials. By attaching a C8 alkyl chain on one of such dyes (BPJ2), this was co-assembled with a surfactant in a micellar template, which, in turn, was used to synthesise an MCM41-like silica network around it. The TEM and XRD diffractograms showed that the regular porosity of the MCM41 silica is maintained even at high concentrations, or loadings, of dye in the template, although from 50% on the structure of the materials appears to lose uniformity. The highest fluorescence quantum yield (0.62) was obtained for the 10% dye-doped sample, whereas at higher concentrations, an inner-filter effect was observed, along with the emergence of ground-state dimers or aggregates. It was also possible to

measure the time traces of energy migration between units of dye molecules at low loadings of 1% and 10%. This was done by using time-resolved fluorescence anisotropy for the first time in the group and showed that the transfer dynamics across the materials upon light absorption is very fast, from 700 ps and decreasing with the dye loading.

5.4 Experimental Section

5.4.1 Synthesis of BODIPY dye (BPJ2)

Octyloxybenzaldehyde (720 µL, 3.3 mmol) was dissolved in anhydrous DCM (60 mL). 2-Ethyl-1,3-dimethylpyrrole (810 µL, 6.6 mmol) was added, and the mixture was stirred for 30 minutes. TFA (45 µL, 0.6 mmol) was added under a nitrogen atmosphere, the mixture turned red, and it was left stirring overnight at room temperature. The complete consumption of the aldehyde was confirmed using TLC plates (silica, eluent: DCM). The oxidation reaction was proceeded by the use of DDQ (700 mg, 3 mmol), which was added to the dark red reaction mixture and stirred for 3.5 hours. Anhydrous triethylamine (3.3 mL, 21 mmol) was added, immediately followed by the addition of $BF_3.OEt_3$ dropwise. The mixture turned quickly yellow and dark green, respectively, and it was stirred overnight under a nitrogen atmosphere. The resulting product was washed with water (3 x 30 mL), dried over Na_2SO_4, and finally rotary evaporated to give a viscous purple oil with green tints. The crude was purified by column chromatography (eluent; Petrol:DCM (1:1). ^{1}H NMR (400 MHz, CDCl3): δ = 7.08 (d, J = 9 Hz, 2H, C*H*$_{Ar}$), 6.92 (d, J = 9 Hz, 2H, C*H*$_{Ar}$), 3.94 (t, J = 6 Hz, 2H, OC*H*$_2$), 2.45 (s, 6H, pyrrole –C*H*$_3$), 2.24 (q, J = 7 Hz, 4H, pyrrole –C*H*$_2$–CH$_3$), 1.76–1.70 (m, 2H, OCH$_2$–C*H*$_2$), 1.46–1.39 (m, OCH$_2$CH$_2$–C*H*$_2$), 1.33–1.15 (m, 8H, –C*H*$_2$–), 1.26 (s, 6H, pyrrole –C*H*$_3$), 0.92 (t, J = 7.5 Hz, 6H, pyrrole –CH$_2$–C*H*$_3$), 0.83 (t, J = 6 Hz, 3H, –C*H*$_3$).
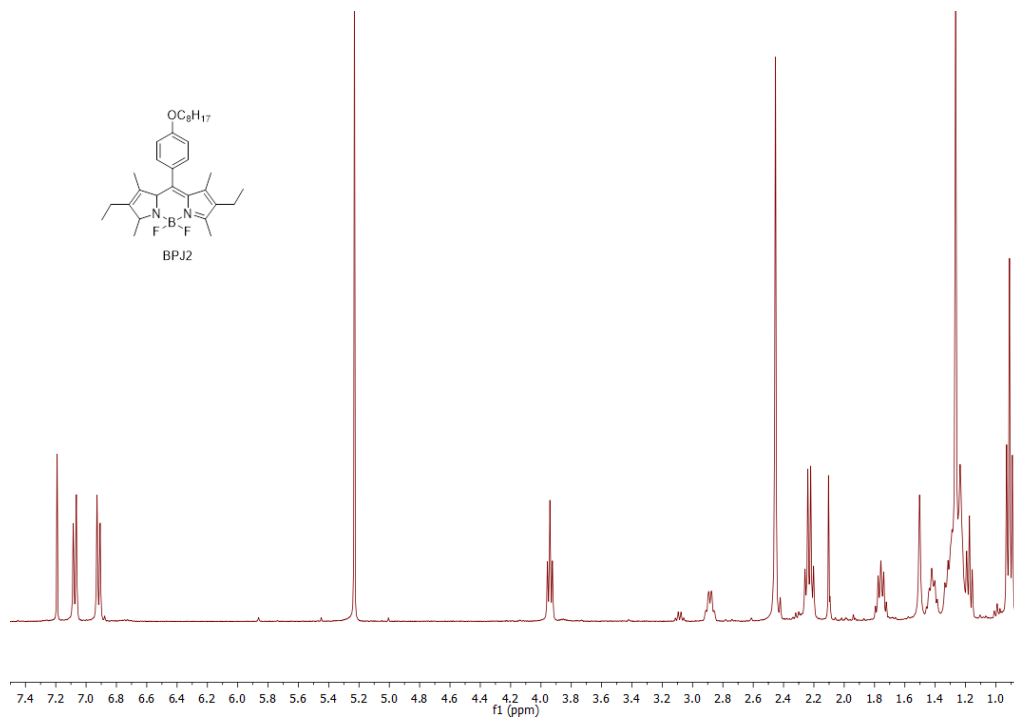
Figure 5.10: ^{1}H NMR spectrum of BPJ2, recorded with Bruker 400 MHz in CDCl$_3$.
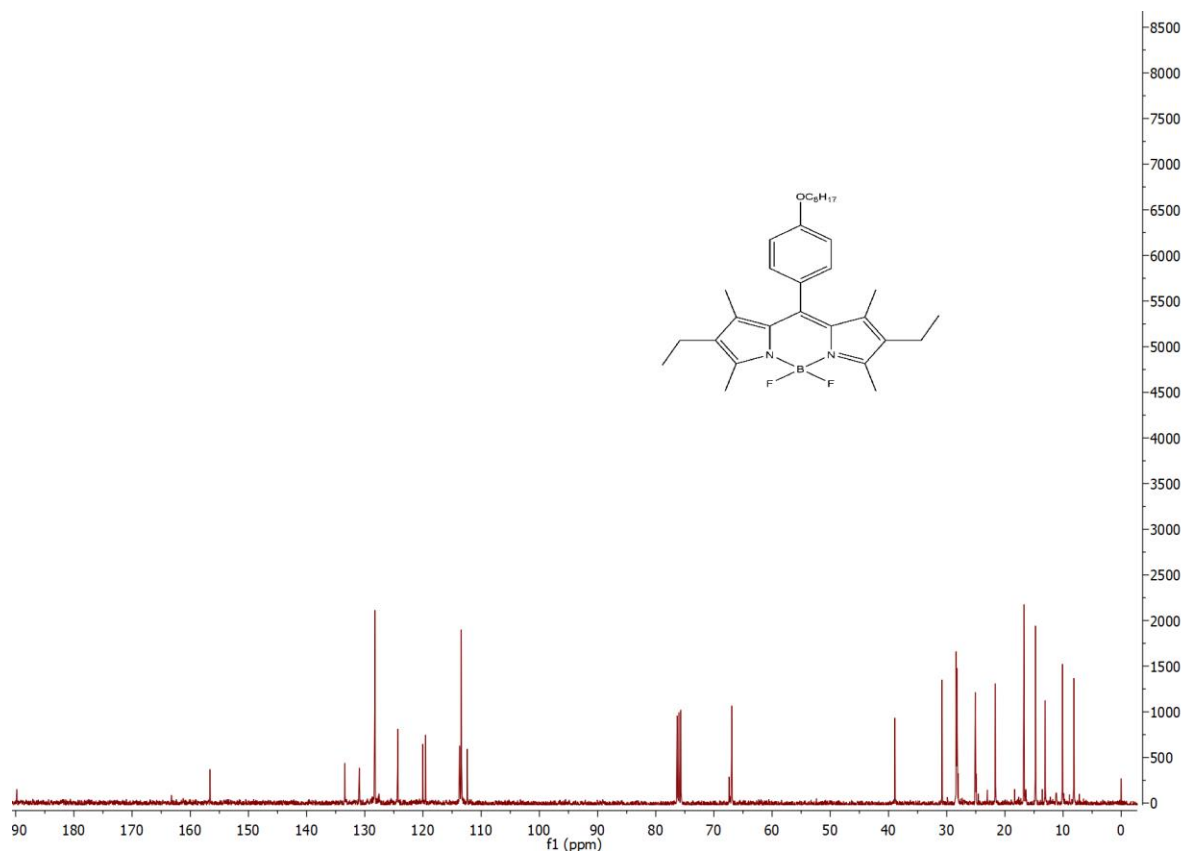
Figure 5.11: ^{13}C NMR spectrum of BPJ2, recorded with Bruker 400 MHz in CDCl$_3$.

5.4.2 Synthesis of the MCM-41 with CTAB and BPJ2 (99:1, 90:10, 80:20, 70:30 and 50:50)

Cetyltrimethylammonium bromide was dissolved in 100 mL of water using an ultrasound bath. BPJ2 was dissolved in a minimal amount of acetonitrile and transferred into 80 mL of water that forms a homogeneous turbid pink-orange mixture. This was then added into the CTAB solution and stirred, followed by the addition of 2 M aqueous NaOH (1.3 mL, 2.6 mmol). The mixture was heated to 80 ^{0}C, and the silica precursor tetraethylorthosilicate (1.7g, 1.8 mL. 8.2 mmol) was added, at which point silica started to form quickly. It was then refluxed for 2 hours, stopped and allowed to cool down to room temperature. The mixture was filtered under the vacuum and washed with water. The filtrate was dried in the desiccator, and a pink solid product was obtained that fluoresced lightly under a UV lamp. The CTAB and BPJ2 were added for each reaction in the following ratios; 99:1 (346 mg, 0.949 mmol CTAB and 4.88 mg, 9.6 µmol BPJ2), 90:10 (315 mg, 0.863 mmol and

134

48.8 mg, 0.096 mmol), 80:20 (280 mg, 0.8 mmol and 97.6 mg, 0.192 mmol), 70:30 (245 mg, 0.7 mmol and 146.4 mg, 0.288 mmol) and 50:50 (175 mg, 0.5 mmol and 244 mg, 0.48 mmol).

References

(1)   Loudet, A.; Burgess, K. BODIPY Dyes and Their Derivatives: Syntheses and Spectroscopic Properties. *Chem. Rev.* **2007**, *107* (11), 4891–4932.

(2)   Ziessel, R.; Ulrich, G.; Harriman, A. The Chemistry of Bodipy: A New El Dorado for Fluorescence Tools. *New J. Chem.* **2007**, *31* (4), 496.

(3)   Altan Bozdemir, O.; Erbas-Cakmak, S.; Ekiz, O. O.; Dana, A.; Akkaya, E. U. Towards Unimolecular Luminescent Solar Concentrators: Bodipy-Based Dendritic Energy-Transfer Cascade with Panchromatic Absorption and Monochromatised Emission. *Angew. Chem.* **2011**, *123* (46), 11099–11104.

(4)   Iehl, J.; Nierengarten, J.-F.; Harriman, A.; Bura, T.; Ziessel, R. Artificial Light-Harvesting Arrays: Electronic Energy Migration and Trapping on a Sphere and between Spheres. *J. Am. Chem. Soc.* **2012**, *134* (2), 988–998.

(5)   Kaloudi-Chantzea, A.; Karakostas, N.; Pitterl, F.; Raptopoulou, C. P.; Glezos, N.; Pistolis, G. Efficient Supramolecular Synthesis of a Robust Circular Light-Harvesting Bodipy-Dye Based Array. *Chem. Commun.* **2012**, *48* (100), 12213.

(6)   Ziessel, R.; Ulrich, G.; Haefele, A.; Harriman, A. An Artificial Light-Harvesting Array Constructed from Multiple Bodipy Dyes. *J. Am. Chem. Soc.* **2013**, *135* (30), 11330–11344.

(7)   Cucinotta, F.; Jarman, B. P.; Caplan, C.; Cooper, S. J.; Riggs, H. J.; Martinelli, J.; Djanashvili, K.; La Mazza, E.; Puntoriero, F. Light-Harvesting Antennae Using the Host-Guest Chemistry of Mesoporous Organosilica. *ChemPhotoChem* **2018**, *2* (3), 196–206.

(8)   Kresge, C. T.; Leonowicz, M. E.; Roth, W. J.; Vartuli, J. C.; Beck, J. S. Ordered Mesoporous Molecular Sieves Synthesised by a Liquid-Crystal Template Mechanism. *Nature* **1992**, *359* (6397), 710–712.

(9)   Vu, T. T.; Dvorko, M.; Schmidt, E. Y.; Tro, B. A. Understanding the Spectroscopic Properties and Aggregation Process of a New Emitting Boron Dipyrromethene (BODIPY). *J Phys Chem C* **2013**, 13.

(10)   Allampally, N. K.; Florian, A.; Mayoral, M. J.; Rest, C.; Stepanenko, V.; Fernández, G. H-Aggregates of Oligophenyleneethynylene (OPE)-BODIPY Systems in Water: Guest Size-Dependent Encapsulation Mechanism and Co-Aggregate Morphology. *Chem. - Eur. J.* **2014**, *20* (34), 10669–10678.

(11)   Haedler, A. T.; Kreger, K.; Issac, A.; Wittmann, B.; Kivala, M.; Hammer, N.; Köhler, J.; Schmidt, H.-W.; Hildner, R. Long-Range Energy Transport in Single Supramolecular Nanofibres at Room Temperature. *Nature* **2015**, *523* (7559), 196–199.

(12)   Michaux, F.; Baccile, N.; Impéror-Clerc, M.; Malfatti, L.; Folliet, N.; Gervais, C.; Manet, S.; Meneau, F.; Pedersen, J. S.; Babonneau, F. In Situ Time-Resolved SAXS Study of the Formation of Mesostructured Organically Modified Silica through Modeling of Micelles Evolution during Surfactant-Templated Self-Assembly. *Langmuir* **2012**, *28* (50), 17477–17493.

(13)   Li, L.; Han, J.; Nguyen, B.; Burgess, K. Syntheses and Spectral Properties of Functionalized, Water-Soluble BODIPY Derivatives. *J. Org. Chem.* **2008**, *73* (5), 1963–1970.

(14)   Fan, G.; Yang, L.; Chen, Z. Water-Soluble BODIPY and Aza-BODIPY Dyes: Synthetic Progress and Applications. *Front. Chem. Sci. Eng.* **2014**, *8* (4), 405–417.

(15)   Kruk, M.; Jaroniec, M.; Sakamoto, Y.; Terasaki, O.; Ryoo, R.; Ko, C. H. Determination of Pore Size and Pore Wall Structure of MCM-41 by Using Nitrogen Adsorption, Transmission Electron Microscopy, and X-Ray Diffraction. *J. Phys. Chem. B* **2000**, *104* (2), 292–301.

(16)   Jarman, B. P.; Cucinotta, F. Photoactive Amphiphiles for the Assembly of Supramolecular Architectures. *Faraday Discuss.* **2015**, *185*, 471–479.

(17)   Yu, X.; Jia, X.; Yang, X.; Liu, W.; Qin, W. Synthesis and Photochemical Properties of BODIPY-Functionalized Silica Nanoparticles for Imaging Cu2+ in Living Cells. *RSC Adv.* **2014**, 9.

(18)   Kumar Panigrahi, S.; Kumar Mishra, A. Inner Filter Effect in Fluorescence Spectroscopy: As a Problem and as a Solution. *J. Photochem. Photobiol. C Photochem. Rev.* **2019**, *41*, 100318.

(19)   Chen, S.; Yu, Y.-L.; Wang, J.-H. Inner Filter Effect-Based Fluorescent Sensing Systems: A Review. *Anal. Chim. Acta* **2018**, *999*, 13–26.

(20)   Granite. What is the Inner Filter Effect? | Edinburgh Instruments | Blog https://www.edinst.com/blog/inner-filter-effect/ (accessed 2021 -06 -29).

(21)   Tleugabulova, D.; Zhang, Z.; Brennan, J. D. Characterization of Bodipy Dimers Formed in a Molecularly Confined Environment. 6.

(22)   Tamgho, I.-S.; Hasheminasab, A.; Engle, J. T.; Nemykin, V. N.; Ziegler, C. J. A New Highly Fluorescent and Symmetric Pyrrole–BF $_2$ Chromophore: BOPHY. *J. Am. Chem. Soc.* **2014**, *136* (15), 5623–5626.

(23)   Choi, S.; Bou, J. Aggregation-Induced Emission Enhancement of a Meso-Trifluoromethyl BODIPY via J-Aggregation. *Chem. Sci.* **2014**, 5.
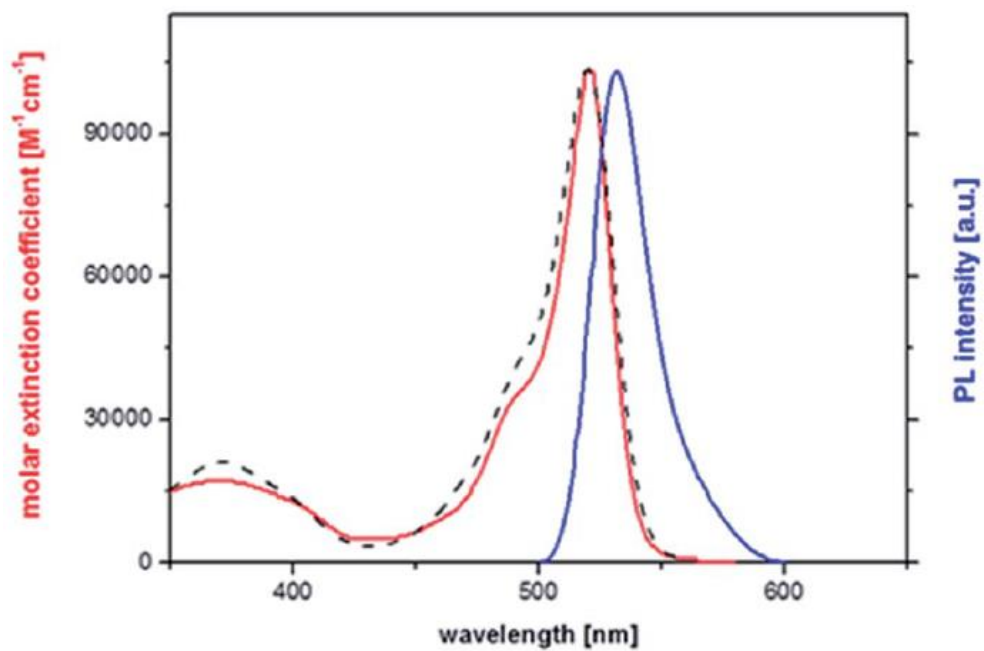
Appendix 5.1: UV-vis absorption (red), fluorescence (blue) and excitation (dashed black) spectra of BPJ2, recorded in a 10^{-6} M acetonitrile solution. Emission was recorded at $\lambda_{exc} = 490$ nm, whereas excitation at $\lambda_{em} = 575$ nm. From reference 16.
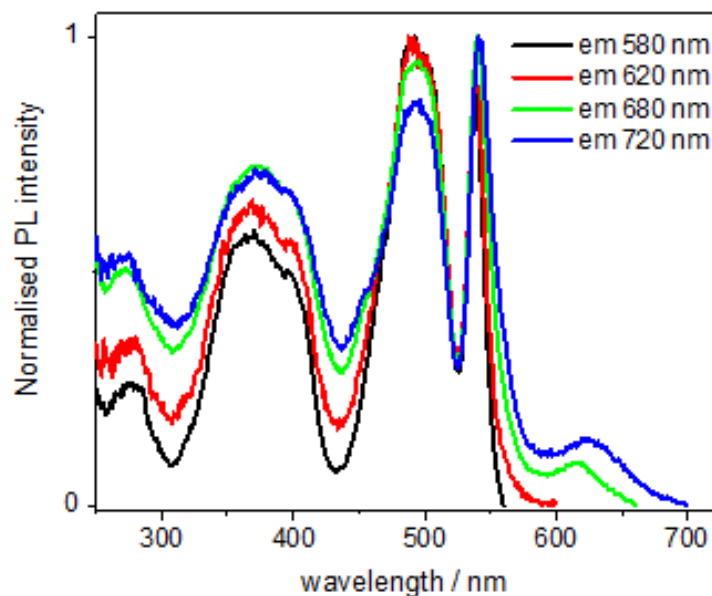
Appendix 5.2: Excitation spectra of the 20% BPJ2-MCM41 sample, recorded at different emission wavelengths, from 0.3 mg/ml cyclohexane suspensions.
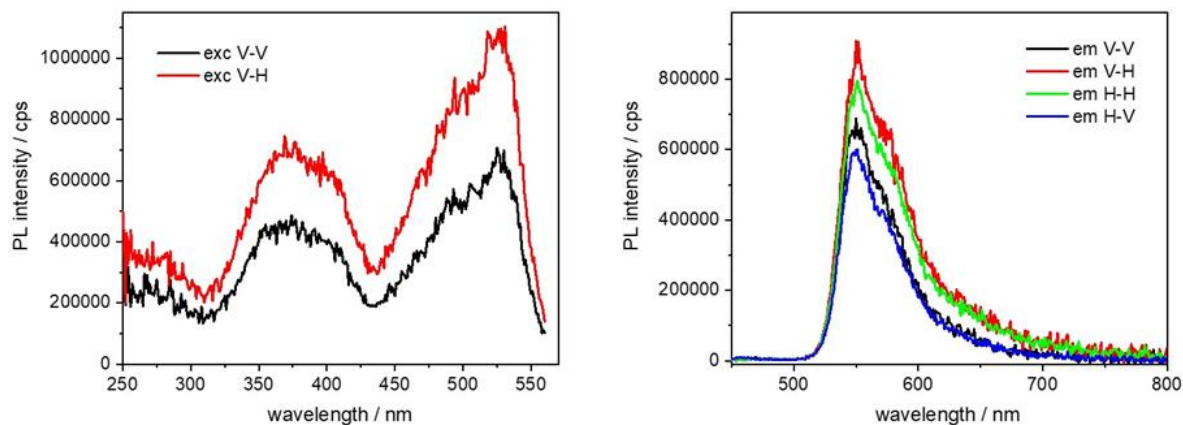
Appendix 5.3: Excitation (left) and emission (right) anisotropy spectra of the 1% dye-loaded silica sample, recorded at λ_{em} = 580 nm and λ_{exc} = 350 nm, respectively, from a powder thin film; the notation in the legend indicates the plane-polarisation of the excitation and the emission light beam.
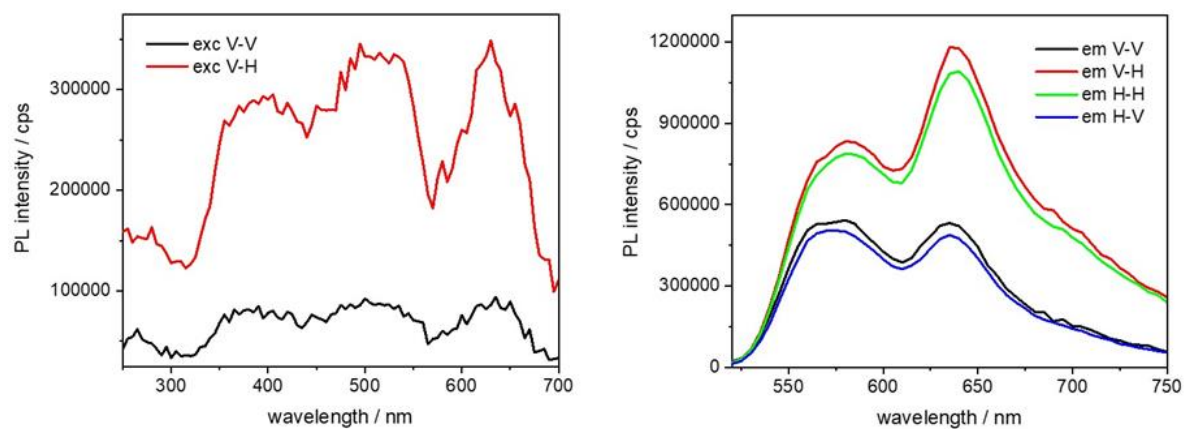
Appendix 5.4: Excitation (left) and emission (right) anisotropy spectra of the 10% dye-loaded silica sample, recorded at λ_{em} = 730 nm and λ_{exc} = 350 nm, respectively, from a powder thin film; the notation in the legend indicates the plane-polarisation of the excitation and the emission light beam.

Chapter 6: New PMO Materials Built from BOPHY Dyes: A Structural and Optical Comparative Study

6.1 Introduction

Studies have shown that the structure and properties of low molecular weight organic chromophores such as BODIPY can be modified or fine-tuned, and this has proven to be an effective strategy to improve light absorption and emission.[1,2] Typically, the core structure of such organic dyes is relatively easy to modify through the introduction of specific functional groups at a variety of different positions, allowing fine changes into absorption and emission wavelengths, which opens the way to several applications in various scientific fields.[3,4] Among them, small organic dyes find use as biological probes, molecular sensors, light-harvesting agents, fluorescent makers and active components in optoelectronic devices such as OLEDs.[7–17]

A similar class of molecules that has recently attracted a great deal of attention is that of BOPHYs, which are synthesised from a subset of the dipyrromethene group. As briefly explained in Chapter 1, a BOPHY dye comprises two pyrrole rings, with one at either side of a two-centred six-membered ring (four 5,6,6,5-tetracyclic rings) containing a BF_2 moiety.[10]
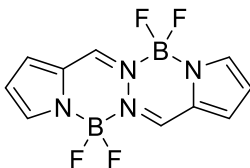
Figure 6.1: Core structure of BOPHY dyes.

This gives BOPHYs a very stable π-conjugated core structure and desirable optical properties, such as high molar extinction coefficients (80,000-100,000 M^{-1} cm^{-1}) and quantum yields (around 70-80%). Also, BOPHYs can easily be prepared via a two-step one-pot synthesis in water or common organic solvents, much alike BODIPYs. In recent years, BOPHYs have been tested in photonics, molecular machines, OLEDs, digital technologies and biological probes.[11–13] One of the earliest applications of BOPHY was given by Jiang and co-workers[14], who showed that the fluorescence behaviour is pH-dependent and therefore the dye could be used as a sensor.[3,15] Later, Mirloup and co-workers[16] developed bulk heterojunction solar cells based on thienyl-BOPHYs exhibiting broad absorption in the visible spectrum (400-800 nm). A further application of BOPHYs was achieved

by Sola-Llano and co-workers, who tested the dyes as singlet oxygen photosensitisers in photodynamic therapy (PDT) and more generally in diagnostics.[17]

Moreover, both BOPHYs and BODIPYs have been utilised in the construction of macromolecular architectures, where covalent attachment or self-assembly was pursued to achieve multi-dye systems with even broader applications than the aforementioned single dye cases. However, they both have limited photochemical stability, a drawback that has prompted research into effective strategies for improvements.[3] One of such strategies involves the use of macromolecular structures, where dyes are embedded into hosts. The latter could be organic or inorganic materials, the common trait being the ability to encapsulate small guests into suitable confined spaces. This is the strategy employed for BODIPY dyes that has been described in the previous chapter. Therein, the results showed that new host-guest antenna materials can be made by introducing the dyes from the start of the assembly process and, in particular, by trapping them inside the templates used for making mesoporous silica.

6.1.1 Aims of this chapter

This chapter will present new silica-based optical antennae, obtained from a different assembly strategy than that used in Chapter 5: here, BOPHY dyes are incorporated into the m-SiO$_2$ framework itself rather than in the micellar template. The structural and light absorption/emission properties will also be discussed and compared with those of the free dye, in order to evaluate whether the new materials possess improved optical properties.

Two BOPHY derivatives have been used for this study, as shown in **Figure 6.2**. BOPHY 1 bears an alkoxysilane side group, whereas BOPHY 2 possesses two of them. The use of each dye was expected to have a different impact on the structure of the PMO materials built from them and also on their luminescence behaviour.
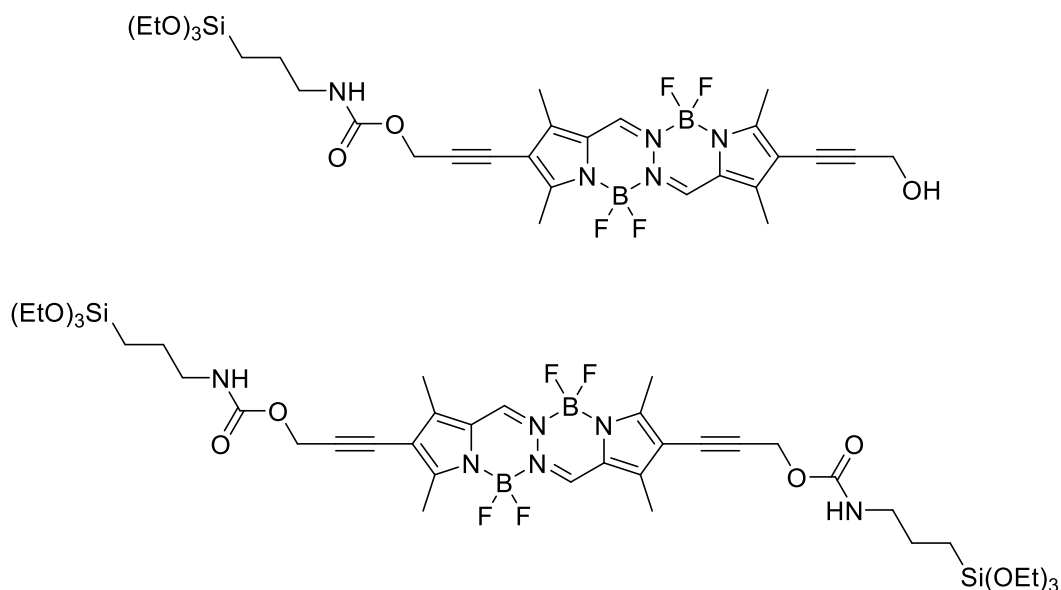
Figure 6.2: Structure of BOPHY 1 (top) and BOPHY 2 (bottom).

6.2   Results and Discussion

6.2.1   The BOPHY precursor: synthesis and optical properties

The dyes used in this chapter, including the precursor OA185 (**Figure 6.3**), were obtained from our research collaborator (Omar Al-Atawi) working with Dr Julian Knight, Newcastle University. The synthesis was carried out according to published literature procedures.[3,4,10,11]
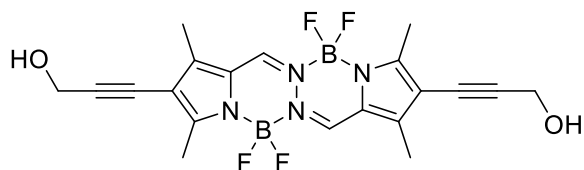
Figure 6.3: Structure of the reference BOPHY dye (OA185).

The structural manipulations of the BOPHY dye through the extension of the π-conjugation using either commercially available or synthesised pyrrole has been reported to fine-tune the optical properties of this complex.[3] The UV-visible spectra presented here (**Figure 6.4**) are measured from

146

a diluted solution of the free precursor OA185, and they are used as a reference for the PMO materials discussed later.
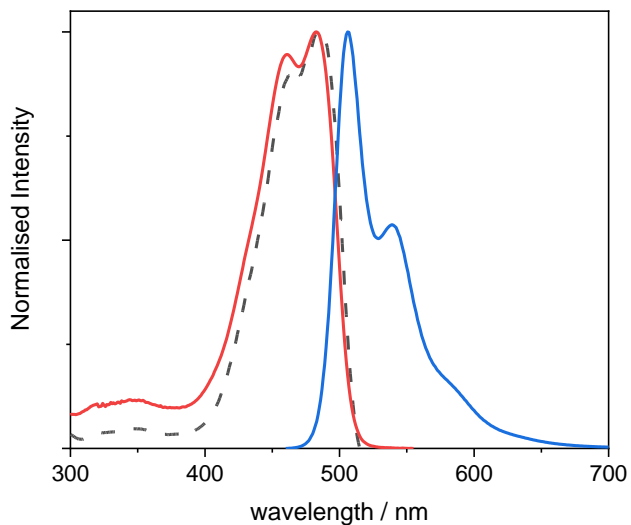
Figure 6.4: Normalised UV-visible absorption (red), excitation (dotted black) and emission (blue) spectra of OA185, recorded from 10^{-6} M THF solutions; excitation was measured at λ_{em} = 540 nm, and emission was measured using λ_{exc} = 440 nm.

The reference BOPHY in tetrahydrofuran (THF) shows two distinct absorption peaks with λ_{max} at 467 nm and 487 nm, with a molar extinction coefficient of 44,264 M^{-1} cm^{-1}. The absorption appears to be slightly red-shifted as compared with the unfunctionalised BOPHY (see **Figure 6.1**), and it is in good agreement with a previous study by Boodts and co-workers.[3,11] The structured shape of the absorption reveals the vibronic progression within the $S_0 \rightarrow S_1$ electronic transition and it confirms the rigidity of the dye.

The photoluminescence emission spectrum also exhibits a structured profile, with peaks at 506 nm and 539 nm and a small Stokes shift of 19 nm with the lowest-energy absorption peak. This confirms that the molecule undergoes small geometric changes between absorption and emission, with little energy lost through vibration at the excited state.[18] Indeed, the fluorescence quantum yield is high (0.86). The excited state lifetime was also measured (see **Appendix 6.1**) and its value of 2.8 ns is in line with typical singlet decays from organic fluorophores.

Dye Silylation

As most BOPHY dyes, OA185 can be functionalised at the α, β and meso positions. In order to incorporate the dye inside the silica framework, alkoxysilane groups were introduced at the β position only (BOPHY 1) and at both β, β^I positions (BOPHY 2). The alkoxysilylation was achieved in two steps: first, by reaction of OA185 with propargyl alcohol (1 equivalent to make BOPHY 1 or 2 equivalents for BOPHY 2), using [1,1′bis(diphenylphosphino)ferrocene]dichloropalladium(II) as a catalyst, all under reflux in dry THF; as a second step, the hydroxyl derivative is reacted with 3-(triethoxysilane)propyl isocyanate, in dry THF with trimethylamine as a base. The product obtained was not purified by column chromatography due to the strong affinity of the alkoxysilane group towards silica and was used straight away to avoid the decomposition of the final product, since most silylated dyes easily decompose, as reported in the literature.[12]

6.2.2 PMO materials with BOPHY 1

We adapted the templated synthetic procedure for MCM-41 silica described by Hoffman and co-workers (see also Chapter 1)[19] and loaded the two different silylated BOPHY into silica separately. As described earlier, BOPHY 1 and 2 are, respectively, mono and bis-silylated. They both undergo hydrolysis and poly-condensation jointly with TEOS,[20] but leading to different outcomes. The PMO materials made using BOPHY 1 have the chromophoric units dispersed through the solid network at the silica interface with the template (see **Figure 6.5**).
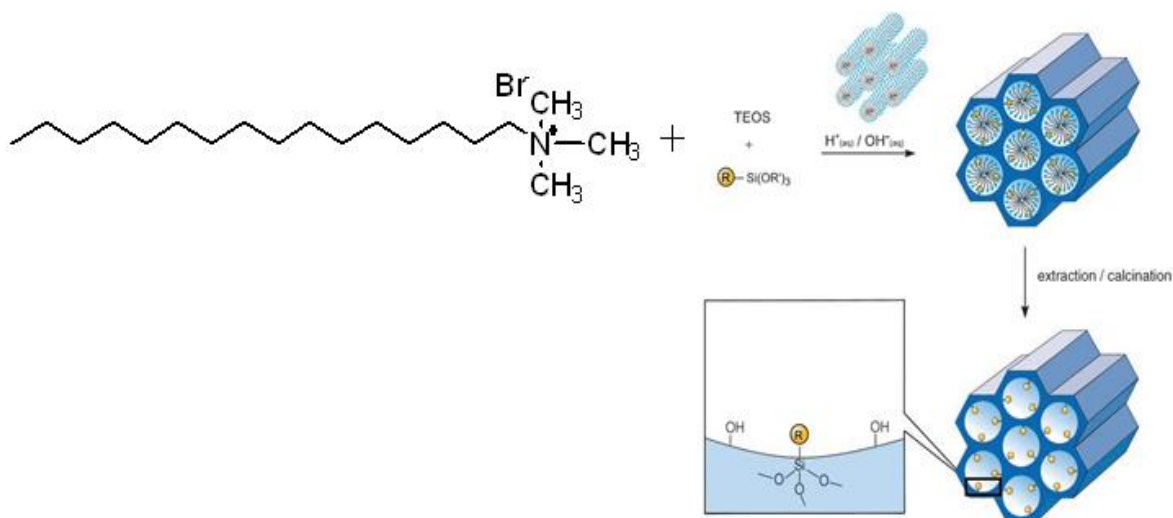
Figure 6.5: General synthetic route for the PMOs made using BOPHY 1; R= BOPHY core structure. Scheme from reference 19.

In order to obtain a homogeneous dispersion of the dye, the addition into the reaction mixture was made simultaneously with TEOS and it was facilitated by dissolving BOPHY 1 in the minimum amount of water with the aid of ultra-sounds. Co-condensation of both dye and TEOS was then allowed to proceed at 100^0 C for 24 hours (see Experimental **6.5.2** for the detailed procedure).

Structural Analysis

As reported in the previous chapters, the structure and the morphology of silica are often disrupted with the increase in the dye concentration, particularly in those cases where the dyes are bulky. BOPHY dyes are relatively small, instead, and we would not expect significant disruptions upon incorporation within the silica structure. Nevertheless, to avoid heavy structural deformations, low dye concentrations were used, with relative ratios BOPHY1:TEOS of 1%, 2% and 5%.
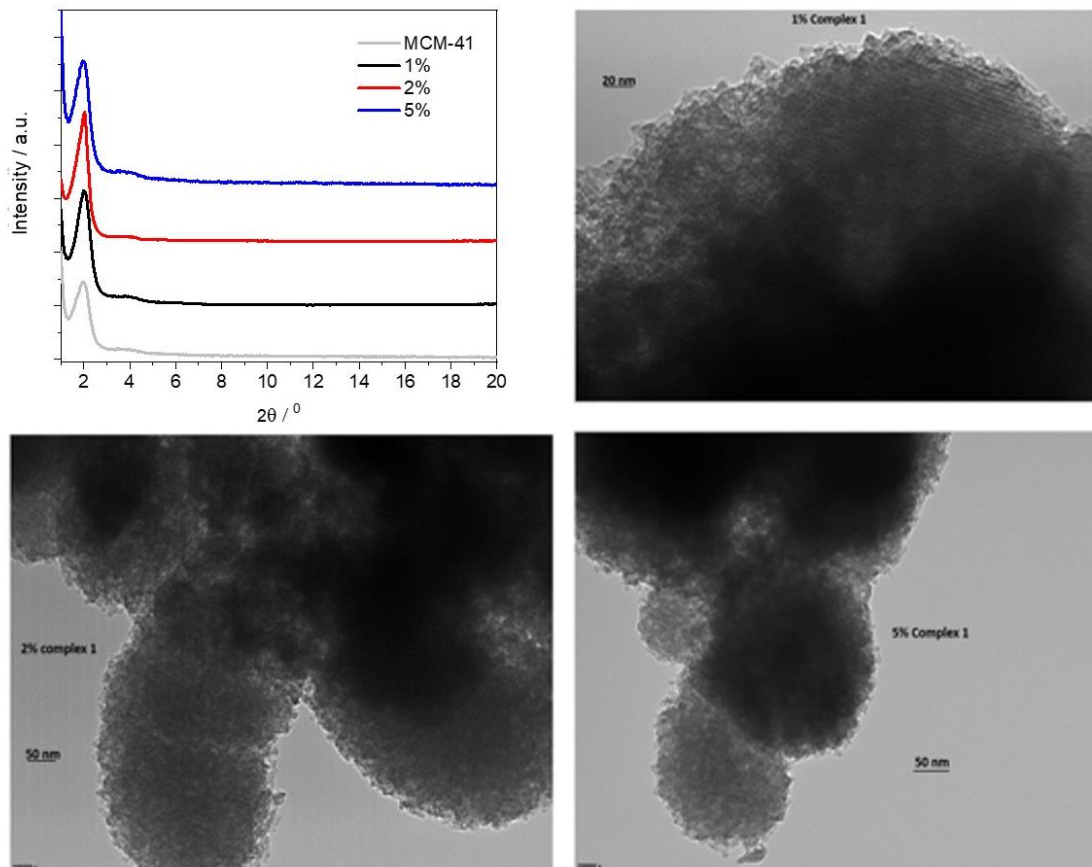
Figure 6.6: Powder X-ray diffraction patterns of the BOPHY1-PMO materials (top left); TEM images of 1% (top right), 2% (bottom left) and 5% (bottom right).

Powder XRD was then performed on the three PMO materials (see **Figure 6.6**) and revealed no changes in structure as compared with plain MCM-41 silica. All three PMOs have the main reflection from the (100) plane around the same 2θ values of 1.97°, which gives a d-spacing of 4.48 nm. It is even possible to observe the (110) reflection, although broad and weak, around 3.8°. This would indicate a certain degree of order in the long range.

The TEM images confirm that the porous structure remains unaltered, with only a slight reduction of the pores diameter, from about 5 nm in the 1% material to 4 nm in the 5%. Also, it can be observed that the particles morphology does not change with dye loading.

Photophysical Properties

The photoluminescence spectra of the three PMO materials were measured from 0.3 mg/mL suspensions in cyclohexane and are shown in **Figure 6.7**. No considerable changes were observed when compared with the free complex, except for an apparent blue-shift of the excitation peaks.
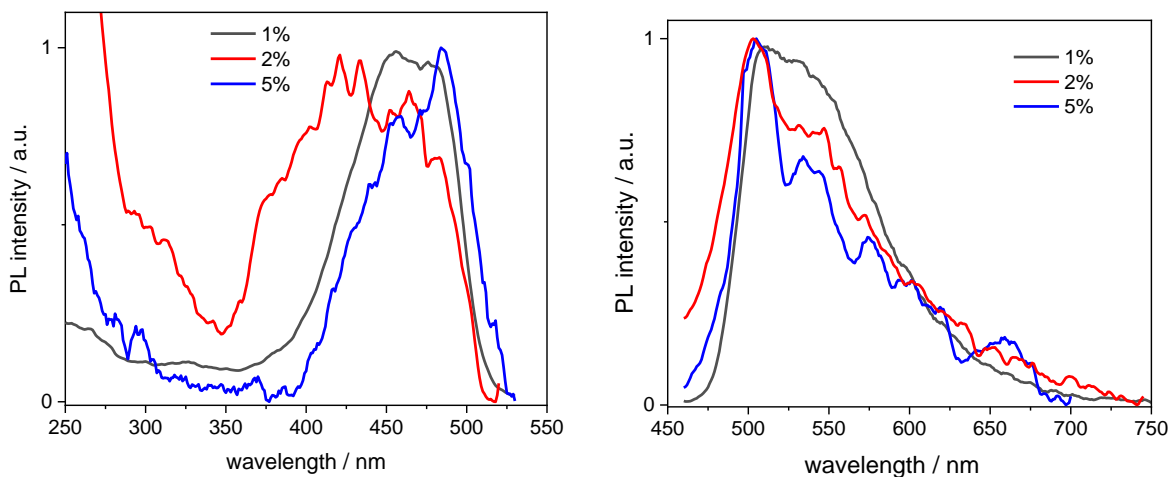
Figure 6.7: Normalised excitation (left) and emission (right) spetra of the BOPHY1-PMO samples, recorded from 0.3 mg mL^{-1} cyclohexane suspensions at λ_{em} = 540 nm and λ_{exc} = 420 nm, respectively.

This is particularly noticeable in the 1% sample, where the excitation maxima lie at 456 nm and 478 nm, about 10 nm blue-shifted in comparison with the free dye. As the loading increases, the excitation band broadens and this might be due to the closer proximity between single dye units, which causes aggregation. Such an effect is not as much pronounced in the emission spectra, which are very similar and match with that of the free dye. The fluorescence quantum yields, though, seem to indicate that the molecules do engage in some intermolecular processes of non-radiative deactivation, such as quenching, when the loading increases: the yields are reduced by a factor of 10 from a value of 0.3 at 1% loading (see also **Table 6.1**).

Table 6.1. Excited-state lifetimes, fluorescence quantum yields, radiative rate constants (k_r) and non-radiative rate constants (k_{nr}) of the BOPHY1-PMOs.

Sample	Decay Traces (Relative Weight)* [ns]	Average τ_{PL} [ns]	Φ_{PL}	k_r [s^{-1}]	k_{nr} [s^{-1}]
OA185	2.8	2.8	0.86	3.1×10^8	5.2×10^7
1%	2.6 (73%) – 11.3 (27%)	4.9	0.3	6.1×10^7	1.4×10^8
2%	2.7 (76%) – 12.6 (24%)	5.1	0.03	5.9×10^6	1.9×10^8
5%	2.3 (77%) – 10.5 (23%)	4.2	0.02	4.8×10^6	2.3×10^8

*Recorded at 540 nm for all samples, using a 475 nm laser excitation.

Vu and co-workers have previously reported a similar trend when studying the aggregation of BODIPY dyes in rigid matrices.[21] Aggregation between single units of dye can easily produce dimers or excimers, with partially overlapped spectra and shorter fluorescence lifetimes.

We then studied the deactivation dynamics occurring at the excited states via time-resolved fluorescence. The decay profiles are shown in **Figure 6.8** and are all fitted with biexponential functions. The overall trend sees the average lifetime decreasing with the loading and the short trace component is in good agreement with the decay of the free dye. Such trace undergoes a slight reduction to 2.3 ns in the 5% sample and this would be in line with previous findings on aggregated dyes mentioned above. It is worth mentioning also that other factors behind the lifetime decrease, besides aggregation, include the dye's environment, which in this case is a silica matrix and might cause the formation of non-fluorescent trap sites.[22–24]
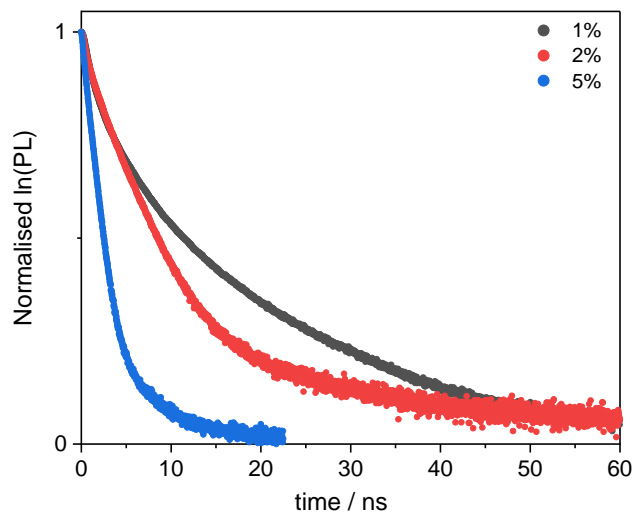
Figure 6.8: Excited state decay profiles of the BOPHY1-PMO samples, recorded at λ_{em} = 540 nm, using a 472 nm laser excitation.

Interestingly, a second, long decay trace emerges in the PMO materials, about 10-12 ns, which is not found when the dye is in diluted solution. This will be discussed in a broader context in the following section.

6.2.3 PMO materials with BOPHY 2

Differently from BOPHY 1, BOPHY 2 possesses two alkoxysilane side groups and its polycondensation with TEOS is expected to make the chromophoric core a bridging unit between the siloxanes (see **Figure 6.9**). This results in the dye becoming an integral part of the silica framework.[19]

The synthesis procedure for the BOPHY2-PMO materials was identical to that described in the previous section and, analogously, three samples were prepared, with 1%, 2% and 5% dye loading (see Experimental **6.5.3** for the detailed procedure).
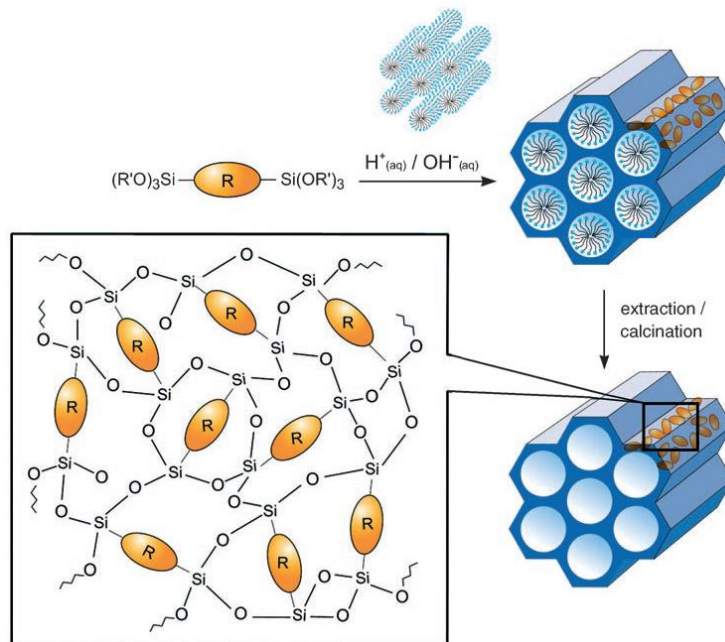
Figure 6.9: General synthetic route for the PMOs made using BOPHY 2; R= BOPHY core structure. Scheme from reference 19.

Structural Analysis

The powder XRD profiles of the three BOPHY2-PMO samples are shown in **Figure 6.10** (top left), in comparison with plain MCM-41 silica. Monitoring the (100) reflection at 1.97°, it is possible to notice a shift towards lower angles as the dye content in the material increases. From 1.97° at 1%, like in plain silica, the peak is observed at 1.92° in the 2% sample and at 1.71° in the 5%. This corresponds to a gradual increase in the d-spacing, from 4.48 to 4.60 nm, up to 5.16 nm at the highest content of dye. This is a remarkable difference in comparison with the BOPHY1-PMOs and it must be correlated to the silica formation mechanism. The trend with the d-spacing can be rationalised as a consequence of the expansion of the silica network during its formation and growth around the micellar template. The introduction into the reaction mixture of an increasing quantity of bis-silylated dye, which is bulkier than TEOS, forces the growing dye-silica network to swell and wrap less tightly around the template than when only TEOS is used.
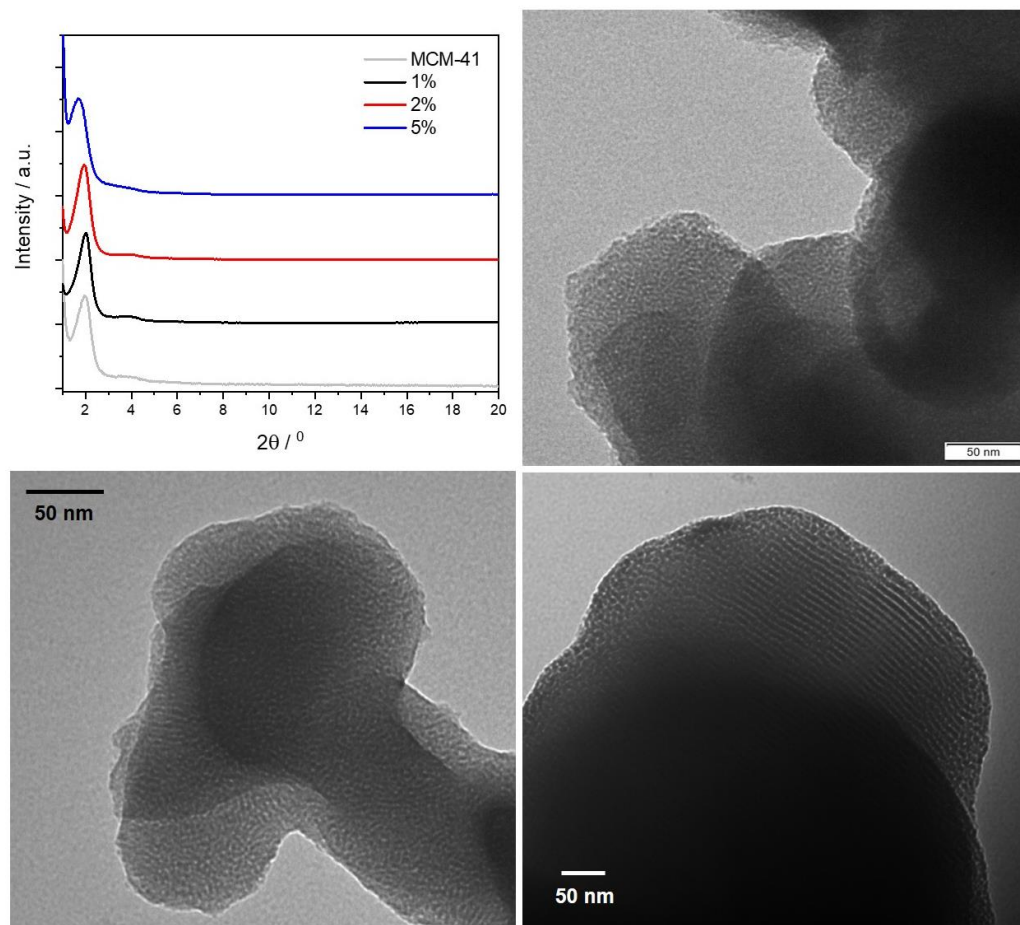
Figure 6.10: Powder X-ray diffraction patterns of the BOPHY2-PMO materials (top left); TEM images of 1% (top right), 2% (bottom left) and 5% (bottom right).

It is also worth mentioning that the secondary (110) reflection is visible around 3.8° and it appears to shift slightly to lower angles in the 5% sample. This would confirm that the network expansion reflects at all dimensions to a certain extent.

The TEM images are in line with the structure and the morphology typically observed for plain silica, with particle size in the 200-300 nm range. A close inspection of the pore size, although limited in accuracy by the relatively small dimensions, reveal a gradual increase in the average diameter, from 4.2 nm in the 1% sample, to 4.7 nm in the 2% and up to 6.7 nm in the 5%.

Photophysical Properties

The photoluminescence spectra of the BOPHY2-PMOs were recorded from diluted suspensions, as for the BOPHY1-PMOs and are shown in **Figure 6.11**. At 1% dye loading, both the excitation and the emission profiles, resemble those of the free dye, with the typical vibronic progression well visible.
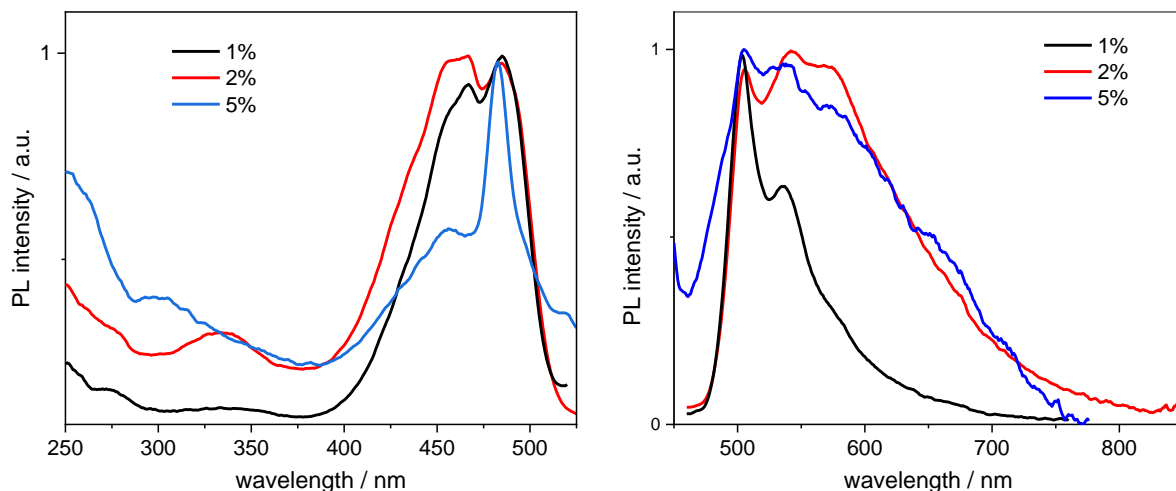
Figure 6.11: Normalised excitation (left) and emission (right) spetra of the BOPHY2-PMO samples, recorded from 0.3 mg mL^{-1} cyclohexane suspensions at λ_{em} = 540 nm and λ_{exc} = 420 nm, respectively.

As the dye loading doubles, one first change can be noticed, as the spectra broaden, particularly the emission. This could be due to the reduction in intensity of the first and the second vibronic transitions, at 505 and 540 nm in emission, respectively. A tight close-packing between dye units within the PMO framework is likely to affect the vibrational degrees of freedom of the chromophores and will hinder some. The effect is even more pronounced at 5% loading and the vibronic progression is almost lost. It should be noted that the sharp, symmetrical peak at 456 nm (blue line in **Figure 6.11**, left side) may well be due to light scattering from the particles and it masks the 0-0 transition.

The increasing concentration of dye units, which reduces the mutual distances, should be the reason for the reduction in fluorescence quantum yields from 22% to 4% (see **Table 6.2**). An interesting

trend is observed, instead, from the time-resolved measurements, so as in the BOPHY1-PMO samples. The excited-state lifetimes were recorded at the emission wavelenegth of 540 nm (**Figure 6.12**) and two decay traces were obtained, the shorter of which matches with the lifetime of the free BOPHY.
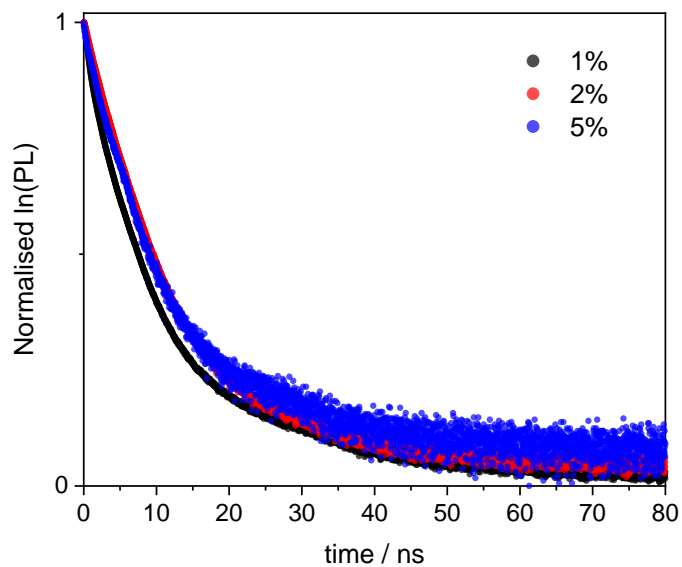
Figure 6.12: Excited state decay profiles of the BOPHY2-PMO samples, recorded at λ_{em} = 540 nm, using a 472 nm laser excitation.

Table 6.2. Excited-state lifetimes, fluorescence quantum yields, radiative rate constants (k_r) and non-radiative rate constants (k_{nr}) of the BOPHY2-PMOs.

Sample	Decay Traces (Relative Weight)* [ns]	Average τ_{PL} [ns]	Φ_{PL}	k_r [s⁻¹]	k_{nr} [s⁻¹]
OA185	2.8	2.8	0.86	3.1×10^8	5.2×10^7
1%	2.5 (80%) – 13.0 (20%)	4.6	0.22	4.8×10^7	1.7×10^8
2%	2.7 (75%) – 12.6 (25%)	4.9	0.07	1.4×10^7	1.9×10^8
5%	2.9 (48%) – 14.0 (52%)	8.6	0.04	4.7×10^6	1.1×10^8

*Recorded at 540 nm from 0.3 mg/ml cyclohexane suspensions, using a 375 nm laser excitation.

The second component is longer than 12 ns and could hardly be justified as prompt fluorescence from isolated units of dyes. Excluding any impurities after repeated synthesis and measurements in water suspensions, it was then hypothesised that a form of delayed fluorescence may originate within the hybrid dye-silica structure. Such behaviour is similar to that reported in Chapter 4, where PMO materials built from zinc(II) quinolinolates showed charge-recombination luminescence. The phenomenon was ascribed to the strong charge-transfer character of the quinolinolates and the preliminary findings on the BOPHY-PMOs presented in this chapter seem to point at an analogous trend. Further investigation would be required to confirm the hypothesis, by means of electrochemical studies.

In addition to this, it is possible to observe the emergence of a low-energy shoulder band in the 5% sample, both in excitation, around 517 nm, and in emission, at 650 nm. To investigate this further, an excitation spectrum at $\lambda_{em} = 650$ nm was recorded, together with an excited state lifetime at the same wavelength (see **Appendix 6.6** and **6.7**). The excitation profile does not provide conclusive evidence of a clear peak a long wavelengths and only few weak side bands can be noted up to 570 nm. Whether they could be a sign of ground state aggregates or an effect of scattering it is difficult

to state. The fluorescence lifetime of the 5% sample, though, gives an indication of a short decay at 650 nm. Along with the traces shown in Table 6.2, a third component was detected, which fits with a 0.8 ns lifetime. This can be tentatively attributed to an aggregated species, most likely a ground-state aggregate of J-type. Such species typically show red-shifted spectral features compared to the monomers and their formation is favoured in planar conjugated molecules.[21]

6.2.4   Fluorescence Anisotropy Studies

It was precisely because the chromophores in question have a conjugated linear structure, along which the dipole moment is oriented, that it was decided to investigate the PMOs further, using fluorescence anisotropy.

As for the materials discussed in the previous chapter, the BOPHY-PMO samples were analysed in the solid state, from thin powder films. As the starting point, the emission and excitation spectra at different orientations (vertical and horizontal) were first measured, to determine the G-factor and evaluate the anisotropic photoresponse of the molecules in the PMOs. All three BOPHY2-PMOs showed such a response and measurable kinetic traces, whereas among the BOPHY1-PMOs only the 1% yielded some evidence of polarisation transfer. Two of the four samples also show different spectral features at each orientation; the 5% BOPHY2-PMO is shown in **Figure 6.13** as the most representative, while the spectra from the other samples can be found in **Appendix 6.8-6.10**.
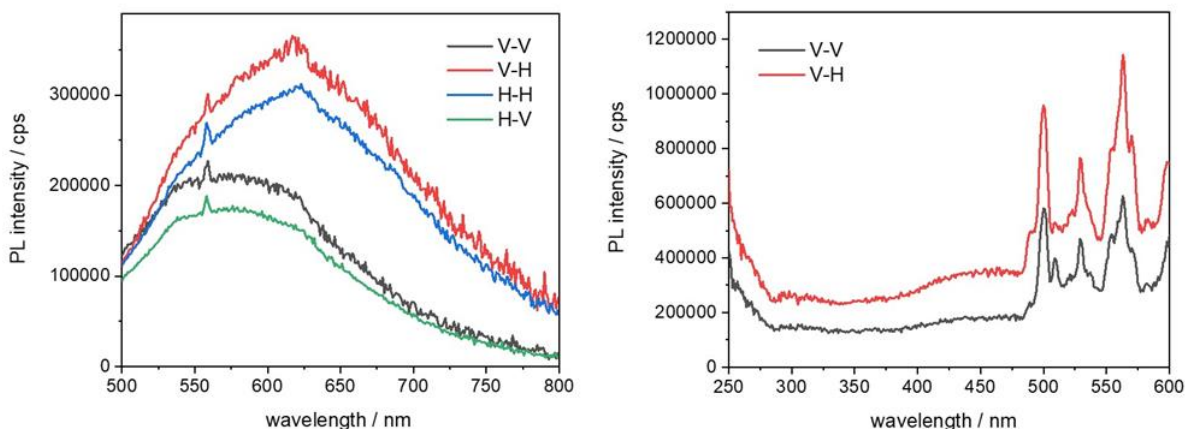
Figure 6.13: Emission (left) and excitation (right) anisotropy spectra of the 5% BOPHY2-PMO, recorded at $\lambda_{exc} = 470$ nm and $\lambda_{em} = 620$ nm, respectively, from a powder thin film; the notation in the legend indicates the plane-polarisation of the excitation and the emission light beam. G-factor $= 2.45$ at 620 nm.

A predominant fraction of dye units seems to be aligned in a preferred orientation, especially in the BOPHY2-PMOs, where the chromophores are an integral part of the framework and are arranged more rigidly than in the BOPHY1-PMOs, where the dyes are still part of the silica material but relatively less rigid, as they are located on the PMO surface. Nevertheless, it was possible to detect anisotropic emission for one of such samples, the 1% BOPHY1-PMO, and a polarisation transfer trace, of about 812 ps (see **Appendix 6.11**).

The excited-state anisotropy decays of the BOPHY2-PMOs are shown in **Figure 6.14**.

160
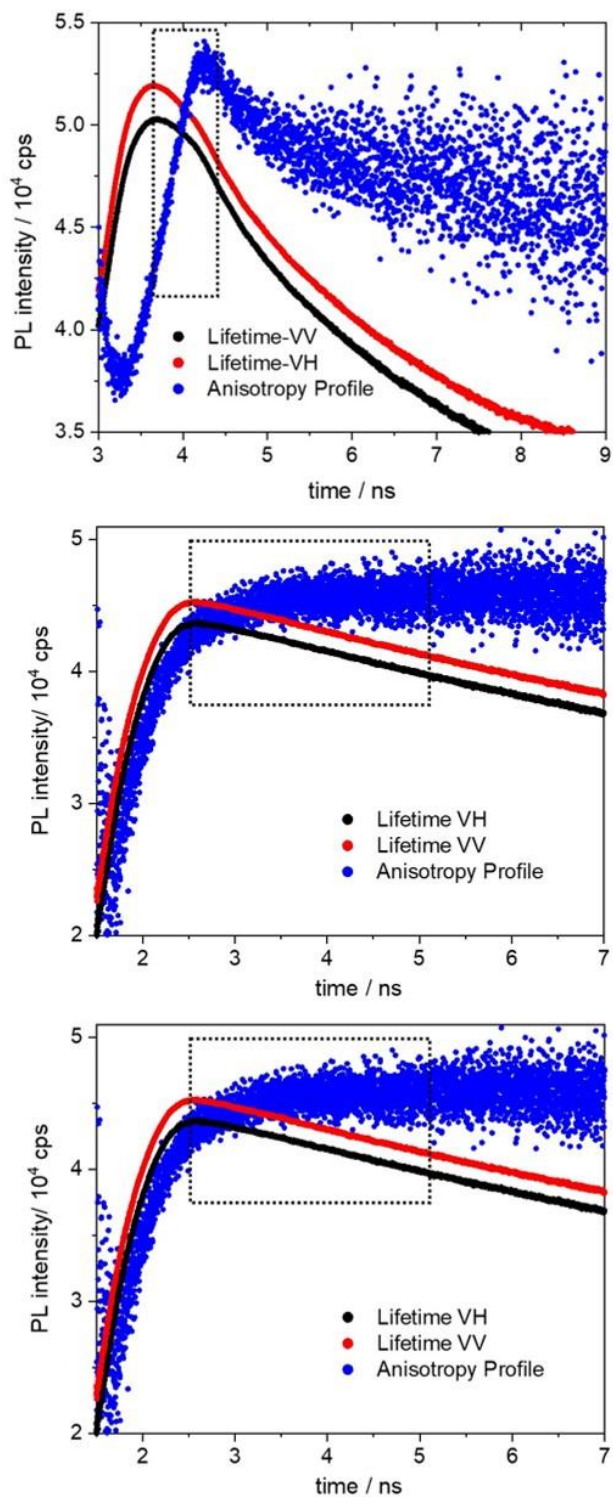
Figure 6.14: Fluorescence anisotropy decay profiles (black and red) of the 1% (top), 2% (middle) and 5% (bottom) BOPHY2-PMO, recorded at 560 nm. The blue profiles are the anisotropy curves generated from the respective decays.

The polarisation transfer time in the 1% BOPHY2-PMO sample is the longest (783 ps) in the series. As the dye loading increases, the transfer time decreases, to 448 ps in the 2% and to 395 ps in the 5% sample. This can be ascribed as an effect of the decreasing distance between units of BOPHY dyes within the PMO framework.

The above time traces are interpreted as the times of excitation energy migration between neighbouring BOPHY units. As the excitation energy is transferred across the material, the emitted light gradually changes its orientation in comparison with the excitation direction and the recorded kinetic profile accounts for the overall timescale of such process.[25-29]

6.3   Conclusions

The synthesis of new PMO materials containing a novel BOPHY dye was successfully achieved. Two different derivatives were used as precursor, one bearing an alkoxysilane group and one bearing two of them, and they were incorporated within the walls of mesoporous silica at relatively low concentrations, up to 5% dye loading.

The structure and the morphology of the new PMOs was analysed using powder XRD and TEM, which proved they are ordered materials, featuring the hexagonal pore arrangement and pore size of a typical MCM-41. The optical study on the materials shows that the fluorescence quantum yields decrease with the dye content within the solid structure, which is attributed to an enhanced non-radiative decay deactivation. The fluorescence anisotropy experiments revealed that all materials show polarised light emission, and, for most samples, it was also possible to determine the polarisation transfer time. This appeared as a very short kinetic trace, decreasing from around 800 to 400 ps as the dye loading increases. This can be attributed to the decreasing distances between single units of BOPHY dyes in the materials, which causes the excitation energy to migrate at an increasingly faster rate. Such property makes the new PMOs very interesting candidates for use as solid-state light-harvesters and sensitisers, although their fluorescence yields require further optimisation. Moreover, the emergence of charge-recombination luminescence in the materials opens the way to future studies on electroluminescence and to develop new hybrid OLEDs.

6.4 Experimental Section

6.4.1 Synthesis and Characterisation of the BOPHY dyes

As stated in section 6.2.1, the BOPHY precursor OA185 and the two silylated dyes BOPHY 1 amd BOPHY 2 were synthesised and characterised by a postgraduate student, Omar Alatawi, from Dr Julian Knight's group.

6.4.2 Synthesis of the MCM-41 with CTAB and BOPHY 1 (99:1, 98:2 and 95:5)

Cetyltrimethylammonium bromide was dissolved in 30 mL of water using an ultrasound bath. This is then followed by the addition of 2 molar NaOH (0.13 mL, 0.26 mmol). The solution was heated to 100^0 C. BOPHY 1 was dissolved in a minimal amount of water (6 mL) and added dropwise concurrently with TEOS (360 µL), forming a homogeneous turbid orange mixture. The mixture was refluxed for 2 hours, stopped and allowed to cool down to room temperature. The mixture was filtered under the vacuum and washed with water. The filtrate was dried in the desiccator, and a pink solid product was obtained that fluoresced lightly under a UV lamp. The CTAB and BOPHY 1 were added for each reaction in the following ratios; 99:1 (69.3 mg, 0.198 mmol and 1.39 mg, 2.00 µmol), 98:2 (68.6 mg, 0.196 mmol and 2.77 mg, 4.00 µmol) and 95:5 (66.5 mg, 0.190 mmol and 6.93 mg, 10.00 µmol).

6.4.3 Synthesis of the MCM-41 with CTAB and BOPHY 2 (99:1, 98:2 and 95:5)

Cetyltrimethylammonium bromide was dissolved in 30 mL of water using an ultrasound bath. This is then followed by the addition of 2 molar NaOH (0.13 mL, 0.26 mmol). The solution was heated to 100^0 C. BOPHY 2 was dissolved in a minimal amount of water (6 mL) and added dropwise concurrently with TEOS (360 µL), forming a homogeneous turbid orange mixture. The mixture was refluxed for 2 hours, stopped and allowed to cool down to room temperature. The mixture was filtered under the vacuum and washed with water. The filtrate was dried in the desiccator, and a pink solid product was obtained that fluoresced lightly under a UV lamp. The CTAB and BOPHY 2 were added for each reaction in the following ratios; 99:1 (69.3 mg, 0.198 mmol and 1.88 mg, 2.00 µmol), 98:2 (68.6 mg, 0.196 mmol and 3.76 mg, 4.00 µmol) and 95:5 (66.5 mg, 0.190 mmol and 9.4 mg, 10.00 µmol).

References

(1) Frath, D.; Benelhadj, K.; Munch, M.; Massue, J.; Ulrich, G. Polyanils and Polyboranils: Synthesis, Optical Properties, and Aggregation-Induced Emission. *J. Org. Chem.* **2016**, *81* (20), 9658–9668.

(2) Qian, H.; Wang, Y.-Y.; Guo, D.-S.; Aprahamian, I. Controlling the Isomerization Rate of an Azo-BF2 Switch Using Aggregation. *J. Am. Chem. Soc.* **2017**, *139* (3), 1037–1040.

(3) Bismillah, A. N.; Aprahamian, I. Fundamental Studies to Emerging Applications of Pyrrole-BF $_2$ (BOPHY) Fluorophores. *Chem. Soc. Rev.* **2021**, *50* (9), 5631–5649.

(4) Lv, X.; Li, T.; Wu, Q.; Yu, C.; Jiao, L.; Hao, E. Polybrominated BOPHY Dyes: Synthesis, Reactivity, and Properties. *J. Org. Chem.* **2018**, *83* (3), 1134–1145.

(5) Ulrich, G.; Goze, C.; Guardigli, M.; Roda, A.; Ziessel, R. Pyrromethene Dialkynyl Borane Complexes for "Cascatelle" Energy Transfer and Protein Labeling. *Angew. Chem.* **2005**, *117* (24), 3760–3764.

(6) Loudet, A.; Burgess, K. BODIPY Dyes and Their Derivatives: Syntheses and Spectroscopic Properties. *Chem. Rev.* **2007**, *107* (11), 4891–4932.

 (7) Hagfeldt, A.; Boschloo, G.; Sun, L.; Kloo, L.; Pettersson, H. Dye-Sensitized Solar Cells. *Chem. Rev.* **2010**, *110* (11), 6595–6663.

(8) Hapuarachchige, S.; Montaño, G.; Ramesh, C.; Rodriguez, D.; Henson, L. H.; Williams, C. C.; Kadavakkollu, S.; Johnson, D. L.; Shuster, C. B.; Arterburn, J. B. Design and Synthesis of a New Class of Membrane-Permeable Triazaborolopyridinium Fluorescent Probes. *J. Am. Chem. Soc.* **2011**, *133* (17), 6780–6790.

(9) Zang, L. Interfacial Donor–Acceptor Engineering of Nanofiber Materials To Achieve Photoconductivity and Applications. *Acc. Chem. Res.* **2015**, *48* (10), 2705–2714.

(10) Li, X.; Ji, G.; Son, Y.-A. Tunable Emission of Hydrazine-Containing Bipyrrole Fluorine–Boron Complexes by Linear Extension. *Dyes Pigments* **2016**, *124*, 232–240.

(11)   Boodts, S.; Fron, E.; Hofkens, J.; Dehaen, W. The BOPHY Fluorophore with Double Boron Chelation: Synthesis and Spectroscopy. *Coord. Chem. Rev.* **2018**, *371*, 1–10.

(12)   Li, X.; Ji, G.; Son, Y.-A. Tunable Emission of Hydrazine-Containing Bipyrrole Fluorine–Boron Complexes by Linear Extension. *Dyes Pigments* **2016**, *124*, 232–240.

(13)   Nemykin, V.; Rhoda, H.; Chanawanno, K.; King, A.; Zatsikha, Y.; Ziegler, C. Unusually Strong Long-Distance Metal-Metal Coupling in Bis(Ferrocene)-Containing BOPHY: Introduction to Organometallic BOPHYs. *Chem. Weinh. Bergstr. Ger.* **2015**, *21*.

(14)   Jiang, X.-D.; Su, Y.; Yue, S.; Li, C.; Yu, H.; Zhang, H.; Sun, C.-L.; Xiao, L.-J. Synthesis of Mono-(p-Dimethylamino)Styryl-Containing BOPHY Dye for a Turn-on PH Sensor. *RSC Adv.* **2015**, *5* (22), 16735–16739.

(15)   Chen, Y.; Qi, D.; Zhao, L.; Cao, W.; Huang, C.; Jiang, J. Boron–Phenylpyrrin Dyes: Facile Synthesis, Structure, and PH-Sensitive Properties. *Chem. – Eur. J.* **2013**, *19* (23), 7342–7347.

(16)   Mirloup, A.; Huaulmé, Q.; Leclerc, N.; Lévêque, P.; Heiser, T.; Retailleau, P.; Ziessel, R. Thienyl-BOPHY Dyes as Promising Templates for Bulk Heterojunction Solar Cells. *Chem. Commun.* **2015**, *51* (79), 14742–14745.

(17)   Sola-Llano, R.; Jiménez, J.; Avellanal-Zaballa, E.; Johnson, M.; Cabreros, T. A.; Moreno, F.; Maroto, B. L.; Muller, G.; Bañuelos, J.; Cerdán, L.; García-Moreno, I.; Moya, S. de la. BOPHYs versus BODIPYs: A Comparison of Their Performance as Effective Multi-Function Organic Dyes. *Dyes Pigments* **2019**, *170*, 107662.

(18)   Montalti, M.; Credi, A.; Prodi, L.; Gandolfi, M. T. *Handbook of Photochemistry*, 3rd ed.; CRC Press: Boca Raton, 2006.

(19)   Hoffmann, F.; Cornelius, M.; Morell, J.; Fröba, M. Silica-Based Mesoporous Organic–Inorganic Hybrid Materials. *Angew. Chem. Int. Ed.* **2006**, *45* (20), 3216–3251.

(20)   Grösch, L.; Lee, Y. J.; Hoffmann, F.; Fröba, M. Light-Harvesting Three-Chromophore Systems Based on Biphenyl-Bridged Periodic Mesoporous Organosilica. *Chem. - Eur. J.* **2015**, *21* (1), 331–346.

(21)   Vu, T. T.; Dvorko, M.; Schmidt, E. Y.; Tro, B. A. Understanding the Spectroscopic Properties and Aggregation Process of a New Emitting Boron Dipyrromethene (BODIPY). *J Phys Chem C* **2013**, 13.

(22)   Meallet-Renault, R.; Herault, A.; Vachon, J.-J.; Pansu, R. B.; Amigoni-Gerbier, S.; Larpent, C. Fluorescent Nanoparticles as Selective Cu(II) Sensors. **2006**, 11.

(23)   Boulu, L. G. Theoretical Investigation of Fluorescence Concentration Quenching in Two-Dimensional Disordered Systems. Application to Chlorophyll a in Monolayers of Dioleylphosphatldylchollne. **1987**, *86*, 5.

(24)   Santos, M. B. On the Distribution of the Nearest Neighbor. 4.

(25)   López Arbeloa, F.; Martínez Martínez, V.; Arbeloa, T.; López Arbeloa, I. Photoresponse and Anisotropy of Rhodamine Dye Intercalated in Ordered Clay Layered Films. *J. Photochem. Photobiol. C Photochem. Rev.* **2007**, *8* (2), 85–108.

(26)   Grauer, Z.; Avnir, D.; Yariv, S. Adsorption Characteristics of Rhodamine 6G on Montmorillonite and Laponite, Elucidated from Electronic Absorption and Emission Spectra. *Can. J. Chem.* **1984**, *62* (10), 1889–1894.

(27)   Breen, C.; Rock, B. The Competitive Adsorption of Methylene Blue on to Montmorillonite from Binary Solution Wih Thioflavin T, Proflavine and Acridine Yellow. Steady-State and Dynamic Studies. *Clay Miner.* **1994**, *29* (2), 179–189.

(28)   Berberan-Santos, M. N.; Nunes Pereira, E. J.; Martinho, J. M. G. Stochastic Theory of Molecular Radiative Transport. *J. Chem. Phys.* **1995**, *103* (8), 3022–3028.

(29)   Nunes Pereira, E. J.; Berberan-Santos, M. N.; Martinho, J. M. G. Molecular Radiative Transport. II. Monte-Carlo Simulation. *J. Chem. Phys.* **1996**, *104* (22), 8950–8965.
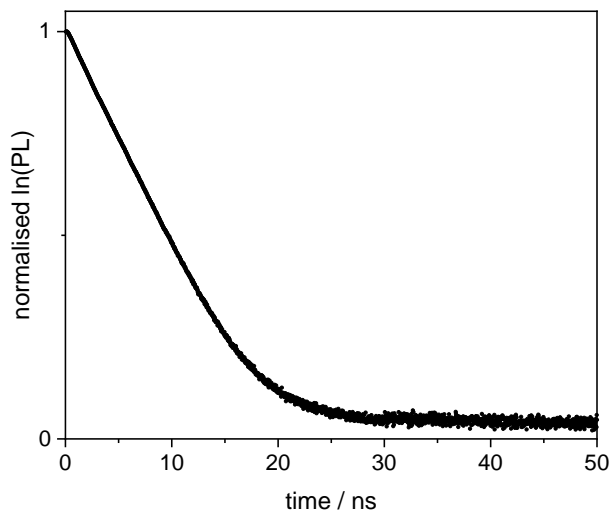
Appendix 6.1: Excited state decay of the BOPHY dye OA185, recorded at 540 nm from a 10^{-6} M THF solution, using a 472 nm laser excitation.
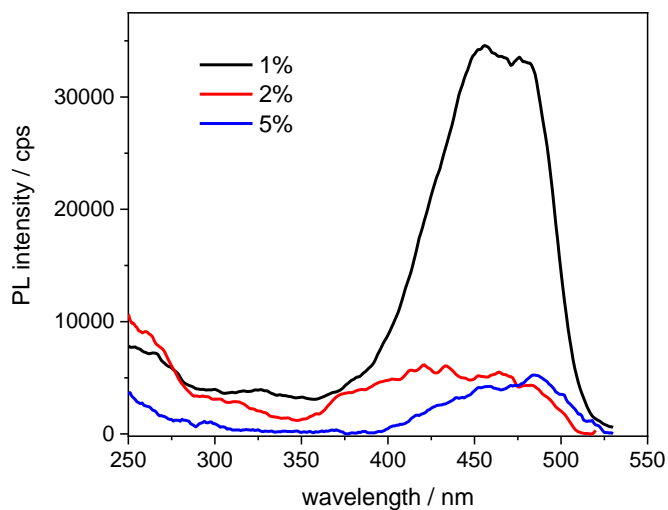
Appendix 6.2: Excitation spectra of the BOPHY1-PMO materials, recorded from 0.3 mg mL^{-1} cyclohexane suspensions at $\lambda_{em} = 540$ nm.
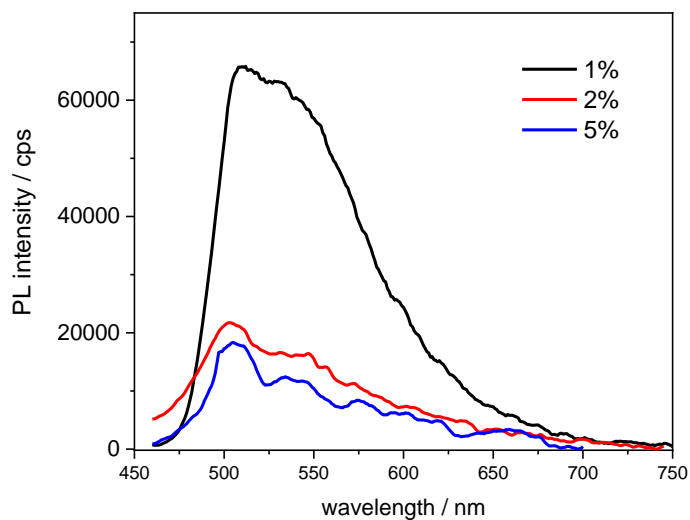
Appendix 6.3: Emission spectra of the BOPHY1-PMO materials, recorded from 0.3 mg mL^{-1} cyclohexane suspensions at λ_{exc} = 420 nm.

Appendix 6.4: Excitation spectra of the BOPHY2-PMO materials, recorded from 0.3 mg mL^{-1} cyclohexane suspensions at λ_{em} = 540 nm.
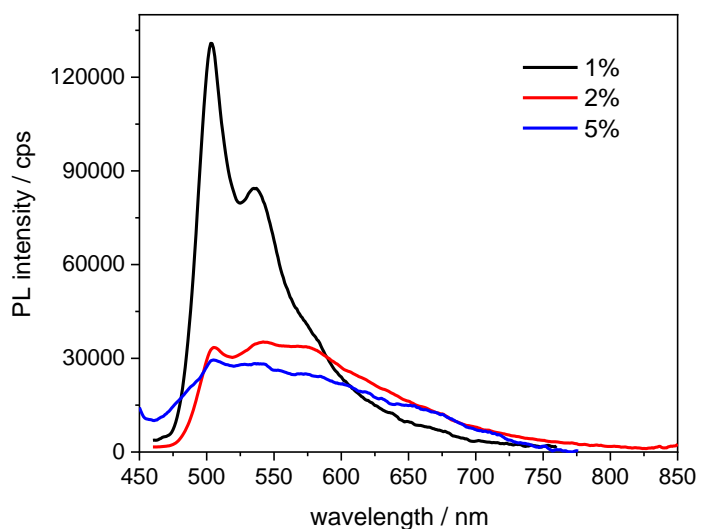
Appendix 6.5: Emission spectra of the BOPHY2-PMO materials, recorded from 0.3 mg mL^{-1} cyclohexane suspensions at $\lambda_{exc} = 420$ nm.
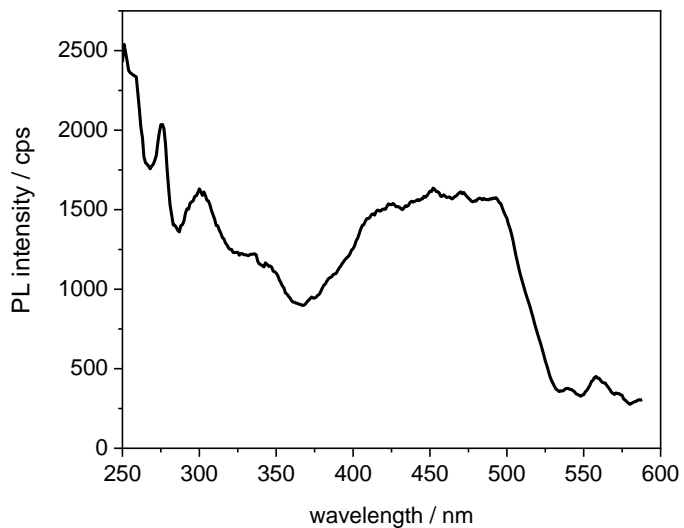
Appendix 6.6: Emission spectra of the BOPHY2-PMO material at 5% dye loading, recorded from a 0.3 mg mL^{-1} cyclohexane suspension at $\lambda_{em} = 620$ nm.
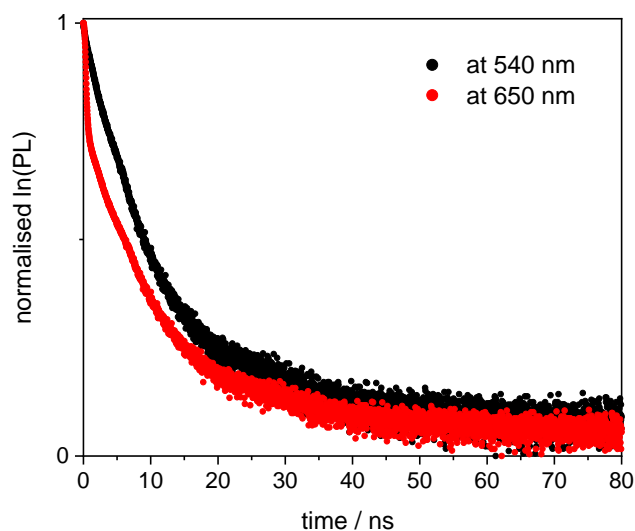
Appendix 6.7: Excited state decay profiles of the BOPHY2-PMO with 5% dye loading, recorded at λ_{em} = 540 nm and at 650 nm, using a 472 nm laser excitation.
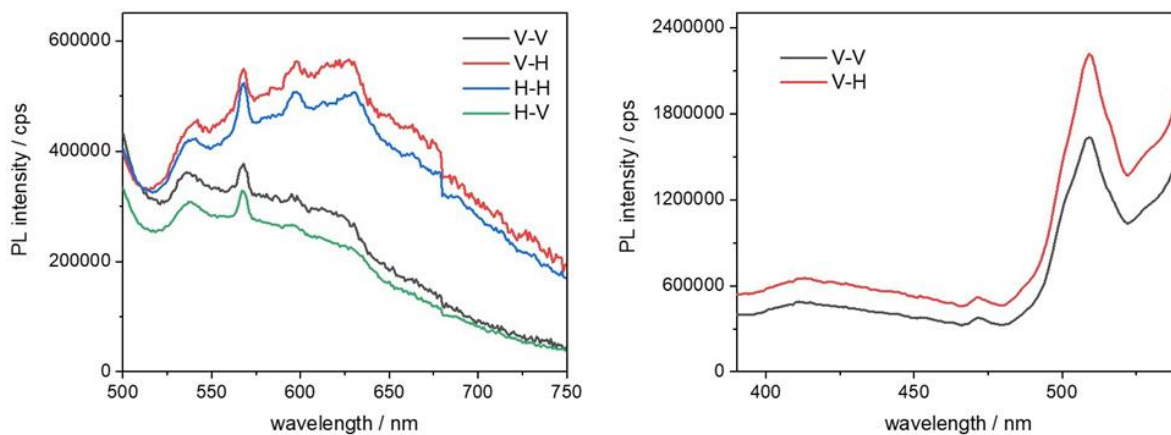
Appendix 6.8: Emission (left) and excitation (right) anisotropy spectra of the 1% BOPHY1-PMO, recorded at λ_{exc} = 480 nm and λ_{em} = 560 nm, respectively, from a powder thin film; the notation in the legend indicates the plane-polarisation of the excitation and the emission light beam. G-factor = 1.81 at 560 nm.
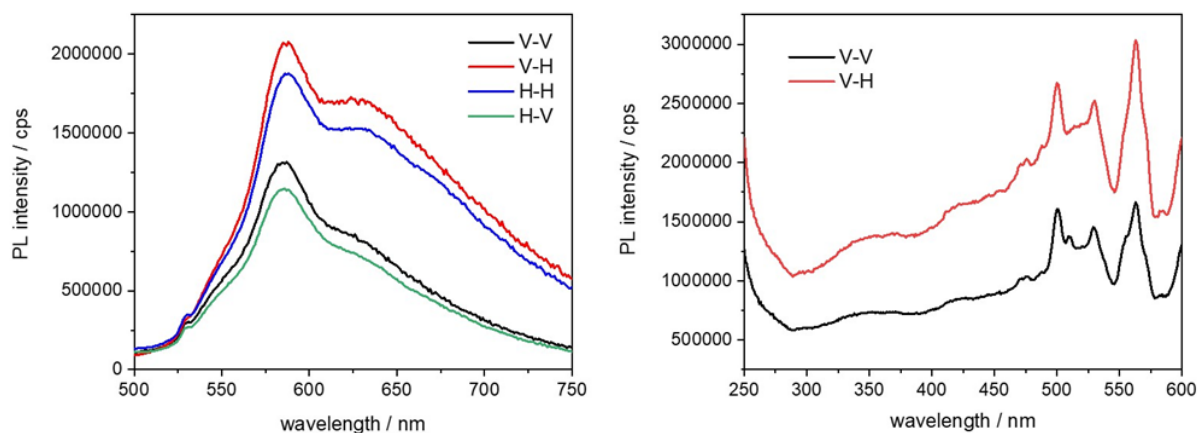
Appendix 6.9: Emission (left) and excitation (right) anisotropy spectra of the 1% BOPHY2-PMO, recorded at λ_{exc} = 440 nm and λ_{em} = 620 nm, respectively, from a powder thin film; the notation in the legend indicates the plane-polarisation of the excitation and the emission light beam. G-factor = 2.41 at 620 nm.
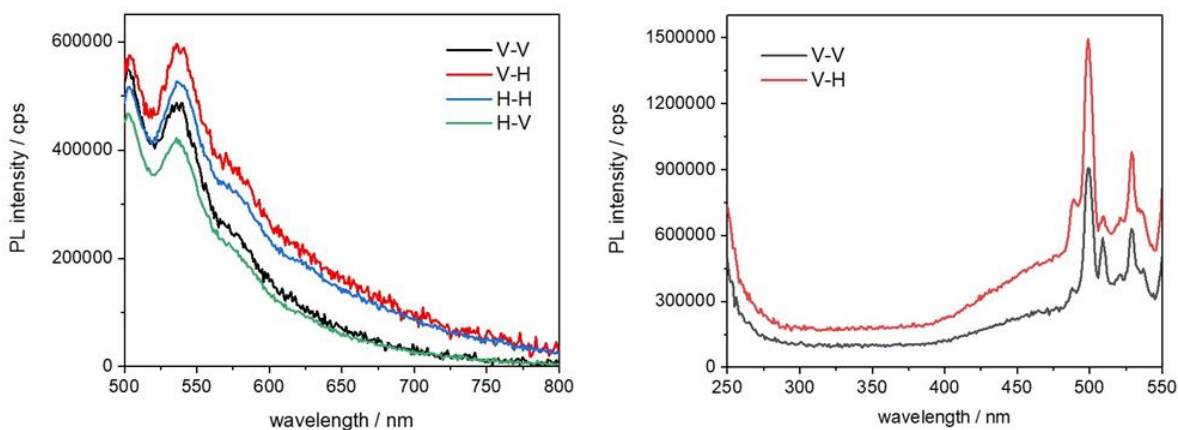
Appendix 6.10: Emission (left) and excitation (right) anisotropy spectra of the 2% BOPHY2-PMO, recorded at λ_{exc} = 470 nm and λ_{em} = 620 nm, respectively, from a powder thin film; the notation in the legend indicates the plane-polarisation of the excitation and the emission light beam. G-factor = 2.45 at 620 nm.

$$R(t) = B_1 e^{\left(-t/\tau_1\right)} + B_2 e^{\left(-t/\tau_2\right)} + B_3 e^{\left(-t/\tau_3\right)} + B_4 e^{\left(-t/\tau_4\right)}$$
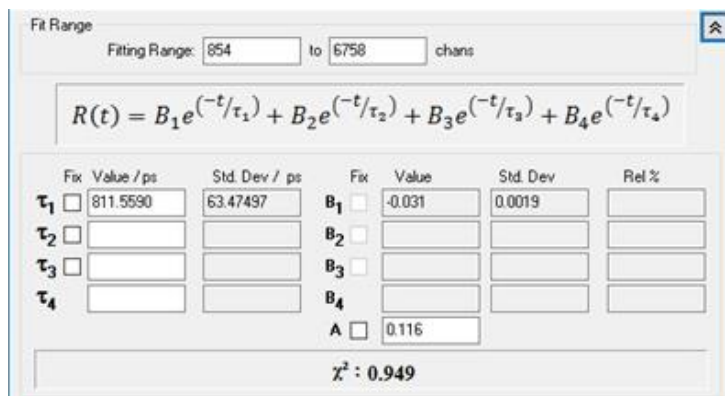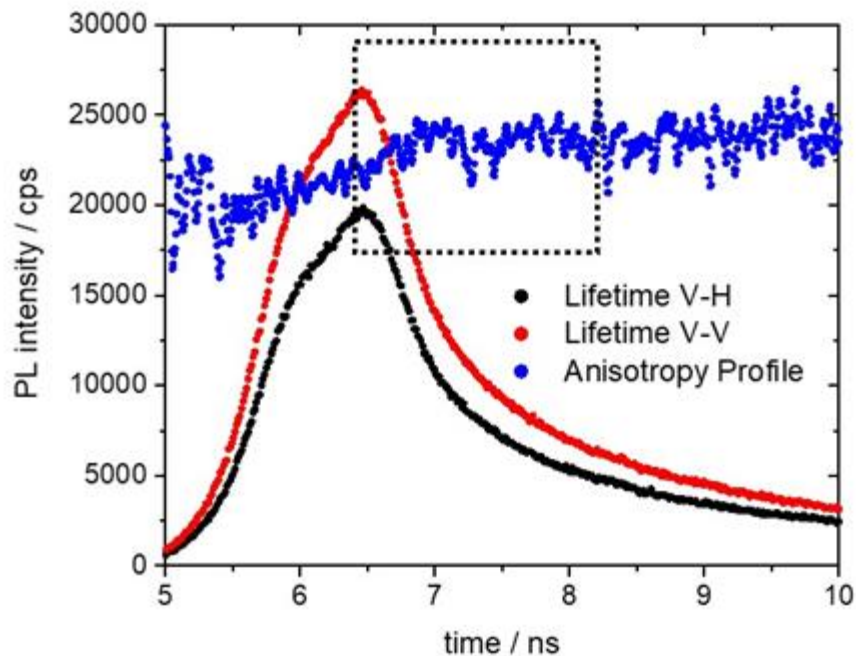
Appendix 6.11: Top: Fluorescence anisotropy decay profiles (black and red) of the 1% BOPHY1-PMO, recorded at 560 nm. The blue profile is the anisotropy curve generated from the two decays. Bottom: fitted time trace from the anisotropy profile, obtained in the range indicated by the dotted square in the top part.

	Fix	Value / ps	Std. Dev / ps		Fix	Value	Std. Dev	Rel %
τ_1	☐	783.3103	42.65389	B_1	☐	0.022	0.0004	100.00
τ_2	☐			B_2	☐			
τ_3	☐			B_3	☐			
τ_4				B_4				
				A	☐	0.207		

$$\chi^2 : 0.857$$

	Fix	Value / ps	Std. Dev / ps		Fix	Value	Std. Dev	Rel %
τ_1	☐	448.4824	5.38190	B_1	☐	-0.098	0.0011	
τ_2	☐			B_2	☐			
τ_3	☐			B_3	☐			
τ_4				B_4				
				A	☐	0.199		

$$\chi^2 : 0.855$$

	Fix	Value / ps	Std. Dev / ps		Fix	Value	Std. Dev	Rel %
τ_1	☐	394.5233	24.55005	B_1	☐	-0.021	0.0005	
τ_2	☐			B_2	☐			
τ_3	☐			B_3	☐			
τ_4				B_4				
				A	☐	0.061		

$$\chi^2 : 1.005$$

Appendix 6.12: Fitted time traces from the anisotropy profiles shown in Figure 6.14, obtained in the ranges indicated by the dotted squares. Top: 1% BOPHY2-PMO; middle: 2% BOPHY2-PMO; bottom: 5% BOPHY2-PMO.

Chapter 7: Summary

Summary

This research thesis presented the use of mesoporous silica to develop new light-harvesting antennae using host-guest chemistry. The rigid host with in-built micellar templates has been used to control the spatial arrangement of the guest dyes and improve their optical properties. The work started with the study of new organic and organometallic dye molecules, which were characterised structurally by NMR and optically with a fluorimeter. Following such first step, new silica-based hybrid materials were built using the above dyes and then characterised both structurally, by TEM and powder XRD, and optically, in order to evaluate whether emergent properties could be observed, such as energy transfer.

Chapter one introduced the general concepts about the search for new light-harvesting materials, considering the broad context of the current global energy challenges and making reference to natural and artificial photosystems. Both systems depend on the successful collection and conversion of sunlight energy, which is granted by the high level of organisation of multiple donor and acceptor molecules. In artificial antennae, the arrangement of dye molecules can be achieved with different types of host materials, such as zeolites and mesoporous silica. The latter was used in the research work presented in this thesis, which focused on mesoporous MCM-41 and COK-12 silica materials, owing to their large surface areas available to guest molecules, ease of synthesis, relatively cheap precursors, high structural rigidity, and high chemical and thermal stability. The chapter also presented some different strategies for synthesising mesoporous silica with a guest molecule. The choice of surfactant and molecular precursors for the solid network determine the final structures and parameters like the pore size, which are peculiar for each of the two types of silica used in this thesis. For MCM-41, the surfactant is cetyltrimethylammonium bromide, with tetraethyl orthosilicate as the precursor, and the resulting pore diameter is between 3 and 4 nm. On the other hand, polypropylene-polyethene glycol (PPG-PEG) and sodium silicate are the surfactant and the precursor of choice for COK-12, respectively, with final pore diameters ranging between 6 and 8 nm. Four new light-harvesting materials have been made and studied in this thesis; two were derived from zinc(II) complexes and the other two from boron-based organic dyes, such as BODIPYs and BOPHYs. We limited our research to the choice of two organic ligands: dipyrromethenes and quinolinolates.
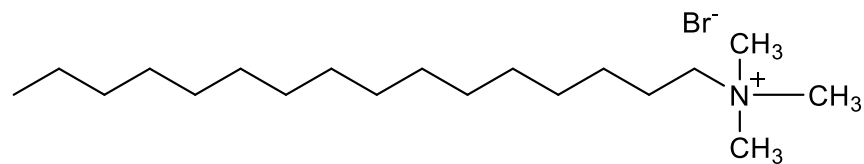
Cetyltrimethylammonium bromide (CTAB)
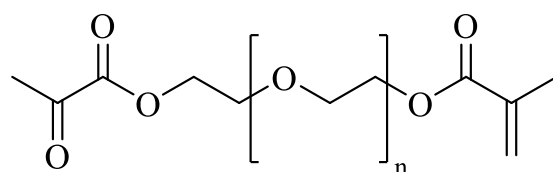
Polyethylene glycol (PEG)

Figure 7.1: Chemical structures of the surfactants used in the synthesis of mesoporous silica: CTAB (top) and PEG (bottom), a polymer with an average of 110 repeating units.

In chapter two, we described all the techniques used for the experimental analyses in this thesis and their principles of operation. They include NMR, TEM, powder XRD, UV-vis spectroscopy and time-resolved fluorimetry.
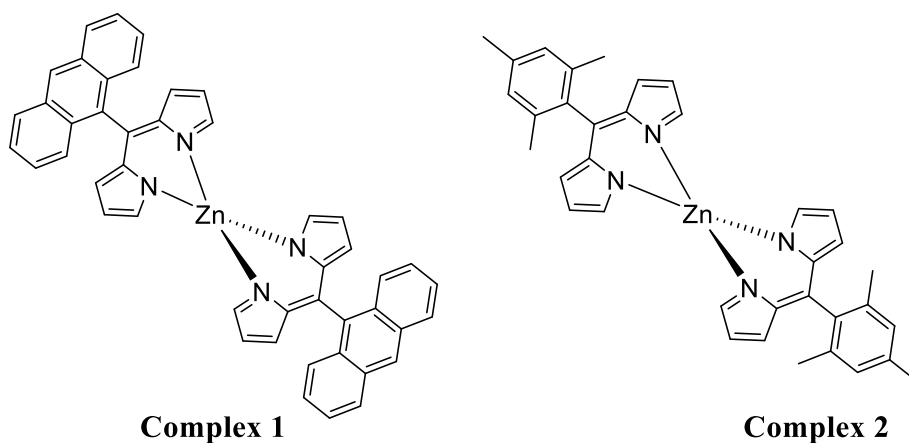
Complex 1   Complex 2

Figure 7.2: Chemical structures of Complex **1** (left) and Complex **2** (right).

Chapter three presented two weakly-emitting zinc complexes (1 and 2), bearing the dipyrromethene ligand. Both complexes were successfully added into the micellar template of the COK-12 at a very low loading (1%). TEM and SAXS studies showed that the structure and morphology of the final materials were retained. The quantum yields of both complexes, when

incorporated into the micelles, improved significantly from less than 0.001 and 0.16 when free in solution to 0.35 and 0.55, respectively, for 1 and 2. It was also found that the type of substituent attached at the meso-position of the ligand has an overall effect on the optical properties and, in the case of complex 1, may promote intermolecular aggregation. Furthermore, complex 2, when incorporated into silica, shows promising photostability and retains its emission intensity compared with the free complex that can easily photo-bleach in less than 2 hours. The hybrid materials built with such complex are good candidates for use as solid-state sensitisers in solar concentrators.
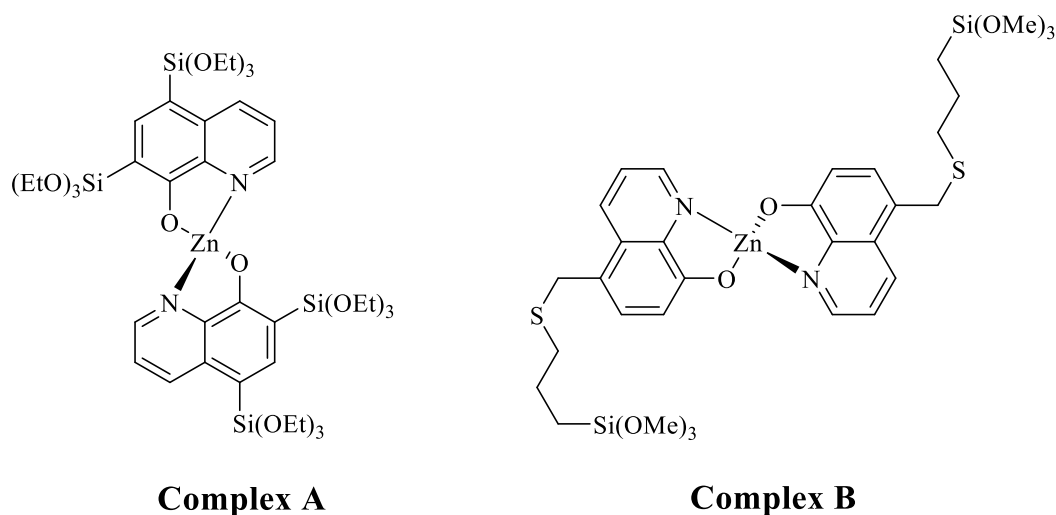
Complex A   **Complex B**

Figure 7.3: Chemical structures of Complex **A** (left) and Complex **B** (right).

We also studied two more zinc(II) complexes in chapter four, both bearing quinolinolate ligands and used to synthesise new PMO materials. The first target in this chapter was the synthesis of both complexes and the encapsulation within the silica wall. The complexes absorb and emit around 265 nm and 550 nm, respectively, and they are also weak emitters in the solution. Complex A was successfully encapsulated on the silica wall at up to 100% loadings, and the resulting quantum yield increased significantly, from 0.26 in solution to 0.56. The TEM images show regular hexagonal arrays of channel-like pores, which are typical of COK-12 and confirm that the structure of the material is retained; the only exception appears to be the PMO with the highest loading. The same structural information showed with complex B, which was made using MCM-41 instead. However, as opposed to the former, the quantum yields do not increase consistently with an increase in loading, and the best performing material is the PMO with 5% loading; this showed a quantum yield of almost 0.05, whereas the value for the free dye in solution is 0.003. Upon

comparison, both PMOs exhibit long excited-state decay traces, indicating charge recombination fluorescence when in the silica framework. Complex A, which showed the highest emission efficiency inside the silica, is a promising material for developing new organic light-emitting diodes.
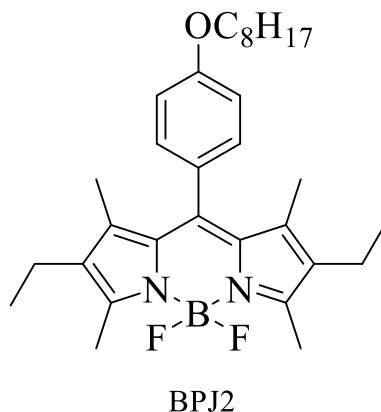
Figure 7.4: Chemical structure BPJ2 synthesised from BODIPY

Chapter five presents detailed research carried out on the photophysical properties of mesoporous silica with a BODIPY dye (BPJ2) loaded in the micellar template. The optimum time for the complete incorporation reaction and to achieve uniform distribution of the guest was found to be 2 hours under reflux. The advantage of the optimal dye dispersion is that it prevents intermolecular aggregation, which causes quenching of the excited states. High loadings, up to 50%, do not alter the structure and the morphology of the final silica materials. Previous findings on this type of material in the group showed that certain factors in the synthesis process, such as the addition of NaOH and TEOS, and oven-drying, induce the formation of a new blue-emitting chemical species. The new findings reported in this chapter helped determine that the drying conditions are playing the crucial role; indeed, by drying the samples in a desiccator at room temperature, no additional chemical species is observed, which confirmed that its formation is triggered by high temperatures (80 ^{0}C). The optical properties of the dye-doped silica sample with 10% loading are the best among the sample series, with a fluorescence quantum yield of 0.62. Furthermore, as the loading increases above 20%, dimers are formed, and an inner-filter effect is observed. Both phenomena are caused by the high concentration of dye molecules within the silica template. One more interesting result was the detection of a short energy migration trace that has been observed with 1% and 10% loadings; this was found to be between 400 and 700 ps, whereas it was impossible to determine

the transfer time accurately for samples with higher concentrations of dye, due to the time resolution of our instrument being limited to 60-80 ps. It is worth recommending further analyses with a technique suitable for sub-picosecond spectroscopy, such as femtosecond transient absorption.
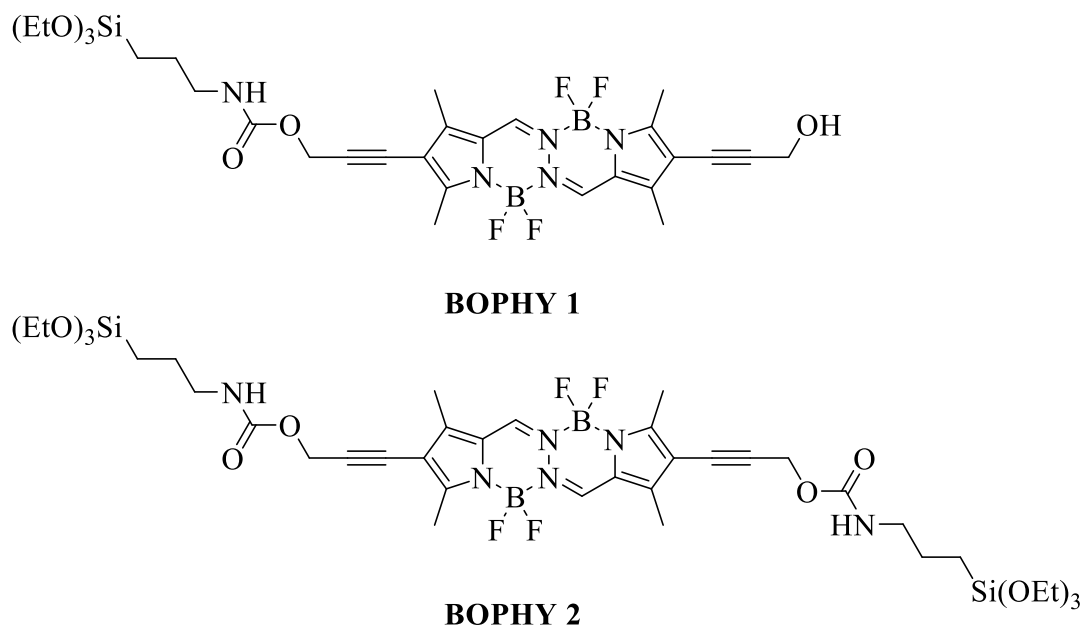
Figure 7.5: Chemical structures of BOPHY 1 (top) and BOPHY 2 (bottom).

The final experimental chapter describes how two different BOPHY dyes with one and two alkoxysilanes were attached to the silica walls to synthesise new PMOs. The free dye has a high quantum yield of 0.86. The fluorescence yield was found to decrease as the loading in the silica walls increases from 1% to 5%. This could be due to the fact that above 1% loading, the distance between single units of dye is reduced, resulting in dyes quenching each other. It was also observed a dual excited-state decay in all PMO materials: a short component (about 2 ns), which matches the typical singlet lifetime of BOPHY dyes, and a long component (up to 20 ns), attributed to delayed fluorescence, which most likely occurs via charge recombination. Moreover, the majority of the samples show a very fast decay trace (from 400 to 800 ps) when analysed by fluorescence anisotropy. This is similar to what was observed from the dye-doped silica materials in chapter 5, and it is ascribed to the occurrence of energy migration between dye units.

In conclusion, the research conducted over the last four years has allowed us to develop new light-harvesting materials using some of the available strategies of incorporating dyes into mesoporous silica. The most promising materials are those built by encapsulation of guest dyes into the micellar template of mesoporous silica. The high rigidity imposed on the dyes and the effective shielding from solvent- and oxygen-induced degradation are the two crucial factors behind the excellent photostability of the materials. The organosilica systems, where the dyes are an integral part of the solid-state structure, need further optimisation in order to increase the luminescence efficiency. Nevertheless, they exhibit interesting properties, such as charge-recombination fluorescence, which is suitable for use in light-emitting devices, and fast energy migration, which can be exploited to design new solid-state photosensitisers. One more area of future expansion for this research is the synthesis of new organometallic dyes, where a central metal ion such as zin(II) is coordinated to two different bidentate ligands, that is, a quinolinolate and a dipyrromethene. It is expected that such heteroleptic complexes will have more pronounced charge-transfer character than the homoleptic ones, a property that can be used to design new artificial photosystems capable of more efficient energy and electron transport.